Design and evaluation of a shape memory alloy-based tendon-driven actuation system for biomimetic artificial fingers

by

Vishalini Bundhoo
BEng., University of Mauritius, 1999

A Thesis Submitted in Partial Fulfillment
of the Requirements for the Degree of

MASTER OF APPLIED SCIENCE

in the Department of Mechanical Engineering

Supervisory Committee

Design and evaluation of a shape memory alloy-based tendon-driven actuation system for biomimetic artificial fingers

by

Vishalini Bundhoo
BEng., University of Mauritius, 1999

Supervisory Committee

Dr. Edward Park, Department of Mechanical Engineering, University of Victoria; School of Engineering Science, Simon Fraser University
Supervisor

Dr. Martin Jun, Department of Mechanical Engineering, University of Victoria
Departmental Member

Dr. Nikolai Dechev, Department of Mechanical Engineering, University of Victoria
Departmental Member

Supervisory Committee
Dr. Edward Park, Department of Mechanical Engineering, University of Victoria; School of Engineering Science, Simon Fraser University
Supervisor

Dr. Martin Jun, Department of Mechanical Engineering, University of Victoria
Departmental Member

Dr. Nikolai Dechev, Department of Mechanical Engineering, University of Victoria
Departmental Member

Abstract

This thesis presents the preliminary work in the development of a biomimetic actuation mechanism for prosthetic and wearable robotic hand applications. This work investigates the use of novel artificial muscle technology, namely, shape memory alloys. The mechanism developed is based on the combination of compliant tendon cables and one-way shape memory alloy wires that form a set of agonist–antagonist artificial muscle pairs for the required flexion/extension or abduction/adduction of the finger joints. For the purpose of this thesis, an anthropomorphic four degree of freedom artificial testbed was developed with the same kinematic properties as the human finger. Hence, the size, appearance and kinematic architecture of the index finger were efficiently and practically mimicked. The biomimetic actuation scheme was implemented on the anthropomorphic artificial finger and tested, in an ad-hoc fashion, with a simple microcontroller-based pulse width modulated proportional derivation (PWD-PD) feedback controller. The tests were done to experimentally validate the performance of the actuation mechanism as emulating the natural finger's joints movement. This thesis details the work done for the finger design process as well as the mechanisms and material used to achieve the actuation and control objectives. The results of the experiments done with the actuation platform are also presented.

Table of Contents

Supervisory Committee ii

Abstract iii

Table of Contents iv

List of Tables ix

List of Figures x

Acknowledgments xiii

Dedication xv

Chapter 1: Introduction 1

1.1 Robotic Technology for Hand Rehabilitation 2
1.2 Motivation 6
1.3 Thesis Objectives 8
1.4 Novel Contribution 9
1.5 Thesis Organization 10

Chapter 2: Literature Review 12

2.1 Articulated Robotic Hands 12
2.1.1 Belgrade/USC Hand 12
2.1.2 Salisbury/JPL Hand (1981) 14
2.1.3 Utah/Mit Hand (1982) 15
2.1.4 NTU Hand 16
2.1.5 DLR Hand 17
2.1.6 Nasa's Robonaut Hand 19
2.1.7 The Shadow Hand 22
2.1.8 Southampton Remedi Hand 24

2.1.9 I-Limb 26
2.2 SMA-Actuated Articulated Hands 28
2.2.1 Hitachi Hand 28
2.2.2 Rugters Hand 29
2.2.3 Other SMA-Actuated Mechanisms 31
2.3 Wearable Monitoring Devices 32
2.3.1 HumanGlove 33
2.3.2 Data Gloves 34
2.3.2.1 Cyberglove II 34
2.3.2.2 Cybergrasp 35
2.3.2.3 Cyberforce 36
2.3.3 The Rugsters Master II-ND Data Gloves 36
2.3.4 Hand Mentor Pro Rehabilitation System 38
2.3.5 Howard (Hand-Wrist Assistance Robotic Device) 39

Chapter 3: Human Hand Physiology 41

3.1 Hand Bones 43
3.2 Hand Joints and Movements 44
3.2.1 Finger Joints and Movement 46
3.2.1.1 Metacarpophalangeal Joint 46
3.2.1.2 Proximal and Distal Interphalangeal joints 48
3.2.2 Thumb Joints And Movement 49
3.3 Finger Musculature 51
3.3.1 Finger flexors 51
3.3.2 Finger extensors 52
3.3.3 Other intrinsic muscles 53
3.4 Extensor Mechanism 54
3.5 Flexor Mechanism 55
3.6 Hand movements and grips 57
3.7 Hand Senses 58
3.7.1 Tactile Sense 58
3.7.2 Proprioception 59

Chapter 4: Design of Biomimetic Artificial Finger Testbed 60

4.1 Anthropomorphically Accurate Size And Appearance 62
4.2 Kinematically-Accurate Motion 67
4.2.1 Finger Kinematic Analysis 71
4.2.1.1 Forward Kinematics 73
4.2.1.2 Inverse Kinematics 74
4.3 Biomimetic Sensory Feedback 76
4.3.1 Sensors for Robotic Hands 76
4.3.2 Artificial Finger Sensory Feedback Mechanism 78

Chapter 5: Biomimetic Actuation Mechanism 81

5.1 Artificial Muscle Actuators 82
5.2 SMA Artificial Muscles 83
5.2.1 Principles of SMA Behaviour 84
5.2.1.1 Shape Memory Effect 84
5.2.1.2 Superelasticity 87
5.2.1.3 Stress-Strain Relationship During SME 88
5.2.1.4 Hysteresis 89
5.3 Biomimetic SMA-Driven Actuation Mechanism 90
5.3.1 Biomimetic tendon architecture 91
5.3.2 Biommetic actuation mechanism 93
5.3.2.1 Actuation Sequence 95
5.3.2.2 Compliant Differetial Actuation 96
5.3.2.3 Limiting Factors 97
5.4 SMA Actuator Selection 99
5.4.1 SMA Actuator Stroke 99
5.4.2 SMA Actuator Force 100
5.4.2.1 Static Forces For Index Finger Functions 100
5.4.2.2 Derivation Of Torque Equations 103
5.4.2.3 Evaluation Of Artificial Index Finger Joint Torques 106

5.4.2.4 Defining SMA Actuator Force 108

Chapter 6: Modeling and Simulation 113

6.1 SMA Mathematical Model 114
6.1.1 Micromechanical Models 114
6.1.2 Macroscopic Models 115
6.2 Liang & Rogers's SMA Model 116
6.2.1 SMA Constitutive Equation 117
6.2.2 SMA Phase Transformation Equations 119
6.3 SMA Heat Transfer Model 122
6.4 Joint Kinematic Model 122
6.5 Dynamic model 123
6.6 Simulation 124
6.6.1 Modeling Parameters 125
6.6.2 Open-loop simulation 126

Chapter 7:Experimental Evaluation of the Biomimetic Actuation Mechanism 130

7.1 Experimental setup 130
7.2 Sensor calibration 135
7.3 Control strategy 139
7.3.1 PWM modulation 140
7.3.2 Control scheme 141
7.4 Experimental results 143
7.4.1 Finger motion 143
7.4.1.1 Open-loop motion 144
7.4.1.2 Closed-loop motion 152
7.4.2 Fingertip force 160
7.4.2.1 Open-loop test 161
7.4.2.2 Closed loop test 162

Chapter 8: Conclusion and Future Work 165

8.1 Conclusion 165

8.2 Discussion and Future Work 166

8.3 Future goal 168

References 170

APPENDIX A 178

APPENDIX B 179

APPENDIX C 184

APPENDIX D 186

List of Tables

Table 3.1: Flexion/Extension ranges of index finger 49
Table 4.1: Finger prototype phalangeal length estimates 64
Table 4.2: Finger prototype joint depth and breadth estimates 64
Table 4.3: Joint center location estimates 64
Table 4.4: D-H Parameters for artificial finger 72
Table 5.1: SMA actuator stroke 100
Table 5.2: Index finger joint flexion angles for various functions 101
Table 5.3: Normalized externally applied forces on the index finger 102
Table 5.4: Joint torques for unit force acting on finger phalanges (index finger) 107
Table 6.1: Numerical simulation parameters for the MCP joint 126
Table 7.1: Joint response times 160

List of Figures

Figure 1.1: MIT MANUS therapy robot 3
Figure 1.2: Handy-1 assistive robot 4
Figure 1.3: Otto Bock SensorHand 5
Figure 2.1: The Belgrade/USC Hand 13
Figure 2.2: Salisbury Hand 14
Figure 2.3: Drivetrain of the Salisbury Hand 15
Figure 2.4: Utah/MIT Hand 16
Figure 2.5: The DLR Hand 18
Figure 2.6: DLR Hand II 19
Figure 2.7: The Robonaut hand 20
Figure 2.8: Robonaut hand mounted on the Robonaut arm 21
Figure 2.9: The Shadow Hand 22
Figure 2.10: Prehension capabilities of the Shadow Hand 23
Figure 2.11: The Southampton Remedi Hand 25
Figure 2.12: iLimb grasping configurations 27
Figure 2.13: The artificial (upper hand) covered by a life-like cosmesis 28
Figure 2.14: Hitachi Hand 29
Figure 2.15: SMA-actuated SLS prototyped robotic finger 30
Figure 2.16: HumanGlove 34
Figure 2.17: CyberGlove 11 system 35
Figure 2.18: CyberGrasp force feedback system 36
Figure 2.19: CyberForce system 36
Figure 2.20: Rutgers Master II Hand – New Design 37
Figure 2.21: Hand Mentor 38
Figure 2.22: HWARD grasping an object during therapy 40
Figure 3.1: Terminology defining hand movement and orientation 42
Figure 3.2: Hand bones – palmar view 44
Figure 3.3: Hand movements 45
Figure 3.4: Joints of the hand 46
Figure 3.5: Volar plate and collateral ligaments at MCP 47
Figure 3.6: a) Extension of the MCP and PIP joints
b) Flexion of the MCP joint
c) Flexion of the PIP without flexion of the MCP joint
d) Flexion of PIP and MCP joint 48
Figure 3.7: Motions of the thumb 50
Figure 3.8: Anatomy of the finger 52
Figure 3.9: Extensors and dorsal hood of the finger 53
Figure 3.10: Simplified model of extensor mechanism 54
Figure 3.11: Flexion of the index finger 56
Figure 3.12: Hand configurations 58
Figure 4.1: The index bends vertically. Other digits' joint axes are oblique causing fingers to converge radially in flexion 61

Figure 4.2: Joint center measured from bone base, phalangeal length and depth, MCP, PIP and DIP joints location..... 63
Figure 4.3: CAD models for the proposed biomimetic artificial finger for the experimental testbed - extended states..... 65
Figure 4.4: CAD models for the proposed biomimetic artificial finger for the experimental testbed- flexed states..... 66
Figure 4.5: Anthropomorphic finger prototype..... 67
Figure 4.6: Finger Kinematic Architecture..... 68
Figure 4.7: Alignment of MCP, PIP, and DIP joints in the extended position..... 69
Figure 4.8: Normal resting position of the finger..... 70
Figure 4.10: Fingertip orientation angle α used as input to the inverse kinematic solution together with x-y-z coordinates of the fingertip..... 75
Figure 4.11: Resistive bend and force sensors..... 78
Figure 4.12: A CAD representation of potentiometers and bend sensor embedded in the artificial finger..... 79
Figure 5.1: Grid-like representation of SMA structure..... 85
Figure 5.2: Methods for bias forces..... 86
Figure 5.3: Stress-strain relationship in superlastic behaviour of SMAs..... 87
Figure 5.4: Stress-strain behavior SMAs in austentic and martensitic phases..... 88
Figure 5.5: Stress-strain curve showing SME as used in SMA actuators..... 89
Figure 5.6: Hysteresis loop in SMAs..... 90
Figure 5.7: Artificial finger tendon configuration..... 92
Figure 5.8: Differential spring-biased SMA joint actuation mechanism..... 95
Figure 5.9: Artificial tendon spring-slack arrangement emulating the..... 97
Figure 5.10: Frames of references and grasping forces on index finger..... 104
Figure 5.11: Forces acting on the finger link..... 108
Figure 6.1: SMA stress – temperature profiles]..... 121
Figure 6.2: Schematic representation of mathematical model for SMA-actuated finger joint..... 125
Figure 6.3: Open loop control of MCP Extension..... 128
Figure 6.4: Open loop Simulation of MCP Flexion..... 129
Figure 7.1: Schematic representation of experimental hardware..... 131
Figure 7.2: DM01-15 SMA actuator from Miga Motor Company..... 132
Figure 7.3: Artificial finger testbed attached remotely placed SMA actuators..... 134
Figure 7.4: Sensor response plot for MCP adduction potentiometer calibration curve..... 136
Figure 7.5: Sensor response for MCP abduction potentiometer calibration curve..... 137
Figure 7.6: Sensor response MCP flexion/extension potentiometer calibration curve..... 137
Figure 7.7: PIP flexion/extension bend sensor calibration curve with a 4^{th} order polynomial fit..... 138
Figure 7.8: Fingertip force sensor calibration curve..... 139
Figure 7.9: PWM-PD control of finger joint..... 142
Figure 7.10: MCP abduction open-loop motion profile..... 146
Figure 7.11: MCP adduction open-loop motion profile..... 147
Figure 7.12: MCP Extension open-loop motion profile..... 148
Figure 7.13: MCP Flexion open-loop motion profile..... 149
Figure 7.14: PIP Extension open-loop motion profile..... 150

Figure 7.15: PIP Flexion open-loop profile 151
Figure 7.16: Closed-loop MCP abduction motion profile and the current profile of the corresponding SMA actuator. 153
Figure 7.17: Closed-loop MCP adduction motion profile and the current profile of the corresponding SMA actuator 154
Figure 7.18: Closed-loop MCP extension motion profile and the current profile of the corresponding SMA actuator 155
Figure 7.19: Closed-loop MCP flexion motion profile and the current profile of the corresponding SMA actuator 156
Figure 7.20: Closed-loop PIP extension motion profile and the current profile of the corresponding SMA actuator 157
Figure 7.21: Closed-loop PIP flexion motion profile and the current profile of the corresponding SMA actuator 158
Figure 7.22: Fingertip and tendon force for open-loop motion of PIP joint 162
Figure 7.23: Sensor A to D counts and measured fingertip force 163

Acknowledgments

It has been a long road and I will try my best to express my sincere thanks to the many people who have been part of the journey…

I would like, first and foremost, express my utmost gratitude to Dr. Edward Park for having given me the opportunity to do this degree and contribute to his research work. I thank you for your support and your patience. It is greatly appreciated.

I would like to give a heartful thanks to my office mates: Dilian Stoikov, Kerem Gurses, Kelly Sakaki, Dan Kerley, Kerem Karakoc, Kevin Huang, Jungkeun Lee, William Liu, Sandra Makosinski and others. You have certainly made the lab a fun place to be. Your friendship is dearly valued and forever cherished. Special thanks go to Dan and Kevin for sharing my modeling and simulation woes. Your help was greatly valued.

I would like to give special thanks to Edmund Haslam, whose genius and resourcefulness never cease to amaze me. I could never have done this research were it not for your expert help in setting up the experiment and the controller. Thank you for support and being a listening ear on so many occasions.

I would like to extend my thanks to Gabriele Gilardi. The simulation and modeling would still have been an unsolved mystery were it not for you. Thank you for taking time to explain the mechanics of the simulation model.

Special thanks also go to Flavio Firmani for taking time out his busy schedule to check my work. Your generous help was highly appreciated.

I would like to thank Dorothy Burrows, Preet Grewal, Doug Thompson, Erin Sebastian and other members of the administrative staff who have helped me figure out the departmental procedures.

A quick hello goes to Naznin Virji-Babul. Although the work at the Queen Alexandra Hospital was not included in this thesis, the experience at QA gave me an invaluable insight of hand rehabilitation efforts on the island.

Last but not least, I would like to give a big shout-out to Imtehaze Heerah, the man of my life. I really cannot imagine being here without your constant help, patience and care. Thank you for sticking by me through thick and thin. I could not have done it without you…

Special thoughts go my parents and sisters. Your well wishes, support and faith in me were felt throughout the miles. Thank you…

Dedication

To husband, family and friends…

Chapter 1

Introduction

The hand is one the most important organs of the human body as it defines our interaction with the material world. With 5 bendable digits, including an opposable thumb, the hand accounts for up to 26% of the human body's movement potential through the tasks of manipulation, prehension and exploration [1]. The functional uniqueness of the human hand arises from the complex geometric arrangement of joints, ligaments and muscles which operate as a coordinated entity to provide a wide range of versatile movements. The intricate mechanics of the hand's musculoskeletal system allows for an extensive range of manipulative tasks with not only high dexterity but also adjustable strength. The fingers and thumb can be bent in a strong grasp, referred to as the power grip, or into the advanced manipulative movement of the precision grip. We can hence hold a pin in a light pinch grip or twist hard enough to unscrew the cap off a bottle or, yet again, hold a hammer in a strong enough grip to drive a nail in a board.

Besides the hand's versatility and flexibility of motion, the hand acts a sensory organ. Millions of tiny sensitive receptors embedded in the skin enable us to sense and interpret information from the physical world. The skin can gather information about pressure, temperature, pain, surface texture and relay that information to the brain through the central nervous system. The fingertips contain the densest areas of nerve endings making the hand the richest source of tactile feedback of the human body [2]. Finally, the hand is also used as means of communication and allows expression of feelings. Hand gestures are an integral part of our body language and enable us to reinforce a spoken word on both the conscious and unconscious level.

Given the prehensive and cognitive importance of the human hand, impairment or the loss of the hand or the digits can be devastating. The resulting loss of functionality prevents one from performing day-to-day activities. It is equally traumatizing on the psychological level as life roles are altered, especially if the hand injury leads to a loss of employment.

Since the hand is most the used functional organ of the human body, it is unfortunately also the most common site of injury or trauma. An estimated 30% of injuries treated yearly are related to hand and finger injury in the work place [4]. A study performed over a period of 5 years in an academic setting indicated that 40% of the injuries recorded were to the hand with 42% musculoskeletal in nature [3]. Concurrently, Statistics Canada reported that, in 2003, nearly 28% of all work-related injuries involved the hand. In the United States, the National Center for Health Statistics estimated 350000 persons with amputation in 2003, 30% if which were upper limb lost. Furthermore, 50000 new amputations were done every year, with 25% consisting of upper limb amputation the most common being partial hand amputation with the loss of one or more digit [5]. Other causes of hand trauma include cardiovascular disease, traumatic accidents, infection, tumors, nerve injury and congenital anomalies [5].

1.1 Robotic Technology for Hand Rehabilitation

Over the last decades, tremendous technological progress has been made in the state-of-the-art of orthoses and prostheses to rehabilitate the injured or lost hand. More specifically, technological advances have lead to a considerable growth in the field of rehabilitation robotics, a special branch of robotics which aims at building robotic devices as a way to rehabilitate, assist, replace or enhance impaired human motor control capabilities. Rehabilitation robots can be broken down into three main categories [5]:

i) Therapy or training robots

These robots are used in upper and lower-limb movement therapies in order to lessen movement weaknesses. The devices help patients practice specific movements to increase mobility or correct the patient's arm motions to improve their movement potential. Therapy robots are typically 2 or 3 degrees of freedom (DOF) robots embedded with sensors which can measure the work done by a patient and quantify, to some extent, recovery which may have occurred. Example therapy robots are the MIT-MANUS (see Figure 1.1), a planar two-joint arm, which helps a disabled person moved the arm across a table in order to move a cursor on a screen to a specific location. Another example is the MIME which uses a PUMA robot arm to move the patient's arm in a desired pattern to improve range of motion.

Wearable monitoring devices are relatively new but a very important component of therapy/training devices. These devices employ wearable actuators and miniature sensor technology with orthoses, prostheses and other therapy assistive devices [6]. They are used to exercise the impaired limb and capture the movement and muscle activity associated with a given set of functional tasks. With hand rehabilitation, wearable devices often take the shape of robotic exoskeletons or sensor embedded gloves [7- 9]. Wearable technology for the upper limb is explored in more details in the literature review (Section 2.3) of this thesis.

Figure 1.1: MIT MANUS therapy robot [5]

ii) Assistive robots

These robotic systems focus on manipulation, mobility or cognition and help impaired individuals in their daily tasks. Assistive robots typically use the residual abilities of the disabled person and often need to be custom-designed to match the patient's existing abilities (e.g. head position control or a special keyboard to activate to the robot). Assistive robots can be:

- Fixed platform - restricted to previously defined location.
- Portable - can be moved with the disabled person

- Mobile autonomous – can automatically move around and perform pre-programmed manipulation tasks

Some examples are the Handy-1, a fixed-platform assistive robot developed in the United Kingdom (see Figure 1.2), which allows a person to eat one bite at a time by the operation of a single switch. MANUS is portable assistant robotic manipulator which is controlled by a joystick. The MANUS arm is attached to a wheelchair and allows severely handicapped people with little or no hand function perform simple manipulative tasks such as opening a door.

Figure 1.2: Handy-1 assistive robot [1]

A new generation of assistive robots have been introduced in the rehabilitative field recently. Cognitive assistant robots can react to sound, touch or light. They allow interaction such that they are able to transmit feedback to the impaired person. These robots are geared towards the promotion of health and growth in the patient. For example, NICO, a humanoid robot developed at Yale University, is designed to mimic the movements of an infant. It interacts with children and helps diagnose disorders like autism [10]. The Sony-CSL

[1] http://www.dinf.ne.jp/doc/english/Us_Eu/conf/tide98/13/!sidemak.jpe

Playground uses the Sony Aibo robot-dog to test the sensori-motor skills of two to three month old babies [11].

iii) Smart prostheses and orthoses

A prosthesis is an artificial extension that replaces a missing body part while orthoses are devices that support or correct musculoskeletal deformities and/or abnormalities of the human body. This branch of rehabilitation robotics aims at the development of artificial limbs or external supports braces to restore the functionality of the impaired limb. The most commonly used prosthetic devices are body-powered prostheses, such as the VASI Hand or the Otto Bock SensorHand. These are typically simple grippers with one or two DOFs with basic open-close motion [12].

Figure 1.3: Otto Bock SensorHand[2]

Since these prosthetic hands only offer minimal functional restoration, much effort has been put in the last decade towards improving the sensory-motor interface of prosthetic hands. The latest prosthetics technology aims at the development of myoelectric prosthetic arms or hand, that is, prostheses which can be controlled by the EMG signals of residual muscles under the skin's surface. Southampton Remedi-Hand is such hand. It possesses a

[2] http://www.ottobockus.com/

five digit hand with an opposable thumb [13]. More recently, i-LIMB, a myoelectric 5-digit prosthesis by TouchBionics (Scotland) was successfully commercialized [14].

1.2 Motivation

As described, rehabilitation robotics include a wide variety of systems ranging in complexity, from simple adaptive tools to advanced microcontroller-driven mechanisms such as upper-limb myoelectric prostheses and lower-limb powered orthoses [15-18]. Although, the advances in materials, computing and control as well as the miniaturization of sensors and actuators have allowed designers to develop highly effective assistive tools, the development of a high DOF, easily wearable and high-bandwidth robotic exoskeleton is an unsolved problem in rehabilitation robotics [19].

In the related field of industrial robotics, advancements made in terms in actuation, transmission, mechanism design, sensing and control have led to in the development of highly dexterous multi-fingered hands such as the Belgrade/USC Hand, Stanford/JPL Hand, and Utah/MIT Hand [20, 21]. Some of the more recent developments include the more human-like NTU Hand [22], DLR Hand [23], NASA's Robonaut Hand [24] and the commercially-available Shadow Hand (from Shadow Robot Company). It can be argued that industrial robotic technologies can be used towards the implementation of successful rehabilitation robots. However, the problem with building similar hand devices for rehabilitation robotics differs considerably from the industrial robotics context, where the industrial hands typically operate in a structured environment with predefined tasks and, often, with no considerations to the human interaction [18]. Rehabilitation robotics has many technical and non-technical challenges with the following issues becoming more apparent and sensitive [17, 26]:

(i) low cost
(ii) low weight
(iii) noiseless actuation
(iv) anthropomorphic size and appearance
(v) user safety
(vi) human-machine interface

(vii) adaptability

To date, current robotic aids cannot yet restore the sensory-motor performance of the impaired hand to match its biological counter part nor can rehabilitative devices match the flexibility or intelligence of the human therapist [25]. To be more effective, rehabilitation robots should also be intelligent enough to recognize the physical and cognitive abilities of the users and adapt to the human needs accordingly so as to provide a higher level of comfort and functionality [18]. Devices developed must be light and wearable and the robot interface must be simple enough to be used by any person Otherwise the rehabilitative device will meet user rejection. For instance, it is a known fact that in the prosthetic hand field, commercially-available devices (e.g. the OttoBock Sensor Hand or the VASI Hand) have faced high user rejection rates owing to the rigidity of the artificial hands, their low grasping stability, heavy weight, the noisy operation of actuators, as well as the unnatural feel and robot-like motion of the fingers.

To find a solution to this problem, engineers and scientists are turning to nature for inspiration and guidance. Nowadays, more researchers are focused on not only at building mechanical systems that will aid the disabled, but strive towards the development of biomimetic (i.e. life-like) systems having the same adaptability, functionality and cognitive abilities as biological systems. This approach is also coined as biomechanical, bionic or anthropomorphic and essentially refers to the partial or total representation of the functional abilities of a living organism into a mechanical system. The trend in reverse engineering of nature is justified by the fact that, with millions of years of evolution, biological systems have evolved into very efficient and effective mechanisms. It is believed that imitating these systems represent enormous potential to improve the tools that we use.

The work in this research is thereby highly motivated by the recognized need for future rehabilitation robots need to be more human-friendly, not only on cosmetic level alone but in function. There have been continued advances made to human-machine interfaces, development in muscle-like actuator and biomimetic control scheme. It is believed that the application of these technologies can lead to more sophisticated and human-like interfaces which will better suit the needs of rehabilitation robotics. Furthermore, as these biomimetic devices become more affordable, lighter in weight, their ability to autonomously aid human motor functions will increase due to the advances in the above component technologies.

1.3 Thesis Objectives

The primary aim of this work is to develop a biomimetic actuation platform which can be used in the rehabilitation field in the healing treatments of the injured hand. Firstly, we looked at the available actuators for biomimetic motion. Industrial dexterous hands, such as those previously named, commonly use conventional electric or pneumatic actuation methods. However, as mentioned, prosthetic or rehabilitation devices are governed by strict size, appearance, weight, noise and cost requirements [26]. Such considerations hamper the free use of conventional actuators and complex motion transmission devices, which are bulky and noisy.

In an effort to provide a more anthropomorphic solution for the actuation system, we investigated a number of novel actuators that exhibit life-like muscle behaviors. These are referred to as 'artificial muscles' owing to their operational similarity to the human muscle. The most common ones are the McKibben pneumatic artificial muscles [27, 28], Shape Memory Alloy (SMA) artificial muscles and electroactive polymers (EAPs) [29, 30]. SMAs have already been successfully implemented in many biomedical applications, such as in the implementation of flexible catheters and endoscopes [31]. In addition, in literature, SMA muscle wires have been proposed as actuators for a number dexterous hand and finger design, including the Hitachi Hand [32]. De Laurentis and Mavroidis proposed a combined use of SMA wires and tendon cables for dexterous prosthetic hand applications [33]. Very recently, Price et al. [34] proposed a three-fingered SMA based prosthetic hand, with bias-type SMA wires (i.e. composed of an SMA element and a bias spring) directly routed through the finger joints in a traversing arrangements.

This thesis proposes the use of SMAs artificial muscles for the development of a biomimetic actuating mechanism. SMAs are lightweight, direct-driven actuators with high power to weight ratio. They present an efficient way to actuate the finger without adding to bulkiness and mechanical complexity. It should be noted that the human hand consist of a complex and versatile arrangement of muscles, tendons and ligaments whose intricate mechanics produces hand motion. The complex nature of the hand's musculature is not mimicked in this thesis. Instead, SMAs are used to replicate only tendons necessary to produce full range of motion of the finger.

Secondly, an anthropomorphically and kinematically accurate physical model of the natural finger is required for biomimetic actuation system mechanism and its subsequent performance evaluation. To that effect, the natural hand and its physiology - the muscle and tendon architecture and sensory abilities – are studied for emulation. Given the anatomic complexity of the natural hand and its sensori-motor functions, biomimetic representation is limited to a few key elements essential for a life-like representation of the human finger.

This work also aims at emulating tactile sensitivity, the most prevalent sense of the hand. Touch is, however the most complex of all human senses and consist of various components many of which are not fully understood yet (e.g. sensation of cold, wetness, tingling). As such, application of basic tactile force sensor is where anthropomorphism ends. Furthermore, this work includes the use of internal sensors to provide position and orientation feedback like the natural finger. While no attempt was made to match the internal proprioceptive sensors of the human finger, the sensors used aim at providing similar spatial information as those relayed by the finger's sensors.

1.4 Novel Contribution

Many SMA-actuated artificial hands implement uni-directional motion of the joint. SMAs are used to pull or push the artificial link while return to the original or starting position is done a reverse-bias mechanism. However, these actuation mechanism fail at the basic level of anthropomorphism in the sense that the human finger is able to move bi-directionally from its rest position, that is, the finger can bend towards the hand's palm or hyper-extend away from the flat palm.

The novel contribution of this thesis is the development of a SMA-based actuation scheme which permits the artificial finger joints to move bi-directionally in a biomimetic fashion. The design of the SMA actuator itself is beyond the scope of this thesis. Instead, off-the-shelf SMA actuators were integrated with compliant tendons for the development of the biomimetic actuation mechanism.

The compliance of the tendons was implemented via the development of spring-slack element in a each SMA muscle wire actuating a joint. Furthermore, an artificial finger platform based on the natural finger kinematics was built, resulting in a 4 DOF finger

mechanism, with 3 active DOFs and 1 passive DOF as it exists in the human finger. The actuation scheme was applied to three active DOFs of the artificial finger. The novel contribution of this work is the unique design of an actuation scheme which allowed the formation of three true agonist-antagonist artificial muscle pairs by enabling:

(i) bi-directional motion (flexion/extension or and abduction/adduction) of the finger joints

(ii) compliance in the tendons via the spring-slack element

(iii) ability to maintain the nominal resting position of the natural finger.

As a result, the proposed actuation scheme was able to produce similar manipulative and functional abilities found in the natural finger, unlike existing SMA-actuated joints which only permit uni-directional motion of finger joints.

1.5 Thesis Organization

Chapter 2 provides an overview of the existing anthropomorphic robotic technologies, including many of the dexterous, humanoid robotic hands that have been built over the last couple of decades. The chapter provides a glimpse of how robotic technology has evolved with time, in terms of mechanical design, actuation and sensory feedback. This chapter also introduces SMA-actuated artificial hands with emphasis on how SMA wires are used for biomimetic motion. Lastly, this chapter focuses on what we can refer to as 'wearable robotics.' These are devices which have stemmed from robotics concepts and which are worn on the human body for rehabilitative therapies of joints, muscles, tendons and ligaments. Hand devices are considered given the scope of this project.

Any attempt at anthropomorphism requires a solid understanding of that which is being emulated. Chapter 3 outlines the biological entities of the human hand, starting from the bone structure, muscles governing hand motion to the hand's sensory characteristics. The manners in which the hand moves are also presented. Given the anatomical complexity of the human hand, only critical elements necessary for anthropomorphic reproduction of the index finger are presented.

Chapter 4 defines the key factors necessary for any object to qualify as human-like. This chapter proceeds to explain the specific characteristics which are incorporated in the

finger design for anthropomorphic accuracy. These are a finger size consistent with the human finger, biomimetic kinematics of the joints and motion, in-built sensory perception. A CAD model of finger is also presented herein.

Chapter 5 presents one of the core objectives of this project: a biomimetic actuation mechanism. This chapter opens with a justification for SMA as the actuator of choice. The characteristics behaviour of the alloy, that stimulated its use as actuators, is covered. This chapter then provides a detailed description the biomimetic actuation mechanism implemented for the artificial finger designed. The tendon layout as well as the SMA actuation sequence necessary for bi-directional motion at any finger joint are presented. Finally, a static torque analysis, relevant for the SMA actuator identification, is presented.

Chapter 6 offers brief introduction to mathematical modeling concepts used to numerical characterize the behaviour of SMA. The mathematical model employed in this work fully describes the thermomechanical behaviour of SMAs with a stress rate and two phase change equations. This chapter also covers the mathematical modeling of one joint of the finger (MCP). A numerical simulation of the SMA-actuated finger joint is illustrated. The simulation is used to evaluate open-loop control of one joint of the finger.

The practicality of the actuation strategy is experimentally validated in this work. Chapter 7 discusses the hardware necessary to perform the experimental tests. This chapter initially puts forward the results of open-loop experiments with the active joints of the artificial finger. A simple control strategy using proportional derivative pulse width modulation controller is presented. The corresponding closed-loop control results are illustrated and discussed. Open and closed loop tests for the fingertip forces are included in this chapter.

Chapter 8 provides a summary of the work done in this thesis. More importantly it poses suggestions for improvement and goals for future work.

Chapter 2

Literature Review

From the engineering standpoint, the implementation of the artificial hand that replicates the anatomy and physiology of the natural one still represents a daunting challenge. A number of attempts have yielded many artificial hands. Each attempt has, however, concentrated on optimizing one particular feature of the hand, such as, the mechanism, the grasping ability, manipulation capability and so on, with one common major trade-off being between system complexity and dexterity. An artificial hand that exactly emulates the human hand in terms of functionality, weight and dimensions, number and organization of joints is yet to be implemented. However, the multi-fingered models implemented so far do represent the enormous advances made in the field of manipulation research. This chapter gives an overview of articulated hands that have been implemented up to now. SMA actuated mechanisms and available wearable technologies are also presented.

2.1 Articulated Robotic Hands

This section presents some of the most relevant artificial hands starting with models which have paved the way for a robotic hand research. The level of anthropomorphic implementation is emphasized, given the scope of this project.

2.1.1 Belgrade/USC Hand

Belgrade/USC hand [35], illustrated in Figure 2.1, was developed jointly as a combined effort by the University of Southern California and the University of Belgrade, Yugoslavia. The Belgrade/USC hand was a human-like end-effector designed for robotic manipulators, namely the PUMA 560 robot.

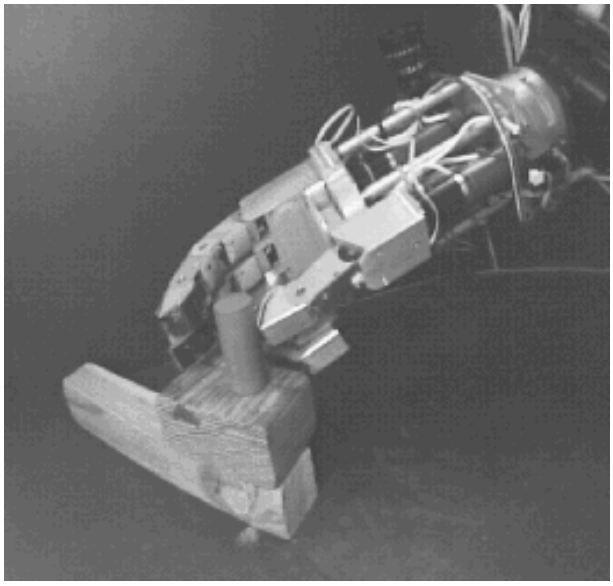

Figure 2.1: The Belgrade/USC Hand [3]

The Belgrade/USC hand was an early representation of an anthropomorphic five-fingered hand with four identical three DOF fingers and an opposable two DOF thumb. In the original design, the five fingers were controlled by a single motor. In later versions, four motors were used, two driving the four fingers and two for the thumb. The motor controlled the first joint and a system of linkages transmitted the lower joint motion to the ones above it. Grasping was accomplished by the closure of all the digits in unison, with the thumb operating twice as fast as the other fingers. When the finger pad encountered an object, all the fingers continued to close until the pressure on all the finger pads were approximately equal. Although, any two fingers in the hand were mechanically coupled, the mechanism allowed for motion of the other fingers if one of the digits was inhibited. The above enabled high degree of shape adaptability and a relatively simple control. Slippage feedback into the control system detected unstable grasps and automatically adjusted the hand configuration for a secure grip. Linear potentiometers were used for joint motion monitoring. Twelve force sensors, two mounted on each digit and two in the palm provided force feedback. The resultant architecture yielded a hand that was well suited for grasping tasks but it was, however, lacking in dexterity for other applications.

---

[3] www-anw.cs.umass.edu/ ~fagg/gallery.html

2.1.2 Salisbury/JPL Hand (1981)

The Salisbury Hand [35], or commonly known as the Salisbury/JPL Hand was designed by Kenneth J. Salisbury as part of his doctoral research (Figure 2.2). The unit was not meant for industrial applications but was sold mainly to universities or research departments for demonstration purposes .

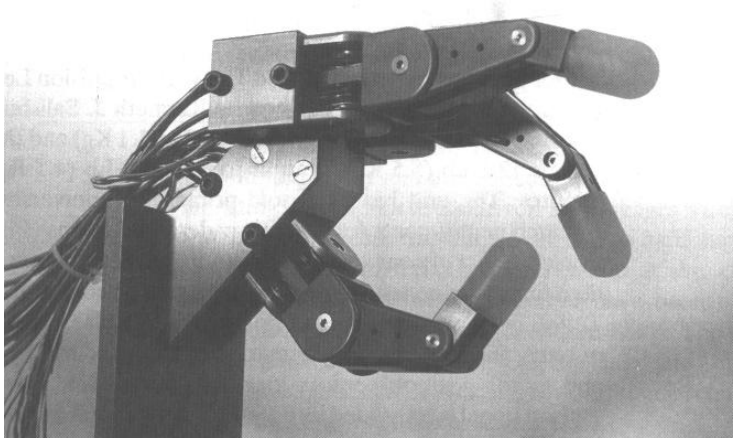

Figure 2.2: Salisbury Hand [35]

The Salisbury Hand possessed three fingers, each with three DOFs. The hand followed the (N+1) drive configuration, which stated that (N+1) tendons and motors are necessary to drive N DOFs. Hence, each finger of the Salisbury Hand was driven by four Teflon-coated cables that slid in Teflon lined conduits. Each of the three fingers was composed of a double-jointed head knuckle that provided the joint with ± 90^{o} of pitch and yaw motions. Another joint after the head knuckle (middle finger joint) allowed for a joint motion range of ± 135^{o}. Unlike the human hand, the pitch and yaw did not intersect. Furthermore, the joint range was greater than the human hand joint range capability. The increased range was primarily implemented as a method to compensate for the absence of a third joint as found at the end of the human finger. Finger position was provided by strain gauge sensors and motor position sensors located behind each middle joint. Fingertips were made of a highly compliant rubber-like material that provided friction and, therefore a secure grip. The advantages of the Salisbury Hand design included simplicity of the modular fingers and low cost of parts. Dexterity was however poor since the joint axis of the knuckle head

stacked one axis above the other. Furthermore, the cables were difficult to route through the wrist. The flexible cable drive was also less reliable than direct drive and push/pull cable had limited power transmission capability.

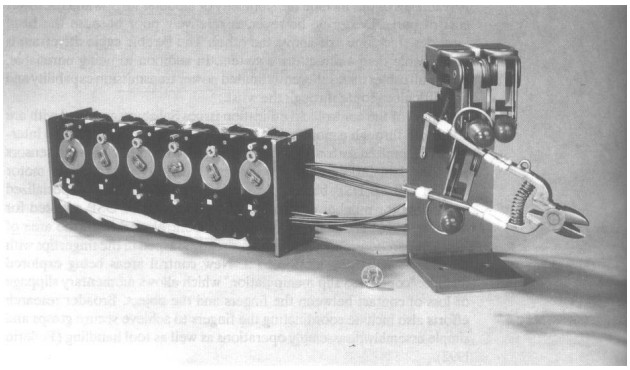

Figure 2.3: Drivetrain of the Salisbury Hand [35]

2.1.3 Utah/MIT Hand (1982)

UTAH/MIT Dexterous Robotic Hand [35, 36] was a pioneer design of a multiple DOF tendon-operated robotic hand of the mid 1980's (see Figure 2.4). The hand was developed for laboratory research on grasping and finger manipulation and introduced innovative feedback sensors and controls. Joint angle information was provided by Hall Effect sensors, which also monitored the tendon tension in the wrist. Sensors located throughout the palm and fingers were used to detect contact with objects.

The UTAH/MIT hand was one of the first robotic hands adopting an anthropomorphic design with outer appearance closely resembling the geometry and size of the human hand. The hand included three 4 DOF fingers, one 4 DOF opposable thumb and a 3 DOF wrist for spatial orientation. Each joint approximated the range of the human hand with approximately 90^o at the three pitch joints and a yaw range of 20^o at the head knuckle. Furthermore, the entire hand was tendon operated with a 2N agonist-antagonist pair configuration (where N is the number of joints being actuated) closely reciprocating the human hand tendon configuration. Pneumatic pistons were used to actuate the joints of the hand and provided a low-weight, high force alternative to the electrical counterpart.

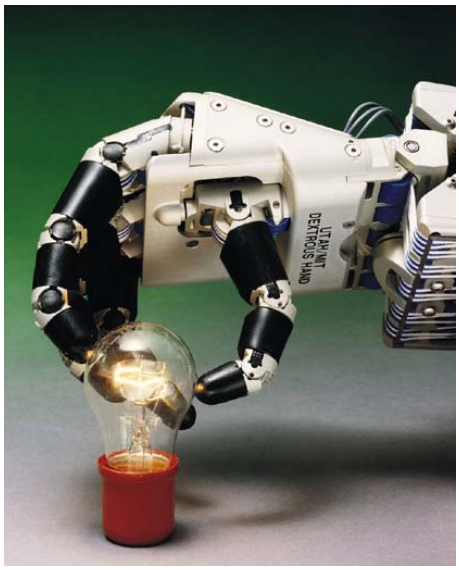

Figure 2.4: Utah/MIT Hand [4]

While the appearance was life-like, the hand mechanism was however non-anthropomorphic. The head knuckle, unlike the human hand's ball-and-socket joint, possessed a yaw axis which was separated from the pitch axis to facilitate tendon routing through that joint. Furthermore, since each joint was actuated by an agonist-antagonist pair of tendons, cabling was very complex and required a separate articulated arm-like frame. While the UTAH/MIT hand possessed a high dynamic performance, enabled by the lightweight cable-tendon design, the reliability of the cable was poor as compared to steel shafts or push/pull rods commonly used in other hand designs. Furthermore, the compliance of the tendons rendered the hand hard to control.

2.1.4 NTU Hand

The NTU hand was developed at the National Taiwan University [37]. The main goal was to develop a dexterous hand for robotics and rehabilitation purposes which emulated the size, the number of DOFs and mechanism of the human hand. The resulting hand was a highly anthropomorphic five-fingered hand with 17 DOFs. The thumb and the first finger had 4 joints, 2 at the knuckle, one at the middle and one at the distal (end) joint. The driving

[4] www.sarcos.com/ telepic_dexhand.html

mechanism of the hand by-passed traditional use of tendon cables and uses a set of efficiently interconnected gear train. All finger segments except the distal segment (fingertip segment) contained a micro motor. The motor drove the gear train to rotate the finger segments. The resulting design was able to perform grasping tasks. Tactile sensors were attached to the inner sides of the finger segments to detect the grasping force. The finger was also modular in design which enabled easy maintenance and replacement of parts when improving the hand performance for rehabilitation purposes. The mechanism was gear driven and, as such, the major drawback was backlash, causing inaccurate joint positioning. The force output of the fingers was also limited to the capacity of the motor and gear strength.

2.1.5 DLR Hand

The DLR hand [38, 39] was a semi-anthropomorphic hand design developed by the German Aerospace Centre design for complex manipulation in space (see Figure 2.5). The main objective was to implement a highly flexible dexterous human-sized where all actuators and sensors are integrated in the palm and fingers. The DLR hand possessed four identical fingers. Each finger has 4 DOFs: 2 DOFs at the base joint for pitch and yaw motions and 2 coupled DOFs at the middle and end joints. Current arrangements of the hand consisted of three fingers and an opposing thumb. Finger joints were actuated by custom designed linear actuators which consisted of a combination of brushless DC motors, tooth belts, harmonic drive gears and bevel gears. Force transmission from the actuator to the joints was done through tendons which rotated pulleys at the finger joints. Two actuators located at the base of the finger controlled the pitch and yaw motions of the finger. A third actuator located in the proximal segment (first finger segment from the knuckle) actuated the middle joint and, by coupling, the distal joint.

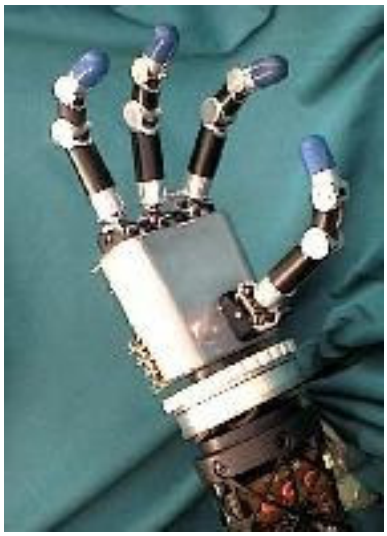

Figure 2.5: The DLR Hand [5]

The finger was equipped with a variety of sensors that literally occupied every available space in the hand: conventional strain gauges measured joint torques, optical position sensors at each joint monitored joint position, customized Hall Effect speed sensors provided information about the motor's rotor and tactile sensors cover each finger and aided in detecting the forces acting on the hand. Several temperature sensors and light barriers were present for security purposes and additionally, the hand was equipped with a six dimensional force torque sensor in the wrist. Although the DLR hand was flexible enough to meet the requirements for autonomous manipulation, due to maintenance problems and the need to reduce weight and production costs, an improved version of the hand was realized, the DLR Hand II (2003), illustrated in Figure 2.6.

[5] www.robotic.dlr.de/.../ hand/previous.html

Figure 2.6: DLR Hand II [6]

The novel features of the DLR Hand II involved fingers that could be bent backwards. Furthermore, an additional minor degree of freedom was enabled the thumb and ring finger to move in opposition during power grasp motions. The hand could hence adopt a "flat'" palm configuration for power grasps or a hand configuration with opposing fingers and thumb for fine manipulation. The level of integration was improved allowing the hand to be removed from a robotic arm in seconds. Finally, a motion teaching was introduced by the use of a data-glove. The DLR Hand has been tested for a number of other applications: teleoperated tasks, tracking and grasping an object with the help of cameras mounted the DLR hand's wrist and as service robot in human environments.

2.1.6 Nasa's Robonaut Hand

The Robonaut Hand [24] is a highly anthropomorphic human-sized hand designed for space-based maintenance operations (see Figure 2.7). The Robonaut Hand was developed by the Johnson Systems Technology branch at the NASA Johnson Space Center. The hand was built to interface with external space station systems that have only human interfaces in order to reduce the burden on the space station crew. The main objectives were to produce a hand that replicated as closely as possible the size, kinematics and strength of a suited astronaut's hand and wrist.

[6] www.robotic.dlr.de/ mechatronics/hand/

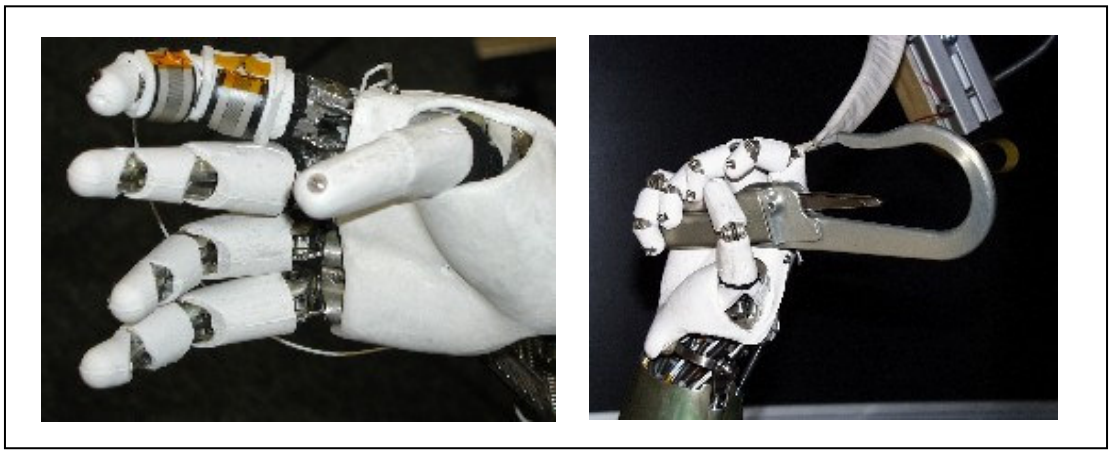

Figure 2.7: The Robonaut hand[7]

The Robonaut hand possesses five fingers with an integrated wrist and forearm, totalling in fourteen independent degrees of freedom. The hand itself can be broken down in two sections: i) the dexterous work set used for manipulation and ii) the grasping set which allowed the hand to maintain a stable grasp during manipulation. The dexterous work set included the index and middle fingers and the thumb. The grasping work set included the ring and little fingers and the palm.

The dexterous fingers constituted of three active DOF at the base and middle joints and a passive DOF at the end joint. The 2 DOF base joint had a yaw of ± 25^{o} and a pitch of 100^{o}. The second and third joints of the fingers were coupled so that they closed with equal angles. The grasping fingers have three pitch joints with 90^{o} of travel each. The thumb had three independent DOFs and was made up of two segments. It is similar in design to the fingers but allowed for more yaw and pitch angles with a base joint of 70^{o} yaw, a 100^{o} pitch and a second thumb joint pitch of 80^{o}. The palm mechanism provided a mount for the fingers and thumb. The fingers were mounted at a slight angle to each other so that they closed similarly to the human hand. The palm also provided an extra degree of freedom by allowing cupping motions which enhanced the grasp stability of the hand. The 2 DOF wrist of the hand had a total travel of ± 70^{o} for the pitch and ± 30^{o} for the yaw. These two axes intersected with each other and also with the centreline of the forearm roll axis. When

[7] robonaut.jsc.nasa.gov/ Hands.htm

connected to the Robonaut Arm (Figure 2.8), these three axes combined at the wrist centre, providing an efficient anthropomorphic kinematic architecture.

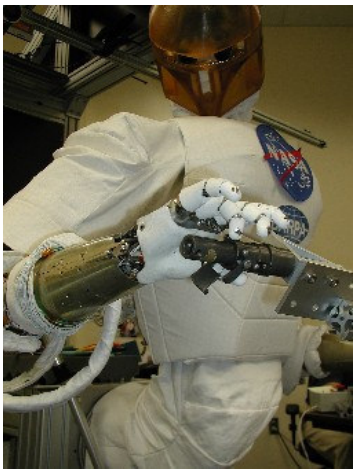

Figure 2.8: Robonaut hand mounted on the Robonaut arm[8]

To match the size of an astronaut's hand, motors and drive electronics are housed in the forearm. All the joints of the fingers are actuated by one leadscrew assembly. Power was transmitted through a flexible drive train. Tendons drives that use complex pulley systems were disregarded owing to wear and low reliability. Instead, flex shafts (have the ability to bend as forces are applied) are used to transmit power from the motors in the forearm to the fingers. The rotary motion of the motor's flex shaft was converted to linear motion using leadscrew assemblies. This resulted in a compact and rugged drive train.

The overall hand is equipped with forty-three sensors, excluding tactile sensing. Each joint is equipped with position sensors and motors with incremental encoders. Load cells are used for force feedback. The design efforts resulted in a highly anthropomorphically dexterous hand whose size and manipulative capabilities closely matched that of a suited astronaut.

[8] static.howstuffworks.com/ gif/robot-robonaut.jpg

2.1.7 The Shadow Hand

The Shadow Hand [40] is one of the most recent implementations of an anthropomorphic robotic hand (see Figure 2.9). The hand was designed by the Shadow Robot Company for CLAWAR Robotics. The main objective of the Shadow Robot Company was to develop a general purpose dexterous robotic that would overcome the common limitations of existing manipulators: restrained applicability and unavailability on the commercial level. In order to reproduce the flexibility, capability and performance of the human hand, the Shadow Hand used the human hand as a model for all designs considerations. This resulted in a hand that was able to operate in all situations where the human being could perform manipulative functions (see Figure 2.10).

Figure 2.9: The Shadow Hand

The hand is made up of four fingers, a thumb and a wrist totalling in 25 degrees of freedom. Each finger possesses four degrees of freedom, two at the base joint for pitch-yaw movements and the two remaining at the middle and distal joints for finger closure. The thumb, on the other hand, unlike the human thumb possesses five degrees of freedom. An extra degree of freedom was introduced at the thumb's second joint for sideways motion. The wrist possesses two degrees of freedom with a pitch range of -90^{o} to 45^{o} and yaw range of -10^{o} to 45^{o}. The two remaining degrees of freedom pertain to the ring and little finger that lift to provide a curl when hand is in a power grasp, for example, when holding a screw driver.

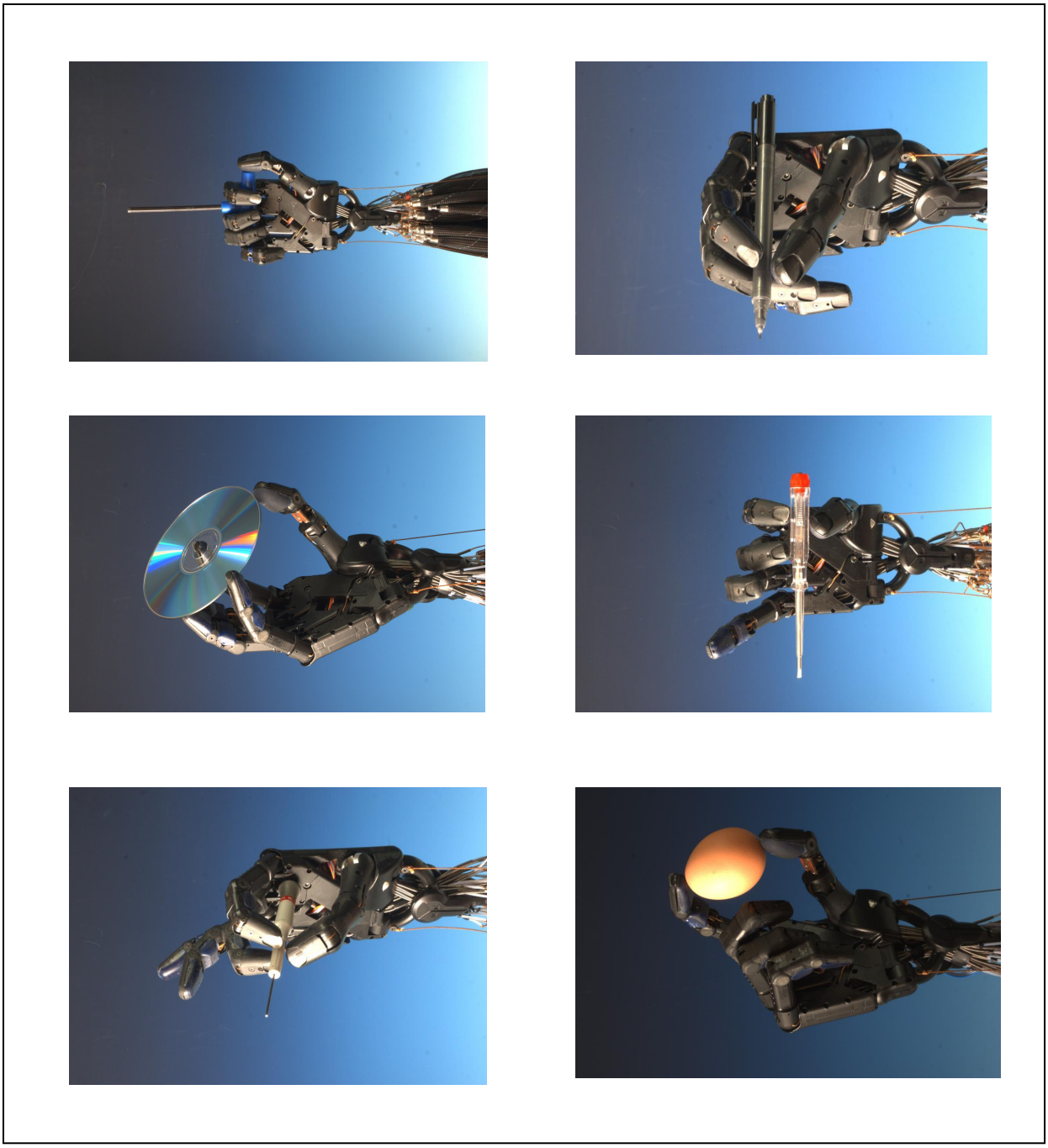

Figure 2.10: Prehension capabilities of the Shadow Hand [9]

[9] http://www.manu-systems.com/shadow_dextrous_hand_en.html

The joints are actuated by 36 pneumatic muscles referred to as “Air Muscles” - a rubber tube covered in tough plastic netting which shortens in length like a human muscle when inflated with compressed air at low pressure. The Air Muscles are densely packed in the forearm. The location in the forearm allows a large number of actuators to be used while keeping the design simple for maintenance. The flexion/extension of the fingers and thumb are done by an agonist-antagonist muscle pairs. Lateral motion of the knuckle joint is achieved by a single muscle and a return spring. All joints are actuated by tendons which are wired through the wrist to the muscles in the forearm. Accurate position of the hand is achieved by the use of Hall Effect sensors. Tactile capability is accomplished by the use an optical sensing mechanism. Currently, a curving palm is the only shortcoming of the hand design. A three-part palm is being proposed permitting some degree of closing around an object. Current work includes production of a more compact hand and improving on the tactile and other sensing modalities.

2.1.8 Southampton Remedi Hand

The Southampton Artificial hand [6, 41], developed at the University of Southampton, has been in existence for several decades. The mechanics of the hand has seen many evolutionary stages where early prototypes were focused on the control philosophy while later designs aimed at signal processing and sensor design. More recently clinical acceptance of the hand has been investigated with the aim at developing a hand for use in the prosthetic field [42]. Southampton Remedi Hand is one of the most advanced myoelectrically controlled prosthesis developed so far, aimed at eliminating common issues of low functionality, heavy weight and lack of sensation of commercially available prostheses.

Figure 2.11: The Southampton Remedi Hand [10]

The Southampton Remedi hand is a 6 DOF hand with four independent 1 DOF digits and a 2 DOF opposable thumb. The four fingers are identical in size and shape with the little finger being smaller in size. To avoid the low mechanical efficiency and backlash issue of tendon-driven or direct driven hands, the finger is driven by a 5-bar linkage system. This mechanism was designed so that the 1 DOF finger followed the natural curling pattern of the human finger. Each digit is powered by a DC motor coupled with a worm-wheel system which prevents the finger from back tracking when power is removed from the motor. The finger has a range of motion of 81^{o} at the base joint. The thumb, powered by 2 DC motors, has a circumdiction (rotate, flex, oppose) and a flexion DOF which enables anthropomorphic motion of this digit

Myoelectric signals are used for open and close motions of the hand with the degree of opening being proportional the muscle tension. While most artificial hands rely on visual feedback to detect slippage (which typically results in the usage of unnecessary large gripping forces), the Remedi hand integrates piezosensor technology with an advanced feedback control system (SAMS – Southampton Adaptive Manipulation Scheme) to replicate the natural control of the hand for slippage. Hence, the fingertip is covered with an array of thick-film sensors which measures grip force (piezoresistive) as well as the onset of slippage (piezoelectric).The controller selects a grip posture such that the contact area between the

[10] http://www.ecs.soton.ac.uk/research/projects/132

fingers and the object is maximized and the grip force minimized. At slip, the grip force is increased, stabilizing the object. At any time, the user can also instruct the hand to increase or decrease the grip force providing better control over the grasping action. Although the SAMS control system is extremely useful in providing cognitive feedback, a new control system which takes into account different levels of control and the patient's control preference is needed [43]. The Southampton Remedi Hand is still in development and not available commercially.

2.1.9 I-Limb

I-Limb [44] is a myoelectrically driven artificial limb developed by Touch Emas Ltd (Scotland) and dedicated for prosthetic application. It has 5 independent digits each controlled by an electric motor. The fingers have three phalanges, like the human hand, with a stationary end joint. The knuckle joint is motor driven and motion transmitted to the middle joint by a tooth belt. Hence, a single motor can cause the whole finger to bend. The thumb is also controlled by a motor and is able to rotate so that it closes to meet the fingers. A microprocessor handles feedback from the motor. Sufficient grip is detected when the motor stops moving against resistance encountered. The microprocessor locks the digit and deactivates the motor until an open signal is received. The hand is configured to perform a number of grips as illustrated in Figure 2.12: a) key grip to hold small flat objects; b) power grip where the digits wrap around an object; c) precision grip for small objects; d) index point useful to operate buttons, e.g., in elevators and keyboards.

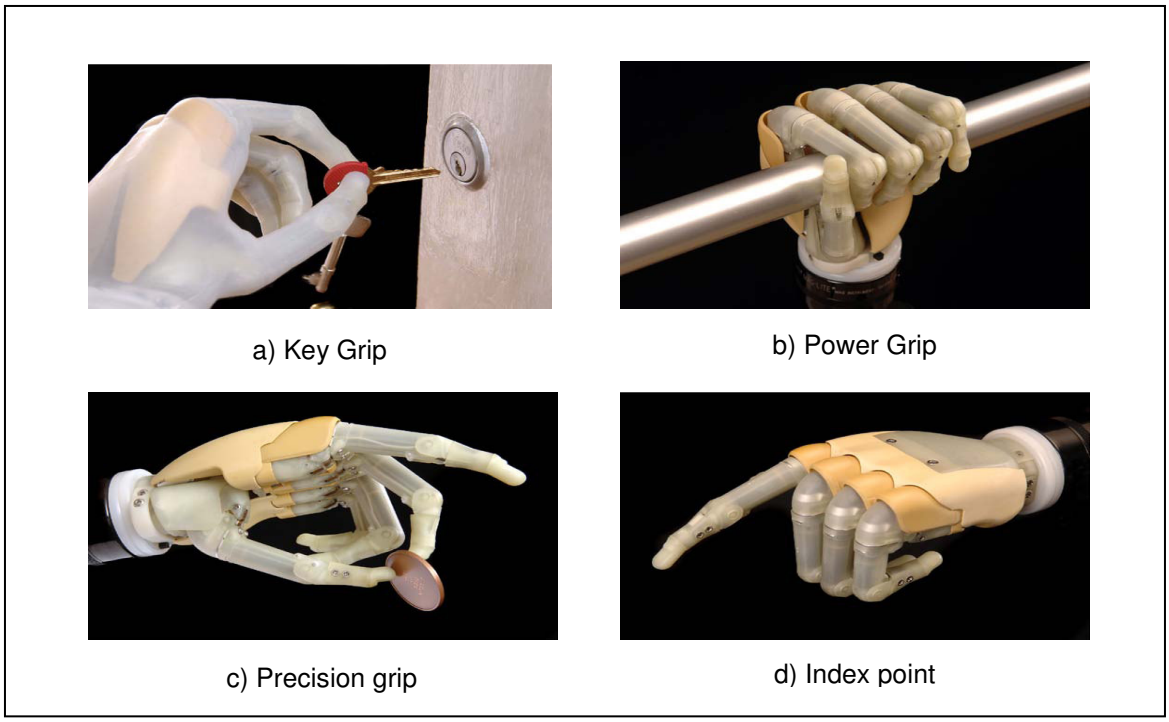

Figure 2.12: iLimb grasping configurations [44]

A modular design was used to build complete hands or partial hands of different sizes with the minimum number of component parts. This enabled parts to be easily replaced at clinics (e.g., a finger can be removed by one screw and replaced). For a biomimetic feel, the hand is covered with a cosmetically appealing life-like skin which moves and looks like the human skin and which protects the hand from dust and moisture. The artificial skin can be translucent or as realistic as the human skin with imitation of the finger nails, pores and hairs (see Figure 2.13). The iLimb is the first fully articulated biomimetic hand which is commercially available. It is available in different sizes for adult males and females and adolescents and has successfully been fitted on numerous patients in the USA and Europe.

Figure 2.13: The artificial (upper hand) covered by a life-like cosmesis

2.2 SMA-Actuated Articulated Hands

This section describes some of the SMA actuated articulated hand which have developed. Focus is placed on the SMA driven mechanisms used to create a biomimetic rendition of the hand's motion.

2.2.1 Hitachi Hand

The Hitachi Hand, illustrated in Figure 2.14, was one of the first articulated hand utilizing novel artificial muscle technologies - Shape Memory Alloys (SMAs). This SMA-actuated hand caused an understandable sensation with its debut in 1984. Its main attributes were its high power-to-weight ratio and compactness. In fact, the Hitachi Hand claimed a 10:1 reduction in weight as compared to other hand designs.

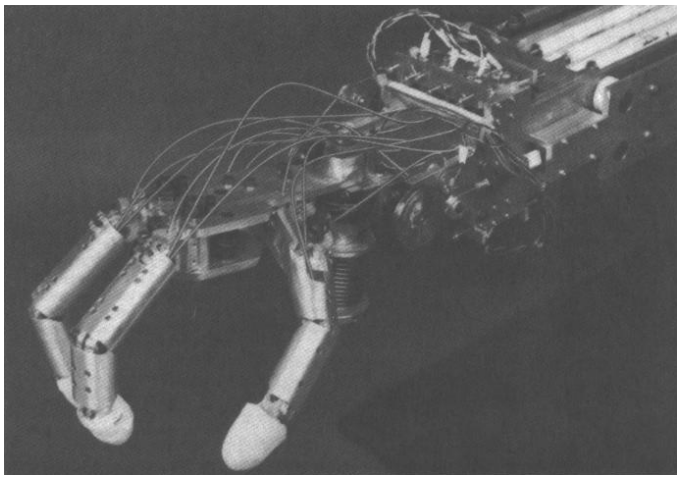

Figure 2.14: Hitachi Hand [35]

The Hitachi Hand constituted of three 4 DOF fingers and a thumb [32]. It also possessed a forearm and a pitch-yaw wrist. It used a large number of SMA wires, actuated in parallel. Electrical heating of the wire resulted in the contraction of the wire against a force spring. On cooling, the wire returned to its original length. The force generated on contraction was used for joint actuation. The joint angle was varied by controlling the current level through the wire, that is, the degree of wire contraction. The Hitachi Hand used 0.02 mm diameter SMA actuators for the fingers. Each DOF of the wrist, on the other hand, were actuated by 0.035 mm diameter SMA wires, set around pulleys. The above mechanism enabled 90^{o} joint travel. Joint positions were sensed by potentiometers.

2.2.2 Rugters Hand

The Robotics and Mechatronics Laboratory of Rutgers University, New Jersey, USA designed a five-fingered, twenty DOF artificial hand, patterned after the human hand [33]. This hand is commonly referred to as the "Rugters Hand" and was designed for prosthetic application. Each digit of the Rutgers Hand has three phalanges similar to the human finger connected by 2 revolute joints. The knuckle joint is a 2 DOF ball end joint permitting lateral (abduction/adduction) movements of $\pm 10^{o}$ as well as flexion/extension movements of 90^{o}. The middle and end joints are 1 DOF flexion/extension joints with a range of motion of 80^{o}. The initial hand prototype was fabricated using the SLS (Selective Laser Sintering) rapid

prototyping technique which enabled a quick three-dimensional rendition of the finger from the CAD model.

The joints of the hand are actuated by a set of cables which attach forward to each joint axis. Tendon cables are routed within the structure of the finger through pivot brackets, which connect the links and allow revolute motions of the latter. The distal and middle links are coupled so that their motions are dependent, similar to the natural movement of the human finger. From the finger, the cables are routed through the middle of the wrist joint and attached an artificial muscle bundle actuator.

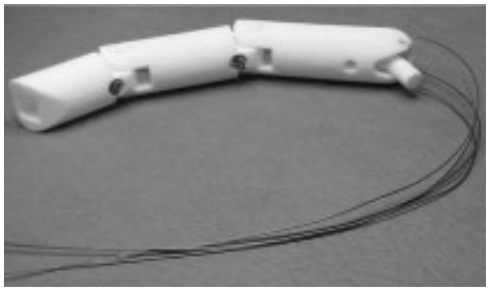

Figure 2.15: SMA-actuated SLS prototyped robotic finger

Actuation of the hand is achieved by a combined action of tendon cables and SMA artificial muscle wires. The SMA bundle actuator consist several SMA wires of different diameters placed parallel to each other and attached between 2 brackets. As the SMA wires contract, the link connected to the SMA actuator (via the tendon cable) move. In the Rutgers Hand, each finger is actuated by four artificial muscle bundles. Two bundles are connected to the knuckle and 2 are connected to the distal joint. One bundle, when actuated, caused flexion at the joint while the other bundle caused the finger to return to its original position. Since a ball end joint is used at the knuckle, lateral motion of the finger is passively induced when the SMA actuators pull on the finger. The Rutgers hand is still in the experimentation phase. Additional work is being done to develop, firstly, a final hand design and secondly, a closed-loop control of the hand.

2.2.3 Other SMA-Actuated Mechanisms

An anthropomorphic finger using SMA springs in a bias-type configuration (i.e. composed of an SMA element and a bias spring) has been designed at the Polytechnic University of Cartegna in Spain [45]. The implemented finger has three independent DOFs. The middle and end joints are capable of flexion and extension whereas the knuckle joint undergoes lateral motions only. The joints of the finger are pulley-driven, that is, steel wires wrap around the pulleys at the finger joints and then connect the actuator. The actuators are SMA-actuated electric pistons. The slider of the piston is connected to an SMA spring. As an electric current shortens the SMA spring, the slider is pulled with force of 450g over a contraction length of 19 mm. The pulling motion of the actuator produces pulley rotation and thereby motion of the finger. A biasing spring, incorporated in the electric piston actuator, returns the finger to its original position.

Very recently, Price et al. [34] proposed a three-fingered SMA based prosthetic hand with bias-type SMA wire. Each finger has 3 revolute joints. The SMA wires are attached directly to the finger structure near the joint. The wires then pass along the link and are directly routed through the finger before being fixed to the end of the link (near the knuckle). Actuation of the SMA actuator (SMA wire length contraction of 5%) induces motion of the finger. Torsion springs placed at each joint provides the bias force to return the joint to its initial position.

A finger spelling robot hand was also recently developed by Terauchi et al which is driven by a combined action of a dc motor and SMA wires [46]. The hand developed has 20 joints and 16 DOFs. The DC motor actuates the first joint (knuckle) joint of the finger. The second and third finger joints are directly driven by SMA wires. A pair of SMA wires is used in a push-pull configuration to actuate one finger joint. A controller carefully applies current to the SMA wire so that when one wire contracts, the opposing wire is allowed to relax. This configuration enables bend motions of 90^{o} at the finger joints.

Numerous SMA-actuated mechanisms have been developed for the actuation of artificial hands or fingers. The reader is required to refer to the following for additional literature [47- 50].

2.3 Wearable Monitoring Devices

We interact with the world using our hands which make the hand very vulnerable to traumas. Hand traumas include occupational injuries which comprise of fractures, dislocations and injury occurring from falls, sudden bending or twisting and sudden impact. These injuries affect the hand's soft tissues, ligaments, tendons, muscles (strains), joints (sprains) and bones. Repetitive motion injuries (also known as occupational overuse injuries or repetitive motion injuries) are another type of hand trauma and occur as a result of repetitive movements of the hand. Repetitive motion injuries affect the muscles, tendons and nerves of the hand (e.g. carpal tunnel syndrome caused by the entrapment of the median at the wrist). Besides injuries, the hand may be affected by number of disorders such as ganglia (cyst around the joint or tendon), deformities, nerve disorders or birth defects [51]. Depending on the severity, hand injuries or disorders may lead to surgery for correction or in extreme cases, amputation.

Treatment approaches for the hand and fingers consists of physical and occupational therapy. Physical therapy focuses on treating the injury whereas occupational therapy focuses on improving the patient's overall functional abilities in order to accomplish daily activities. The treatment path varies depending on the type, location and severity of the injury. However, a common hand rehabilitation process involves the use of custom-fabricated splints, braces or orthoses to rest and protect the affected muscles and joints for the correction of the injury. This is followed by movement hand therapy which typically consists of exercise programs to increase motion, dexterity and strength of the hand. Eventually, training in the performance of daily tasks through adapted methods and equipment is done, prior to a return to the normal life [51].

Conventional movement therapy carried out at hand clinics requires a hand therapist to perform the gentle, repetitive movements of the hand with the patient. The movement therapy treatment requires intense attention of the hand therapist over a long period of time. Improvement of the hand function is assessed by the measurement the range of motion of the finger, strength and ability to perform functional tasks. Traditionally, the range of motion is measured using goniometers while the grip strength is measured by mechanical dynamometers. While the functional assessments made by traditional methods have value, these methods provide static measurement and do not allow the assessment of the sensory-

motor function while the task is being done. Moreover, it is questioned whether the movement therapy done in the clinical environment is truly representative of the gestures a patient performs in the real life. Given the above, it is clear that detailed information about the specific hand movement collected in the patient's home environment would aid in improving the effectiveness of the movement therapy. However, a complete evaluation and analysis of the movement is difficult to perform given the time constraints of the hand therapist and the limited resources of rehabilitation hospitals [7]. Furthermore, the cumbersome and expensive equipment used in a clinical setting cannot be transferred to the patient's home. As such, a number of autonomous and portable wearable systems for clinical applications have emerged lately. These systems help simplify the process of physiological data collection. They can exercise the muscles and joints of the injured with minimal intervention of therapists and, as such, add valuable data to the patient's chart without requiring additional time and effort from the therapist. Wearable systems range from simple monitoring devices for mobility assessment to advanced devices which enable the patient to perform motor tasks that they would not be able to otherwise achieve.

Advancement made in robotics have been a provided a boost to wearable systems. Integrating the design efforts of robotic systems with wearable technology has enabled the development of more complex and flexible orthoses and prostheses. However, the most appealing advancement in robotics is the development of miniature sensors, powerful actuators and implementation of control algorithms which permit wearable technology provide reliable monitoring performance and data collection. This section gives a brief overview of wearable technology currently being used and/or in development.

2.3.1 HumanGlove

The HumanGlove (Humanware, Pisa, Italy) is a wireless sensing glove designed to measure the hand's posture using twenty-two Hall Effect sensors [53]. Four sensors are placed along each finger, three to measure extension/flexion of the interphalengeal joints and one for the adduction/abduction motion of the knuckle joint. Another four sensors are used to measure flexion/extension of the two joints of the thumb and the motion of the base joint during opposition and adduction/abduction motions of the thumb. The remaining two sensors

lie at the wrist and measure extension/flexion and adduction/abduction motions of the wrist respectively. A virtual reality software allows realtime feedback of the hand movements. Data from the sensors are stored and processed by the software, which displays the joint angle profile as well as the angular velocity and acceleration of each joint. Since the glove allows the effective recording of hand movements when performing dynamic functional tasks, it can be used in the hand function assessment and improve rehabilitation treatments.

Figure 2.16: HumanGlove[11]

2.3.2 Data Gloves

Immersion Corporation (San Jose, Ca) is a manufacturer of a number of gloves which are used to sense the position of the individual fingers and provide force feedback to the hand and arm. CyberGlove, CyberGrasp and CyberForce are the trademark gloves of this company [53]. These gloves can be used to capture movement information of the hand to improve rehabilitation methods by assessment of the dynamic motion of the hand.

2.3.2.1 Cyberglove II

The CyberGlove is a sensorized stretch fabric which covers the hand except the finger tips [53]. 18 resistive bend sensors are embedded in the glove and are used to translate hand and finger motion into joint angle data. Each finger uses three bend sensors, two for finger flexion and extension and one for lateral finger motion. The remaining sensors are embedded

[11] http://www.hmw.it/prodotti_e.html

in the glove and measure thumb crossover, palm arch and lateral motions at the wrist. Motion tracking sensors can also be mounted on the glove's wristband to measure the position and orientation of the forearm. The glove is calibrated at the beginning of each session to minimize measurements errors due to varying hand sizes. Data set are read through a serial port at the rate of 70 hand configurations per second. The CyberGlove has seen applications in prototype evaluation, biomechanics and animation.

Figure 2.17: CyberGlove 11 system [53]

2.3.2.2 Cybergrasp

CyberGrasp is an exoskeleton which fits over the CyberGlove and adds resistive force feedback to each finger [53]. Grasping force is provided by a network of tendons which are routed from remotely located actuators, via the exoskeleton, to the fingertips. Each finger is controlled by one actuator, which is programmed to prevent the user from exerting a damaging force on an object. The CyberGrasp allows full range of motion and has been used in telerobotic applications, to allow an operator to control a remotely-located robotic hand and literally "feel" the object being manipulated. The CyberGrasp has been used to rehabilitate children with cerebral palsy.

Figure 2.18: CyberGrasp force feedback system [53]

2.3.2.3 Cyberforce

CyberForce is an armature designed to work with the CyberGrasp exoskeleton and adds resistive force feedback to the hand [53]. Realistic ground forces are applied to the hand and arm through tiny motors embedded in the glove. As such, the CyberForce system allows one to feel the weight, inertia and surface resistance when handling virtual objects. In addition to applying forces, the system also allows positional tracking of the hand and accurately measures the translation and rotation of the hand in three-dimension.

Figure 2.19: CyberForce system [53]

2.3.3 The Rugsters Master II-ND Data Gloves

Rutgers Master II as a haptic interface for the hand and designed to be worn like a glove. Rutgers Master II-ND is a redesigned version of the earlier Rutgers Master II hand

[54]. The main structure of the Rutgers Master II ND hand consists of a small platform on which four custom-made pneumatic cylinders were mounted. Hall Effect sensors embedded on the mounts holding the cylinders and non-contact infrared sensors mounted inside the cylinders provide to position and force feedback.

The Rutgers Master II-ND (RMII-ND) has the same structure as the Rutgers II hand with the difference that the RMII-ND does not use a supporting glove. Instead, an L-shaped exoskeleton is mounted directly in the palm (see Figure 2.20). The platform placement allows full flexion of the fingers. The four custom pneumatic actuators mounted on the L-shaped platform are arranged in a direct-drive configuration and connect the palm to the thumb, index and middle fingers. The direct-drive actuators eliminate the otherwise necessary use of cables and pulleys and result in a much more compact and light structure. The inside layer of the platform contains four highly flexible pneumatic tubes, which when bent with the user's hand motion, cause small resistive forces at the fingertip. The pneumatic actuators mounted at the base of the finger structure permit flexion/extension of all the finger joints as well as the adduction/abduction of the base joint. The force feedback structure consist of Hall effect sensors which measure flexion/extension and the adduction/abduction angles while the infrared sensors measure the displacement of the fingertip with respect to the base.

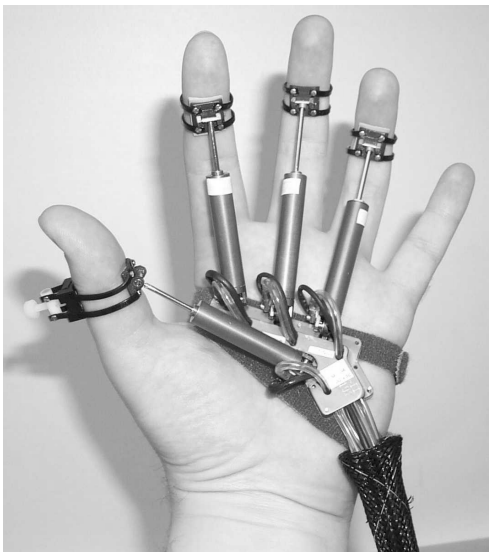

Figure 2.20: Rutgers Master II Hand – New Design [54]

The actuators are driven by pneumatic Pulse Width Modulated (PWM) servo-valves. The haptic interface consists of an embedded Pentium PC, pneumatic valves and electronic boards for reading the glove sensors and implementing pressure control. The embedded processor communicates with a host computer using RS232 communication and enables 300 hand position data and force values to be transmitted every second. Rutgers Master II-ND has been successfully integrated with several types of virtual reality applications, ranging from hand rehabilitation to military command and control.

2.3.4 Hand Mentor Pro Rehabilitation System

The Hand Mentor (Kinetic Muscles Inc, Tempe AZ) [56] is a commercially available hand rehabilitation device for stroke patients. The Hand Mentor is a single DOF device which applies controlled resistive forces to the hand and the wrist and delivers hand therapy by active repetitive motions. The patient's hand is fitted into the exoskeletal structure which contains potentiometers and force-sensing resistors (see Figure 2.21). The device hence can monitor the position of wrist and fingers during flexion-extension motions and the force applied on the hand by the system actuator respectively.

Figure 2.21: Hand Mentor [12]

The patients initiate hand motion and receive assistance only when they cannot complete the movement themselves. For that purpose, compliant high-power air muscle actuators are included in the exoskeleton. Furthermore, the device incorporates surface

[12] http://www.devicelink.com/expo/awards/awards/index.php?catId=-1&year=-1

electromyography (EMG) electrodes which rest against the patient's muscles. An interactive display shows the EMG level associated with the hand movement. The EMG levels displayed provide feedback to the patient regarding muscle activation patterns and allow the patient to exercise the hand and the wrist.

With the help of the EMG signals, the Hand Mentor has the capability to modify treatment protocols to target specific hand issues. Hence, the Hand Mentor can be used to decrease flexor tone of the fingers and wrist by stretching the muscles of the finger beyond the patient's limit of motion (Spasticity Reduction Protocol). The Hand Mentor can improve the movement capability in the fingers and wrist (Motor Control Protocol) and increase the wrist extensor muscle activity (Muscle Recruitment Protocol). Moreover, the Hand Mentor software provides clinician reports and performance goal settings to continuously challenge patients at all levels of rehabilitation. Although designed for stroke patients, the Hand Mentor can be used for hand injuries which need rehabilitative therapy to help restore the range of motion and muscle strength. The Hand Mentor is a useful tool for occupational and physical therapists and can help improve the contact time with the patient for a more efficient therapy routine.

2.3.5 Howard (Hand-Wrist Assistance Robotic Device)

The HWARD [55, 56] is a robotic assistive device (developed by researchers at the University of California) designed for rehabilitation of stroke patients. The HWARD is a pneumatically actuated desk mounted exoskeleton. The exoskeleton wraps around the patient's hand and is attached to the thumb and fingers of the hand (see Figure 2.22). During therapy, patients will grasp and release of variety of objects of different size, shape, surface texture and temperature. The patients initiate the movement and HWARD completes the movement only if the patients cannot do so themselves. For that purpose, the HWARD hand pneumatically is actuated by air cylinders.

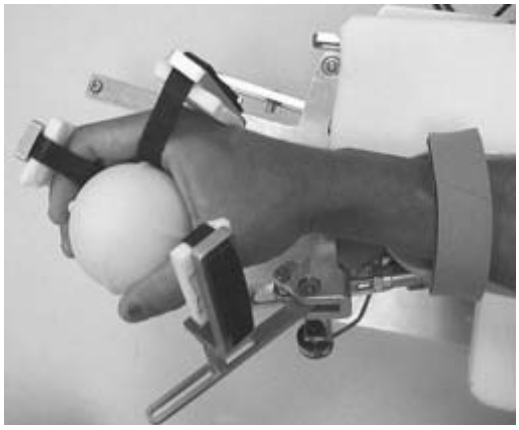

Figure 2.22: HWARD grasping an object during therapy [56]

The exoskeleton itself is a three DOF mechanism which allows flexion and extension of the fingers and thumb about the base joint as well as rotational movement of the fingers, thumb and wrist. Rotary potentiometers embedded in the structure allow measurement of the joint angles at the fingers, thumb and wrist. Pressure sensors mounted on the sides of the air cylinder measure pressure levels and hence the forces applied. The device is interfaced with a computer. The Visual Basic based control software allows the therapist to control the functions of the exoskeleton, execute training protocols given the patient's rehabilitative requirements and collect position and force data for improved therapy movements. Ultimately, the device not only aims at retraining the brain to perform grasp and release functions, but it also promotes tactile sensation in relation to grasping by the use of real objects during therapy.

The reader is referred to [56] for a complete overview of exoskeleton systems and wearable orthoses for the upper arm and hand disabilities. Furthermore, literature with respect to research and development in the field wearable systems and rehabilitative hand exoskeletons is available in [57-61].

Chapter 3

Human Hand Physiology

One of the objectives of this thesis is the development of a test bed which is an anthropomorphic rendition of the human finger. The first emulation step of life-like finger involves of a study of the natural hand in order to extract the elements that are essential for the reproduction of a mechanical counterpart. Given the anatomical complexity of the natural hand, it is necessary to define and clarify some frequently used terms in this chapter to facilitate the contextual description of the hand and promote the reader's understanding of the hand's features. Figure 3.1 gives a pictorial view of some of the terms described below.

- Proximal and distal are terms which define the location of an anatomical component with respect to a central point. Hence, the distal section of a finger would refer to the fingertip whereas the proximal section of the finger would refer to the base of the finger.
- Palmar surface refers to the inner surface of the hand while the dorsal surface refers to the back side of the hand.
- The frontal plane is the plane parallel to the axis of the hand when the fingers extended. The sagittal (or medial) plane lies perpendicular to palm of the hand, that is, perpendicular to the frontal plane. The frontal and sagittal axis of the hand both run through the middle finger.
- Flexion and extension for the hand uses the hand's frontal plane as reference. Flexion refers to the movement of bending a joint so that the finger moves away from the frontal plane so as to close the hand. Extension, on the hand, refer to the movement in which the fingers move towards the frontal plane to form a flat palm
- Adduction is the movement which brings an anatomical component closer to the sagittal plane. Abduction movements draws the anatomical component away from the sagittal plane.

- Ulnar is derived from ‘ulna’ which refers to the outer long bone of the forearm bone (bone on the opposite side of the thumb). ‘Ulnar’ hence refers to a direction opposite the thumb. Radial is derived from ‘radius’, the inner long bone of the forearm located on the thumb side. ‘Radial’ hence refers to the direction towards the thumb.
- The articular surface refers to the surface of a joint at which the ends of the bones meet.
- The term finger only applies to the four longer digits of the hand and not to the thumb. Hence the hand has five digits, four fingers and a thumb.
- Phalange refers to the finger bones as well as the finger segment itself.

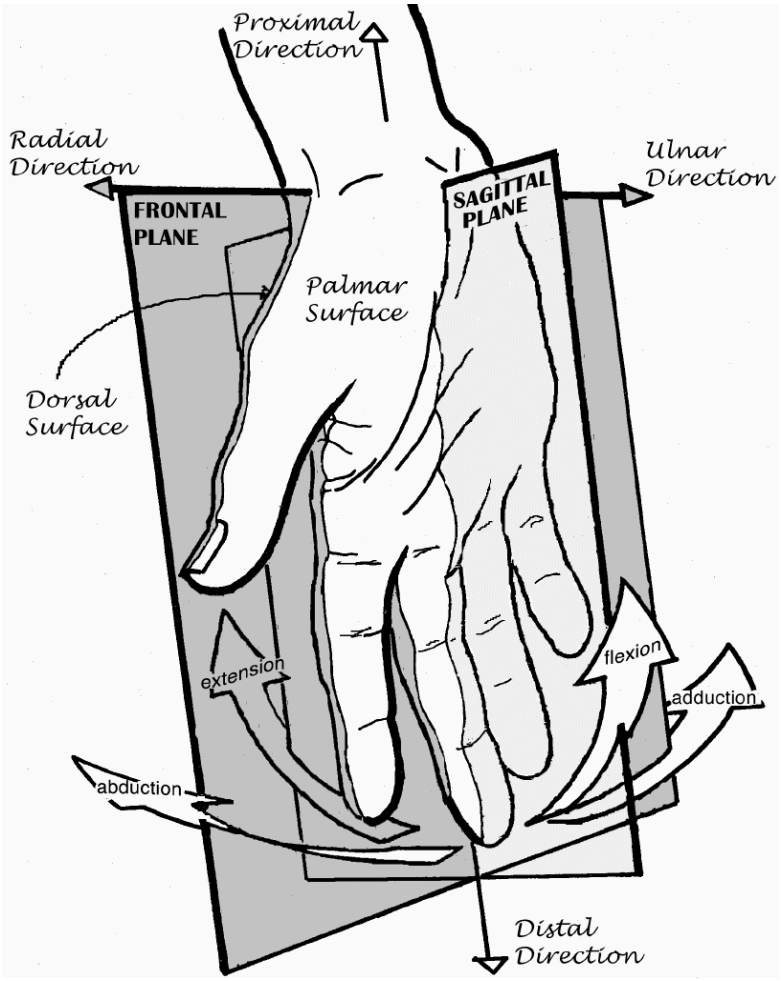

Figure 3.1: Terminology defining hand movement and orientation [62]

3.1 Hand Bones

Although, the musculoskeletal aspects of hand functions have yet to be clearly defined, a detailed topological analysis of the bone structure has been accomplished. The main bones of the hand are briefly described in this section as per [63, 64].

The human hand skeleton is made up of 27 bones, categorized into three sections as illustrated in Figure 3.2 :

i) Carpals - these are the bones of the wrist. They constitute two rows of four bones and three bones respectively.

ii) Metacarpals - these are bones form the palm of the hand. They are tubular bones with round heads and squarish bases. The hand has 5 metacarpals.

iii) Finger phalanges - these are intercalated bony segments which constitute the finger. Each of the four fingers of the hand is made up of three intercalated bony segments:

- The proximal phalange
- The intermediate (or middle) phalange
- The distal phalange.

The proximal and middle phalanges are considered to be long bones with tapered shafts at the top and convex at the bottom. The dorsal surfaces of the proximal and middle phalanges are smooth and rounded whereas the palmar surfaces are flattened and more roughened. The extremities of the shafts are referred to as heads on the distal side and bases on the proximal side. Unlike the proximal and middle phalanges, the distal phalange is small and convex on the dorsal side. Furthermore, the thumb lacks the intermediate phalange and is made up of only proximal and distal phalanges.

Figure 3.2: Hand bones – palmar view

3.2 Hand Joints and Movements [65]

The joint between each finger phalange is spanned by muscles, tendons and ligaments. Furthermore, to prevent compressive forces to damage the joints during hand movements, joints are surrounded a joint capsule. Synovial fluid covers the inner layer of the joint capsule and articular cartilage, maintaining the joint surfaces lubricated and keeping friction between the bony segments minimal. Fibro-cartilaginous plates, referred to the volar plate, slide along the heads and bases of contacting joints and provide joint stability.

Joint motion occurs as a result of articulation of the finger bones along articular surfaces and is characterized by the combined action of the above-described muscles, tendons, ligaments, synovial joint capsules and volar plates. These anatomical features are critical to joint motion as they restrain the movement of the bones with respect to each other and prevent six DOF motion of the joints. The hand and its digits are therefore capable of movements into two planes only: adduction and abduction in the frontal plane and extension/flexion in the sagittal plane (see Figure 3.3). This section briefly describes the joint structure of the human hand with starting the finger joints and following with the thumb joints.

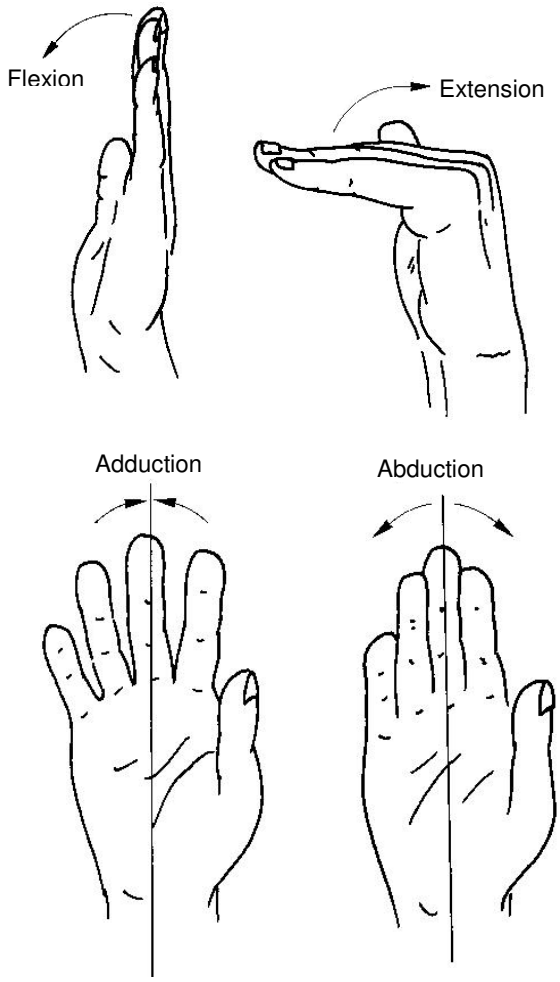

Figure 3.3: Hand movements [66]

3.2.1 Finger Joints and Movement [65]

The fingers of the hand have three joints: the metacarpophalangeal joint, the joint closest to palm; proximal interphlalangeal joint at the middle joint of the finger; the distal interphalangeal joint located at the end of the finger.

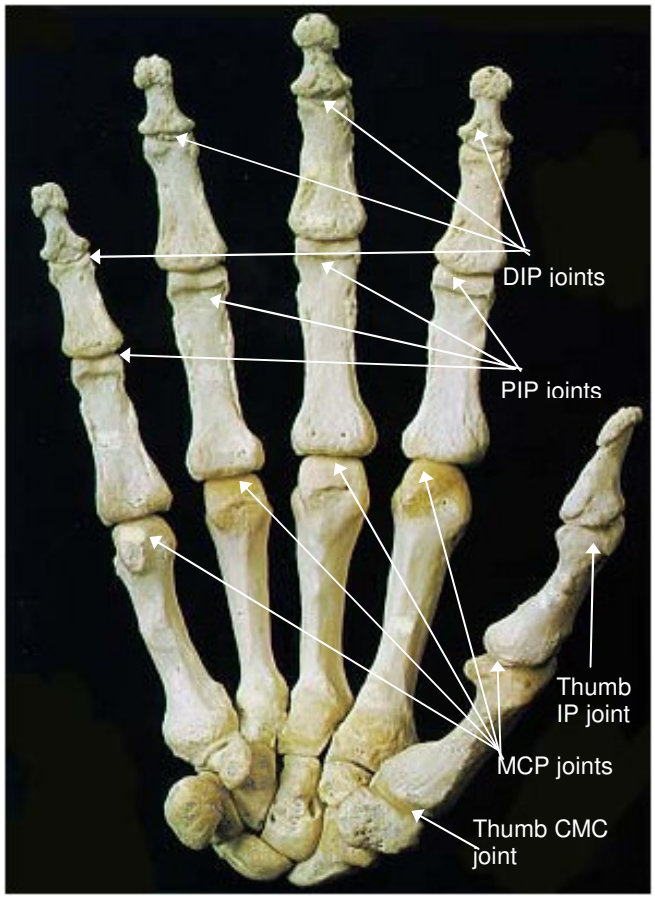

Figure 3.4: Joints of the hand

3.2.1.1 Metacarpophalangeal Joint

The metacarpophalangeal joint (MCP joint) connects the convex head of the four metacarpals with concave base of the proximal phalanges. It is a condyloid type joint with two degrees of freedom (DOF): flexion/extension and adduction/abduction. The MCP joint has a poorly mated surface and a joint capsule which is lax and mobile when the finger is extended. Joint stability is achieved by the presence of the volar plate, attached to the base of

the proximal phalange (Figure 3.5) and two collateral ligaments. The plate resists tensile stresses and therefore restricts hyperextension of the fingers. Its flexible attachment, however, permits the proximal bone to glide down the surface of the metacarpal head during flexion (Figure 3.5:). Deep transverse ligaments span the volar plates of the finger and further promote the stability of the joint. The collateral ligaments spanning the MCP joint are slack in extension permitting a full-range of adduction and abduction motion at the MCP. At full flexion, tension in the collateral ligaments are however maximal accounting for minimal adduction/abduction in that position. Different parts of the collateral ligaments are taut at various points in the range of motion of the MCP thereby providing stability of the joint as it flexes.

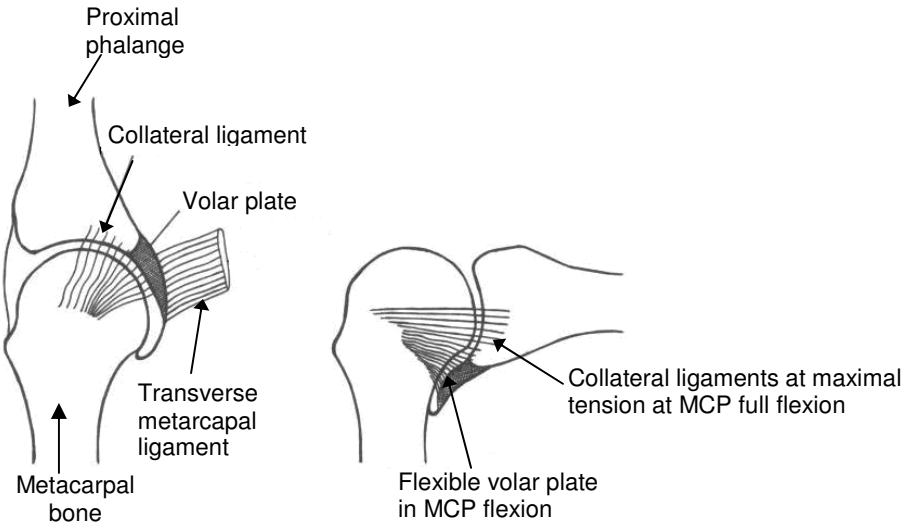

Figure 3.5: Volar plate and collateral ligaments at MCP [65]

The finger's MCP is thereby capable of a full flexion of 90^o in the sagittal plane and adduction/abduction ranges of 20^o about the medial axis in the frontal plane when the fingers are fully extended. The MCP range of the fingers increases progressively from 90^o on the radial side to about 120^o on the ulnar side at the little finger's MCP. Because of its shape, the index finger is also capable of 40^o adduction/abduction, the greatest for all fingers of the hand. This range of motion is only possible when the joint is extension because of the reduced tension of the collateral ligaments in this position.

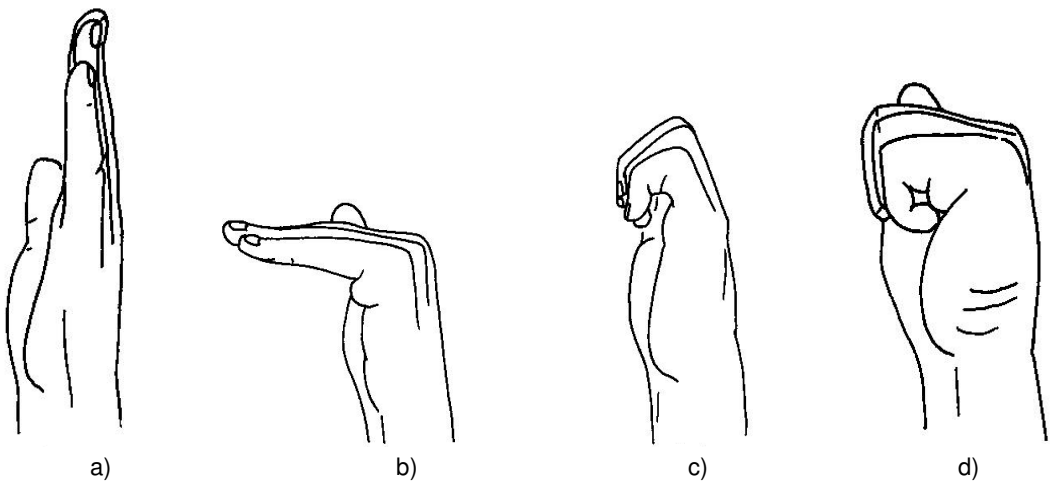

Figure 3.6: a) Extension of the MCP and PIP joints b) Flexion of the MCP joint c) Flexion of the PIP without flexion of the MCP joint d) Flexion of PIP and MCP joint.

3.2.1.2 Proximal and Distal Interphalangeal joints

The finger constitutes of two interphalangeal joints: a proximal interphalangeal joint (PIP) between the head of the proximal phalange and the base of the middle phalange and the distal interphalangeal joint (DIP) between the head of the middle phalange and the base of the distal phalange (see Figure 3.4). The bases of the middle and distal phalanges have shallow concave facets with a centre ridge and sit on the pulley-shaped head of the phalange proximal to it. The PIP and DIP joints are synovial hinge joints with one DOF: flexion and extension. Similar to the MCP, the PIP and DIP joints possess of a joint capsule, a volar plate and collateral ligaments (see Figure 3.11) which govern their range of motion. Similar to the MCP, the volar plates reinforce the lax joint capsule for joint stability while the varying tautness of the collateral ligaments provide support through the PIP and DIP range of motions. Unlike the MCP joints, the volar plates of PIP and DIP joints are not connected by a deep transverse ligament.

Articulation of the PIP and DIP joints are coupled through extensor and flexors tendons dynamics, that is, the DIP cannot flex/extend independently of the PIP joint. The PIP is capable of maximum extension/flexion of about 100^{o} with the DIP flexing with slightly smaller angle. The index finger is found to have the most independent extension/flexion

ranges with a PIP range of 110^o and a maximum extension/flexion of 80^o the DIP. In general, the range of motion of the index is found to be as shown in Table 3.1.

INDEX JOINT	RANGE
MCP Adduction/Abduction	40^o
MCP Flexion/Extension	90^o
PIP Flexion/Extension	$100^o – 110^o$
DIP Flexion/Extension	80^o

Table 3.1: Flexion/Extension ranges of index finger

3.2.2 Thumb Joints and Movement [65]

Although the thumb is not emulated in this research, a brief description of the thumb and its movement is included since the thumb is a critical contributor in the hand's manipulative abilities and defines the motion of the fingers of the hand, that is, the finger's posture and movement are best understood when defined with respect to the thumb's mobility.

Thumb anatomical structure differs considerably from the fingers. The thumb has three active joints used for motion: the carpometacarpal joint, the metacarpal joint and the interphalangeal joint (see Figure 3.4).

3.2.2.1 Thumb Carpometacarpal joint

The carpmetacarpal joint (CMC joint) connects the base of metacarpal bone of the thumb and the most lateral carpal bone of the wrist (see Figure 3.4). While the finger's CMC joints are virtually immobile, in the thumb the CMC is saddle type joint (opposing surfaces are reciprocally concave-convex) which permits high mobility of the thumb. Hence, besides flexion/extension and adduction/abduction movements, it possesses an additional DOF – it can move in opposition to the other fingers by a combined motion of flexion, adduction and some circular rotation referred to as circumdiction (Figure 3.7). Circumdiction motion is critical in the hand's grasping functions as it enables opposition movements whereby the thumb tip is brought into contact with the little finger's tip. The thumb CMC is capable of an

abduction/adduction angle of about 80^{o} and a flexion/extension between 40^{o} to 50^{o}. Since the thumb is rotated 90^{o} with respect to the fingers, the term extension, flexion, adduction and abduction are used as if the thumb was inline with the fingers. Hence, flexion and extension of the thumb occurs in the frontal plane, where adduction and abduction occurs in the sagittal plane (Figure 3.7).

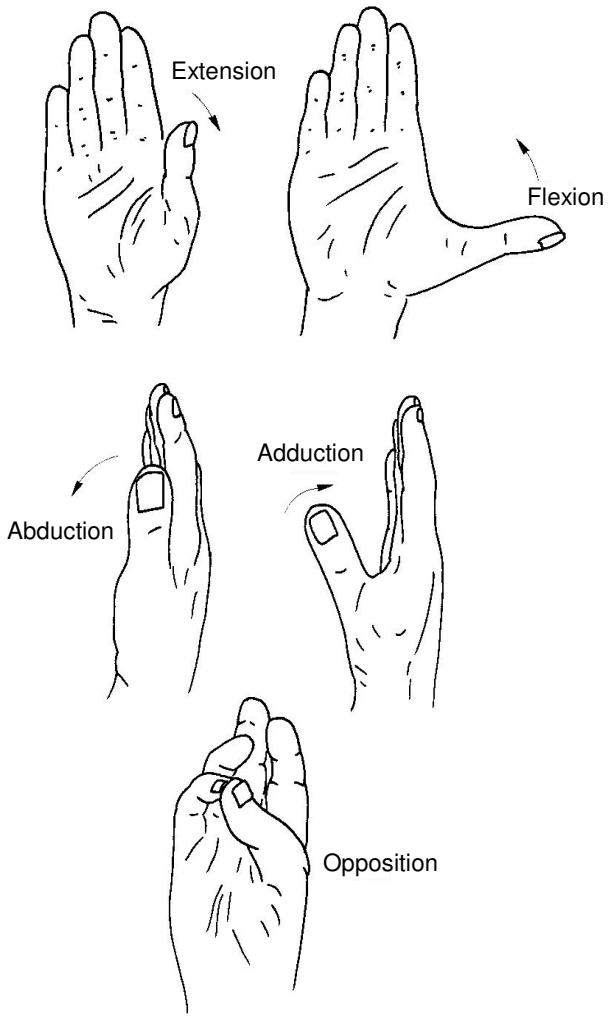

Figure 3.7: Motions of the thumb [66]

3.2.2.2 Thumb Metacarpophalangeal and Interphalangeal joints

The thumb MCP and IP joints are similar in design and location to the fingers. MCP joint is a synovial condyloid type joint between the head of the metacarpal and base of the proximal phalange. Being a condyloid joint, it is capable of flexion/extension of 53^{o} (in the frontal plane) and adduction/abduction angle of 42^{o} (in the sagittal plane). However, unlike

the fingers MCP, a certain amount of axial rotation is possible at the thumb MCP, which is important for opposition movements of the thumb.

The thumb's IP joint is a synovial hinge joint with flexion and extension of about 110^{o} occurs in the frontal plane. Similar to the finger, MCP and IP joint stability provided by the loose fibrous cartilage surrounding the joint and collateral ligaments crossing the joints.

3.3 Finger Musculature

Human muscles apply forces by contraction. The natural muscles can be categorized into two groups: i) extrinsic muscles – heavy lifting muscles located in the forearm responsible for finger flexion and extension and ii) intrinsic muscles – weaker muscles originating from the palm and used for adduction/abduction and other precision movements of the fingers [63, 65].

Tendons are formed by the connective tissues that bind the parallel muscle fibers together. In the case of extrinsic muscles, these tendons connect the controlling arm muscles to the finger structure, spanning over multiple joints in the arm and the hand. In the finger, the tendons form an intricate web-like structure and attach directly to the finger bones. Contraction of the arm muscles produces a complex interplay between tendons resulting motion at the joint. Since the tendons are collagen-based with non-linear stiffness characteristics, they get stiffer as are stretched and permit the finger joint to flex or extend with a limited range only. Tendons also contract and allow the finger to return to its original position after flexion/extension or adduction/abduction. The dynamic and highly redundant nature of the tendon structure renders the finger actuating anatomy complex and difficult to fully comprehend and model. As such, only the tendons essential for the index finger flexion and extension are studied. Furthermore, the thumb's musculature is excluded in this section.

3.3.1 Finger flexors [65, 67]

Finger flexion is produced by the action of two extrinsic flexors: flexor digitorum superficialis (FDS), flexor digitorum profundus (FDP). The FDS and FDP muscles pass down the anterior side of the forearm to the wrist. At the wrist, the FDS and FDP each divide

into 4 tendons. The tendons pass through the palm (on the palmar side) and are inserted into the fingers. The FDS tendon attaches the base of the middle phalange while the FDP attaches to the distal phalange (illustrated in Figure 3.8). The FDS flexes the PIP joint only whereas the FDP flexes both the PIP and DIP joints. During gentle pinches and grasps, the FDP acts alone. The FDS functions alone only when flexion at the DIP is not required. Usually, the FDS tendon acts as a reserve muscle and joins the FDP by increasing its activity when more flexor force is required.

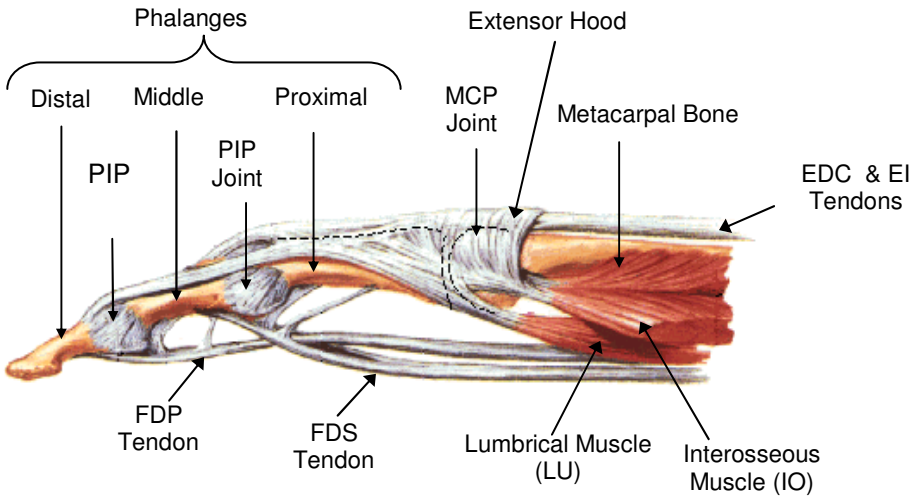

Figure 3.8: Anatomy of the finger

3.3.2 Finger extensors [65, 67]

The two main extrinsic extensors are the extensor digitorum (ED) and extensor indicis (EI). These extensor muscles pass posteriorly over the wrist and are held down by the extensor retinaculum, a band of fibrous tissue lying across the posterior side of the carpal bones. The ED divides into four at the wrist, passes on the dorsal side of the hand and inserts into each finger of the hand. The EI lies adjacent to the index finger and blends with ED tendon on the ulnar side. As they travel into the fingers, the extensor tendons become turns into a web-like structure which rides on the dorsal surface of the finger at the MCP joint (Figure 3.9). This web-like structure is known as the extensor hood since it acts during extension motions of the fingers

In the index's extensor mechanism, the EI muscle merges with the ED muscle proximal to the extensor hood at the MCP approximately. The hood then separates into separate into three bands: the central band inserts on the dorsal of the middle phalange and the lateral bands rejoin and insert on the dorsal side and at the base of the distal phalange. The ED and EI muscles are the only muscles that are capable of producing extension at the MCP even though they have no direct attachments to the proximal phalange.

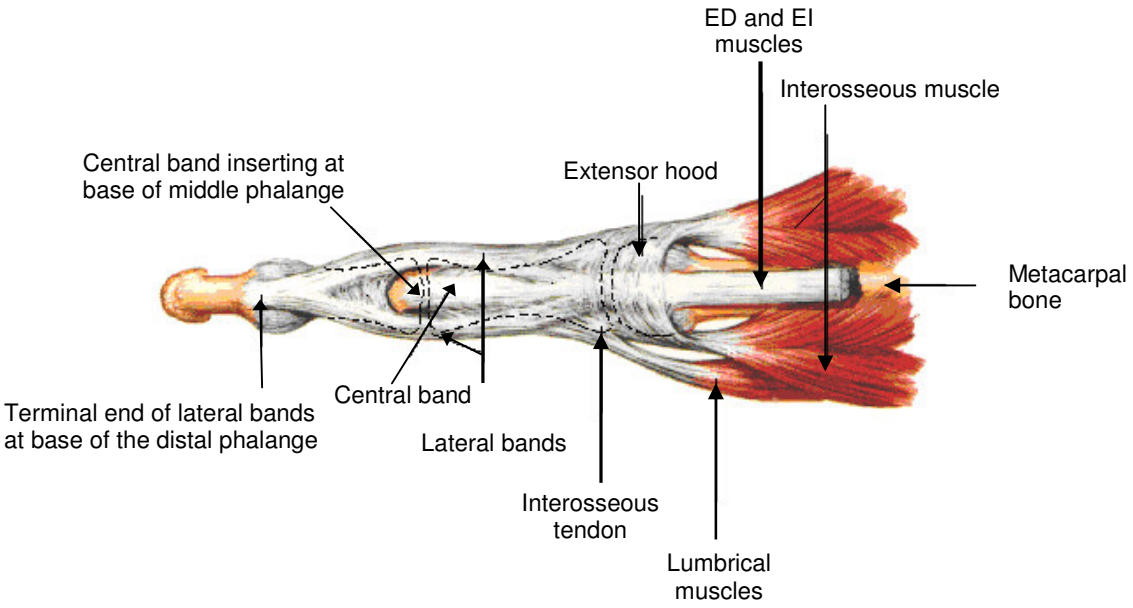

Figure 3.9: Extensors and dorsal hood of the finger

3.3.3 Other intrinsic muscles [67]

Beside the above extrinsic flexors and extensors, three intrinsic muscles are necessary for finger motion. These are the lumbricals (LU), the dorsal interossei and the palmar interossei (IO muscles). The lumbricals are four muscles that originate from the FDP muscle and insert on the dorsal surface of the finger (see Figure 3.9). They act in the flexion of the MCP and the extension of the IP joints by balancing the flexion and extension of the fingers. The dorsal interossei are four muscles that originate between the metacarpal bones, on the dorsal side while the palmar interossei are three muscles that originate between the metacarpals, on the palmar side. The dorsal interossei muscles act in abduction motions and

assist in the extension of the DIP. On other hand, the palmar interossei help adduction movements of the finger and in the flexion of the MCP and extension of the IP joints.

3.4 Extensor Mechanism [68, 69]

As described in Section 3.3.2., the finger's extensor mechanism consist ED and EI muscles which merge with the extensor hood at the MCP approximately. The hood then separates into separate into a central band which inserts on the dorsal side of the middle phalange and two lateral bands which rejoin and insert on the dorsal side the distal phalange as a single tendon. Beside the above extrinsic flexors, the extensor mechanism also consists of two intrinsic interossei muscles (IO), located radially and ulnarly. These have various lateral attachments to the finger bones. They are connected to the sides of the proximal phalange and they insert on the dorsal side of the middle and distal phalanges at the same connection points as the hood's lateral bands. An intrinsic muscle (LU), in turn, connects radially to the middle phalange. Figure 3.10 is a simplified model of the extensor tendon configuration.

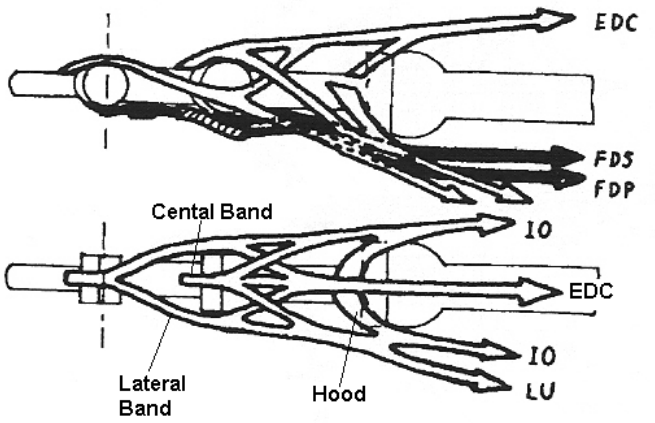

Figure 3.10: Simplified model of extensor mechanism [68]

Owing to the complex network of extrinsic and intrinsic muscles constituting the extensor mechanism, the action of a muscle can only be considered within the network and with respect to all other muscles connected to it. The IO works in opposition and controls the adduction and abduction motions of the finger, with the help of the stabilizing LU muscle.

Extension of the MCP is brought about by the active contraction of the EDC muscles. This creates tension, which pulls the hood proximally over the MCP joint and extends the proximal phalange. The IO and LU tendons become active and turn into extensors contracting simultaneously to assist the EDC muscles in extending the MCP. Extension occurs when the EDC torque exceeds the intrinsic flexor torques at the MCP.

The PIP and DIP are dorsally crossed by the ED lateral and central bands. The interosseous muscles and lumbricals have attachments at the central and lateral bands of the EDC as well as the extensor hood. Consequently, a tension in the ED, IO and LU produces extension at both the PIP and DIP. A point to be retained is that the ED and the intrinsic IO and LU muscles cannot produce extension of the IP joints independently. ED contraction requires an active contraction of the IO and LU for extension. Similarly, the IO and LU muscles cannot generate sufficient tension for extension without the contribution of the ED muscle.

One distinct feature of the extensor mechanism is multi-functionality of the lateral bands. Firstly, they assist the IO muscles in the adduction/abduction movements when the interosseous muscles work as antagonists. Secondly, they aid in the extension of the IP joints when the ED, IO and LU muscles contract. Thirdly, and most importantly, through passive tension on the lateral bands between the PIP and DIP joints, extension of the PIP is accompanied by passive extension of the DIP.

3.5 Flexor Mechanism [68]

Tension in the extrinsic FDP flexor (attached to the distal phalange) produces flexion of the PIP and DIP joints whereas tension in FDS muscle (attached to the middle phalange) flexes the PIP joint only. Unlike the middle and distal phalanges, the proximal phalange does not have any flexor muscles attached to it. Flexion at the MCP occurs by the action of the hood structure at the MCP joint. Although known as extensor hood owing to its critical usage in extending the finger, the extensor hood also acts during flexion motions of the fingers. In fact, this structure allows the MCP to flex independently of the other joints.

As the FDS and FDP pull the middle and distal phalanges into flexion, the hood portion of the extensor mechanism slides over the MCP towards the palmar side of the hand.

When the lumbricals and interosseous muscles (connected to the hood structure as shown in Figure 3.11) cross over the centre of MCP joint axis, these muscles become active and operate as MCP flexors. The hood structure hugs and pulls the proximal phalange to achieve full flexion of the MCP joint. When the MCP joint is fully flexed, the IO muscles resume their original of antagonist muscles but, rotate the finger rather than moving it laterally. As the two distal joints continue to flex, the extensor hood is pulled distally. The lateral bands of the hood slip around the sides of the finger to find the shortest path between the origin of the bands and their insertion point at the base of the distal phalange. In doing so, the lateral bands thereby couple and coordinate the motions of the PIP and DIP joints. The passive tension in the lateral bands causes the DIP to flex more slowly than the PIP. At the end of the finger flexion, the DIP locks the finger's flexor musculature in the flexed position.

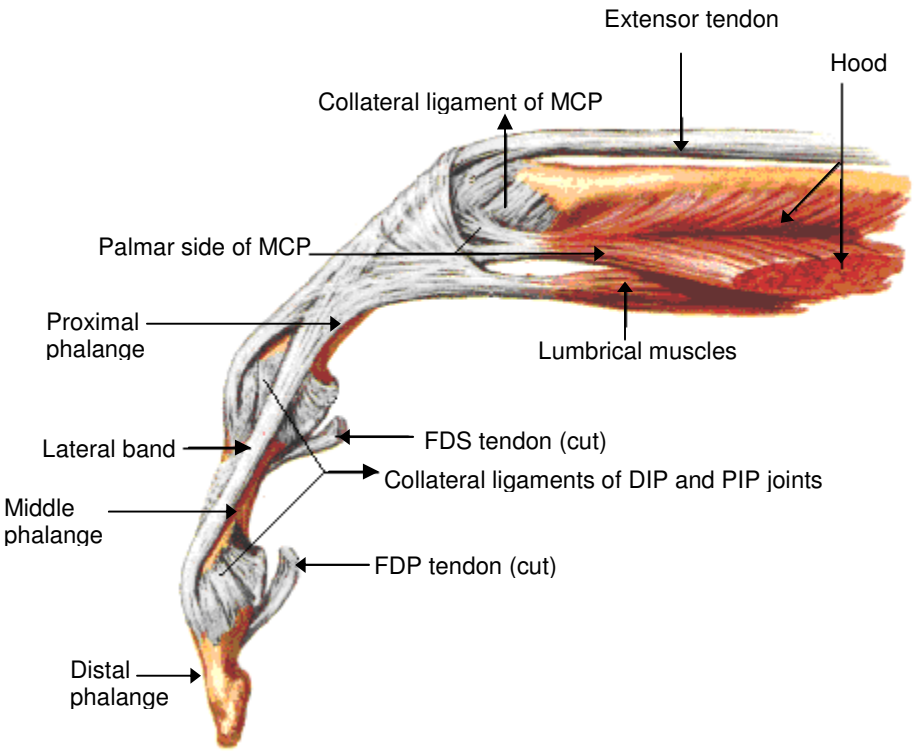

Figure 3.11: Flexion of the index finger

3.6 Hand movements and grips [65, 70]

The hand joints can be moved in characteristics manners with controlled contraction of muscles. When joint motion is resisted, the above described muscular-tendinous systems allow the hand to exhibit functional strength. The resulting hand formations have been classified using various anatomical and functional standards with Napier's grip classification being the most widely recognized standard

Napier classified the grips of the hand into two broad categories, grasp and pinch, with a number of variations two configurations in between as shown in Figure 3.12 [70]. The pinch grip involves placement of the inner fleshy surface of the thumb in opposition to the adjacent fingers (index and middle). Such a grip requires stabilization of the three joints of the fingers and the three joints of the thumb. Stabilization is brought about by the interaction of both the extrinsic and intrinsic muscles so that the resultant force is generated solely in the contact area between the thumb and fingers. In this case, the force exerted at the index tip (by the FDP, some contribution of the FDS and the dorsal interossei) must balance the force applied by the thumb to maintain static equilibrium. Further manipulation of the object in a pinch type grip involves subtle changes in the tensions of the muscles involved. This allows for fine, discreet motion of the fingers and thumb for more intricate tasks [65, 70].

The grasp function involves wrapping the palm around an object with the fingers and thumb initially extended, followed by a flexion of the digits around the object. The grasp requires the use of both extrinsic and intrinsic flexors. The FDP produces most of the flexion of the fingers and the FDS assists the FDP when a greater grip force is required. The intrinsic IO muscles contribute in grip stability by aiding the MCP adduction/abduction while the extrinsic ED contracts so as to increase joint compression. The thumb has the most variable position in the power grasp as it flexes and abducts. Numerous force distribution patterns are possible in this case, depending of the type of grasp and object being held [70].

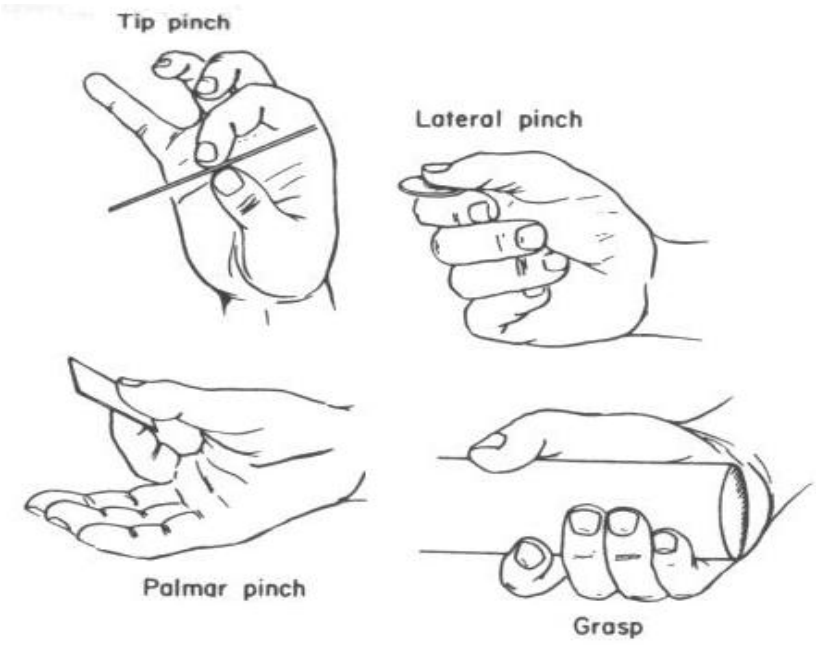

Figure 3.12: Hand configurations [70]

3.7 Hand Senses

Besides its primary prehensile and manipulative functions, the hand also acts as a sense organ. The hand senses can be grouped into internal and external senses. The external hand senses, or tactile sense, refer to the tiny receptors embedded in the skin that capture and relay sensations of contact, pain, cold and heat to the brain through the central nervous system [2, 67]. The internal senses, or proprioceptive senses, refer to receptors that are found within the human body, attached to joints, tendons and muscles enable humans to perceive body movements in space.

3.7.1 Tactile Sense

The hand's prime sensory apparatus is the tactile sense, which can be defined as our ability to feel objects in the physical world. This is the most complex of the five human senses, involving a wide array of tiny sensory nerve endings or receptors distributed through different layers of the skin which capture and relay a large number of sensations to the brain, the three main sensitivities being pressure perception, temperature and pain. Other common,

but unclassifiable, experiences include hardness, wetness, itchiness, tickling and so on [2]. Some parts of the body, notably the hairless surfaces of the body have a larger number of nerve endings and are therefore more sensitive. While pain and temperature sensations are essential for injury prevention and regulating the body temperature respectively, contact and pressure distribution are the fundamental sensory input for finger dexterity. The skin surface not only measures the contact force, but monitors changing contact parameters with object. Hence, slips incidents can be prevented through the sensing of contact forces as well as inertial and gravitational forces. The fingertips contain the densest areas of nerve endings making the hand the richest source of tactile feedback for the human body [2].

3.7.2 Proprioception

Mechanoreceptors, located in deeper tissues around the joints and capsules, are stimulated by the compression, tension and displacement of the skin and joint tissues. These receptors measure the activity of the muscles, the stress in of tendons, the position of the skin with respect to the touched surface and the angle position of joints. The proprioceptors relay information to the brain which enables humans to perceive body movements, position and orientation in space and well as assess the external force the human body is subjected to. Proprioceptors fire impulses to the brain which, in turn, interprets the information relayed by the sense organ by causing, for example, hand joints or muscles movements [2].

Chapter 4

Design of Biomimetic Artificial Finger Testbed

Robotic technology has greatly evolved in recent years, culminating in articulated artificial robotic hands that possess the biomechanical qualities of the human hand. However, on the biggest challenges in robotic design is the ability to integrate all the actuators, drive systems, sensors, joint systems and power sources into a compact design. This issue is further enhanced in biomimetic design where the casing must also follow strict anthropomorphic requirements of weight, size and appearance. Hence, in literature (see Chapter 2), many artificial fingers that subscribe to an anthropomorphic design and functionality typically consist of 2-3 hinge-like parallel joints. Fingers purporting a biomimetic 4 DOFs architecture have active bending at one or two joints only while motion transfer systems (e.g. four bar linkage systems or gear trains) passively actuate the remaining joints of finger. In addition, to reduce mechanical and transmission complexity, the MCP joint often constitutes of decoupled axes instead of the condyloid intersecting joint type of the human finger. Anthropomorphic systems which do integrate all the anatomical features for normal hand motion are often complex mechanical entities that have compromised cosmetology for functionality.

Since the anatomical basis of hand mechanics leading to hand motion is highly complex and because of known limitations in implementing biological resemblance using available actuating technologies, control architectures and materials, the intricate characteristics of the natural finger were not replicated in this work. Instead, as with any biomimetic strategy, our design goal in this research was to maintain the physical attributes of the natural finger, at the same time matching its functionality. Hence, the degree of emulation was limited to the following key factors, which were deemed essential characteristics of a biomimetic artificial finger:

(i) anthropomorphically-accurate size and appearance;

(ii) kinematically-accurate motion
(iii) biomimetic sensory feedback, and
(iv) tendon-driven agonist-antagonist biomimetic actuation.

The index finger is used as the model for emulation since this finger's adjacency to the thumb leads to it having the greatest mobility of all the hand's digits. With the thumb, the index finger is also the most used digit of the hand in general pointing and pinch motions of the hand. Furthermore, the index finger flexes solely in the sagittal plane, while the other digits oblique joint axes causing fingers to converge towards the lateral side of the wrist in flexion (shown in Figure 4.1). Modeling of the finger flexion in the sagittal plane only simplifies the design of the index finger.

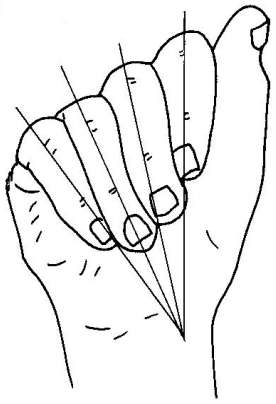

Figure 4.1: The index bends vertically. Other digits' joint axes are oblique causing fingers to converge radially in flexion [66]

Our key design constraints were to achieve the aforementioned biomimetic characteristics in an artificial index finger in a cost-effective and lightweight manner for rehabilitation robotic applications (e.g. prosthetics/orthotics or wearable exoskeletons). This section describes the biomimetic philosophy behind the design of the artificial finger, which is used to test the proposed tendon-driven actuation mechanism. The biomimetic actuating mechanism will itself be discussed in the following chapter.

4.1 Anthropomorphically Accurate Size and Appearance

Since one of the primary goals of this work was to maintain the physical attributes of the natural finger, an anthropometric size was desired. Data pertaining to hand dimensions are available from a number of sources. Garrett gave a detailed account of the hand anthropometric properties after a study of 56 males and females of the US Air force personnel [71, 72]. Poznanski compiled bone length measurements through radiographic study of the hand [73]. Chao et al. measured distances between coordinate systems defined at the approximate centre of rotation of the phalanges' heads and at the approximate centers of the articular concave surfaces of the joints to fully dimension the phalanges' lengths [70]. Moreover Frievalds et al. compiled data representing phalange lengths as a percentage of the hand length [74] while Buccholz et al. modeled the hand anthropometry as a function of external hand measurements, namely, hand length and breadth [75].

An analysis of the hand data showed discrepancies in hand dimensions from above sources, possibly owing large variances in physical attributes between individuals of different age, gender and ethnicity [76]. While all hand data conveyed the phalange lengthwise dimensions and the finger joint center positions, only the data presented by Buccholz et al. inferred phalangeal breadths (finger segment width from the palmar perspective) and depths (finger size from the radial/ulnar perspective). Furthermore, the hand anthropomorphic data was conveniently expressed in terms of statistically derived coefficients which enabled phalangeal lengths, phalangeal breadths and depths and joint centre data to be calculated from hand length, hand breadth and bone length. Hence, phalangeal length estimates are obtained by multiplying the phalangeal length coefficients by an overall hand length; joint depth and breadth estimates are obtained by multiplying segment breadth and depth coefficients by the hand breadth; and joint center location estimates are obtained by multiplying the joint center ratios by the phalangeal lengths [75].

Given the detailed finger anthropometry data available, Buccholz et al. hand data was used for an anthropomorphic model of the index finger. However, to better understand the phalangeal dimensions proposed in this thesis, it is necessary to define the points of reference used in formulating the lengths, breadths and depths of the finger phalanges:

- In any kinematic model of the finger, it is necessary to define the location of the centers of joint rotation. Both Chao et al and Buccholz et al. corroborate that the joint

axis can be approximated to be at the centre of curvature of the bone proximal to the joint in question [70, 75]. This assumption is extended to the design of our artificial finger.

- Hand length is defined as the distance between the distal wrist crease to the tip of the long finger of the extended hand.
- The hand breadth is the distance measured on the dorsal surface between the index's and the little finger's MCP.
- Phalangeal length is the bone length as measured from the base of the bone to the base of the articulating bone distal to it.
- The phalangeal breadths and depths are measured at the joint center, for example, the middle phalange depth is the phalangeal depth measured at the PIP joint.
- The anatomical position of each joint center was measured with respect to concave base of the phalange.

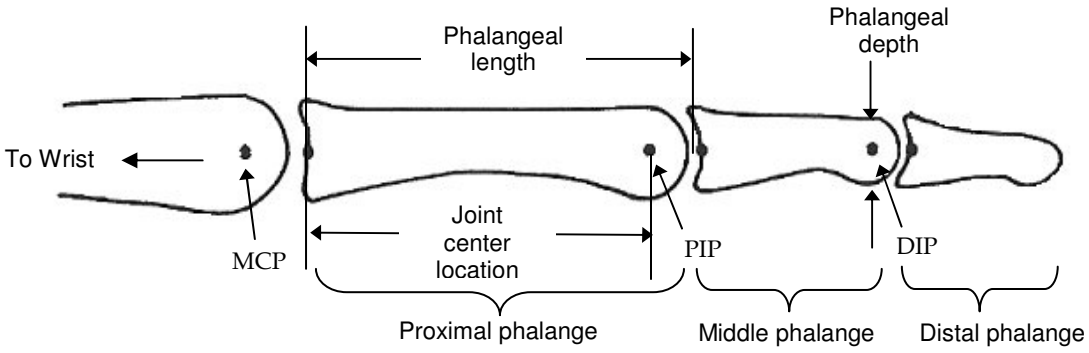

Figure 4.2: Joint center measured from bone base, phalangeal length and depth, MCP, PIP and DIP joints location.

In this research work, the hand length is based on anthropometric measurements made by Buccholz et al. [75]. The hand length of 182.9 mm and hand breadth of 81.1mm were used as the average adult hand size. Appendix A provides the anthropomorphic hand details used for the derivation of above hand length and breadth. The resulting phalangeal lengths, breadth, depths for the index finger are summarized in Tables 2, 3 and 4. The finger prototype link lengths, breadths and depths were extrapolated from the anthropomorphic hand dimensions presented in the tables below.

SEGMENT	PHALENGEAL LENGTH COEFFICIENT	LENGTH (mm)
PROXIMAL	0.245	44.8
MIDDLE	0.143	26.2
DISTAL	0.097	17.7

Table 4.1: Finger prototype phalangeal length estimates

JOINT	JOINT DEPTH COEFFICIENT	DEPTH (mm)	JOINT BREADTH COEFFICIENT	BREADTH (mm)
MCP	0.275	22.3	0.244	19.8
PIP	0.198	16.0	0.215	17.4
DIP	0.166	13.5	0.198	16.0

Table 4.2: Finger prototype joint depth and breadth estimates.

JOINT	JOINT CENTRE RATIO	JOINT CENTRE LOCATION (mm)
MCP	0.900	76.2*
PIP	0.909	40.8
DIP	0.887	23.2

Table 4.3: Joint center location estimates

*The phalangeal length in Table 4.1 was used for all joint center calculation except for the MCP joint center location. The MCP location was measured from the proximal end of the metacarpal bone length, which calculated to be 84.7 mm.

Besides anthropomorphic measurement, biomimetic modeling was also extended to the finger geometry. The artificial finger was designed within the boundaries of the physical dimensions presented in Table 4.1 to Table 4.3 to closely resemble the contours of the natural finger. The finger prototype hence has a flat dorsal surface and a palmar finger curvature which approximated the fleshy contour of the human finger. The finger's cross-sectional area

progressively decreased towards the fingertip to mimic the tapered look of the natural finger. Overall contour adaptations were made to accommodate mechanical stops, rotational shafts and to allow for space to route the driving cables of the finger links within the finger structure. Figure 4.3 and Figure 4.4 are the CAD representations of the resulting artificial finger design, which is anthropomorphically consistent with the natural finger.

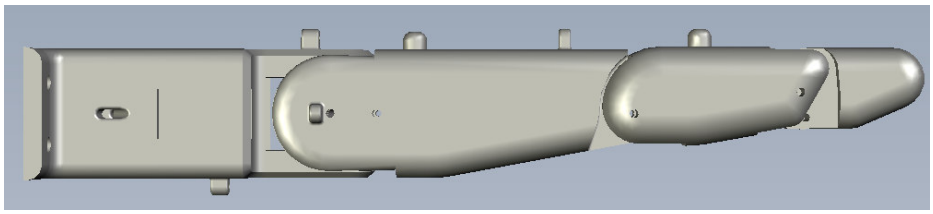

a) Side View

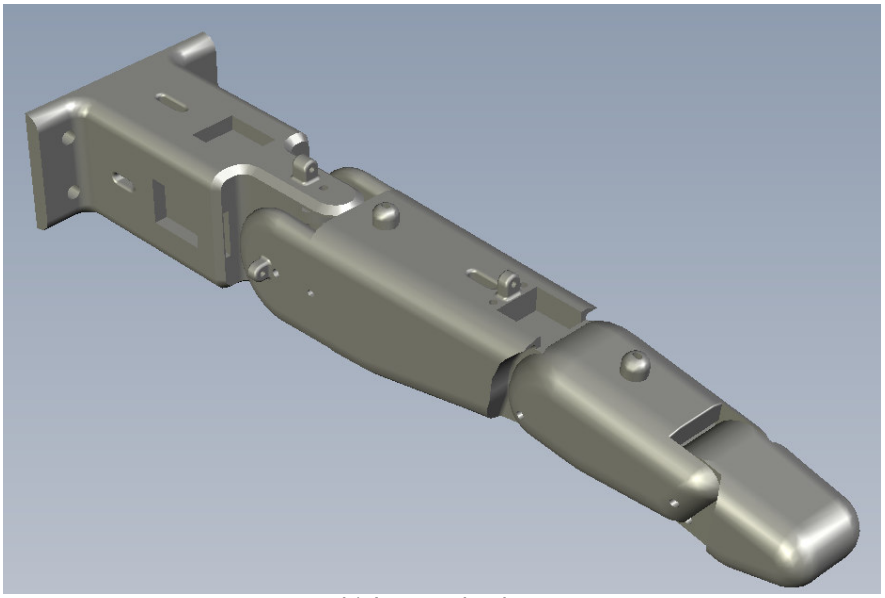

b) Isometric view

Figure 4.3: CAD models for the proposed biomimetic artificial finger for the experimental testbed - extended states

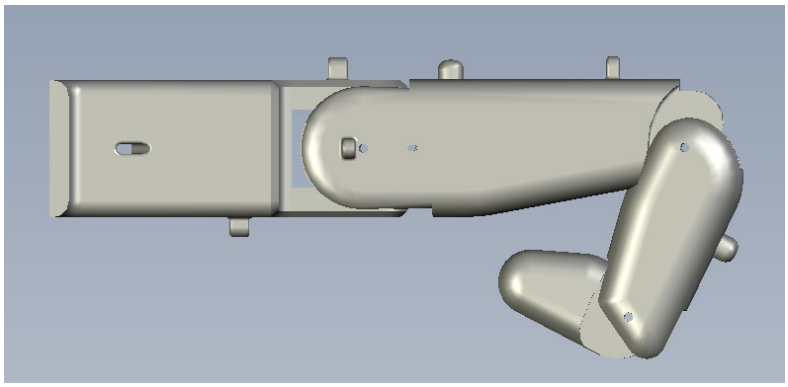

a) Side View

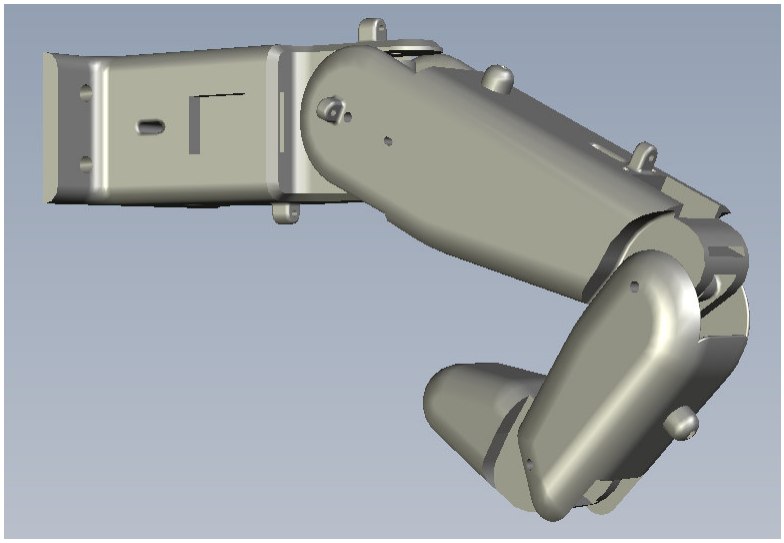

b) Isometric view

Figure 4.4: CAD models for the proposed biomimetic artificial finger for the experimental testbed- flexed states

The finger prototype was designed using SolidWorks CAD modeling software. The finger linkages were then built using the rapid prototyping technique, which allows parts to be built directly from digital 3D CAD data. More specifically, the stereolithography process, a process which uses a computer-controlled ultra violet laser to cure cross-sectional slices of a liquid photopolymer resin into solid shapes, was used. Since stereolithography adds layers to produce a final part, the rapid prototyping technique allows parts with complex contours and hollowed interiors to be manufactured fairly easily, cost-effectively and with very fast turnarounds as opposed to standard machining methods which involve removing material

from a block to create complex shapes and internal voids. Figure 4.5 shows the anthropomorphically shaped finger links built. Note the complex contour and the hollow finger structure which hosts the finger's actuating cable and sensors.

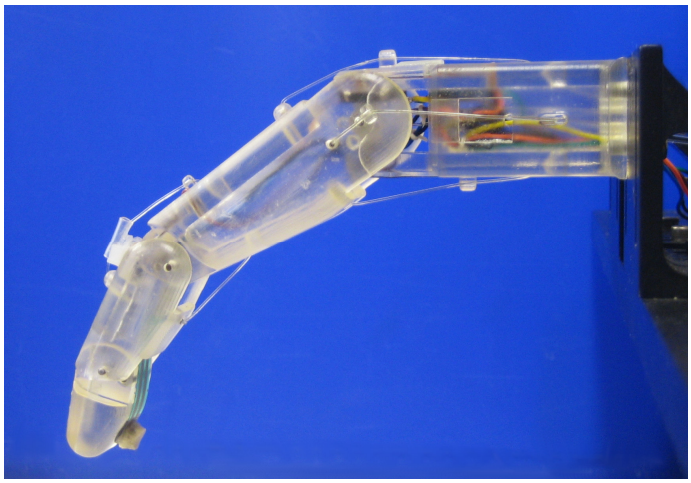

Figure 4.5: Anthropomorphic finger prototype

4.2 Kinematically-Accurate Motion

To enable biological motion resemblance, the artificial finger was modeled after the natural kinematics of the human finger. The biomimetic artificial finger is hence made up of three links corresponding to the proximal, middle and distal phalanges of the human finger. Joint movement in the natural hand is described by the movement of the finger bone segments along articular surfaces. The convex and concave topologies of the contacting bone extremities characterize the human finger joint as ball-type joints. However, the finger joints are spanned by muscles, tendons and ligaments which restrain the latter from having a six DOF motion. These kinematic constraints allow simplifications to be made when modeling the finger movement. Hence, the 2 DOF articulations at the MCP are replicated using a universal joint, which mimics the biaxial nature of this joint. The PIP and DIP joints are modeled as hinge joints since they are 1-DOF joints with articulation in the sagittal plane only. Kinematic hand anthropometric investigations performed by Buchholz et al [75, 81] further suggested that an anatomical estimate of the joint center location can be defined at the head of the bone proximal to the given joint and that these joint centers remain fixed along

the entire range of motion of the phalanges. Transferring these features in our model, fixed axes of rotations were implemented at the head of the proximal and middle phalanges for the PIP and DIP joints respectively. In these joints, rotation occurs about a shaft common to the head of the proximal phalange and base of the middle phalange for the PIP joint and the head of the middle phalange and base of the distal phalange for the DIP. In addition, the DIP joint is implemented as a passive joint. In the natural finger, lateral bands (which originate from the extensor hood) couple the DIP and PIP joints, enforcing their passive interdependence. In the artificial finger, a four-bar linkage mechanism was mounted into the finger structure to coordinate the PIP and DIP in flexion and extension, thereby replicating the natural motion and rotational ranges of the two finger joints. The DIP joint is hence a passive joint whose motion is dependent on the PIP joint motion.

The range of motion at joints of the artificial finger reflects those of the natural index finger, as shown in Table 3.1. A flexion/extension range of 90^o and adduction/abduction of 40^o is modeled at the MCP. Similarly, flexions/extensions of 100^o at the PIP joint and 80^o at the passive DIP joint are modeled. The flexion and extension limits of all the joints are achieved by mechanical stops, incorporated within the structure of the links. In summary, Figure 4.6 represents the kinematic architecture of the artificial finger.

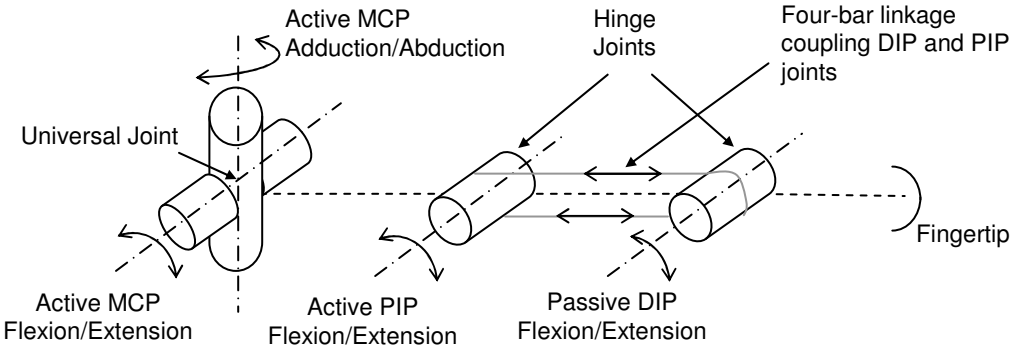

Figure 4.6: Finger Kinematic Architecture

A significant consideration in emulating the human finger is that, in its normal extended position, the finger does not lie in a rigidly straight line along the frontal plane. The middle and distal links are connected at an angle to the proximal link. This finger characteristic was modeled in the finger prototype as shown in Figure 4.7, which illustrates

the finger joints in the normal extended state. For kinematic simplicity, the active joint centres of rotation lie in the same plane as the frontal plane in the extended position.

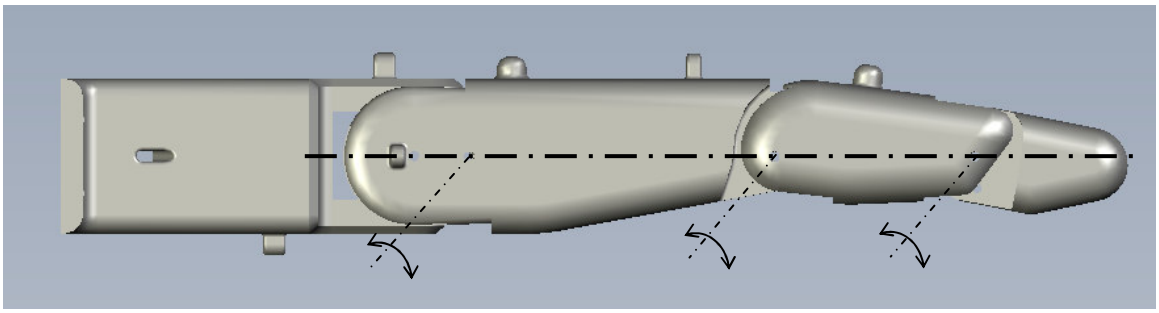

Figure 4.7: Alignment of MCP, PIP, and DIP joints in the extended position

Furthermore, in the normal resting position of the hand, the proximal phalange is at an angle to the palmar plane while the finger segments are also at an angle to each other. Goniometric measurements of the finger's joint angles were performed on a test sample consisting of six subjects to determine the resting posture of the finger links. Based on these measurements, it was determined that the proximal link's resting position is at 40^{o} flexed with respect to the palmar plane while the middle link rests at an angle of 20^{o} with respect to the proximal link phalange. These normal resting positions of the joints were implemented in the artificial finger as shown in Figure 4.8. It is to be noted that in both resting and extended positions, the middle and distal links of the finger maintain a slightly bent (but at varying) position to each other, as they are connected at angles using the internal four-bar linkage mechanism, to replicate the natural posture of the corresponding segments.

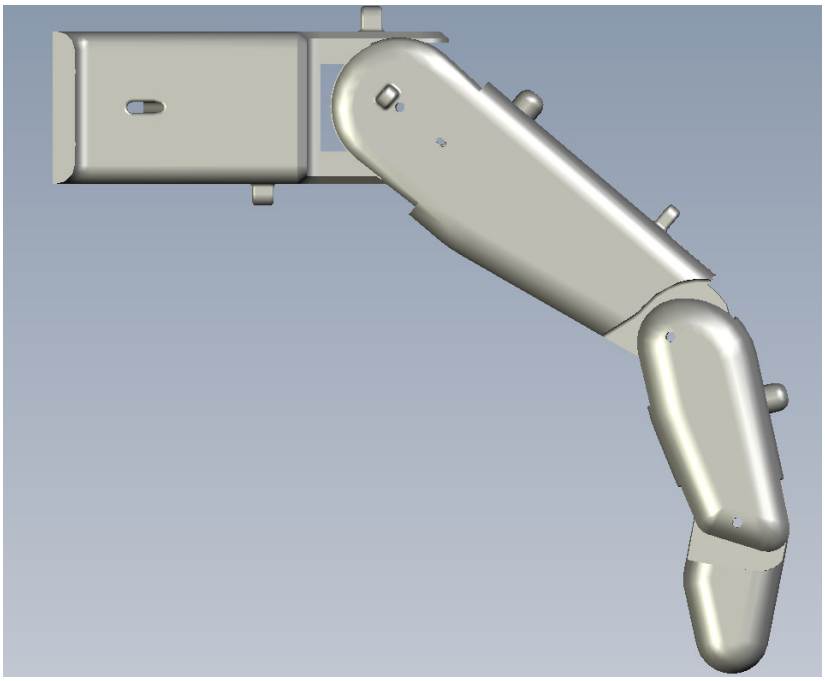

a) Side View

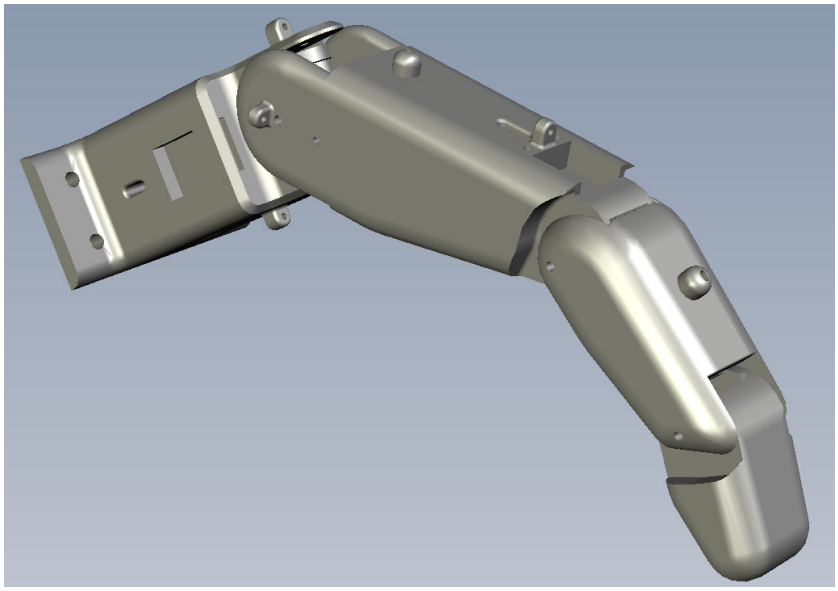

b) Isometric view

Figure 4.8: Normal resting position of the finger

4.2.1 Finger Kinematic Analysis

One important aspect of biomimetic design is the ability to position the artificial finger linkages through its anthropomorphic range of motion for dexterous manipulation tasks. Since the human finger can be biomechanically simplified to a linkage system of bony segments paralleling a robotic manipulator construction, robotic theories and methods can be applied to determine the spatial orientation and location of the artificial finger. A kinematic analysis of the artificial was thus done to mathematically describe the relationship between the angular position of each joint and the fingertip location. In this work, the artificial finger was modeled as a three-link robot fixed to a base corresponding to the palm. The Modified Denavit-Hartenberg notation, which describes the kinematic structure of a robot by a series of transformation between successive coordinate systems of the kinematic chain, was used [80]. This notation represents a link/joint pair as two translations and two rotations.

The first step in defining the artificial finger's geometric configuration involves assigning frames to each joint of the structure. For the artificial finger, frame {0} is assigned to the point where the finger meets the palm. This is coincident with the frames assigned to the MCP abduction/adduction and MCP flexion/extension joints (frame {1} and frame {2} respectively). Frame {3} and frame {4} are located at the PIP and DIP joint respectively. The frame coordinates are defined as per the following rules:

- Z_i points along the i^{th} joint' axis of rotation.
- X_i lies along the common perpendicular between two consecutive joint axes, or if the axes intersect, along the normal plane containing the two axes.
- Y_i completes the right-hand co-ordinate system.

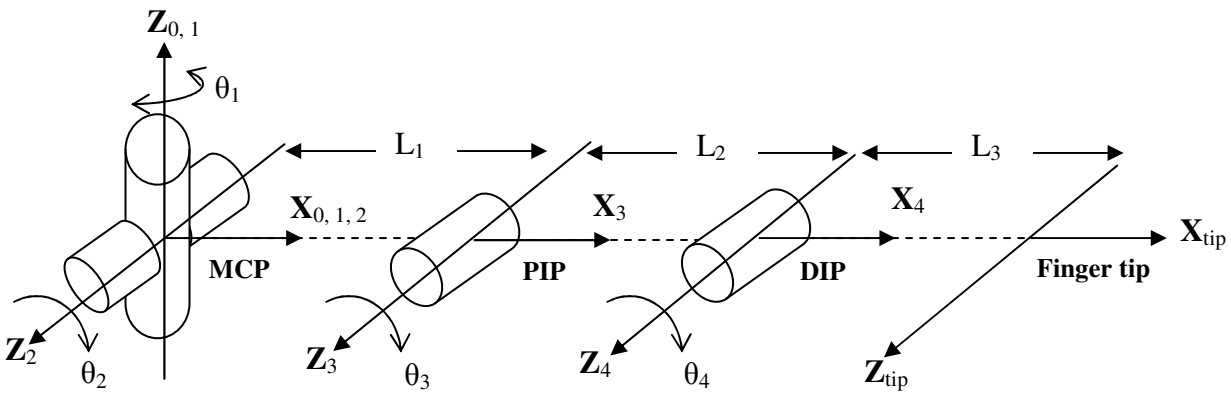

Figure 4.9: Zero-displacement diagram of the finger which the reference position when all the joint variables are zero.

The transformations between links are homogeneous matrices derived from four link parameters referred to as the D-H parameters:

- θ_i: the angle between $\hat{X}_{i-1}$ and $\hat{X}_i$ measured about $\hat{Z}_i$ (joint angle rotation)
- α_i: the angle between $\hat{Z}_i$ and $\hat{Z}_{i-1}$ measured about $\hat{X}_i$ (twist angle)
- a_i: the distance from $\hat{Z}_i$ and $\hat{Z}_{i+1}$ measured along $\hat{X}_i$ (perpendicular distance)
- d_i: the distance from $\hat{X}_{i-1}$ to $\hat{X}_i$ measured about $\hat{Z}_i$ (offset between joints)

The modified Denavit-Hartenberg parameters for the finger are as shown in Table 4.4. It is to be noted that clockwise rotation of the joints is taken as negative and anticlockwise rotation as positive, as follows using the right-hand rule about the joint axes.

I	**α_{i-1}**	**a_{i-1}**	**d_i**	**θ_i**	**i+1**
0	0	0	0	θ_1	1
1	90^o	0	0	θ_2	2
2	0	L_1	0	θ_3	3
3	0	L_2	0	θ_3	4
4	0	L_3	0	0	Tip

Table 4.4: D-H Parameters for artificial finger

4.2.1.1 Forward Kinematics

The forward kinematic problem involves concatenating individual link transforms to yield a single transform that fully describes the position and orientation of the fingertip with respect to the base reference frame. Using D-H parameters defined in Section 4.2.1, the following link transforms (**n**, **o**, **a**, **p**) are evaluated:

$$ {}^{0}_{1}T = \begin{bmatrix} c_1 & -s_1 & 0 & 0 \\ s_1 & c_1 & 0 & 0 \\ 0 & 0 & 1 & 0 \\ 0 & 0 & 0 & \end{bmatrix} \qquad {}^{1}_{2}T = \begin{bmatrix} c_2 & -s_2 & 0 & 0 \\ 0 & 0 & 0 & 0 \\ s_2 & c_2 & 1 & 0 \\ 0 & 0 & 0 & 1 \end{bmatrix} \qquad {}^{2}_{3}T = \begin{bmatrix} c_3 & -s_3 & 0 & L_1 \\ s_3 & c_3 & 0 & 0 \\ 0 & 0 & 1 & 0 \\ 0 & 0 & 0 & 1 \end{bmatrix} $$

$$ {}^{3}_{4}T = \begin{bmatrix} c_4 & -s_4 & 0 & L_2 \\ s_4 & c_4 & 0 & 0 \\ 0 & 0 & 1 & 0 \\ 0 & 0 & 0 & 1 \end{bmatrix} \qquad {}^{4}_{tip}T = \begin{bmatrix} 1 & 0 & 0 & L_3 \\ 0 & 0 & 1 & 0 \\ 0 & -1 & 0 & 0 \\ 0 & 0 & 0 & 1 \end{bmatrix} $$

where ${}^{i}_{i+1}T$ is the link transform between link i and $i+1$ and c_i and s_i represent $\cos\theta_i$ and $\sin\theta_i$ respectively. Concatenating link transforms, we obtain the transformation that relates the frame $\{0\}$ and the fingertip frame.

$$ {}^{0}_{tip}T = {}^{0}_{1}T \; {}^{1}_{2}T \; {}^{2}_{3}T \; {}^{3}_{4}T \; {}^{4}_{tip}T $$

$$ {}^{0}_{tip}T = \begin{bmatrix} c_1c_{234} & -c_1s_{234} & s_1 & L_3c_1c_{234} + c_1(L_2c_{23} + L_1c_2) \\ s_1c_{234} & -s_1s_{234} & -c_1 & L_3s_1c_{23} + s_1(L_2c_{23} + L_1c_2) \\ s_{234} & c_{234} & 0 & L_3s_{234} + L_3s_{23} + L_1s_2 \\ 0 & 0 & 0 & 1 \end{bmatrix} $$

Hence, the position vector of the fingertip is given by:

$$ \begin{bmatrix} p_x \\ p_y \\ p_z \end{bmatrix} = \begin{bmatrix} L_3c_1c_{234} + c_1(L_2c_{23} + L_1c_2) \\ L_3s_1c_{23} + s_1(L_2c_{23} + L_1c_2) \\ L_3s_{234} + L_3s_{23} + L_1s_2 \end{bmatrix} $$

in which L_1, L_2 and L_3 are the proximal, middle and distal link lengths, respectively; p_x, p_y and p_z are the Cartesian coordinates of the fingertip; $\cos\theta_i = c_i$; $\sin\theta_i = s_i$; $c_{ij} = \cos(\theta_i + \theta_j)$; $s_{ij} = \sin(\theta_i + \theta_j)$, $c_{ijk} = \cos(\theta_i + \theta_j + \theta_k)$ and s_{ijk}, $= \sin(\theta_i + \theta_j + \theta_k)$ with i, j, k = 1, 2, 3 and 4, corresponding to the MCP adduction/abduction angle, the MCP, PIP and DIP flexion/extension angles respectively.

4.2.1.2 Inverse Kinematics

The inverse kinematic solution of the finger joint involves manipulating of the set of non-linear equations produced by the forward kinematic solution to determine the fingers joint angles given the Cartesian coordinates of the fingertip location. The manipulation of the non-linear equations obtained in the forward kinematic solution is explicitly described in Appendix B of this report. The joint angles in terms of the Cartesian coordinates of the fingertip are as follows:

- $\theta_1 = a\tan 2(p_y, p_x) + n\pi$ (n= 0, 1)

- $\theta_2 = a\tan 2(s_2, c_2)$ where $s_2 = \dfrac{(L_2 L_3 p'_x) + (L_2 c_3 + L_1) p'_z}{L_1^2 + L_2^2 + 2L_1 L_2 c_3}$

  $c_2 = \dfrac{(L_2 c_3 + L_1) p'_x + L_2 s_3 (p'_z)}{L_1^2 + L_2^2 + 2L_1 L_2 c_3}$

  $p'_x = L_2 c_{23} + L_1 c_2$ and $p'_z = L_2 s_{23} + L_1 s_2$

- $\theta_3 = a\tan 2(s_3, c_3)$ where $c_3 = \dfrac{(p'_x)^2 + (p'_y)^2 - L_2^2 - L_1^2}{2L_1 L_2}$

  $s_3 = \pm\sqrt{(1 - c_3^2)}$

- $\theta_4 = a\tan 2(-(o_x c_1 + o_y s_1, o_z)$ - $(\theta_2 + \theta_3)$

  from $\theta_2 + \theta_3 + \theta_4 = a\tan 2(-(o_x c_1 + o_y s_1), o_z)$

The angles θ_1, θ_2, θ_3 and θ_4 are the adduction/abduction angle of the MCP joint, the flexion/extension angles of the MCP, DIP and PIP joints respectively. The first step in the inverse kinematic solution involves evaluating the elements of the transformation frame that relates the base frame to the fingertip. The input to the inverse kinematic problem would, in our case, be the x, y and z coordinates of the fingertip. However, the artificial finger is a biomimetic 4 DOF finger that is being used for a 3 DOF positioning task. As such, a 1 DOF redundancy exists, which complicates the inverse kinematics problem since the three Cartesian coordinates of the fingertip are not sufficient to solve the set of non-linear equations by the inverse kinematic solution. Various methods are available in literature to deal with redundant systems. However, a simple and straightforward approach is presented in [83], which is adopted in our work. The redundancy issue is resolved by specifying a fingertip orientation angle with respect to the base reference frame, in addition to the fingertip Cartesian position information. This orientation angle, α, is measured between the x-axis of the base reference frame and the x-axis of the fingertip frame as shown in Figure 4.10. With this additional parameter, the finger joint values can be fully defined. The joint equations of the inverse kinematic solution are presented in Appendix B.

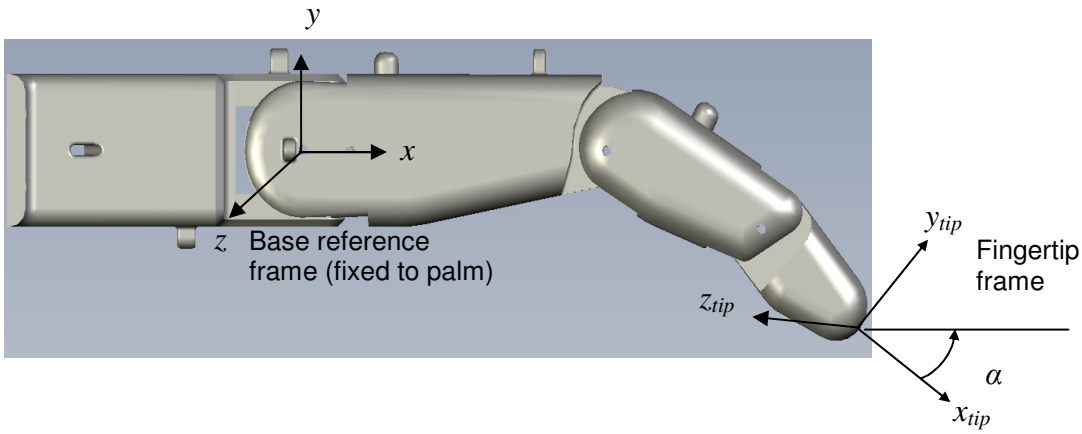

Figure 4.10: Fingertip orientation angle α used as input to the inverse kinematic solution together with x-y-z coordinates of the fingertip.

4.3 Biomimetic Sensory Feedback

The continuous measurement of position and contact forces which occur when an artificial hand interacts with the environment has become increasingly important as researchers aim for more precise manipulation and grasping control and diverse applications of artificial end-effectors. Dependence on sensory feedback is crucial for the successful application of many articulated hands. This is especially true when designing rehabilitations robots whose users are disabled individuals with limited physical, communication and cognitive abilities. Sensory feedback is crucial in a making a robotic system which is sufficiently safe and capable of coexisting with and, most importantly, benefit the disabled person.

4.3.1 Sensors for Robotic Hands

The human hand is rich with tactile and movement sensors. Installing equivalent artificial sensors in a robotic end-effector and returning information from these sensors in a usable form is still challenging. In literature, sensory feedback has been accomplished by embedding miniaturized sensors in the hand, or in the case of touch feedback, embedding sensitive material in the fingertips of the end-effector (see Chapter 2). The most common sensor configurations in robotics employ the physical properties of materials capable of converting a mechanical stimulus into a measurable quantity. The following are conventional sensor types which have been used to mimic the sensory-motor capabilities of the hand [77]:

- Resistive devices

  When subject to an external force, these materials register a change in electrical resistance which, when measured, provides information regarding the magnitude of the force exerted. Well-known resistive sensors are potentiometers and strain gauges. Strain gauges have been used in early models of the Stanford/JPL and the UTAH/MIT hand for force sensing. Another class of resistive sensors utilize the piezoresistive effects whereby a polymeric material exhibits decreased resistance when pressure is applied normal to its surface. The elastic deformation of piezoresisitive sensors have been extensively used in the design of tactile sensors. Piezoresistive tactile sensors are typically covered with a

conductive rubber or foam to act as a protective skin and pressure transducer. Piezoresistive sensors have been used in the DLR hand.

- Piezoelectric devices

Piezoelectric material convert mechanical stress into a voltage potential proportional to the force applied. The sensors are very robust and can be used in the measurement of force, pressure and acceleration. The major disadvantage is that they cannot be used to measure static forces. Piezoelectric sensors have been used it the UTAH/MIT hand.

- Capacitive sensors

Capacitive sensors are based on changes in the capacitance of a parallel set of electrodes. This sensor responds to forces that cause a change either the distance between the two plates or the effective surface area of the capacitor. This sensor type has also used with the UTAH/MIT hand.

- Inductive sensors

Inductive sensors depend on the displacement of a movable part within the sensor construction which leads to a change in inductance or magnetic resistance. The LVDT (Linear Variable Differential Transformer) is a common inductive sensor used for measuring linear displacement with high accuracies. Other such sensors use magnetoresistive materials, which exhibit a change in magnetic field when mechanical stress is applied.

- Photoelectic/optical sensors

Optical technology has also been used in the construction of robotic tactile sensors. The underlying principle of optical tactile sensors relies on detecting the changes in reflected light conducted by an optical fiber embedded on a finger tip surface [78, 80]. The optical fiber is often covered by or embedded in an elastomer membrane. New technologies by Tactex Controls Inc. (Victoria, BC, Canada) have led to the development of a touch pad called ‘Kinotex’ (produced under license from the Canadian Space Agency). Unlike embedded opto-electronic sensors, Kinotex sensors use optical fibers to

send light signals into a cellular foam. Force applied on the foam sensing surface causes the light intensity to change, which when measured provides force information.

The reader is referred to [77 - 80] for description of other types of less common robotic sensors and for a descriptions of the practical application of the above-described sensing technologies.

4.3.2 Artificial Finger Sensory Feedback Mechanism

In this thesis, resistive sensors where chosen for implementing sensory feedback in artificial finger. As mentioned, resistive sensors use variable resistive characteristics of some conductive materials (e.g., conductive rubber, carbon, or polymer) to relay information about mechanical motions or forces. They offer a cost-effective solution and have a number of other appealing features - compactness, lightweight, good repeatability, and sensitivity. Three different types of resistive sensors were chosen: thin-film flexible bend sensors, miniature rotary potentiometers, and thick-film flexible force sensors.

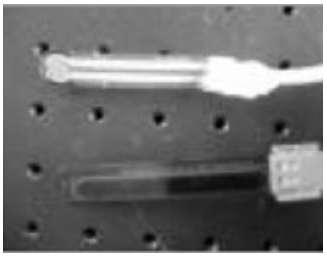

Figure 4.11: Resistive bend and force sensors

Bend sensors consist of a thin flexible membrane coated with thin patches of carbon whose resistance changes when bent in convex/concave shapes. The change in resistance is proportional to the extent to which the membrane is bent. For this research, the commercially available bend sensor from Flexipoint Sensor System Inc. (Draper, UT, USA) was chosen. The Flexpoint bend sensor technology consists of a thin polymide film coated with a carbon/polymer-based ink. When the film is bent, the micro separation of the coated ink changes the electrical resistance of the film. Among commercially available resistive bend

sensors, Simone et al. et al. suggested the Flexpoint bend sensors to be the most accurate and repeatable for measuring the natural finger flexion. [61]. Simone et al. inference was based on the evaluation and characterization of a number of commercially available bend sensors for use in a wearable monitoring glove.

For the present work, we chose a sensor with no polyester overlaminate, and mounted it within the upper inner layer of the artificial finger structure to act as internal proprioceptive sensors, providing positional feedback of the PIP flexion/extension movements. It is to be noted that the motions of the DIP and PIP joints are interconnected through the planar four-bar linkage mechanism. Hence, since the DIP joint is a passive joint dependent on the PIP joint motion, given the position of the PIP joint, the position of the DIP joint can be easily determined without the use of a DIP joint dedicated bend sensor.

While the bend sensors proved to be highly sensitive and reliable for the monitoring of the PIP extension/flexion movements, miniature rotational potentiometers (Panasonic EVWAE4001B14) were employed for measuring the MCP adduction/abduction movements and extension/flexion movements. The potentiometers were embedded on the central axis of the MCP joint for positional feedback of the flexion and extension angles as well as adduction and abduction angles.

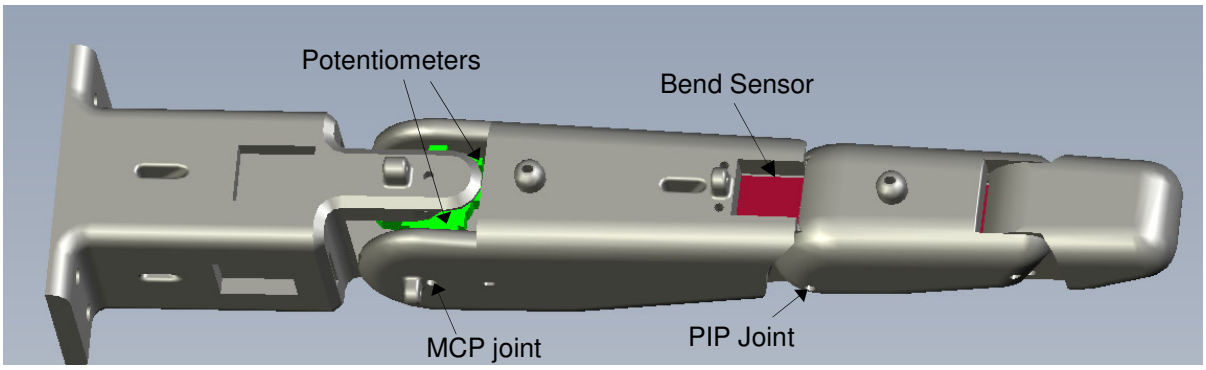

Figure 4.12: A CAD representation of potentiometers and bend sensor embedded in the artificial finger

Although many different types of biomimetic tactile sensors have been proposed [80, 84 - 86], it is still very difficult to replicate the multi-faceted properties of the biological skin structure that is capable of multiple tactile sensing modes (see Section 3.7.1). Hence, in this

research, only one tactile component – contact force - was monitored. The sensor is a commercially available polymeric thick-film force sensitive resistor (FSR) from Interlink Electronics. The force sensor was applied only to the fingertip (proven sensory input location for finger dexterity) of the artificial finger, and then covered it with a layer of elastomeric foam to evenly distribute any applied force and improve the repeatability of the measurements. Although this type of sensor is generally appropriate for qualitative rather than precision measurements, the performance was found to be sufficiently accurate for measuring fingertip forces.

Chapter 5

Biomimetic Actuation Mechanism

Human finger joint motion is produced by contracting muscles in the forearm and palm which are attached to the finger bones through a convoluted network of interdependently acting tendons and ligaments. Muscles are able to alter and tune their stiffness for the performance of different manipulative tasks. Furthermore, although each muscle is believed to have a primary function, a combination of many muscles produces finger motion with a known redundancy in muscle contribution. To date, it has not been determined which muscle synergy will work towards achieving a static position. As such, the emulation of the complex hand muscular architecture remains an unattained benchmark. A partial physical modeling of the finger anatomy, namely the extensor mechanism, was achieved by Wilkinson et al. [68]. However, most biomimetic anatomical representations of the natural hand tend to mimic the features of the muscular architecture and not the exact tendon network itself [26, 42, 45, 47, 49, 50, 69].

In this research, large simplifications of the complex tendon architecture was made possible due to the fact that the natural finger joints were mechanically represented as simple 2 DOF universal (MCP) and 1 DOF hinge (PIP, DIP) joints. This is an acceptable level of emulation for hand rehabilitation robotics which aims at matching functionality more than the hand muscular arrangement. The natural tendons and ligaments, which as well as producing motion also restrict the finger joint to 1 DOF and 2 DOF motion, were not modeled.

Furthermore, this work also focuses on the biomimetic joint articulation. To do so, non-traditional muscles actuators were chosen. These muscle-like actuators present higher power to weight ratio and have become an attractive alternative for their potential to produce life-like motions and eliminate the forced-tradeoff between dexterity (number of DOFs) and anthropomorphic size, weight and appearance. They are believed to be a better match for the

dynamic, light-weight, compact natural muscles which have balanced force generation (active tension), elastic (passive tension) and damping abilities as compared to conventional DC, pneumatic or hydraulic actuators, which tend to be bulky, energy inefficient, heavy-mass actuators. In this work, direct-drivable SMA wires are used, mainly owing to their operational similarity to the human muscles – they contract producing actuation forces - as well as their ability to produce relatively high forces as compared to traditional actuators. The motivation for using SMAs is further expanded in the following sections of this chapter.

5.1 Artificial Muscle Actuators

Three actuating technologies are currently available for muscle-like actuation: McKibben pneumatic muscles, SMA actuators and Electroactive polymers (EAPs). McKibben actuators work figureby inflating an inner bladder sheathed by a mesh webbing which contracts lengthwise when radially expanded. These actuators were specifically developed for artificial limb research in the 1950s and 1960s and have been extensively used in biomimetic robotics [27]. However, the pneumatic system requires external components such as valves and air compressors as well as non-linear controllers. These components are bulky and noisy and cannot be discreetly and easily incorporated in small biomimetic end-effectors.

EAPs refer to a class of polymer that exhibit the ability to undergo a change in shape and size in response to electrical stimulation [87]. Although EAPs have existed for a while, their application as artificial muscles have only been considered since the 1990's only, with the advent of a new polymer class that is capable of large displacements [88]. EAPs have large actuation strains, low densities, can be engineered to produce bending motions as well as stretch and contract and are very resilient. However, while EAPs have a high potential for application as biological muscles, they are considered to be far from being the practical choice of engineers for actuation. The main reason is that, to get EAPs to generate large forces and operate over long periods of time, an improved understanding of the basic principles that drive the EAP materials is required [89]. To date, there are no documented database of the material's properties and no computational models or analytical tools to relilably characterize the response of the materials. Efforts are still being applied to get a

better undertstanding of the parameters that control the force and deformation of this material [89]. Furthermore, they are not easily available commercially and are not robust enough (low bandwidth and actuation force) for rehabilitation hand applications [87, 88].

SMAs artificial muscles refer to a group of metallic elements that present the ability to return to their original shapes and size when heated above a characteristic temperature, referred to as the transition temperature. This phenomenon was first discovered in 1932 in a cadmium and gold alloy. In 1958, researchers (Change and Read) demonstrated that this phenomenon could be used to do mechanical work. However, the field of SMAs was only revolutionized in the 1960s with the discovery of less expensive alloys with larger deformation ratios such as nitinol-titanium alloys [90]. Since then, a large number of commercial products using SMAs were introduced in the 1970's - couplings and fasteners for piping systems and electrical connectors, thermal sensors, catheters (non-invasive surgery tools), eyeglass frames, vibration control and damping tools [90, 91]. However, the most popular application of SMAs is their use as actuators. The direct-drivable SMA wires behave like the biological muscle - they contract with high strains upon activation and yielding high enough forces for actuation [91]. SMAs have to date been successfully used in many robotic hand applications [32, 33, 45, 47-50].

5.2 SMA Artificial Muscles

The following are the desired properties of SMAs which have motivated their use as in the biomimetic actuation system:

- Compact, light-weight with high power to mass ratio - SMAs require less power than conventional electric or pneumatic actuators for the generation of equivalent actuating forces. They also do not consume space and are low in weight, permitting the realization of mechanically efficient actuation system designs.
- Direct-driven - SMAs are commonly used in the form of wires that are activated through resistive heating (by an electric current) with no need for complex and bulky transmission systems. This drastically reduces the complexity of the finger's driving mechanism, with more space available within the finger structure for tendon cables and sensors.

- Noiseless operation – SMA actuators operates with no friction or vibration allowing extremely silent movements. This is an important requirement for prosthetic systems.

SMAs however also have limitations which need to be considered before applying them in any robotic scenario. A large portion of the power applied is dissipated as heat leading to low power efficiencies. At the temperature at which the actuator operates, the maximum achievable efficiency is measured to be approximately 10%. The speed of actuation is dependent upon the rate of cooling of the wire leading to low bandwidths. Cooling techniques such as water immersion, heat sinking and forced air, have been used to improve the SMA wire cycle time. However, even if these methods improve actuation speeds, they also cause an increase in power consumption as more heat is required to actuate the wire within the cooling medium. Furthermore, even though SMAs exhibit relatively large strains (8% for Nitinol), only a fraction of the net strain can be utilized in order to maximize the actuator lifetime. Clever designs that convert the small strains into large motions are required. SMA contraction is highly non-linear owing to temperature hysteresis during joule heating of the material. As such, SMAs actuators are difficult to effectively control.

5.2.1 Principles of SMA Behaviour

This section describes the characteristic behavior of SMAs that enables the emulation of the natural muscles. SMAs experience a phase change, on thermal activation, which allows it to return to its original shape upon heating. As such, the alloy is able to contract, exerting a force in the process, as it occurs in the human body. The key usable effects associated with this phase change are the Shape Memory Effect (SME) and superelasticity.

5.2.1.1 Shape Memory Effect

Shape Memory Effect (SME) describes the heat-induced phenomenon whereby SMAs return to their original dimensional configuration when heated beyond a threshold phase transformation temperature. This phenomenon is referred to as thermoelastic martensitic transformation and occurs due to a change in the material's crystallographic

structure between two phases: austenite and martensite. Martensite is the low temperature phase when the alloy is soft and malleable whereas austenite is the high temperature phase where the alloy is hard.

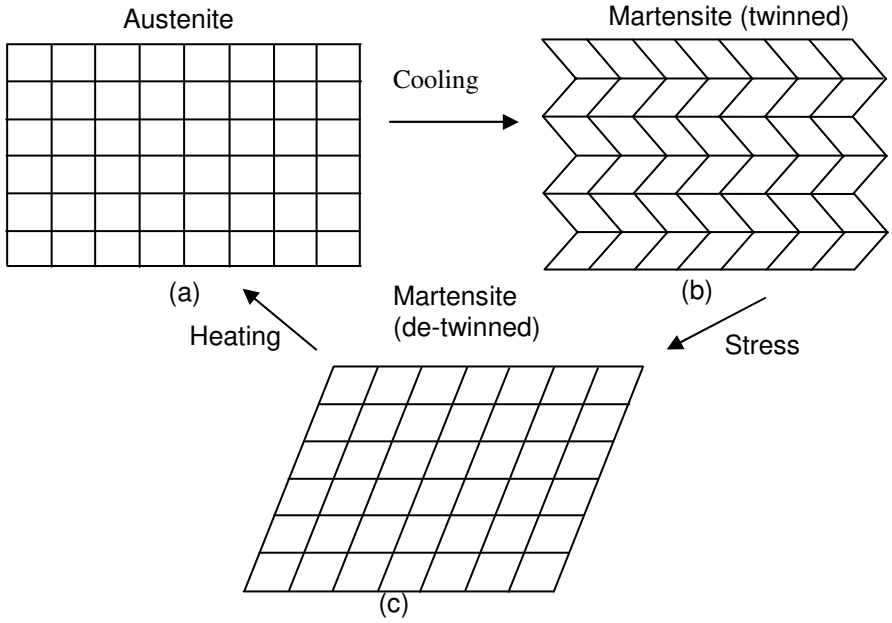

Figure 5.1**:** Grid-like representation of SMA structure [91]

To illustrate the nature of the phase transformations in the alloy, consider the SMA lattice cell depicted in Figure 5.1. Austenite possesses a cubic lattice structure (Figure 5.1a) in which the grains (represented a by one box of the grid) are perpendicular to each other. When the material is cooled below the transition temperature, the grains rearrange themselves producing a highly twinned martensitic structure (Figure 5.1b). Now, if stress is applied on this twinned martensitic structure, the grains rearrange themselves and align in the same direction (Figure 5.1c) forming de-twinned martensite. Physically, martensite detwinning is viewed as large plastic deformations/strains of the material. Subsequent heating of martensite causes the material to return to the more stable high-temperature original austenitic shape (Figure 5.1a) and the plastic deformation is recovered. The shape memory effect described above, whereby the only the parent austenitic phase is 'remembered' by the alloy, is referred to as the one-way SME. It is however possible to make an alloy remember both the parent austenite phase and the martensite shape simultaneously.

This is referred to as the two-way SME. In this case, the alloy exhibits two stable phases: a high-temperature austenite phase, apparent on heating and a low-temperature martensite phase, apparent on cooling.

The shape memory effect can be exploited for the design of devices/actuators. This is done by training the material to remember a specific shape in the austenitic condition. When used as linear actuators, SMAs are commercially available as prestrained (trained to remember a shorter than actual length on heating) martensitic wires. Joule heating (application of an electric current for thermal activation) beyond the transition temperature triggers the phase transformation to austenite where the stretched wire contracts to the prestained length. If no load is applied, the wire contracts freely, which is referred to as 'free recovery'. On the other hand, if the wire is constrained, a considerable force is exerted on contraction. This is referred to as 'constrained recovery'. Now, when the contracted wire is cooled, it returns to the martensite state (twinned) where the material is malleable. A reverse-bias force is needed to return the wire to its original length. Bias forces can be created by many methods: gravitational pull, spring, magnetic force, opposing muscle wire (illustrated in Figure 5.2).

The above shape memory effect is a one-way SME in the sense that, once the SMA wire's shape has been recovered by heating, a reverse-bias force is required to re-introduce the strain in the cooled material. As opposed, in the two-way SME actuator, the SMA actuator will automatically revert to its original length on cooling, without application of a bias force.

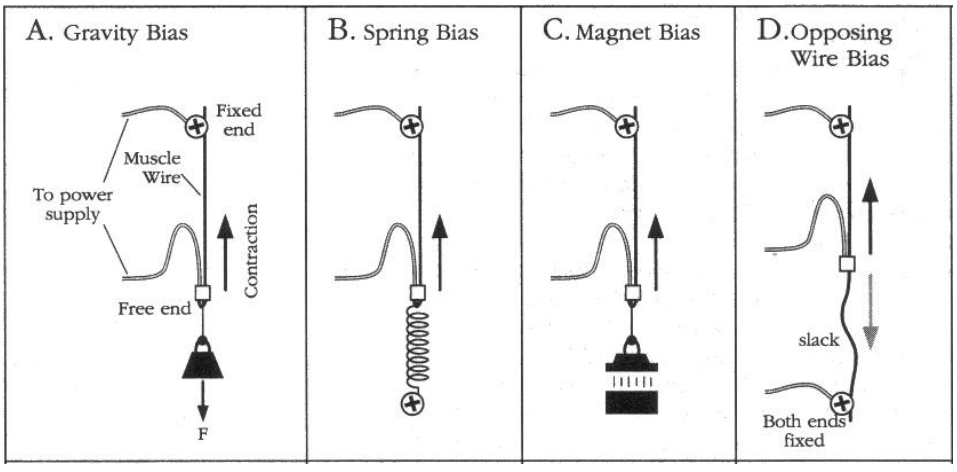

Figure 5.2: Methods for bias forces [90]

5.2.1.2 Superelasticity

Superelastic behaviour or pseudoelasticity is defined as the ability to induce martensitic phase transformation by pure mechanical loading when the material is in the austenitic phase. This phenomenon is referred to as stress-induced martensitic transformation and allows maximum strains of 10%. These strains are fully recoverable upon unloading, given loading occurs when the material is fully austenite, that is, above A^{0f} (see Figure 5.3). This behaviour of SMAs is not used in this work and hence only briefly explained below.

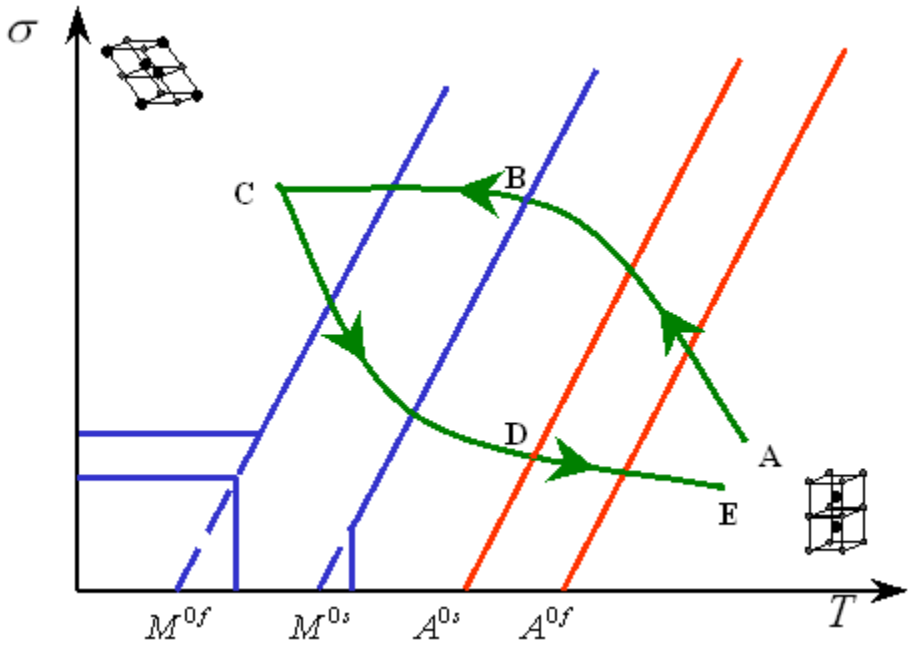

Figure 5.3: Stress-strain relationship in superlastic behaviour of SMAs [96]

The material is initially in the parent austenitic phase at A. When a load is applied, the material initially behaves elastically. However, on continuous application of stress above a critical value, phase transformation from austenite into martensite is initiated until, at C, the transformation is complete and the material is a fully martensite. At a temperature above A^{0f} at which loading occurs, martensite is unstable. Hence, upon removal of the load, reverse transformation occurs, with strain recovery. Phase conversion starts to form until the material reverts to austenite at E. The stress-induced martensite formation allows SMAs to be strained several times more than ordinary metal alloys without being plastically deformed which accounts for what is described as a rubber-like behavior.

5.2.1.3 Stress-Strain Relationship during SME

Under optimum conditions and no load, martensitic phase transformations can cause shape memory strain to be as high as 8%. When constrained to the original length and upon heating above the transformation temperature, SMAs can also generate high stress values. The effects of SME can be better understood by looking at the stress-strain relationship of SMAs as illustrated in Figure 5.4 .

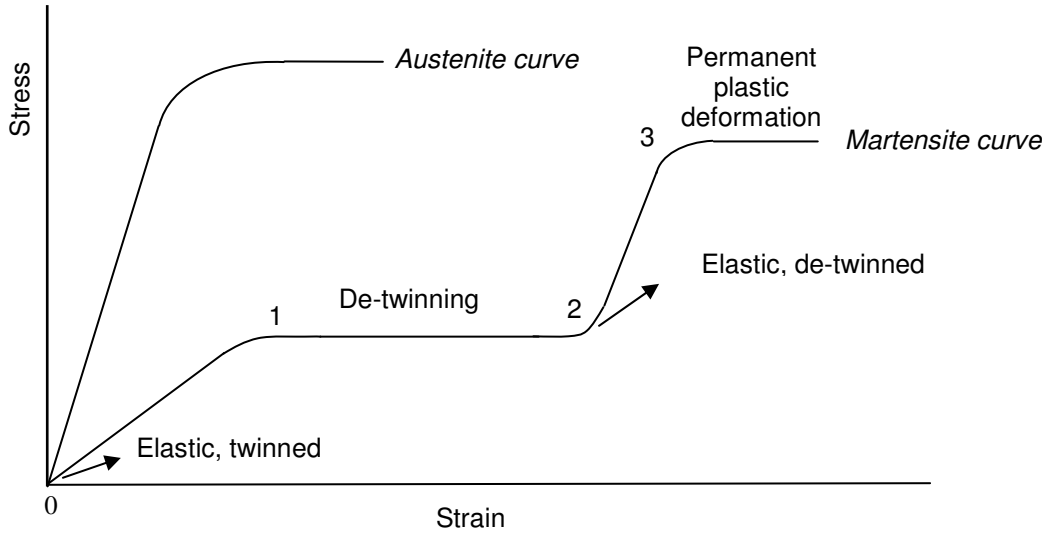

Figure 5.4: Stress-strain behavior SMAs in austentic and martensitic phases [91]

At 0, the SMA is in the twinned martensite state. For small stresses (region 0 to 1), the stress-strain relation of martensite is linear and can be modeled by Hooke's Law. However, above 1, the material starts de-twinning and exhibits elastic behaviour with large strains obtained on application of minimal stress. At 2, the martensitic structure is completely de-twinned. On continuous application of stress, a second elastic region occurs between 2 and 3. Up to level 3, heating of the martensite material is able it to return to its original shape through SME. However, at 3, plastic deformation occurs, which cannot be recovered by SME. Commercially, SMA wires are only used in the regions of 0 to 2 primarily. The detailed behaviour of SMAs through the cyclic phase rotation when SME is used for actuation purposes is illustrated through Figure 5.5.

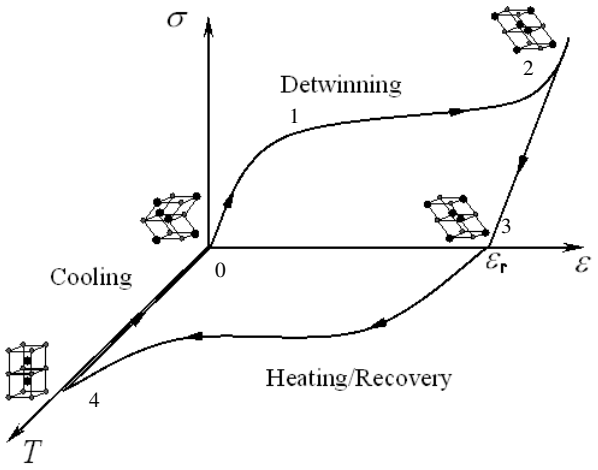

Figure 5.5: Stress-strain curve showing SME as used in SMA actuators [96]

Assume that SMA wire is originally in the high temperature austenitic phase. On cooling (region 4 to 0), twinned martensite is produced. Stress application, for example by the application of a reverse-bias load on an SMA wire, causes the martensite to de-twin and large strains are observed (region 0 to 2). When the de-twinned martensite wire is unloaded (region 2 to 3), the material recovers a small percentage of the strain. The residual strain ε_r, is inelastic and cannot be recovered by unloading but only by heating. Heating causes transformation of the de-twinned martensite into austenite (region 3 to 4) and the wire returns to its original shape.

5.2.1.4 Hysteresis

The SME is not a thermodynamically reversible process. Heat losses during the phase transformation phases (owing to internal friction or structural defects) cause hysteretic behaviour of SMAs. The shift between the austenite and martensite phases is characterized by four transition temperatures: the martensite start (M_s), martensite finish (M_f), austenite start (A_s) and austenite finish (A_f) temperatures. Figure 5.6 illustrates the temperature difference loop, referred to as the hysteresis loop in SMAs.

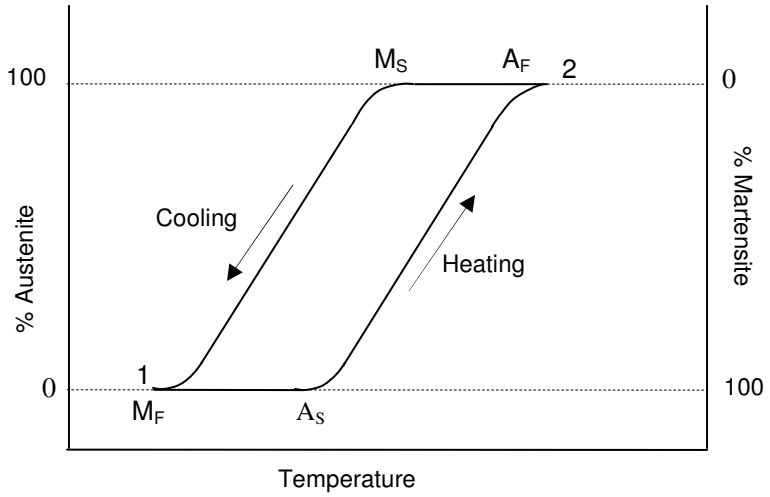

Figure 5.6: Hysteresis loop in SMAs [91]

At 1, the material is 100% martensite. On heating, the crystalline structure of the material changes and austenite starts to appear at A_s. The transformation continues until the material is a 100% austenite at A_f (at 2). On cooling, the reverse process occurs. However, the material does not follow the same transition curve as the heating curve (see Figure 5.6). When austenite is cooled, martensite transformation starts at M_s. Transformation is completed at M_f (at 1), where the material is a 100% martensite again.

5.3 Biomimetic SMA-Driven Actuation Mechanism

This thesis proposes the use of SMAs artificial muscles for the development of a biomimetic actuating mechanism. Since the goal of this work is to define a simple and practical system with as much anthropomorphic consistency as possible for the level of physical emulation achieved, the complex nature of the hand's musculature is not mimicked. Instead, SMAs are used to actuate only tendons necessary to produce full range of motion of the finger. The following section describes the biomimetic actuation scheme developed with the use of off-the-shelf SMA artificial muscle wire actuators.

5.3.1 Biomimetic tendon architecture

A tendon transmission system is chosen in the finger design, with actuators placed remotely from the finger joint axes. This replicates the extrinsic nature and the tendon-drive configuration of the biological finger. Furthermore, remotely located actuators also help relax the actuator size constraints, reduce the net mass of the finger as well as the finger dimensions.

With the tendon configuration, flexible cables are routed from the remote SMA actuators and are attached directly to the finger structure. The commonly used 2N tendon configuration is chosen, where N is the number of active DOFs in the finger. For the artificial finger, N=3 (2 at the MCP and 1 at the PIP) leading to a total of six tendons required to actuate the finger. This is because the DIP joint is a passive joint, that is, the PIP and DIP joints are inter-connected by a four-bar linkage system to replicate the inter-dependency of the PIP and DIP joints (as it exists in the human finger). As such, only three active DOFs of the 4 DOF finger need to be actuated, which reduces the number of tendons attachment to the finger.

Chao et al. [70] defined the exact location of each natural tendon on the finger bones (see Appendix C). These values were used as a basis for our tendon wire point of insertions, within the limitations of our finger skeleton. A further consideration, however, involved defining tendon wire locations that would minimize the subsequent SMA wire force requirements. In an unopposed (i.e., without bias force) joint flexion, the flexion moment is measured at each joint by multiplying the tension in the flexor tendon and the perpendicular distance from the tendon to the axis of the joint, which is equal to the cross-sectional radius of the finger. In our design, since this cross-sectional value does not vary substantially along link lengths, the tendons can be attached anywhere along the links without significantly altering the required actuator force values. In this case, the tendon attachment to the finger were chosen at practical locations so as to minimize tendon entanglement within the finger structure and to facilitate the incorporation of other finger components such as joint rotational shafts, mechanical stops and tendon guides in the finger structure. As mentioned above, the reduction of actuator force requirements was not considered a decisive determining criteria for the tendon locations. The final tendon configuration for the artificial finger is depicted in Figure 5.7.

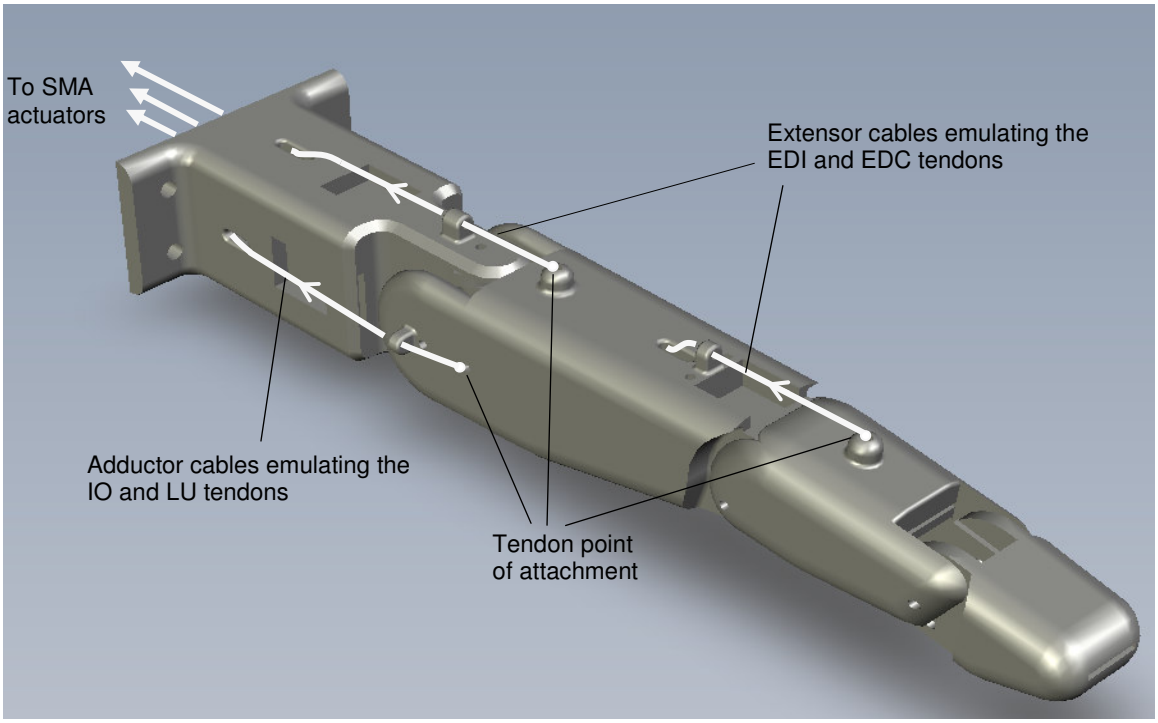

a) Flexor and adductor tendon configuration

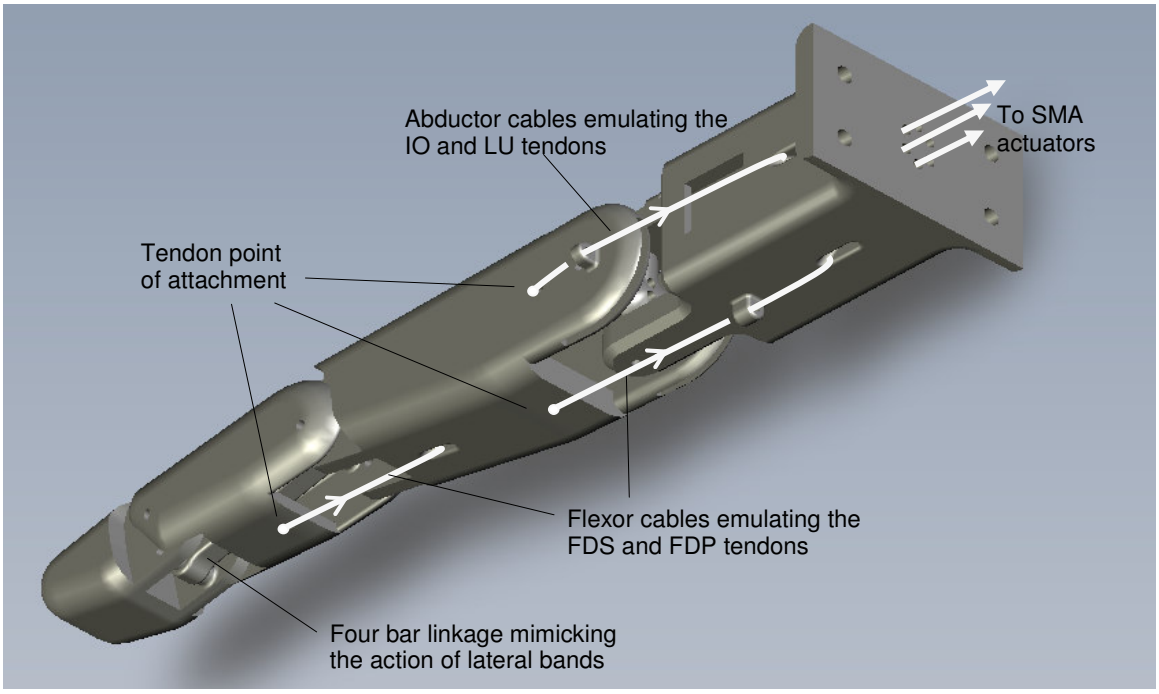

b) Extensor and abductor tendon configuration

Figure 5.7: Artificial finger tendon configuration

Two flexor cables were attached to the proximal and middle links emulating the FDS and FDP tendons. Two extensor cables were attached on the dorsal surface of the proximal and middle links, emulating the EDC and EI tendons. Finally, two adductor/abductor cables were connected to the ulnar and radial sides of the proximal joint mimicking the IO and LU tendons. The flexor, extensor, and adductor/abductor cables act as antagonist muscles enabling flexion/extension at the MCP and PIP and adduction/abduction at the MCP. As already mentioned, the DIP joint flexion/extension is coupled to that of the PIP joint by the implementation of the miniature four-bar linkage mechanism between those two joints inside the artificial finger structure. The four-bar linkage mimics the action of the natural finger's lateral bands, coupling the PIP and DIP joints so that both joints attain their maximum flexion angles (100° at the PIP and 80° at the DIP) simultaneously. While the natural finger has no direct flexor and extensor attachment points to the proximal phalange (i.e., the MCP flexion/extension occurs through the action of the sliding extensor hood), the proposed tendon configuration has attachments to the proximal link. This enables emulation of the natural finger kinematics without exactly mimicking the tendon attachments of the natural finger.

5.3.2 Biomimetic actuation mechanism

The choice as to what type of actuation mechanism to implement in this work was based on kinematics and biomechanical features of human finger. When the human finger is in its normal resting position, it maintains a nominally flexed position (see Figure 4.8). Full range of motion can only be achieved by moving the finger in both flexion and extension directions about its nominal resting position.

Spring-biased SMA artificial muscle wire actuators (mechanism where the spring's opposing force returns the SMA wire to its original length on cooling) have commonly been used for the actuation to robotic joints. For example, Price et al. [34] or Elahinia and Ashrafiuon [92] have used such SMA spring-biased systems where link rotation is produced by the action of a one-way SMA actuator and the link's return to the original position is made by a bias spring (either linear or torsional) connected in opposition to that actuator. However, this type of bias-force mechanism can only produce uni-directional link motion,

that is, the SMA actuation mechanism can only be used to pull/push the artificial finger in one direction (e.g. flexion or abduction) and not in the other direction (e.g., extension or adduction). Bi-directional motion of a robotic joint can only be implemented by the use of two opposing SMA actuators in a differential-type configuration [94]. In this case, another SMA actuator (as compared to a spring) reverse-biases the active SMA actuator. This opposing SMA actuator can, in turn, also initiate link rotation in the opposite direction as well.

The use of a differential type SMA actuation was, as such, the obvious choice for the artificial finger joints as this would permit bi-directional (or differential) agonist–antagonist pulling motion about each finger joint. However, a crucial biomechanical characteristic of the finger's kinematic architecture which needed to be replicated is the elasticity of the natural muscle–tendons. Such compliance is a necessary element in rehabilitation robotics as it provides a stabilizing effect during contact tasks (e.g., gripping), especially in an unstructured environment [93].

The resulting actuation mechanism, that encompasses both bi-directional motion about the finger's resting position and compliance of the tendons, was implemented by employing a pair of spring-biased SMA actuators and using the latter in a differential-type configuration about a finger joint. Hence, a spring-biased SMA actuator is used for flexion motion while another spring-biased SMA actuator is used in opposition for extension motion about the same joint of the artificial finger. The use of the springs in each actuating tendon enabled the emulation of compliant tendons. A schematic diagram of the proposed biomimetic compliant differential actuation mechanism set up to actuate each joint of the finger is shown in

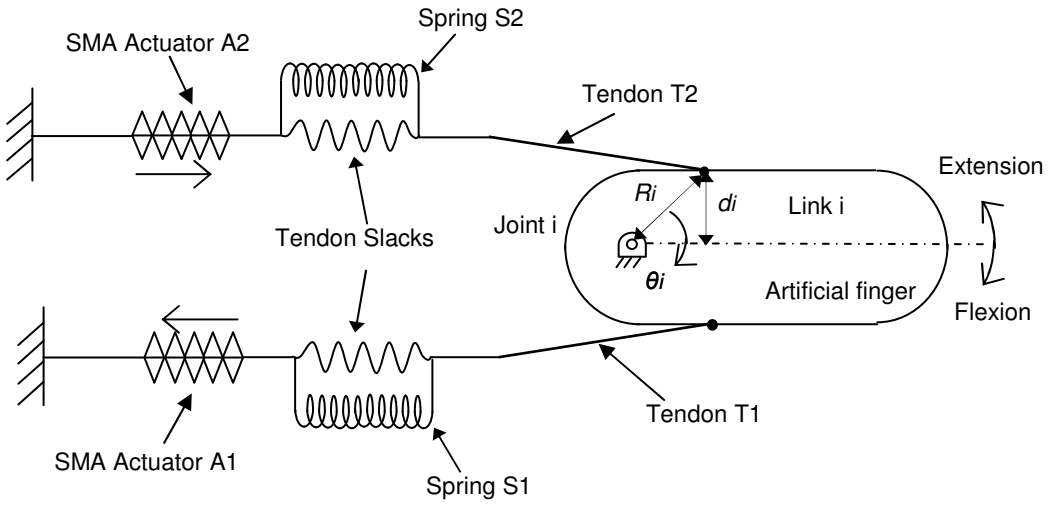

Figure 5.8: Differential spring-biased SMA joint actuation mechanism

One end of the tendon cable is attached to the artificial finger structure, mimicking the attachment of the natural tendon to the finger bones, while the other end of the tendon cable is tied to the SMA actuator. As stated previously, the SMA actuators are placed remotely to the finger joint, similar to the natural finger's extrinsic musculature. Joint rotation is produced by the contractile action of the two SMA actuators, placed in opposition to each other in a double spring-biased fashion. The actuator provides force only in the powered direction while the opposing spring provides an external reset force to return an un-powered actuator to the rest position. The actuation sequence will be covered in details in the following section.

It is to be noted that since only 3 of the 4 DOFs of the artificial finger are active DOFs (DIP joint is a passive joint driven by the PIP joint), the above described SMA actuation mechanism is implemented for the MCP adduction/abduction, MCP flexion/extension and PIP flexion/extension motions only. This results in a total of 6 SMA actuators required to fully actuate the 4-DOF finger.

5.3.2.1 Actuation Sequence

In the proposed differential spring-biased actuation mechanism shown in Figure 5.8, the spring S1 biases the SMA actuator A2, while the spring S2 biases the SMA actuator A1.

Flexion occurs by the contraction of A1 while extension occurs by the contraction of A2. As an SMA actuator (A1 or A2) contracts, the spring in the tendon cable to which the actuator is connected to (we will refer this tendon as the "active tendon") expands, absorbing the slack in the active tendon until the cable is fully stretched and taut. While the finger can rotate simultaneously during the absorbing of the slack (depending on the spring stiffness), at the point where the active tendon is stretched and taut, any further contraction of the SMA actuator acts directly on the finger alone, rotating it about the joint axis. Simultaneously, as the finger starts to flex or extend, the spring in the opposing tendon (we will refer this tendon as the "passive tendon") expands and the slack in the passive tendon is absorbed while the finger rotates about the joint axis. When an SMA actuator (A1 or A2) is deactivated and its contraction force is removed, the springs S1 and S2 will to return to their original positions. The spring in the active tendon recreates the slack. The spring in the opposing passive tendon reverse-biases the SMA actuator, and while doing so, exerts a pulling force on the artificial finger structure which returns the joint to its original position. Note that the springs in both the active and passive tendons need to be stretched whether the artificial finger moves into a flexed or extended state with respect to its normal resting position.

5.3.2.2 Compliant Differetial Actuation

Passive compliance is introduced in the tendon cables of the artificial finger by connecting the reverse-bias spring in parallel to a slack portion of the tendon cable (see Figure 5.9). With this arrangement, as the SMA actuator pulls/contracts, the spring in the corresponding tendon elongates until the slack is absorbed and the tendon is taut. At this point, the tendon can be considered to have "infinite" stiffness and further SMA actuator contraction causes tension to be transferred to the finger for link rotation. This simple spring-slack artificial tendon effectively mimics the nonlinear stiffness of the natural tendon whose stiffness tends to 'infinity' as it approaches its natural limit of extension. The dual spring-biased configuration permits the two SMA actuators to work as an agonist–antagonist pair, enabling both active extension and flexion of the joint. Hence, as the link flexes or extends, the compliant opposing tendon yields and stretches permitting the flexion or extension motion to occur.

Figure 5.9: Artificial tendon spring-slack arrangement emulating the natural tendon's compliance

5.3.2.3 Limiting Factors

While the nonlinear stiffness property of the biological tendons limits the flexion/extension range of the natural finger, the limit on the range of motion of the artificial finger is dependent on the following two factors:

(i) SMA actuator's contraction range—the SMA actuator's stroke range must be sufficiently large to first absorb the slack in the active tendon to which it is connected in order to produce joint rotation

(ii) Slack length in the passive tendon opposing the motion—the link cannot rotate beyond the elastic limit of the opposing tendon.

As such, the proposed actuation mechanism demands a careful balance between the allowable tendon slack and the SMA contraction range to generate the desired range of motion.

In this work, it is assumed that the tendon is held securely against the curved articular surface of the proximal bone of the joint, with the tendon wire lying parallel to the central axis of the finger and that each tendon remains fixed to their remote attachment point throughout the link motion. For the above, configuration, the SMA actuated tendon contraction that would enable a joint rotation through an angle θ_i can be approximated by:

$$\Delta l_{A_i} = R_i \theta_i \tag{5.1}$$

where Δl_{A_i} is the SMA actuator contraction length, R_i is the radius of rotation and θ_i is the rotation angle about the joint *i*.

Considering the actuation mechanism depicted in Figure 5.8, the slack in the tendon T_1 that allows for the link *i* to reach a full extension can be approximated by:

$$\Delta X_{T1} = R_{ext_i}\theta_{ext_i} \tag{5.2}$$

where R_{ext_i} is the extension radius of rotation and θ_{ext_i} is the full extension angle about the joint *i*.

Similarly, the slack in the tendon T_2 that allows for the link *i* to reach a full flexion is given by

$$\Delta X_{T2} = R_{flex_i}\theta_{flex_i} \tag{5.3}$$

where R_{flex_i} is the flexion radius of rotation and θ_{flex_i} is the full flexion angle about the joint *i*.

As mentioned, the SMA strain range should account for both the tendon slacks in T_1 and T_2 as well as for the actual or "effective" joint rotation. Hence, the maximum SMA contraction lengths required at full joint extension/flexion are given by:

$$\Delta l_{A1} = \Delta X_{T1} + R_{flex_i}\theta_{flex_i} \tag{5.4}$$

$$\Delta l_{A2} = \Delta X_{T2} + R_{ext_i}\theta_{ext_i} \tag{5.5}$$

Substituting Eq. (5.2) into Eq. (5.4) and Eq. (5.3) into Eq. (5.5), the SMA contraction lengths can be expressed as follows:

$$\Delta l_{A2} = \Delta l_{A1} = \Delta X_{T2} + \Delta X_{T1} \tag{5.6}$$

This indicates that an identical contraction length (i.e., $\Delta l = \Delta l_{A1} = \Delta l_{A2}$) can be used for the two opposing SMA actuators as long as the net contraction length is properly distributed between the two tendons. One of the practical limitations of the chosen differential SMA actuation configuration is that, due to the presence of the slacks in the tendons, only a portion of the SMA strain ranges are available to cause the effective joint rotation. However, because of the fact that two SMA actuators are employed for active bi-directional rotation of each joint DOF, its overall range of motion is still greater than that of

an equivalent single spring-biased SMA actuation mechanism (with no slack). Furthermore, the combined action of the spring and SMA in the tendon cable mimics the characteristics of the natural muscle–tendon, providing power only during contraction, yet providing compliance to deal with an opposing load as well. Also note that SMA actuators can be controlled in partial contraction, allowing finger links to be partially flexed and extended. The use of the two opposing SMA actuators per DOF allows the additional benefit of more precise finger positioning, as the direction of motion can be quickly reversed at any point during joint rotation.

5.4 SMA Actuator Selection

Two defining criteria come into play when selecting the SMA actuator: i) the actuator stroke and ii) the force output. The SMA wire contraction length must be sufficient to pull the finger link throughout its full range of motion about the joint axis. Also, the force output of the SMA actuator must produce joint torques which are high enough to maintain the finger in static equilibrium when the finger is in pinch and grasp configurations. This is specially important in the case of rehabilitation robotics where the target users are have limited motor functions and rely on the rehabilitative robot for motion and grip stability.

The following sections describe the evaluation of the SMA actuator stroke and actuator force necessary to activate the joints of the artificial finger. These stroke and force values defined are used to select the appropriate off-the-shelf SMA actuator to be used in this work.

5.4.1 SMA Actuator Stroke

As derived in Section 5.3.2.3, an identical contraction length (i.e. $\Delta l = \Delta l_{A1} = \Delta l_{A2}$) can be used for the two opposing SMA actuators, that is

$$\Delta l = \Delta l_{A1} = \Delta l_{A2} \tag{5.7}$$

The active contraction of the SMA actuator, Δl, is related to the joint angle θ_i by the following equation , as derived by eq (5.1) and eq (5.3):

$$\Delta l = R_{ext_i}\theta_{ext_i} + R_{flex_i}\theta_{flex_i} \tag{5.8}$$

Given that the maximum extension and flexion ranges are know for each finger joint, the necessary SMA contraction needed to produce full range of motion can be calculated. This is presented in Table 5.1.

JOINT MOTION	MAXIMUM JOINT RANGE	MAXIMUM SMA ACTUATOR STROKE
MCP ADDUCTION/ABDUCTION	40 ^{o}	8.2 mm
MCP EXTENSION/FLEXION	90 ^{o}	26.6 mm
PIP EXTENSION/FLEXION	100 ^{o}	23.2 mm

Table 5.1: SMA actuator stroke

5.4.2 SMA Actuator Force

In this thesis, required actuator force to maintain static equilibrium of the finger when pushing on an object is determined by performing a static torque analysis of the finger joints. The joint torque is calculated for the static phase of an isometric grip, that is, grip where there is a static constant force exertion by the finger segments without any resulting joint motion. This torque is used with the finger's equation of motion to determine required SMA actuator force values to maintain static equilibrium. It is to be noted that since the aim of this work is the development of an anthropomorphic finger platform for testing of a biomimetic actuation mechanism, the scope of the finger force analysis is limited to static forces. The finger dynamics, that is, the actuator forces required to cause finger motion are not considered at this point.

5.4.2.1 Static Forces for Index Finger Functions

Chao et al. [70] experimentally studied the forces acting on the index finger for a number of simulated static grasp functions used in daily activities. These functions included basic pinch, grasp, extension-flexion, adduction-abduction. The index finger joint orientation angles for various static functions as defined by Chao et al. are presented in Table 5.2. These joint flexion angles were defined with respect to the index finger's neutral position, which Chao et al. defined as being the straight extended finger.

FUNCTION	JOINT FLEXION ANGLE /DEGREES		
	MCP	PIP	DIP
TIP PINCH	48	50	25
LATERAL PINCH	20	35	20
GRASP	62	48	23
ABDUCTION	0	0	0
ADDUCTION	0	0	0
FLEXION	45	0	0
EXTENSION	0	0	0
CYLINDRICAL GRIP	23	72	55

Table 5.2: Index finger joint flexion angles for various functions [70]

During experimental assessment of the externally applied forces, Chao et al. determined that six phalangeal force distribution patterns are possible in grasps [70]. The most common "Type 2" force distribution, where the distal phalange carries the maximum force followed by the middle and the proximal, is presented here. In this configuration, the forces vectors are assumed to apply approximately at the middle of each phalange. The resulting externally applied forces (magnitude, orientation and point of application) to simulate index finger functions are presented in Table 5.3. The magnitude of the forces are normalized to one based on the maximum force applied. Realistic forces can be obtained from the presented dimensionless units by multiplying the forces in Table 5.3 by actual measured externally applied forces. Similarly, the point of application of the given forces is normalized with respect to the length of the middle phalange. The real location of the force on the phalange can be obtained by multiplying the point of application in Table 5.3 by the middle phalange length.

FUNCTION	POINT OF APPLICATION (ON PHALANGE)			ORIENTATION OF APPLIED FORCE (DIRECTIONAL COSINE)			MAGNITUDE OF FORCE	PHALANGE
	X	Y	Z	X	Y	Z		
TIP PINCH	0.55	-0.10	0.0	-0.707	0.707	0.0	1.0	Distal
LATERAL PINCH	0.20	-0.10	0.0	0.0	0.0	1.0	1.0	Middle
GRASP	0.55	0.0	0.0	0.0	1.0	0.0	1.0	Distal
	0.79	0.0	0.0	0.0	1.0	0.0	0.34	Middle
	1.35	0.0	0.0	0.0	1.0	0.0	0.66	Proximal
ABDUCTION	0.0	0.0	-0.28	0.0	0.0	1.0	1.0	Middle
ADDUCTION	0.0	0.0	0.28	0.0	0.0	-1.0	1.0	Middle
FLEXION	0.44	-0.2	0.0	0.0	1.0	0.0	1.0	Distal
EXTENSION	1.66	0.32	0.0	0.0	-1.0	0.0	1.0	Proximal
CYLINDRICAL GRIP	0.48	0.44	0.0	0.0	1.0	0.0	1.0	Middle

Table 5.3: Normalized externally applied forces on the index finger
adapted from values in [70]

It is to be noted that adaptations were made to the force vectors presented by Chao et al. in order to account for a different frame of reference used in this thesis. Chao et al. used a primary Cartesian coordinate system located at the approximate centre of rotation of the phalangeal heads (joint axes) with the x-axis projecting along the phalangeal shafts, through the centre of rotations of the joints towards the wrist. The y-axis was projected dorsally and the z-axis radially (for the right hand) [70]. In this thesis, the force vectors were interpreted with respect to D-H frame notation (see Section 4.2.1), which projects the x-axis along the phalangeal length towards the fingertip, the y-axis dorsally and the z-axis ulnarly (for the right hand). This resulted in an inversion x and z point of application values as well as an inversion of the directional cosine of the x and z force components (final values presented in Table 5.3).

5.4.2.2 Derivation of Torque Equations

Joint torques will balance the external forces acting on the finger in a static situation. In this work, the joint torques necessary for static equilibrium during grasping are derived using the Jacobin matrix. The Jacobian is a time-varying transformation relating joint and Cartesian velocities and is expressed as:

$$J = \frac{\partial X}{\partial \theta} \tag{5.9}$$

where ∂X is the velocity of the finger in the Cartesian frame and $\partial \theta$ is the finger joint velocities. The transpose of the Jacobian matrix is known to map the Cartesian forces acting on the finger into equivalent joint torques as per the following equation:

$$\tau = J^T F \tag{5.10}$$

where F is the Cartesian force-moment vector, τ is the joint torque vector and J is the finger Jacobian (the reader is referred to [82] for a detailed description of the evaluation of the above torque equation).

Jacobians must be written with respect to a frame of reference. The same frames of reference as used for the finger kinematic analysis (Section 4.2.1) are used for the static torque analysis. Hence, frame {0} is assigned to the point where the finger meets the palm, frame {1} and {2} are assigned to the MCP adduction/abduction joint an MCP flexion/extension joint respectively. Frame {3} and frame {4} are located at the PIP and DIP joint respectively. The reference frame {0} coincides with frame {1} and {2} as illustrated Figure 4.9.

When the Jacobian is written with respect to frame {0}, then force vectors acting on the finger and written with respect to frame {0}can be transformed into joint torques as per:

$$\tau = {}^{o}J^{T\,o}F \tag{5.11}$$

The Jacobians, in this work, are derived with respect to the base reference frame {0}. Now, the externally applied forces that occur on the proximal, middle or distal phalanges, given the index's static function (see Table 5.3), are only known in terms of the frames assigned to the respective proximal phalangeal joint. For example, a force acting on the fingertip is expressed with respect to the frame located at the DIP joint, forces on the middle phalange are known with respect to the frame at the PIP joint and so on. For the purpose of

torque calculations as per eq. (5.11), force-moment transformations are used to express the manipulation and grasping external forces acting on the finger phalanges into the base reference frame {0}.

Let the grasping force acting on proximal link be F_A, on the middle link be F_B and on the distal link be F_C (see Figure 5.10). Each of these forces will induce joint torques. Since F_A acts on the proximal phalange, it causes a joint torque at the MCP only. F_B, acting on the middle phalange, will cause joint torques at both the MCP and PIP joints. F_C on the other hand will generate torques on all finger joints since it acts on distal phalange.

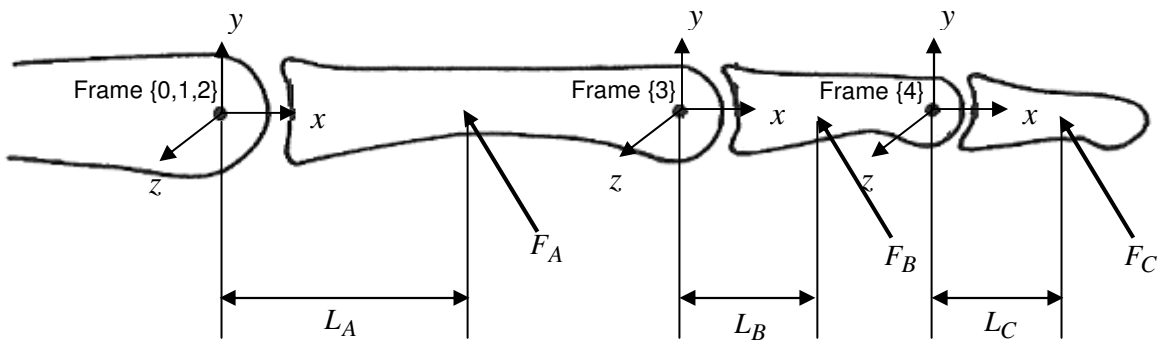

Figure 5.10: Frames of references and grasping forces on index finger

The first step in the derivation of the torque equations involves converting the individual forces acting on the finger into the reference frame {0}. The force vectors written with respect to frame {0} are then transformed into individual joint torques by the use of the Jacobian matrix (also written with respect to the reference frame). Once the resulting joint torques from F_A, F_B and F_C are evaluated, the net torque, τ, acting on the finger is then given by the summation of the torques generated by these three forces, that is:

$$\tau = \tau_A + \tau_B + \tau_C \tag{5.12}$$

where $\tau_A =$ torque generated by F_A at the MCP joint

$\tau_B =$ torques generated by F_B at MCP and PIP joints

$\tau_C =$ torques generated by F_C at MCP, PIP and DIP joints

The torque equations for each force component, as calculated the Jacobian matrix are given by:

$$\tau_A = \begin{pmatrix} -f_{z_A} L_A c_2 + m_{x_A} s_2 + m_{y_A} s_2 + m_{y_A} c_2 \\ f_{y_A} L_A + m_{z_A} \\ 0 \\ 0 \end{pmatrix} \tag{5.13}$$

$$\tau_B = \begin{pmatrix} -f_{z_B} L_1 c_2 - f_{z_B} L_B c_{23} + m_{x_B} s_{23} + m_{y_A} s_2 + m_{y_B} c_{23} \\ f_{x_B} L_1 s_3 - f_{y_B} L_1 c_3 + f_{y_B} L_B m_{Z_B} \\ f_{y_B} L_B + m_{z_B} \\ 0 \end{pmatrix} \tag{5.14}$$

$$\tau_C = \begin{pmatrix} -f_{z_C} L_2 c_{23} - f_{z_C} L_1 c_2 - f_{z_C} L_C c_{234} + m_{x_C} s_{234} + m_{y_C} c_{234} \\ f_{x_C} L_2 s_4 - f_{y_C} L_2 c_4 + f_{x_C} L_1 s_{34} + f_{y_C} L_1 c_{34} + f_{y_C} L_C + m_{z_C} \\ f_{x_C} L_2 s_4 + f_{y_C} L_2 c_4 + f_{y_C} L_C + m_{z_C} \\ f_{y_C} L_C + m_{z_C} \end{pmatrix} \tag{5.15}$$

where $F_A = \left(f_{x_A}, f_{y_A}, f_{z_A}, m_{x_A}, m_{y_A}, m_{z_A}\right)$

$F_B = \left(f_{x_B}, f_{y_B}, f_{z_B}, m_{x_B}, m_{y_B}, m_{z_B}\right)$

$F_C = \left(f_{x_C}, f_{y_C}, f_{z_C}, m_{x_C}, m_{y_C}, m_{z_C}\right)$

L_1, L_2, L_3 = Link lengths (see Figure 4.9)

L_A, L_B, L_C = Point of application of forces along link length (Figure 5.10)

As per eq. (5.12), the net finger joint torques for different static postures is made by the summation of torques at each joint.

$$\tau = \begin{pmatrix} \tau_1 \\ \tau_2 \\ \tau_3 \\ \tau_4 \end{pmatrix} = \tau_A + \tau_B + \tau_C \tag{5.16}$$

where τ_1 and τ_2 refer to the torques at the MCP joint owing to adduction/abduction and extension/flexion respectively; and τ_3 and τ_4 are the PIP and DIP joint torques respectively.

The detailed evaluation of the elements of the Jacobian matrix, finger force-moment transforms required to express the forces exerted on the finger phalanges in into reference frame {0} and the evaluation of the individual torques τ_A, τ_B, τ_C as generated by the force components acting on the finger are presented in Appendix D.

5.4.2.3 Evaluation of Artificial Index Finger Joint Torques

For this preliminary analysis, some assumptions are made. Firstly, only externally applied forces will be considered, that is, the forces acting on the finger when grasping or pushing an object. This means that any internal forces owing to the compliance of the finger structure and joint friction are assumed negligible. Secondly, a point contact model with friction is used for the external forces, that is, each contact point on the finger, by an object, exerts a pure force, normal and tangential to the finger surface. No moments are exerted.

The vector forces as well as the point of application of the forces on the finger phalanges, as presented in Table 5.3, are applied to the artificial index finger. The index finger is considered to be in the same static postures as presented by Chao et al. (illustrated in Table 5.2). However, the artificial finger's neutral position in this work is the normal resting position where the proximal link is at 40^o flexed with respect to the palmar plane while the middle link rests at an angle of 20^o with respect to the proximal link phalange. These normal resting positions of the joints are taken into consideration when determining the MCP and PIP angular positioning of the artificial finger in different static postures. As for the DIP, the four-bar linkage determines the DIP's position based on the PIP angular configuration. The DIP's angular position, as guided by the four-bar mechanism, was also considered. The MCP, PIP and DIP angles are presented in Table 5.4.

Given known incident forces and joint angular positions, the torque equations evaluated in Section 5.4.2.2 can used determine the joint torques for various static positions of the index finger. Table 5.4 summarizes the resulting joint torques when moving the finger into different grasping configurations from the normal resting position and for unit normalized forces acting on the finger. As mentioned before, τ_1 and τ_2 are the torques at the MCP joint; τ_3 and τ_4 are the PIP and DIP joint torques, respectively.

FINGER CONFIGURATION	τ_1 (NMM)	τ_2 (NMM)	τ_3 (NMM)	τ_4 (NMM)	JOINT ANGLES (^{o}) MCP	PIP	DIP	POINT OF APPLICATION
PINCH GRIP	0	84.1	35.7	10.5	-8	-30	-24	Distal
LATERAL PINCH	-51.4	0	0	0	20	-15	-12	Middle
GRASP	0	117.1	47.1	14.9	-22	-28	-22.4	Distal, Middle, Proximal
ABDUCTION	-37.5	0	0	0	40	20	16	Middle
ADDUCTION	37.5	0	0	0	40	20	16	Middle
FLEXION	0	77.5	-37.8	-11.9	-5	20	16	Distal
EXTENSION	0	-44.8	0	0	40	20	0	Proximal
CYLINDRICAL GRIP	0	-43.1	13.0	0	17	-52	-41.6	Middle

Table 5.4: Joint torques for unit force acting on finger phalanges (index finger)

To note, by convention, clockwise rotation of the joints (flexion) is taken as negative and anticlockwise rotation (extension) as positives. Abduction and adduction angles are assumed to be 20^o from the straight extended position. Furthermore, the torque values in Table 5.4 need to be multiplied by a factor equivalent to the magnitude of the force acting on the finger phalanges to obtain realistic torque values

Furthermore, it is to be noted that the coupling between the PIP and DIP joints alters the torque input requirements for the PIP joint. In this thesis, a four-bar dynamic analysis was not performed. The four-bar mechanism linking the PIP and DIP joints was instead approximated to a pulley system. As such, since the rotation at the PIP joint induces rotation of the DIP joint, then, assuming no power loss in transmission, the net power input at the PIP (P_{PIP}) can be considered as the summation of the power required to drive the PIP and DIP. Hence, net power requirement at the PIP joint,

$$P_{PIP} = P_3 + P_4 = \tau_3\omega_3 + \tau_4\omega_4 \tag{5.17}$$

where P_3 is the power to drive the PIP joint only; P_4 is the power to drive the DIP joint solely; ω_3 is the PIP's angular speed and ω_4 is the DIP's angular speed.

Since the PIP and DIP attain their full flexion range (80^o for DIP and 100^o for PIP) within the same time interval, then rate which DIP rotates with respect to the PIP is given by the following equation:

$$\omega_4 = 0.8\omega_3 \tag{5.18}$$

Substituting eq (5.18) in eq (5.17):

$$P_{PIP} = \tau_3\omega_3 + \tau_4(0.8\omega_3) \tag{5.19}$$

$$P_{PIP} = \omega_3(\tau_3 + 0.8\tau_4) \tag{5.20}$$

Hence, the net torque input at the PIP joint can be calculated as:

$$\tau_{PIP} = \tau_3 + 0.8\tau_4 \tag{5.21}$$

5.4.2.4 Defining SMA Actuator Force

The static torque analysis of the finger enabled the torque values at the finger joints to be determined for various finger postures. The SMA actuator force necessary to generate these torques can be derived from the static equation of motion for a given finger link. Consider the forces acting on the finger, as shown in Figure 5.11.

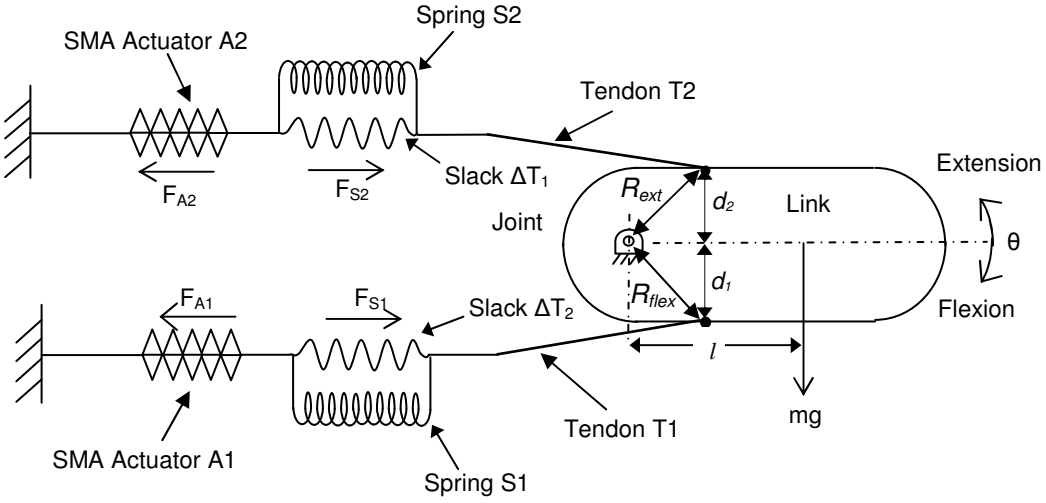

Figure 5.11: Forces acting on the finger link

As previously stated, it is assumed that the tendon is held securely against the curved articular surface of the proximal bone, with the tendon wire lying parallel to the central axis of the finger link. It is also assumed that each tendon is constrained to remain fixed to their remote attachment point throughout the link motion and that the un-actuated SMA wire does

not undergo elastic deformation during joint motions. Given the above, for a link in static equilibrium, the torque at the joint is given by the following equation:

$$\tau = F_2 d_2 - F_1 d_1 - mgl\cos\theta \tag{5.22}$$

where: F_1 = force in tendon T_1

F_2 = force in tendon T_2

m = mass of the finger link

d_1, d_2 = normal distance between joint and tendon location

l = distance of the center of mass with respect to the joint center location

θ = joint angle rotation with respect to the frontal plane for extension/flexion

I. Actuator force in finger flexion

The net force in tendon T_1 is the net force output of the SMA actuator A_1, F_{A_1}, and the force in the spring S_1, F_{S_1}, that is

$$F_1 = F_{A_1} - F_{S_1} \tag{5.23}$$

Given that during flexion, the opposing actuator A_2 is not active, then the force in T_2 consists of the force in spring S_2, that is, at static equilibrium:

$$F_2 = F_{S_2} \tag{5.24}$$

Substituting eq (5.23) and eq (5.24) in eq (5.22):

$$\tau = F_{S_2} d_2 - (F_{A_1} - F_{S_1}) d_1 - mgl\cos\theta \tag{5.25}$$

Rotational motion of the finger can only happen when the slack in T_1 is fully absorbed, that is, when S_1 is extended by slacks ΔX_{T_1}. The resulting force in S_1 is given by:

$$F_{S_1} = k\Delta X_{T_1} \tag{5.26}$$

where k is the spring constant.

As described in Section 5.3.2.3, the slack in the tendon T_1 should be such that it enables full extension of the link. Once the slack in parallel to the spring has been absorbed, the spring cannot extend any further. Hence, substituting eq. (5.2) in eq. (5.26)

$$F_{S_1} = k(R_{ext}\theta_{ext}) \tag{5.27}$$

where R_{ext} is the radius of rotation for link extensions and θ_{ext} is the full extension angle

about the joint.

In the normal resting position, the springs S_1 and S_2 are in slight tension to maintain the finger in equilibrium. Let the initial spring extension be Δx_1 and Δx_2 for S_1 and S_2 respectively. As the finger link flexes, S_2 is stretched by the initial extension Δx_2 as well as a length equivalent to the rotational angle θ of the link. The force in S_2 can hence be expressed as:

$$F_{S_2} = k(R_{flex}\theta + \Delta x_2) \tag{5.28}$$

where R_{flex} is the radius of rotation for link extensions

If τ_{flex} joint torque induced during flexion, the torque eq. (5.22) can be written as:

$$\tau_{flex} = k(R_{flex}\theta + \Delta x_2)d_2 - (F_{A_1} - k(R_{ext}\theta_{ext}))d_1 - mgl\cos\theta \tag{5.29}$$

The force in SMA actuator A_1 for static positioning of the finger link after flexion is derived as:

$$F_{A_1} = \frac{\left(k(R_{flex}\theta + \Delta x_2)d_2 - k(R_{ext}\theta_{ext})d_1 - mgl\cos\theta - \tau_{flex}\right)}{d_1} \tag{5.30}$$

II. Actuator force in finger extension

During finger extension, the SMA actuator A_1 is not active. The force in T_1 only consists of the force in spring S_1, that is, at equilibrium:

$$F_1 = F_{S1} \tag{5.31}$$

On the other hand, the force in tendon T_2 is the net force output of the SMA actuator A_2, F_{A_2}, and the force in the spring S_2, F_{S2}, that is

$$F_2 = F_{A_2} - F_{S_2} \tag{5.32}$$

Substituting eq (5.31) and eq. (5.32) in eq (5.22):

$$\tau = (F_{A_2} - F_{S_2})d_2 - F_{S_1}d_1 - mgl\cos\theta \tag{5.33}$$

Rotational motion of the finger can only happen when the slack in T_2 is fully removed, that is, S_2 is extended by slacks ΔX_{T2}. The resulting force is S_2 is given by:

$$F_{S_2} = k\Delta X_{T_2} \tag{5.34}$$

where k is the spring constant.

The slack in the tendon T_2 should enable full flexion of the link with the spring extension being limited by the slack length ΔX_{T_2}. Hence, substituting eq (5.3) in eq (5.34)

$$F_{S_2} = k(R_{flex}\theta_{flex}) \tag{5.35}$$

R_{flex} is the radius of rotation for link flexions and θ_{flex} is the full flexion angle about the joint.

As the finger link extends, S_1 is stretched by the initial extension Δx_1 as well as a length equivalent to the rotational angle θ of the link. The force in S_1 can hence be expressed as:

$$F_{S1} = k(R_{ext}\theta + \Delta x_1) \tag{5.36}$$

where R_{ext} is the radius of rotation for link extensions

If τ_{ext} joint torque induced during flexion, the torque eq (5.22) can be written as:

$$\tau_{ext} = (F_{A_2} - k(R_{flex}\theta_{flex}))d_2 - k(R_{ext}\theta + \Delta x_1)d_1 - mgl\cos\theta \tag{5.37}$$

The force in SMA actuator A_2 for static position of the link after extension is derived as:

$$F_{A_2} = \frac{\left(\tau_{ext} + k(R_{flex}\theta_{flex})d_2 + k(R_{ext}\theta + \Delta x_1)d_1 + mgl\cos\theta\right)}{d_2} \tag{5.38}$$

The same approach is used to evaluate the actuator force for adduction and abduction movements, with the exception that the mass effect is ignored since the link weight acts normal to the plane of motion. The static torque values evaluated in Section 5.4.2.3 are for unit force values applied on the finger phalanges. Realistic torques are obtained by multiplying the torque values calculated by the actual forces acting on the finger. Kargov et al. [95] experimentally analyzed the grip force distribution of the human hand when fulfilling everyday tasks. The maximum contact force was found to be 3.8 N at the proximal phalange of the index finger.

For force analysis purposes, an average grasping force magnitude of 5 N is assumed as it is well within the range which the natural finger would sustain. Realistic torques values for various finger postures are calculated by multiplying torque values in Table 5.3 with a

magnitude of 5. It is to be noted that the static torque analysis performed translates the forces acting on the finger phalanges into a resulting torque at the finger joint. To maintain static equilibrium, an opposing and equal torque necessary. The above accordingly adjusted torque values are used with SMA actuator force equations (5.30) and (5.38). The maximum actuator force for MCP adduction/abduction motions was hence calculated to be 28.9 N for lateral pinch postures. The maximum actuator force for the MCP and PIP flexion movements were 54 N and 50 N respectively for grasp functions.

These force values were used as the starting point for actuator selection. However, in the process of choosing the appropriate actuator for this work, we were made increasingly aware of the difficulties involved in obtaining actuators with the desired specifications. This was evidenced by a major lack of off-the-shelf SMA actuators that could be directly used for robotic application. The biggest supplier of SMA wires (Mondo-tronics, CA, USA) listed a wide range of SMA wires and springs which could potentially be applied in this work. However, this called for the fabrication of an appropriate housing to hold the large lengths of SMA wire or numerous springs required for actuation and to convert the SMA contraction into a steady usable stroke.

Eventually, we opted for SMA actuators from Miga Motor Company. Miga Motor Company was found to be the only company, to the author's knowledge, to provide an off-the-shelf commercial line of modular SMA actuators. The highest end of the available modular actuator, the DM01-15, was chosen. The DM01-15 SMA actuator is capable of a half inch linear pull stroke and a maximum contracting force of 20N with actuating voltages ranging from 9V to 28V. This actuator did not meet the exact stroke and force requirements as calculated. However, it was deemed to be acceptable for preliminary testing purposes since the joints did not have to be actuated throughout the full range of motion. Furthermore, no or minimal external forces were to be applied to the artificial finger during the experimental testing. Coupled with the smaller ranges of motion, a 20 N actuation force was estimated to be sufficient. This was later confirmed by experimental tests done and described in Chapter 7.

Chapter 6

Modeling and Simulation

The main usable characteristic of SMAs is the shape memory effect where the alloy's phase transformations can be used to generate motion or force. Cyclic transitions between the austenite and martensite phase, however, occur with large hysteresis. If the cycle is completed, then hysteresis loop is referred to as the major hysteresis loop. On the other hand, if the phase transition does not complete, a different phase return path is taken, which leads to what is referred to minor hysteresis loops (smaller phase transition loops within major loops). As such, the SMA stress-strain response is: i) non-linear, ii) temperature dependent and iii) sensitive to the number and sequence of phase cycles [98]. Furthermore, continuous cycling through the phases also induces a permanent plastic strain in the material. This is referred to as the initial material strain and can accumulate for over 2000 cycles.

The development of a mathematical model that captures the complex SMA behaviour, i.e., the non-linear stress and strain change at all temperature ranges, the hysteretic behaviour and the change of mechanical properties due to fatigue, is very challenging. Different approaches have been undertaken in SMA model development. Some researchers have chosen to simplify the material's behaviour by creating models in which the phase temperatures are the same for heating and cooling, neglecting the hysteresis effects [91]. Others have only approximated the hysteresis effect, ignoring minor hysteresis loops that occur during the phase transition between martensite and austenite. Often, only part of the SMA behaviour is modeled, e.g., only the superelastic behaviour of SMAs is modeled and the SME is ignored. Furthermore, given that a model that fully represents the unique behaviour of SMAs can be developed, researchers are faced with the additional challenge of maintaining the model simple enough so that a computational algorithm can be implemented. Indeed, the ultimate aim of modeling is to use computer simulation tools to better understand the thermomechanical properties of the material and therefore, reduce time and cost for

actuator design. To date, work is still being done towards the development of an optimal SMA model that fully describes the SMA's complex operation.

This chapter illustrates the Matlab/Simulink simulation of an SMA-actuated joint of the artificial finger based on a chosen macromechanical model of SMA alloys. The author's contribution to the modeling and simulation work is an in-depth analysis of the modeling frameworks used to characterize SMA behavior and choosing the most suitable SMA mathematical model for this work. The other components necessary to fully model the artificial finger joint (SMA heat transfer model, joint kinematic and dynamic models) were also chosen or developed by the author. However, the final Matlab/Simulink simulation was developed by Gilardi et al. [97]. This simulation was used to evaluate the potential success of the biomimetic actuation scheme with open-loop control.

6.1 SMA Mathematical Model

The modeling framework used for SMA model development varies mainly in the choice of internal variables, the kinetic equations defining the internal variables and energy relations [98]. Depending upon the material laws used to describe the SMA behaviour, SMA models can be grouped in two categories: micromechanical models and phemenological or macroscopic models [99, 100].

6.1.1 Micromechanical Models

These models study the effects of phase transformations on the microscopic scale through the construction of energy equations that describe (i) the local strains, or (ii) behaviour of a representative control volume of the material. These relations are then averaged or homogenized to derive the material macroscopic models [101].

Some examples of the work done using this framework include [99]:

- Patoor et al. (1983) - They developed a model based on the martensite variant in each every material grain. The macroscopic deformation was computed by evaluating the martensitic volume proportion in the material. This model does not take into account the hysteresis effect.

- Sun and Hwang (1993) - Similar to Patoor's, a model based on the martensite variant in small material volume was developed. This model covers most of the characteristic temperature range of SMAs. However, a constitutive equation exists for each temperature range, which complicates the computational implementation of this model.
- Leclerc et al. developed a model for the superelastic behaviour of SMAs which accounted for the three-dimensional stress states of SMAs and hysteresis subcycles. A simpler model was later proposed, which neglected hysteresis. Experimental tests, however, did not validate the model developed.
- Ganghoffer et al. - Finite element modeling of martensitic transformation in each grain of the material has been studied by Ganghoffer et al. This model correctly represented the twinning process as well as the internal stresses due to martensite formation. However, they are not helpful for modeling of actual SMA devices.

6.1.2 Macroscopic Models

This type of model describes the material behaviour of SMAs without any description of the underlying phase mixture during phase transformations. These models mainly require experimental knowledge of SMA behaviour [99].

Some examples of macroscopic models developed are:

- Tanaka's approach – Tanaka developed thermomechanical constitutive equations and kinetic equations based on the thermodynamic properties of SMAs. In this model, the total change in stress is assumed to be proportional to three components (i) an elastic component proportional to the Young's Modulus and change in strain, (ii) a transformational component proportional to the phase coefficient and martensite volume fraction and (iii) a thermal component proportional to the thermoelastic coefficient and the change in temperature [102]. Although this model represents the three-dimensional stress states, it is valid only in case of simple loadings since it is very difficult to appropriately compute the martensite fraction in relation to the stress and temperature for a complex load.

- Liang and Rogers – This model has the same constitutive equation as Tanaka's model. However, in contrast to Tanaka's model, a cosine function is used to model the martensite volume fraction instead of an exponential function [103].
- Brinson et al. – They further developed Tanaka's constitutive model by separating the martensite variables into stress-induced and temperature-induced martensite. The overall martensite volume fraction is modeled as the summation of these two martensite fractions [102].
- Boyd and Lagoudas – In this model, the martensite fraction is also expressed in terms of temperature and stress. However, this model mainly aims at modeling SMA based composites [99].
- Bilinear models– These models approximate the austenite, phase transformation and martensite domains by three separate straight lines. Owing to this simplification, models therefore, only represent superelasticity. Similar models have been proposed by Muller and Xu, who describe hysteresis by two parallel lines, implying constant stress during phase transformation. Bradon and Rogers have also proposed a similar model, with the exception that the transformation slopes cannot be zero [99].

The reader is referred to work in [99], [101] and [102] for a detailed description of above SMA mathematical models.

6.2 Liang & Rogers's SMA Model

Most SMA models developed which are derived by a study of the underlying physics of the material are not suitable for modeling as regards control and design of SMAs as actuators. These models are often too complex, variables and coefficients used in the models are difficult to identify and real-time implementation of such models are not feasible. Literature has revealed that macromechanical models are the ones are most commonly used in technological applications since are most easily implementable and have parameters which can be experimentally determined [103-108].

The SMA model most suitable for design-oriented modeling was found to be those based on Tanaka's constitutive equations, which is made of: i) a basic governing equation

that describes the material stress rate in terms of the rate of change of the strain, temperature and percentage martensite material and ii) another set of equations that relates the percentage martensite to the temperature and stress [109]. The chosen model for this simulation is Liang and Rogers's SMA model which uses the same basic governing equation as Tanaka's [103]. The equation describing the volumetric percentage of martensite in the material is, however, modified by using a cosine function instead of an exponential function.

6.2.1 SMA Constitutive Equation

The basic governing equation for SMAs, in its general form, is given by [103]:

$$\dot{\sigma} = D\dot{\varepsilon} + \Theta\dot{T} + \Omega\dot{\xi} \tag{6.1}$$

where the equation constants are:

D = Young's modulus

Θ = Thermoelastic tensor

Ω = Phase transformation tensor

and the equation variables are:

ε = Green Strain

T= Temperature

σ = Second Piola-Kirchoff stress

ξ = Volumetric fraction of martensite in the SMA

The phase transformation tensor, Ω, and Young's modulus, D, are both a function of the percentage martensite, ξ, in the material and are given by [104]:

$$D(\xi) = (1-\xi)D_A + \xi D_M \tag{6.2}$$

where D_A = Austenite Young's Modulus and D_M = Martensite Young's Modulus.

$$\Omega(\xi) = -D\varepsilon_t \tag{6.3}$$

where ε_t is the residual strain, the maximum strain that can be recovered through the phase transformation.

The martensite volumetric fraction is not necessarily constant between the austenite and martensite phases and will be defined in the following section.

Now, the strain is itself made up two component strains, ε_e, which is the elastic strain and ε_t is the transformation strain caused by detwinning martensite

$$\varepsilon = \varepsilon_e + \varepsilon_t \tag{6.4}$$

Since the actuation mechanism developed for this work has a spring is connected in series with the SMA actuator, the net actuation strain can be modified to include the spring's contribution.

$$\varepsilon = \varepsilon_e + \varepsilon_t + \varepsilon_s \tag{6.5}$$

where ε_s is the strain as induced by the spring.

Given that the spring's Young modulus is D_s and the spring constant is K_s eq. (6.1) can be rewritten as:

$$\dot{\sigma} = D\dot{\varepsilon}_t + D\dot{\varepsilon}_e + D_s\dot{\varepsilon}_s + \Theta\dot{T} + \Omega\dot{\xi} \tag{6.6}$$

If the SMA's spring constant is k_D, then the equivalent spring constant of the SMA-spring system is given by:

$$k_{eq} = \frac{k_s k_D}{k_s + k_D} \tag{6.7}$$

The equivalent Young's modulus of the SMA-spring system is given by:

$$D_{eq} = \frac{k_{eq} L_w}{s_w} \tag{6.8}$$

where l_w is the length of the tendon wire and s_w is the cross-sectional area of the wire.

Substituting eq. (6.7) into eq. (6.8):

$$D_{eq} = \frac{k_s k_D}{k_s + k_D} \frac{L_w}{s_w} \tag{6.9}$$

Now, the SMA wire's Young's modulus as the wire elastic deforms is:

$$D = \frac{k_D L_w}{s_w} \tag{6.10}$$

Substituting eq. (6.10) into eq. (6.11)

$$D_{eq} = \frac{k_s}{k_s + k_D} D \tag{6.11}$$

The SMA constitutive equation for the spring and SMA system is given by:

$$\dot{\sigma} = D\dot{\varepsilon}_t + D_{eq}(\dot{\varepsilon}_e + \dot{\varepsilon}_s) + \Theta\dot{T} + \Omega\dot{\xi} \tag{6.12}$$

6.2.2 SMA Phase Transformation Equations

The last set of equations that need to be considered during the analysis and modeling of SMAs is the laws relating the phase transformation. These equations express the martensitic volumetric fraction, ξ, in terms of temperature, *T*, the initial martensitic volumetric fraction ξ_o and the stress σ (if applicable) [104].

I. Cooling phase

The martensitic fraction as austenite to martensite phase change is given by:

$$\xi = 1 - \xi_o Cos\left[a_M \left(T - M_f\right)\right] + \frac{1+\xi_0}{2}$$

$$\text{where} \begin{cases} 1 & T < M_f \\ \xi & M_f > T > M_s \\ 0 & T > M_s \end{cases} \tag{6.13}$$

M_s refers to the temperature at which martensite starts to form whereas M_f is the temperature at which the alloy fully martensitic. Eq. (6.13) is applicable when the temperature decreases from M_s to M_f only and, also for cases where the phase transition is stress independent, i.e., temperature-driven only as it occurs during free recovery. If both the stress and the temperature are the driving factors, eq. (6.13) needs to be changed to address the stress effect. Since a stress increase is analogous to a decrease in temperature, a linear

modification of the temperature term is performed. It should be noted that the presence of stress also affects the temperature range validity of the transformation equation, as shown by the eq. (6.15 and 6.16). The generalized austenite to martensite phase equation is then given by:

$$\xi = 1 - \xi_o Cos\left[a_M \left(T - M_f\right) + b_M \sigma\right] + \frac{1+\xi_0}{2}$$

$$\text{where } \begin{cases} 1 & T < M_f \\ \xi & M'_f > T > M'_s \\ 0 & T > M_s \end{cases} \tag{6.14}$$

The stress-dependent martensitic temperatures are given by:

$$M'_f = M_f + \frac{\sigma}{C_M} \tag{6.15}$$

$$M'_s = M_s + \frac{\sigma}{C_M} \tag{6.16}$$

Furthermore, other parameters of the eq. (6.14) are:

$$a_M = \frac{\pi}{M_s - M_f} \tag{6.17}$$

$$b_M = \frac{-a_M}{C_M} \tag{6.18}$$

in which $C_M = \frac{\sigma}{M'_f - M_f}$, an experimentally-derived curve fitting parameter that represents the slope of the line of the martensite transformation temperatures with stress (illustrated in Figure 6.1).

II. Heating phase:

$$\xi = \frac{\xi_o}{2}\left\{Cos\left[a_A\left(T - A_s\right)\right] + 1\right\} \qquad \text{where } \begin{cases} 1 & T < A_s \\ \xi & A_s > T > A_f \\ 0 & T > A_f \end{cases} \tag{6.19}$$

Similar to the austenite to martensite phase transition, the above equation represents a stress-free phase transformation. For a stress and temperature dependent phase transition, the

generalized equation is also obtained by a linear modification of the temperature term of eq. (6.19). Hence:

$$\xi = \frac{\xi_o}{2}\{Cos[a_A(T - A_s) + b_A\sigma] + 1\} \qquad \text{where} \begin{cases} 1 & T < A_s \\ \xi & A'_s > T > A'_f \\ 0 & T > A_f \end{cases} \tag{6.20}$$

The stress-dependent austenitic temperatures are given by:

$$A'_f = A_f + \frac{\sigma}{C_A} \tag{6.21}$$

$$A'_s = A_s + \frac{\sigma}{C_A} \tag{6.22}$$

Other parameters of eq. (6.20) are:

$$a_{A=} \frac{\pi}{A_f - A_s} \tag{6.23}$$

$$b_A = \frac{-a_A}{C_A} \tag{6.24}$$

in which $C_A = \frac{\sigma}{A'_f - A_f}$, an experimentally-derived curve fitting parameter that represents the slope of the lines of the austenite transformation temperatures with stress (illustrated in Figure 6.1).

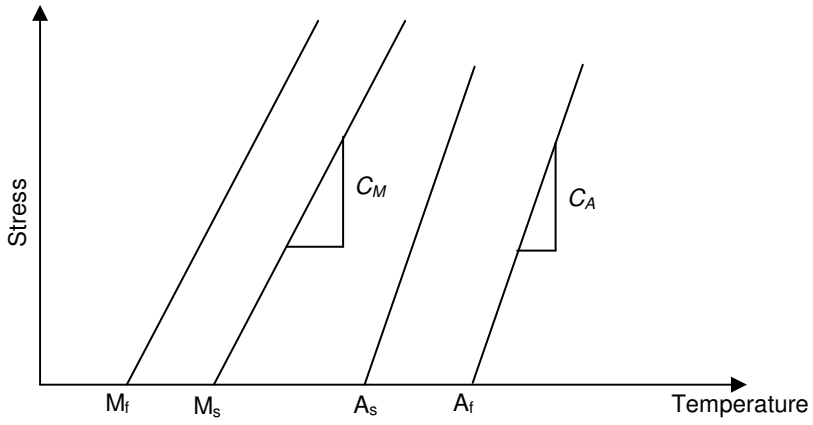

Figure 6.1: SMA stress – temperature profiles [104]

6.3 SMA Heat Transfer Model

As mentioned beforehand, the extent to which SMA wires elongate and contract is dependent upon the rate at which heat is imparted to it. Some of the electrical heating used to heat the wire while the remaining heat is lost by convection. As such, to fully define the SMA wire operation, it is important to portrait the way in which heat is transferred to the material. The SMA heat transfer model is given by the following equation [92]:

$$mc_p \frac{dT}{dt} = \frac{V^2}{R} - hA(T - T_\infty) \tag{6.25}$$

where: V = Voltage

R = Resistance per unit length

c_p = Specific heat capacity

m = mass per unit length

T_∞ = Ambient temperature

A = Cooling surface area

h = Heat convection coefficient

The heat convection coefficient, h, is further approximated by a third order polynomial of second order of temperature to improve the heat transfer model:

$$h = h_o + h_2 T^2 \tag{6.26}$$

6.4 Joint Kinematic Model

The ultimate goal, in this work, is to control the angular joint position of the artificial finger by adequately controlling the SMA wires elongation and contraction, i.e., the wire strain. The tendon wire length, l, is related to the joint angle θ by the following equation:

$$\Delta l = R\Delta\theta \tag{6.27}$$

Dividing by the initial wire length l_0:

$$\varepsilon = \frac{R\Delta\theta}{l_0} \tag{6.28}$$

Let the contracting SMA wire that causes clockwise rotation (flexion) be denoted as Wire 1 and the opposing SMA wire be referred as Wire 2 (as shown in). Given that clockwise rotation is taken as negative rotation and contractile strain is negative, then the

$$\varepsilon_2 = \frac{R(\theta_0 - \theta_i)}{l_{2_0}} \tag{6.29}$$

$$\varepsilon_1 = \frac{R(\theta_i - \theta_0)}{l_{1_0}} \tag{6.30}$$

where: θ_0 = initial joint angle

θ_i = current/desired joint angle

l_{1_0} = initial SMA Wire 1 length

l_{2_0} = initial SMA Wire 2 length

R = radius of rotation

6.5 Dynamic model

Again, let the contracting SMA wire that causes flexion be denoted as Wire 1 and the opposing SMA wire be referred as Wire 2 (see Figure 5.8). The dynamic torque equation is given by:

$$I\ddot{\theta} = F_2 d_2 - F_1 d_1 - mgl \cos\theta - \tau_f \tag{6.31}$$

where F_1 = force in tendon T_1

F_2 = force in tendon T_2

m = mass of the finger link

d_1, d_2 = normal distance between joint and tendon location

l = distance of the center of mass with respect to the joint center location

θ = joint angle rotation with respect to the frontal plane for extension/flexion

τ_f = frictional moment at the joint

I = Moment of inertia (about the z-axis).

The frictional moment is modeled using the Coulomb-Viscous model as described in [97]. Let τ_{drv} be the total external driving torque, that is,

$$\tau_{drv} = F_2 d_2 - F_1 d_1 - mgl\cos\theta \tag{6.32}$$

The frictional moment is given by:

$$\tau_f = \begin{cases} sign(\dot{\theta})(M_{DF} + C_{DF}\left|\dot{\theta}\right|) & \text{if } \left|\tau_{drv}\right| > \tau_{SF} \\ \tau_{drv} & \text{if } \tau_{drv} > \tau_{SF} \end{cases} \quad (6.33)$$

where M_{DF} = the dynamic friction moment

C_{DF} = dynamic friction coefficient

τ_{SF} = static friction moment

6.6 Simulation

For the preliminary analysis, only the MCP joint of the finger was used for simulation purposes. Furthermore, the simulation was performed with only one actuator being active a time, that is, the finger was moved either in flexion or extension movements by using activating only one actuator at a time. Matlab/Simulink was used to build the finger simulation based on the mathematical models defined. This simulation model was implemented by Gilardi et al. [97] and is represented in Figure 6.2. It is to note that the 'SMA Acutator 2' block is structured exactly as the "SMA Actuaor 1" block (see Figure 6.2). The details of the 'SMA Acutator 2' block is omitted to maintain visual simplicity of the diagram. This simulation model was used in this thesis with a variation in some modeling parameters used and with a modified joint kinematic model as compared to [97].

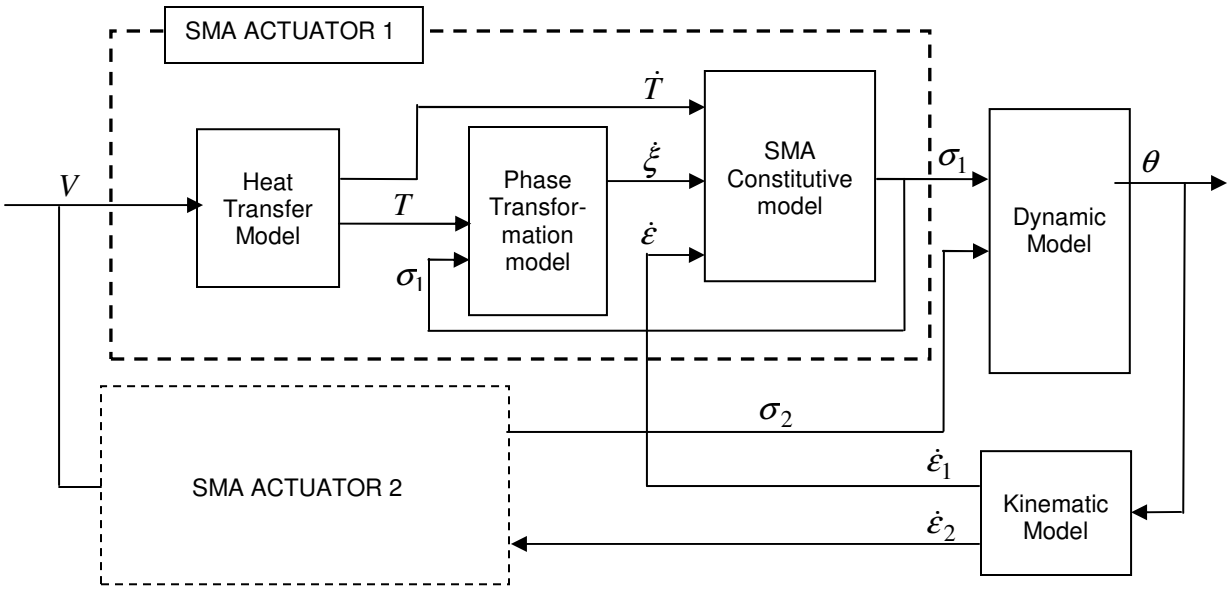

Figure 6.2: Schematic representation of mathematical model for SMA-actuated finger joint

6.6.1 Modeling Parameters

The finger's geometric parameters were obtained from the CAD model built. One of the challenges in the modeling of the system was a lack consistent resource for all parameters describing the shape memory effect. In this work, SMA wire parameters were obtained from the manufacturer (Miga Motor Company) and other required SME-related parameters were borrowed from literature, namely from [90] and [92]. The parametric uncertainty was addressed to some level by a sensitivity analysis done, that is, a parametric analysis of the MCP flexion movement with an open-loop control. This analysis indicated that the system was sensitive to the parameters in the friction model and heat convection model. As such, experimental parameter identification was use to determine the values for the heat convection coefficients h_0 and h_2, and the dynamic friction coefficient (the reader is referred to [97] for a detailed description of parametric analysis performed).

Table 6.1 lists the simulation parameters used and their numerical values. The thermoelastic factor, Θ, was assumed to be zero since as per the SMA actuator design, thermal expansion of the SMA wire does not generate any length variation in the wire. Furthermore, a

maximum deformation of 3% to 5% is recommended for Nitinol (SMA wires used in the actuator) [90]. Hence maximum strain of 4% is chosen for this simulation

PARAMETER	DESCRIPTION	VALUE
l_o	Initial wire length	0.385 m
D	Wire diameter	$0.375 \times 10^{-}3$ m
c_p	Specific heat of wire	322 J/Kg^{o}C
R	Resistance per unit length	8 Ω/m
ρ	Density	6450 kgm^{-3}
h_o	Heat convection coefficient	70
h_2	Heat convection coefficient	0.001
T_{amb}	Ambient Temperature	23 °C
M_s	Martensite start temperature	80 °C
M_f	Martensite finish temperature	60 °C
A_s	Austenite start temperature	75 °C
A_f	Austenite finish temperature	110 °C
C_A	Austenite curve fitting parameter	10.3e^6 Pa/^{o}C
C_B	Martensite curve fitting parameter	10.3e^6 Pa/^{o}C
Θ	Themoelastic tensor	0
Ω	Phase transformation tensor	20.6e^8
D_M	Martentisite	28 GPa
D_A	Austenite	75 GPa
ε_R	Residual Strain	2.3 %
K_s	Spring constant	140 N/m
M_{SF}	Static moment	0.01 Nm
C_{DF}	Dynamic Friction Coefficient	0.02
M	Link mass	0.011 Kg
l	Centre of mass	0.022 m
I	Inertia	1.253×10^{-5} kgm^2

Table 6.1: Numerical simulation parameters for the MCP joint

6.6.2 Open-loop simulation

A constant voltage of 8V was used for SMA activation as this was experimentally determined to be the voltage level which enabled the SMA wire contraction without inducing

over-heating of the wire. The MCP joint was considered to be in the normal resting position, that is, in a starting position of 40^{o} with respect to the frontal plane (note flexion is taken as negative rotation). The open-loop control plots for extension and flexion are presented in Figure 6.3 and Figure 6.4 respectively.

As mentioned, only actuator is activated at a time with the opposing actuator acting as a bias spring only. In this configuration, the open-loop simulation suggests that both joint extension and flexion are possible. Joint angular rotation starts and ends according to the SMA actuation patterns, that is, joint motion starts when the SMA wire is at the austenite start temperature of 75 °C. Joint rotation is complete when the conversion to austenite is complete at a temperature of 110 °C. Given the simulation parameters used for the SMA actuator and finger, a maximum extension and flexion of 25^{o} from the normal resting position was estimated to be possible.

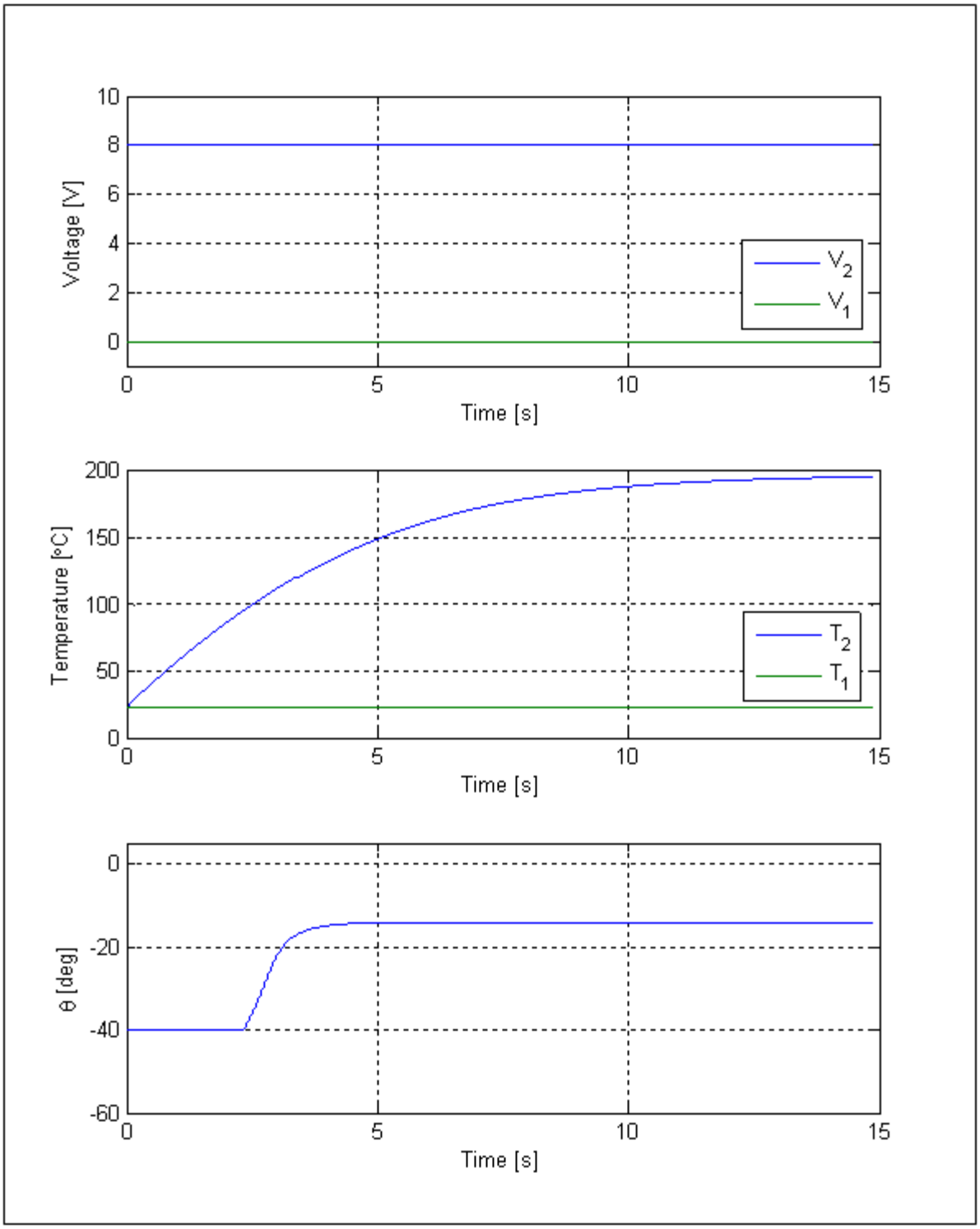

Figure 6.3: Open loop control of MCP Extension

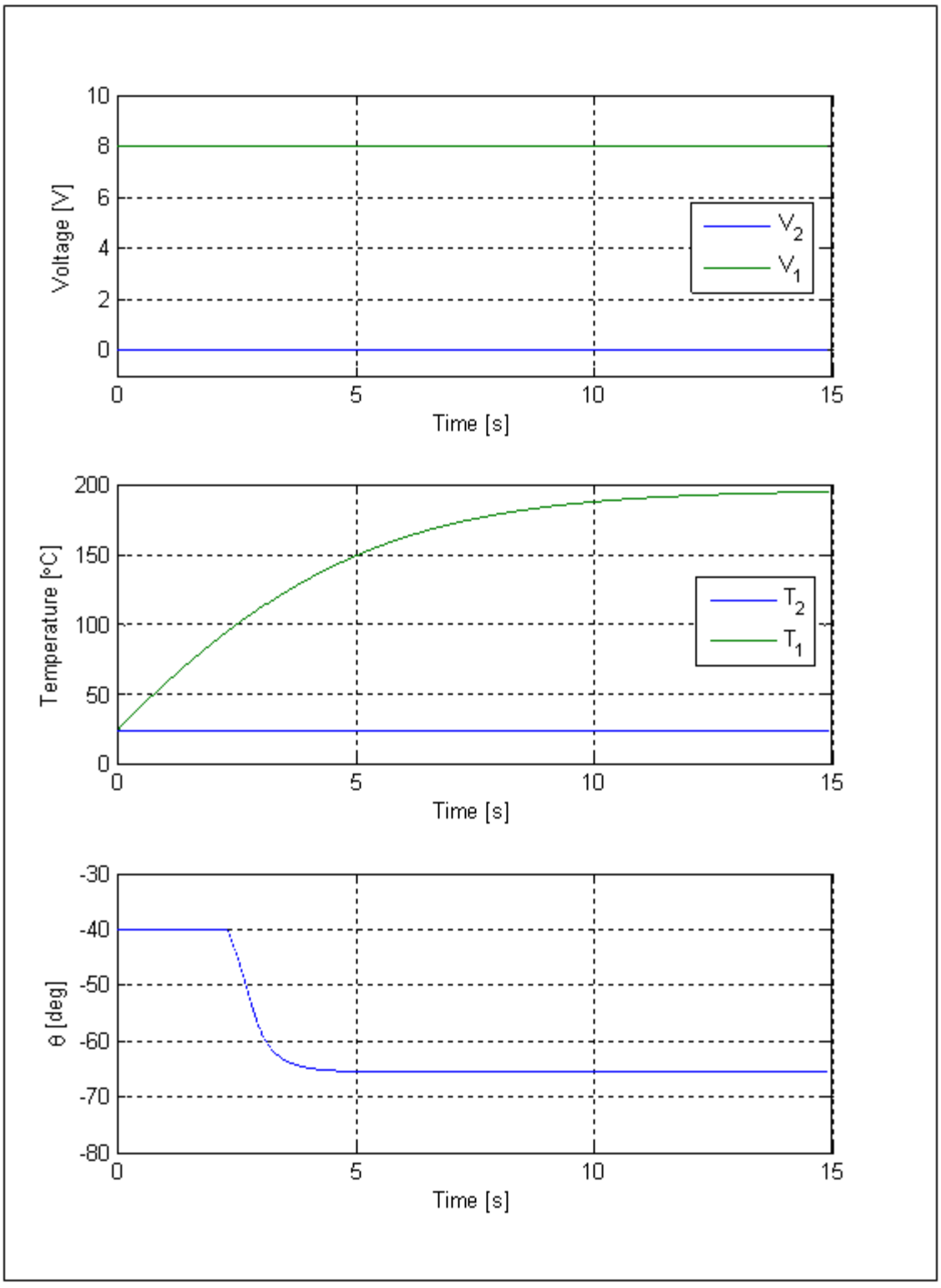

Figure 6.4: Open loop Simulation of MCP Flexion

Chapter 7

Experimental Evaluation of the Biomimetic Actuation Mechanism

The primary motivation for this work is the development of a biomimetic actuation system for rehabilitation purposes using novel lifelike actuators, which in this case, chosen to be SMA artificial muscles. Since the human hand is the one of the most important organ used for interaction with the physical world, this problem was applied to an artificial anthropomorphic representation of the human finger.

This chapter outlines the experimental tests performed to validate the actuation strategy chosen. Focus is placed on the finger MCP adduction/abduction, MCP flexion/extension and PIP flexion/extension movements since these are the 3 active DOFs of the 4 DOF finger (the DIP is a passive joint whose flexion and extension is dependent on the PIP joint motion). Furthermore, this chapter also covers the control scheme used to operate the artificial finger. A simple and straight-forward control scheme is initially used for flexion and extension motions of the finger in this preliminary investigation. However, the system is set up to accommodate a more complex control scheme for a wide variety of finger motions in later applications. The fingertip forces, as generated by the SMA actuated finger, are also investigated.

7.1 Experimental setup

The experimental setup, schematically represented in Figure 7.1 consists of a biomimetic artificial finger mounted on an L-shaped bracket, affixed on an optical breadboard. The finger prototype was constructed from liquid resin using a stereolithography rapid prototyping system. The stereoligrathy process built the finger links by adding 0.10 mm

layers of an epoxy based photo curable liquid resin. This process is of high resolution and enabled the implementation of the complex details and anthropomorphic contours of the finger prototype. The capability to produce anthropomorphically shaped hollow parts was the prime motivator for using the rapid prototyping technique in this work. Furthermore, the time and cost saving feature of the rapid prototyping technique enabled several test finger models to be built before the final working model was implemented. The final finger prototype was manufactured with Vantico CibaTool SL5510 resin using the 3D Systems SLA 3500 solid imaging system at the University of Manitoba.

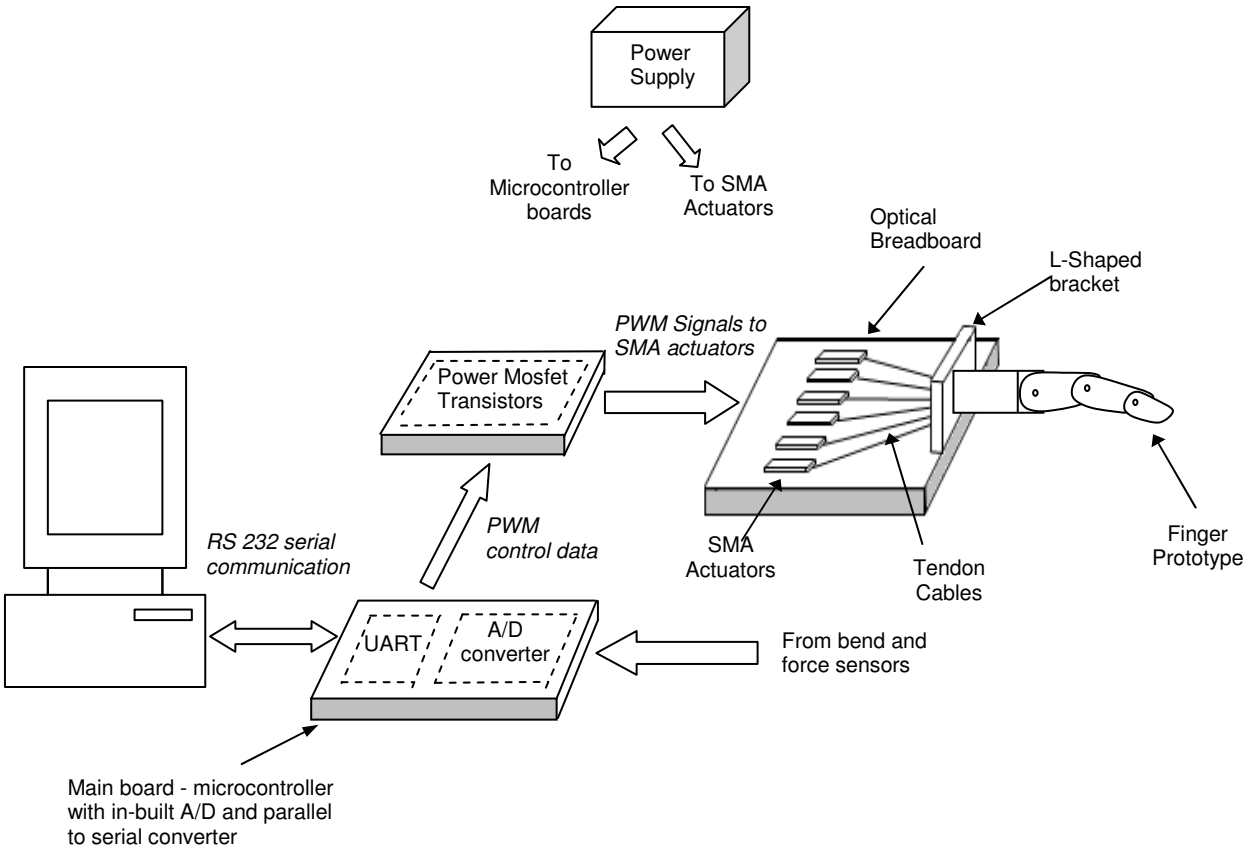

Figure 7.1: Schematic representation of experimental hardware

SMA actuators were mounted on the optical board as well. SMA actuators, supplied by Miga Motor Company, were used for this work. The highest end of the available modular actuator, the DM01-15, was chosen. The DM01-series has low power requirements and the patented internal architecture enables relatively large stroke lengths in a compact, lightweight

(less than 10% the weight and volume of a comparable motor or solenoid), ready-to-use housing. The DM01-15 SMA actuator chosen is capable of a half inch linear pull stroke and a maximum contracting force of 20N with actuating voltages ranging from 9V to 28V. As shown in Figure 7.2, the DM01-Series SMA actuator comes in small packaging with the housing body is designed to be mounted on a flat plane. A sample mounting-kit was provided with each actuator and included miscellaneous hardware which simplified the actuator attachment to optical breadboard. This actuator is designed to provide force only in the powered direction, returning to the un-powered position if un-constrained. If constrained, an external reset force is required in order to return an un-powered actuator to the rest position. In this work, a bias-spring provided the reset force.

Figure 7.2: DM01-15 SMA actuator from Miga Motor Company[13]

Artificial tendon cables were directly attached to the finger structure emulating the natural tendon's attachment to the human finger. The tendons were routed through the finger core and connected to their corresponding SMA actuators located remotely to the joints, on the optical beard board. A Teflon coated microfibre line (SpiderWire's Stealth) was chosen for the tendon cables. This allowed the creation of strong tendons that were also resistant to twisting and abrasions and could easily be routed and fitted within the finger structure, without risking failure through frictional contacts or sharp bends. Most importantly, the material's Teflon coating provided a very low coefficient of friction – an important consideration where the tendons had to pass through several guides and traveled in directions at various angles. In addition to providing a mounting surface, the aluminum optical breadboard also acted as a heat sink, improving the cooling rate of the SMA actuators during finger motion. Although practical in this experimental configuration, this heat sinking

[13] http://www.migamotors.com/Products.html

method cannot be applied in an orthotics/prosthetic scenario where other cooling mechanisms need to be investigated. Figure 7.3 depicts the artificial finger with tendon cables routing through the finger core and attached to six remote SMA actuators (two SMA actuators for each active DOF of the finger). The finger's starting position during the experimental testing was similar to the natural finger's normal resting position (see Figure 7.3), which is the proximal link positioned at 40^{o} to the metacarpal link and PIP at 20^{o} to the proximal link.

The SMA actuators were operated by the application of Pulse Width Modulated (PWM) signals. This enabled a more uniform heating of the SMA wires as compared to joule heating with a direct electrical current (see section 7.3.1 for more details). Varying the duty cycle of the PWM signal permitted different levels of electrical heating to be provided to the SMA wires resulting in controlled contraction of the actuator and hence controlled motion of the finger. In this work, the duty cycle of the PWM was determined based on a reference finger position or a desired fingertip force to be achieved**.**

For preliminary evaluation purposes of this actuation mechanism, a microcontroller was programmed with a simple ad-hoc proportional derivative controller (described in Section 7.3.2) to control duty cycle of the PWM signal, that is, the finger motion. The PIC16F917 microcontroller from Microchip Technologies was chosen for this purpose. The PIC16F917 is a low cost flash-based microcontroller, possessing in-built PWM modules capable of 10-bit PWM signals with a maximum frequency of 290 kHz. The duty cycle and frequency of the PWM can be specified by writing to specific hardware registers in the microcontroller. This enabled the direct generation of PWM signals on several pins, under software control. The PWM signal has a value ranging from 0 to 1023 (based on a 10-bit signal) resulting in PWM duty cycle ranging from 0% to 100%. The microcontroller also featured an in-built analog-to-digital (A/D) converter with a 10-bit resolution for up to 8 channels. The microcontroller can be programmed using a serial method and possesses an on-board UART (Universal Asynchronous Receiver/Transmitter) for RS232 communication. The microcontroller is ideal for this work as it provides a flexible platform for an embedded application. Furthermore, it has a wide operational voltage range (2.0 V to 5.5 V), making it ideal for battery operated applications.

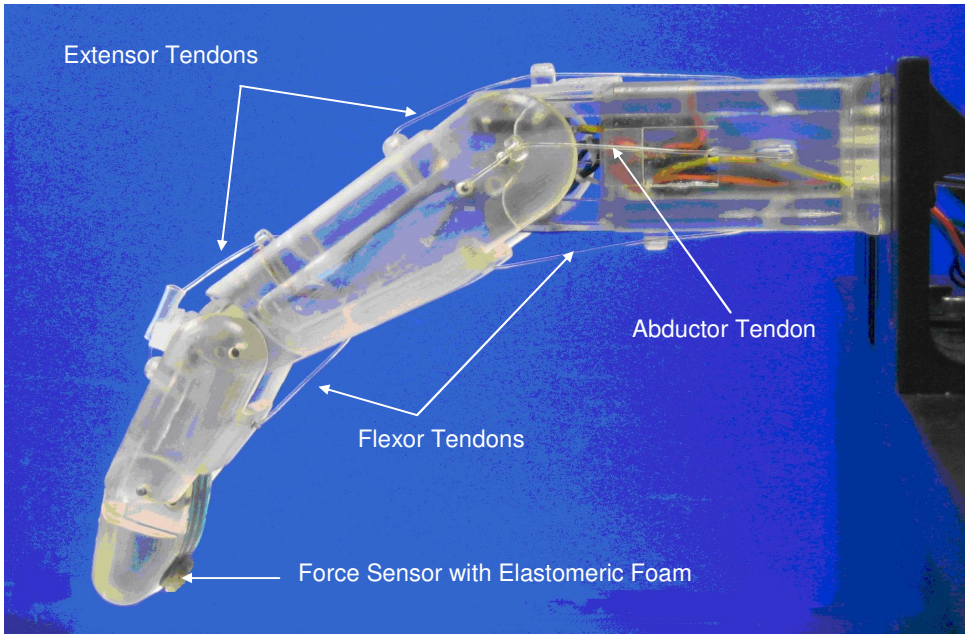

a) Artificial finger prototype constructed using SLA-3500 RP machine loaded with Vantico CibaTool SL5510 resin. Finger in the natural resting position.

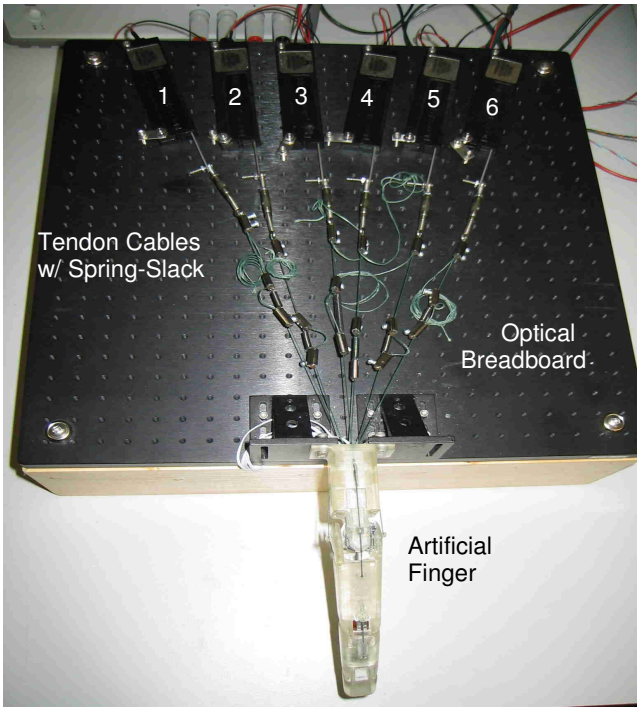

b) Artificial finger and six SMAs mounted on optical breadboard

Figure 7.3: Artificial finger testbed attached remotely placed SMA actuators

A terminal program running on the host PC was implemented for communication with the finger's microcontroller. A user interface was built, based on a menu structure with text prompts generated by the microcontroller's firmware. Since the duty cycle of the PWM control signals were based on a set of reference values which, as mentioned beforehand, is a desired joint positional angle or fingertip force, the terminal program required these reference values to be entered. The terminal program also required control gains to be entered since gains were being experimentally determined by observations of the finger motion and not analytically calculated and programmed in the microcontroller. Once entered in the terminal program, the serial configuration data was sent by the host PC through an RS232 port. This data was processed by the microcontroller's built-in UART that performed serial to parallel data conversion to microcontroller (UART also performed parallel to serial from the microcontroller to the host PC).

Once desired joint positional finger positions (or a fingertip force) as well as control gains and were entered, the control scheme programmed on the microcontroller generated PWM control signals with a frequency of 225 Hz. The generated PWM control signal operated power MOSFET transistors, which acted as switches to modulate the voltage applied to the SMA actuators. Positional and force feedback were achieved by the use of the resistive sensors embedded in the finger structure as described in Section 4.3. The microcontroller's built-in analog-to-digital (A/D) converter translated analog feedback information from the finger sensors to a digital form suitable for handling by the microcontroller. The microcontroller's firmware sampled the position of the finger in space by reading the appropriate sensors at 100 Hz, and generated appropriate closed-loop PWM control signals (duty cycles of varying widths) until the desired finger position or force value was reached. As such, given the desired joint angle (or fingertip force), the finger was capable of operation as a standalone device. The general layout for position control of the finger is illustrated in Figure 7.1.

7.2 Sensor calibration

To provide valid experimental results, it was necessary to calibrate the various angle sensors and fingertip force sensor employed in the system. For all sensors used, calibration

was done in terms of the number of A/D counts reported by the microcontroller's built-in A/D converter. Calibration of the various joint angle sensors was performed using a goniometer designed for human finger joint angle measurement. Calibration of the fingertip force sensor was performed by static loading of the sensor using a series of weights of known mass and a load cell.

The rotary potentiometers selected for the measurement of the MCP flexion/extension and MCP adduction/abduction are inherently linear devices and, beyond simply correlating joint angles with the resulting A/D count values and applying a basic straight line fit, no further manipulation of the data was required. The calibration curves for MCP adduction and abduction are shown in Figure 7.4 and Figure 7.5 respectively while the calibration for MCP flexion/extension is shown in Figure 7.6.

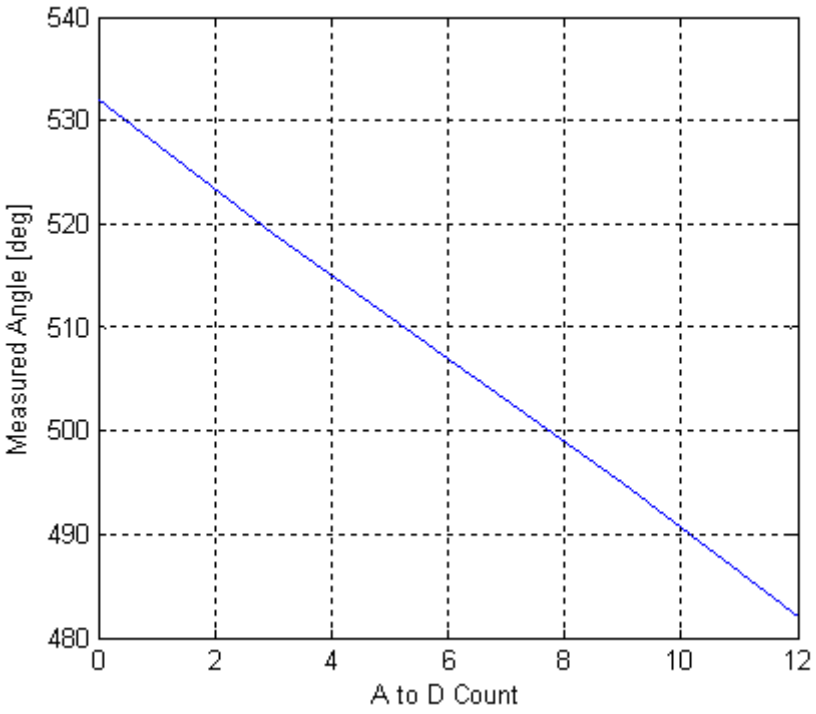

Figure 7.4: Sensor response plot for MCP adduction potentiometer calibration curve

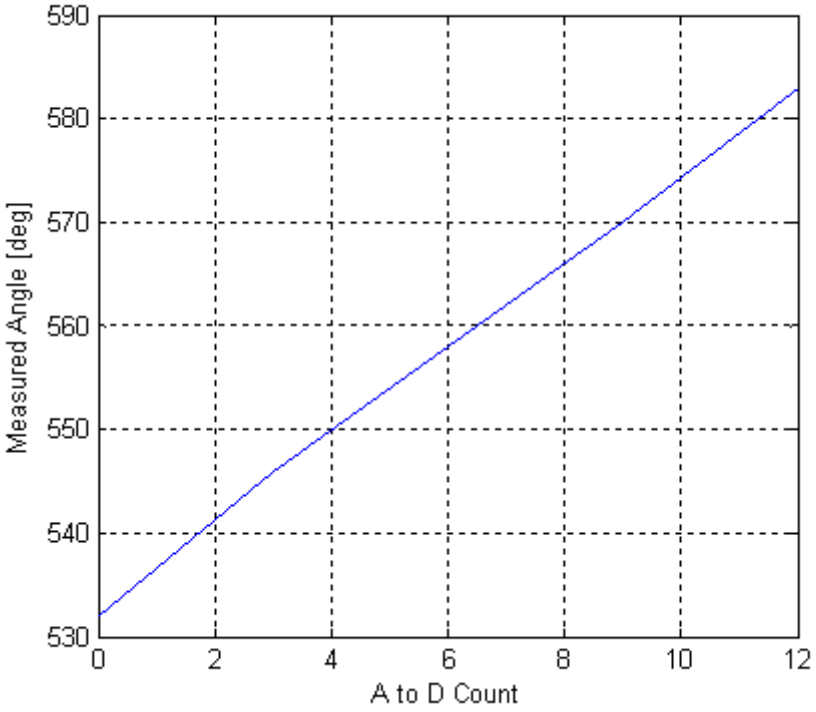

Figure 7.5: Sensor response for MCP abduction potentiometer calibration curve

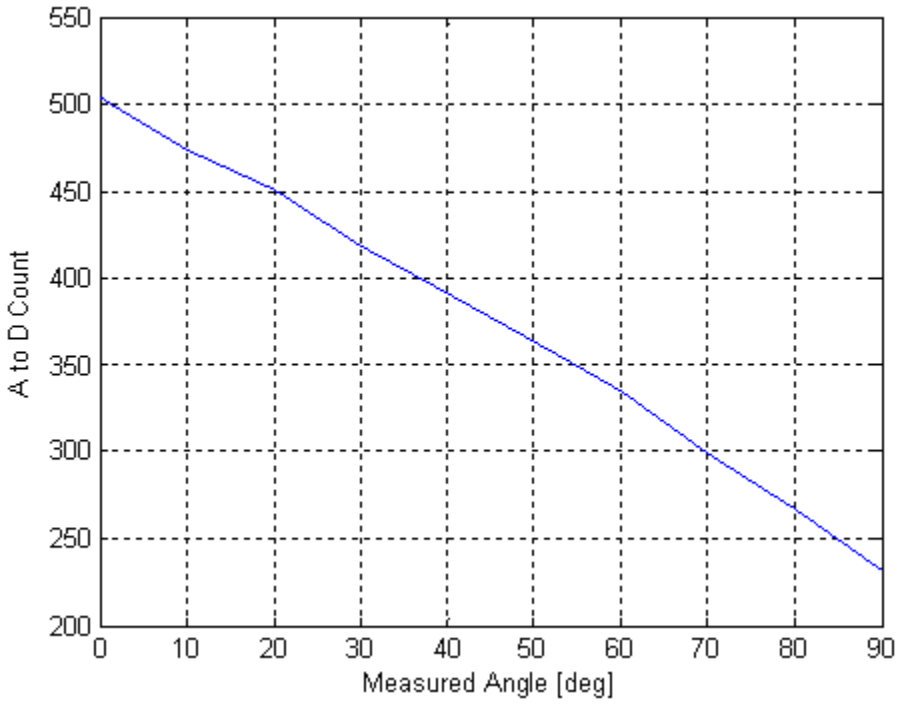

Figure 7.6: Sensor response MCP flexion/extension potentiometer calibration curve

The resistive bend sensor used for the PIP flexion/extension measurements and the resistive force sensor used to measure fingertip forces are nonlinear in their responses. It was found that the embedded control algorithms were sufficiently robust that the linearization of the output from these sensors was unnecessary. However, it was necessary to plot the sensor's response and find a fourth order polynomial fit to the response curves. This facilitated the creation of a look-up table for the microcontroller to interpret count angles into the appropriate count number, vice versa. Figure 7.7 shows the response of the bend sensor used at the PIP while Figure 7.8 represents the fingertip force sensor calibration curve.

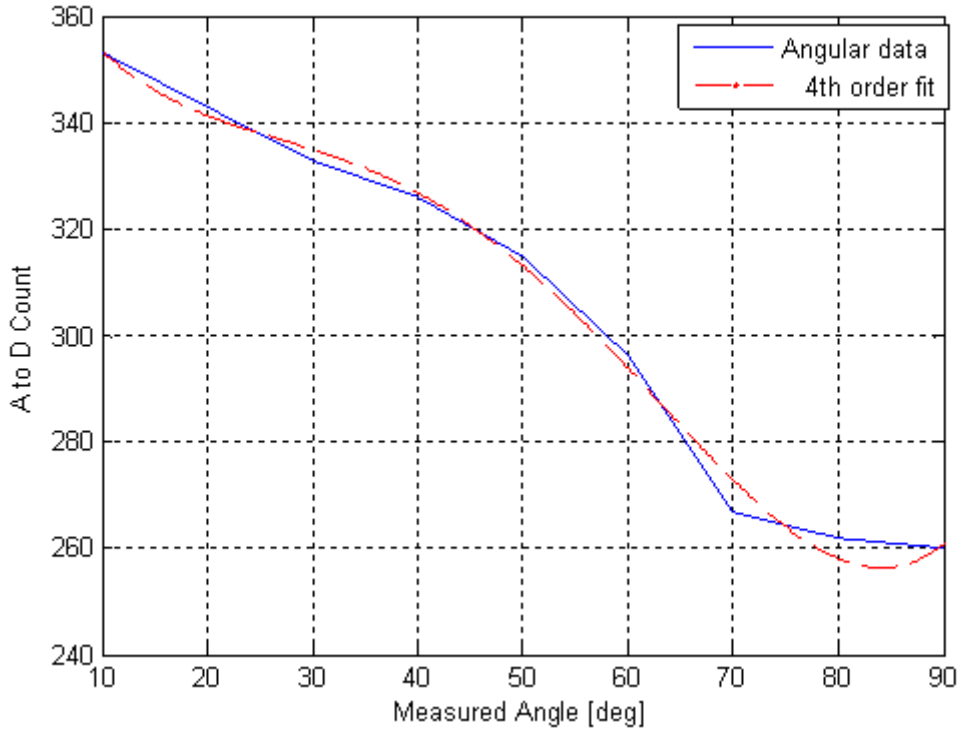

Figure 7.7: PIP flexion/extension bend sensor calibration curve with a 4th order polynomial fit

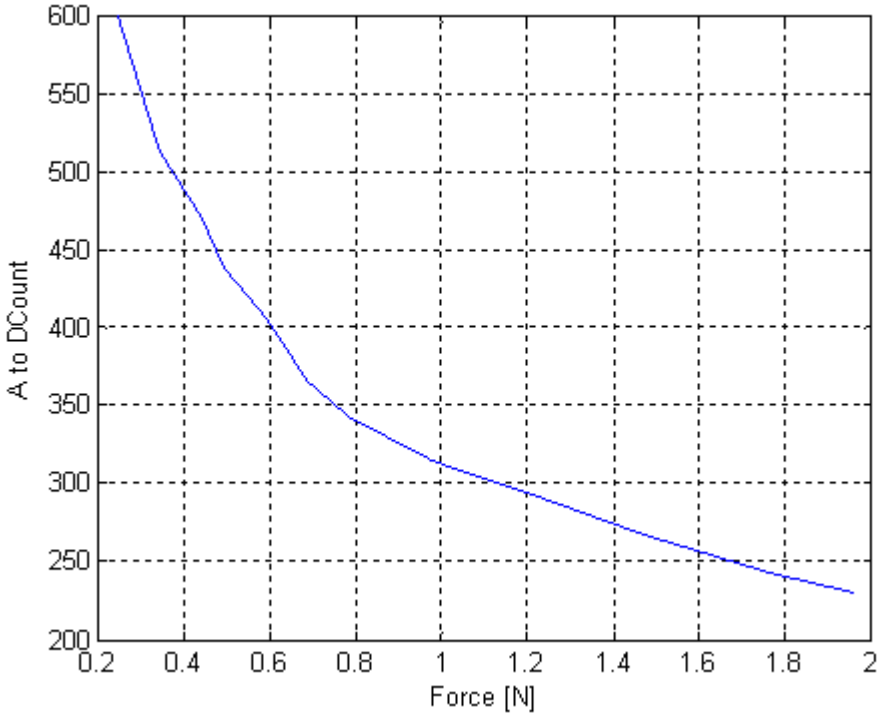

Figure 7.8: Fingertip force sensor calibration curve

7.3 Control strategy

SMAs are inherently nonlinear and hysteretic in nature and, as such, pose a challenge as far as the implementation of an accurate and robust controller is concerned. Furthermore, the dynamic behaviour of SMAs is highly dependent on the fabrication process, alloy content and training. High parametric uncertainty accompanies the nonlinear SMA models [92, 110] available in the literature, further complicating the design of a controller. A robust controller is required in order to account for all nonlinearities and allow precise control of the proposed spring-biased differential SMA actuation system. In literature, it has been shown that the most effective control methods involve the use of PWM in conjunction with some form of a PID controller [34, 110 - 113]. Variable controllers [92, 106] or sliding mode controllers [114, 115] are also successful.

In this work, the focus was placed on quick testing and evaluation of the actuation mechanism is done with a simple and practical embedded pulse-width-modulated proportional-derivative (PWM-PD) controller. PWM voltage signals are, hence, used as the

control variable. The PW modulator is integrated with a PD feedback controller to improve the system robustness. The controller implemented is firmware-based. The proportional (K_p) and derivative (K_d) gain terms are user-programmable.

7.3.1 PWM modulation

During SMA actuation, the martensitic and austentic transformation rates of the SMA wire are controlled solely by the rate at which heat is transferred to and removed from the wire. In the case of electrical (or joule) heating, heat transfer is dictated by the level of current applied. While electrical heating using direct current (DC) is very effective in rapidly increasing the material's temperature, merely turning the current off once the desired actuator position is reached is not a solution. This is because the actuators return to their initial extended position once the current is removed and the actuator cools. As such, a means of varying the amount of heating power supplied to the actuator SMA wire is required to maintain the SMA wire in contracted state without over-heating.

A direct control of DC voltage applied to the actuator presents one way to vary the amount of current applied and hence, the heating that the SMA wire experiences. This would enable a direct control of the degree to which a state change progresses so as to maintain desired SMA contractions. However, the control of the actuator's voltage is not efficient since a large portion of the energy applied, when not used for the SMA wire contraction, is simply dissipated as waste heat. To reduce low energy efficiency characteristic of the electrical resistance of SMA wires, the pulse width modulation technique is used [110, 111]. PWM is a more practical approach where the averaging effect of the on-off voltage durations coupled with the relatively slow response time of an SMA element, enables a uniform heating and effective control over the transformation process. Little heat is generated with this method of control. This is advantageous since rechargeable batteries can be used to provide power to the SMA actuators in stand-alone, ambulatory applications in rehabilitation robotics. In addition PWM has the advantages of being robust to disturbances and easily implemented using microprocessors

7.3.2 Control scheme

The PWM signals applied are voltage signals of uniform height and variable duration. Varying the duty cycle of the PWM signal varies the average control energy that is directed to the SMA actuator. Increasing the duty cycle increases the applied energy, causing the temperature of the actuator to increase, thus increasing the rate of actuator contraction. If the duty cycle is reduced below the actuation threshold, the wire cools below the actuation temperature, and a reverse bias force will then cause the SMA wire to stretch towards its original pre-strained length. If the duty cycle is, on the other hand, maintained at just the threshold actuation value, the SMA wire maintains its existing length without any change in strain. The actuator contraction rate is, thereby, controlled by varying the duty cycle of the applied voltage until the desired angular position is achieved. Note that the maximum applicable voltage is 28 V for the chosen Miga Motor's SMA actuator. However, this voltage level reduces the SMA actuator life and may cause overheating. As such, a voltage level of 8 V was chosen for the PWM signal since this voltage level yields adequate actuator response without compromising actuator life. As mentioned, a constant PWM frequency of 225 Hz was used with the duty cycle capable of being varied from 0 to 100 %. Experimental identification showed that a minimum 20% threshold duty cycle was required to maintain the SMA actuator in a steady activated state.

The set-point for the controller is a desired angular position, θ_d. The positional sensors (bend sensors and potentiometers) measure the actual angular position, which is fed back to the controller. The error signal, *e(t)*, which is the difference between the desired and measured values, is fed into the controller and a proportional error term and a derivative error term are applied. The proportional and derivative error terms are then added/subtracted the current PWM signal value to produce the final control signal (PWM count ranging from 0-1023) as shown in eq (7.1) and eq (7.2). This resulting value is then scaled to provide a corresponding PWM value somewhere between 0 and 100 % duty cycle. The finger sensors are read at a rate of 100 Hz with the PWM signal being updated after every 10 reads. As such, the controller introduces a delay of 10ms between each PWM signal value adjustment during control of the finger joint.

For finger flexion:

$$c_d(t) = c_a(t) + k_d * e(t) + k_p * e(t) \tag{7.1}$$

For finger extension:

$$c_d(t) = c_a(t) - k_d * e(t) - k_p * e(t) \tag{7.2}$$

where $c_d(t)$ = desired PWM control signal

$c_a(t)$ = current PWM control signal

k_d = derivative gain

k_p = proportional gain

$e(t)$ = error term (difference between desired and actual angular position or difference between the desired and actual fingertip force))

In case of fingertip force for closed-loop force control, the set-point for the controller is a desired fingertip force. Similar to position control, the controller measures the force sensor at the fingertip and PWM signals generated base of the difference in the desired and actual fingertip force until the desired fingertip force is achieved.

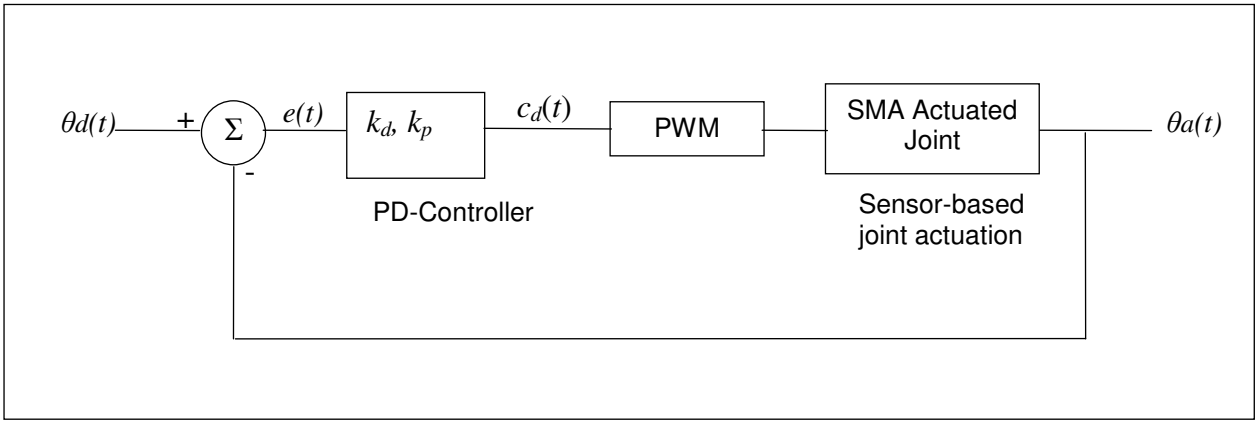

Figure 7.9: PWM-PD control of finger joint

Figure 7.9 represents the PWM-PD controller implemented for the finger. The controller gains (K_p and K_d) used in this thesis are obtained and tuned using direct experimental observations rather than a complex nonlinear mathematical model of the

system. The resulting gain values varied depending on the particular joint DOF being activated and the direction of actuation (e.g. flexion vs. extension), ranging typically from 500 to 10,000. It was found that the response time of the controller, which had an update rate of 10 ms, and large gain values were possible without instability or overshoot problems. The PD feedback controller possessed a satisfactory stability margin for stand-alone operation of the biomimetic artificial finger. The end result was a microcontroller based system capable of controlling the finger joint under a fully-embedded PWM-PD control.

7.4 Experimental results

The purpose of the following experiments was to demonstrate the 3 DOF active motion (excluding the 4^{th} passive DOF) of the biomimetic artificial finger via the proposed spring-biased differential SMA-based tendon-driven actuation system. Open-loop tests were first performed to assess the effectiveness of the actuation mechanism designed, most specifically with respect to the agonist-antagonist motion of each active finger joint. Closed-loop tests were then carried out to assess the performance of incorporating feedback control into the system.

7.4.1 Finger motion

As shown in Figure 7.3, the artificial finger was placed in the nominal resting position to mimic the natural posture of the human finger when at rest. The springs and the slacks in the tendons were adjusted under slight tension to always maintain the finger in this initial position when the SMA actuators are inactive. The MCP joint was thus positioned at 40^{o} to the metacarpal link and the PIP joint at 20^{o} relative to the proximal link. The passive DIP was automatically positioned by the four-bar linkage coordinating the PIP and DIP joint motion. Joint motion was initiated by a user request to move the link into a desired position. The controller generated a PWM signal of fixed duty cycle for open-loop motions and variable duty cycle for closed-loop motions. The open-loop duty cycle was limited to 50% to avoid over-heating of the SMA wires inside the actuator and hence permanent damage.

Given the points of attachment of the elastic tendons from the finger's joint centers and the slack required in each tendon, the required minimum SMA contraction length was calculated to be at least 1 inch as per Eq. (5.6). However, although the tendon slacks were set up to enable full ranges of joint motion (i.e. -50^o flexion, 40^o extension and -/+20^o adduction/abduction at the MCP; -80^o flexion and 20^o extension at the PIP joint about the resting position), the actual range of motion tested was restricted due to the limited stroke of the Miga Motor's SMA actuators that we employed (the actuators only had a 0.5 inch stroke; 1 inch stroke SMA actuators are being custom-built for this work). Our preliminary experimental testing showed that only the following joint ranges could be obtained repeatedly in the open-loop configuration without damaging the SMA actuators: MCP adduction/abduction of +/−15^o, MCP extension/flexion of +/−20^o, and PIP flexion of −25º and extension of +15^o about the resting position.

7.4.1.1 Open-loop motion

Since SMA contraction responds to temperature changes caused by joule heating, the average current delivered to the SMA wire was measured. Open-loop tests showed that an average of about 0.7 to 0.8 A was sufficient to produce joint motion. This was achieved by setting the PWM to a 50% duty cycle. The open-loop graphs (Figures Figure 7.10Figure 7.15) indicate agonist-antagonist motion, but slow return of the finger link.

Once actuator power was applied, a time delay of approximately 5-10 seconds was observed before joint motion occurred. This delay corresponds to the SMA actuation time (about 1 second at a constant 8 VDC for the unconstrained actuator), as well as the time required for the initial slack to be absorbed from the tendon cables before the actuator effects joint motion. The MCP adduction/abduction and MCP flexion/extension desired joint positions were achieved within 50-55 seconds while PIP flexion/extension desired joint position was achieved within 35- 40 seconds of the actuation start time (power applied). The rate of motion for MCP abduction/adduction as well as MCP flexion/extension was much slower than that for PIP flexion/extension. The relatively high joint settling times at the MCP are related to the high torques required to move the entire finger structure at that joint, while at the PIP, the SMA actuator acts on the middle and distal links only.

Since the actuation time of the MigaMotor actuator is dependent on the input power, the speed at which the joints attain the desired position can be increased by using actuating voltages higher than 8V. For instance, the actuation at 28V is 0.1 second for the unconstrained actuator [116]. However, if actuated rapidly at a higher voltage, the SMA wire passes through the transition temperature very quickly and may become overheated if power is not swiftly removed. The manufacturer hence recommends using a voltage level which will result in an actuation time of 1s. At this voltage level, the actuator cannot be damaged through over-heating by keeping the power turned on for a long period of time. This voltage level was determined to be 8V and hence used for open-loop experimentations, even though this entailed a slower rate of motion of the finger structure.

The plots (Figure 7.10 - Figure 7.15) show that the double spring-bias, firstly, permitted bi-directional motion of the finger joints. However, a satisfactory return of each joint to its starting position was not obtainable in most instances. A margin of error of up to a maximum of 8% subsisted some instances. Once the power was removed, the return process was slow and unsteady in all open-loop cases, with an unacceptable return period in the 20 to 30 second range. This behavior is due to the high cooling times associated with the Miga Motor SMA actuators that prevent their fast return - return to the unpowered position is documented to be 3-15s for the unconstrained actuator [116]. Forced cooling however can drastically increase the return rate.

The open-loop plots also show unsteady and irregular and uneven motion of the finger, with joint motion occurring in step-like motion patterns. This is attributed to the ‘sticky’ effect of the SMA actuator. The SMA wires in the actuator are tightly wound in layers, with a plastic plate placed between each SMA wire layer. The plastic plates glide with respect to each other as the SMA wire contracts. It was observed that as the temperature of the wire increased, the wire would melt into the plastic plates preventing smooth contraction of the SMA wire. The slight jerks in the finger motion are attributed to when the SMA wire force was high enough to force the plates to move relative to each other.

Even though the actuation strategy enables successful bidirectional operation of the finger joints, the open-loop results indicate that this control method is inadequate for SMA operated joints. The next section looks at the closed-loop operation of the finger joints.

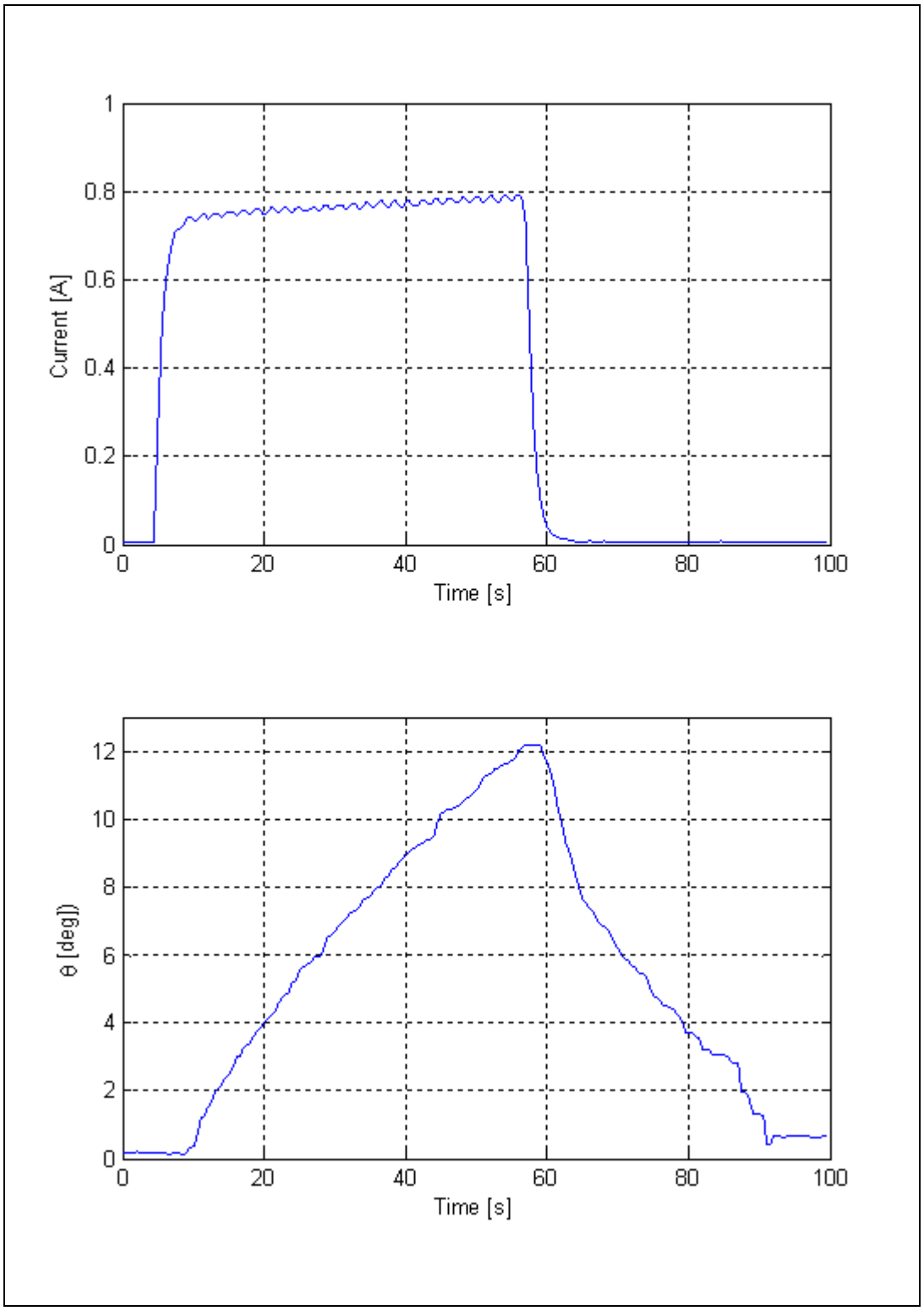

Figure 7.10: MCP abduction open-loop motion profile

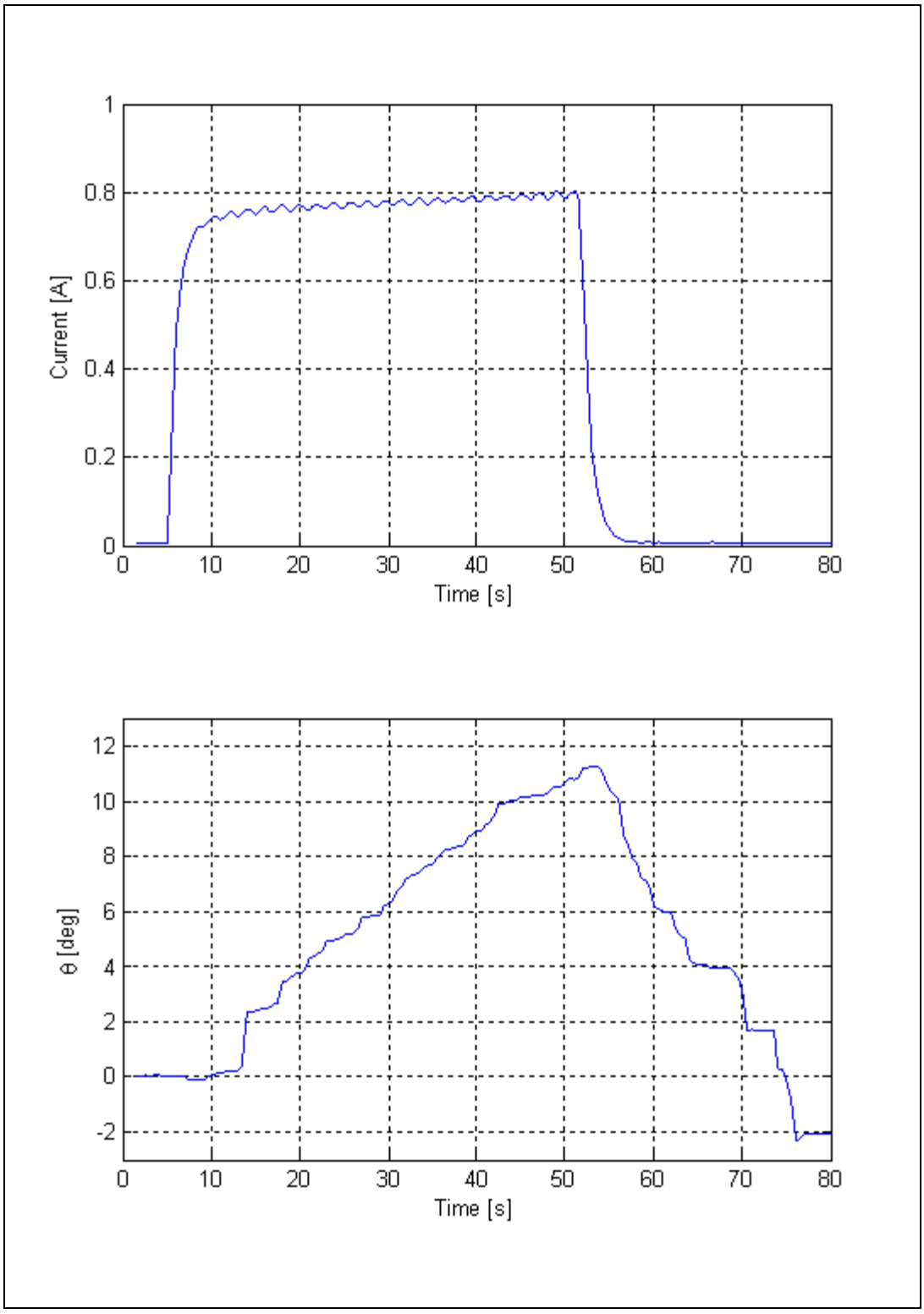

Figure 7.11: MCP adduction open-loop motion profile

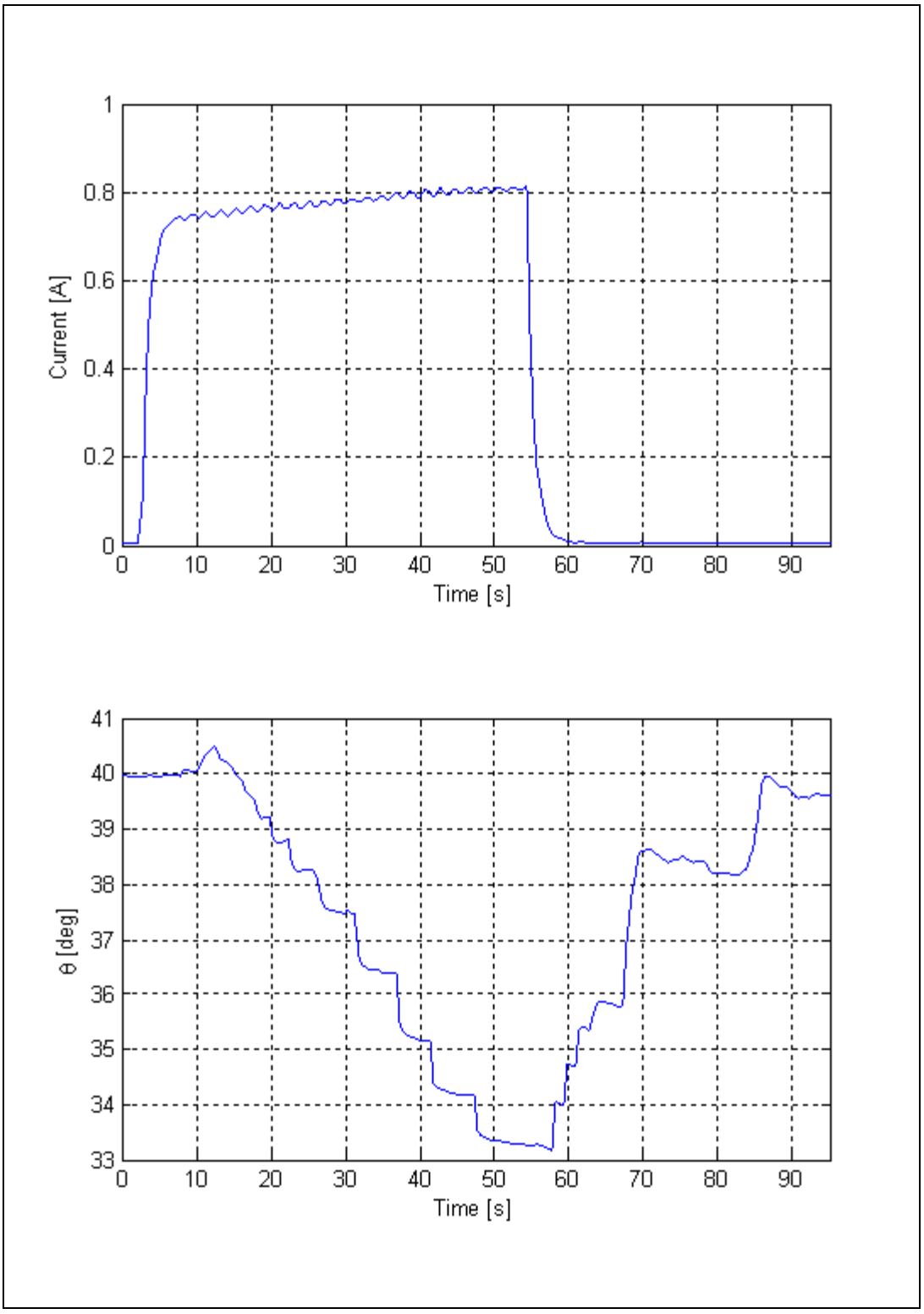

Figure 7.12: MCP Extension open-loop motion profile

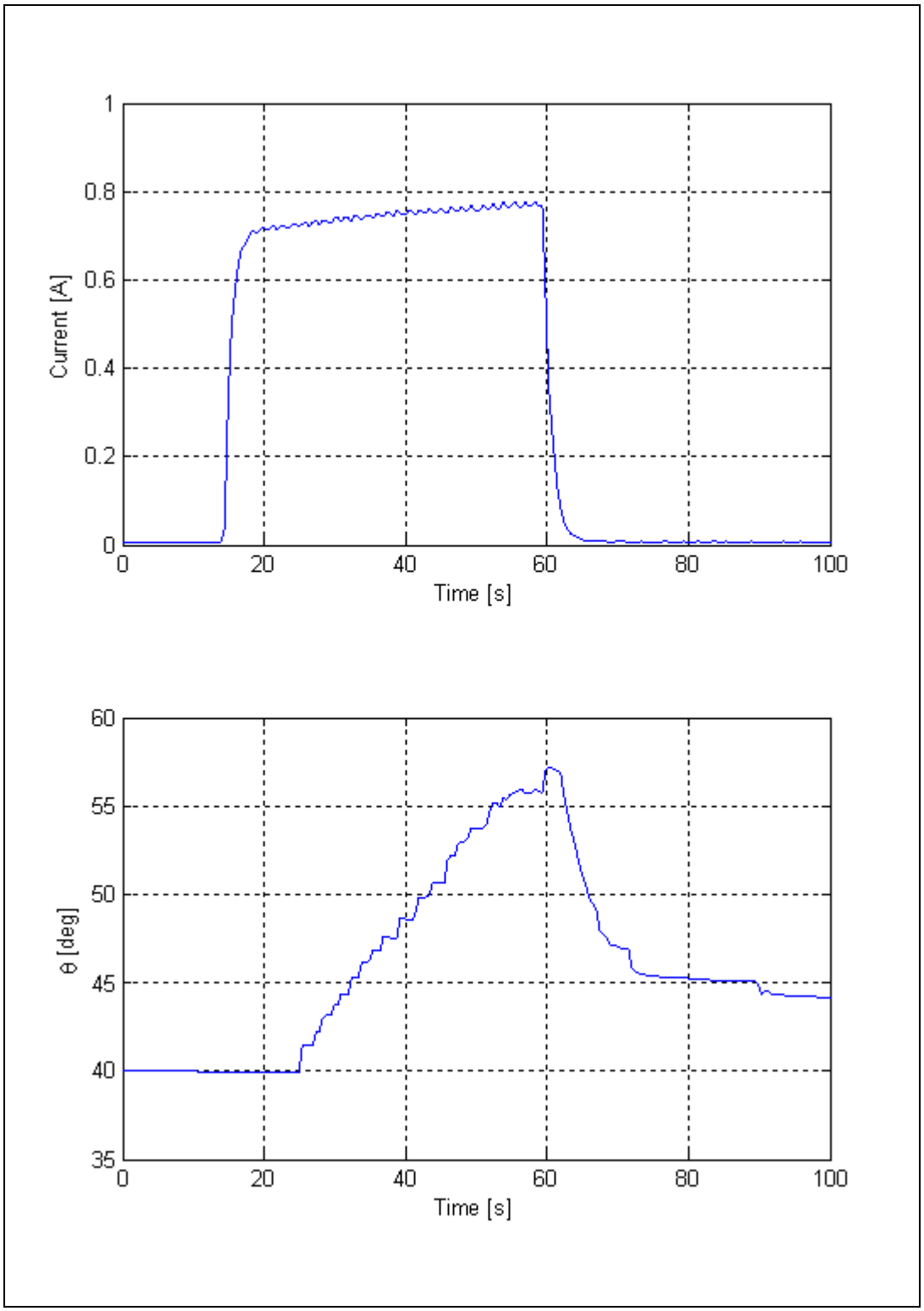

Figure 7.13: MCP Flexion open-loop motion profile

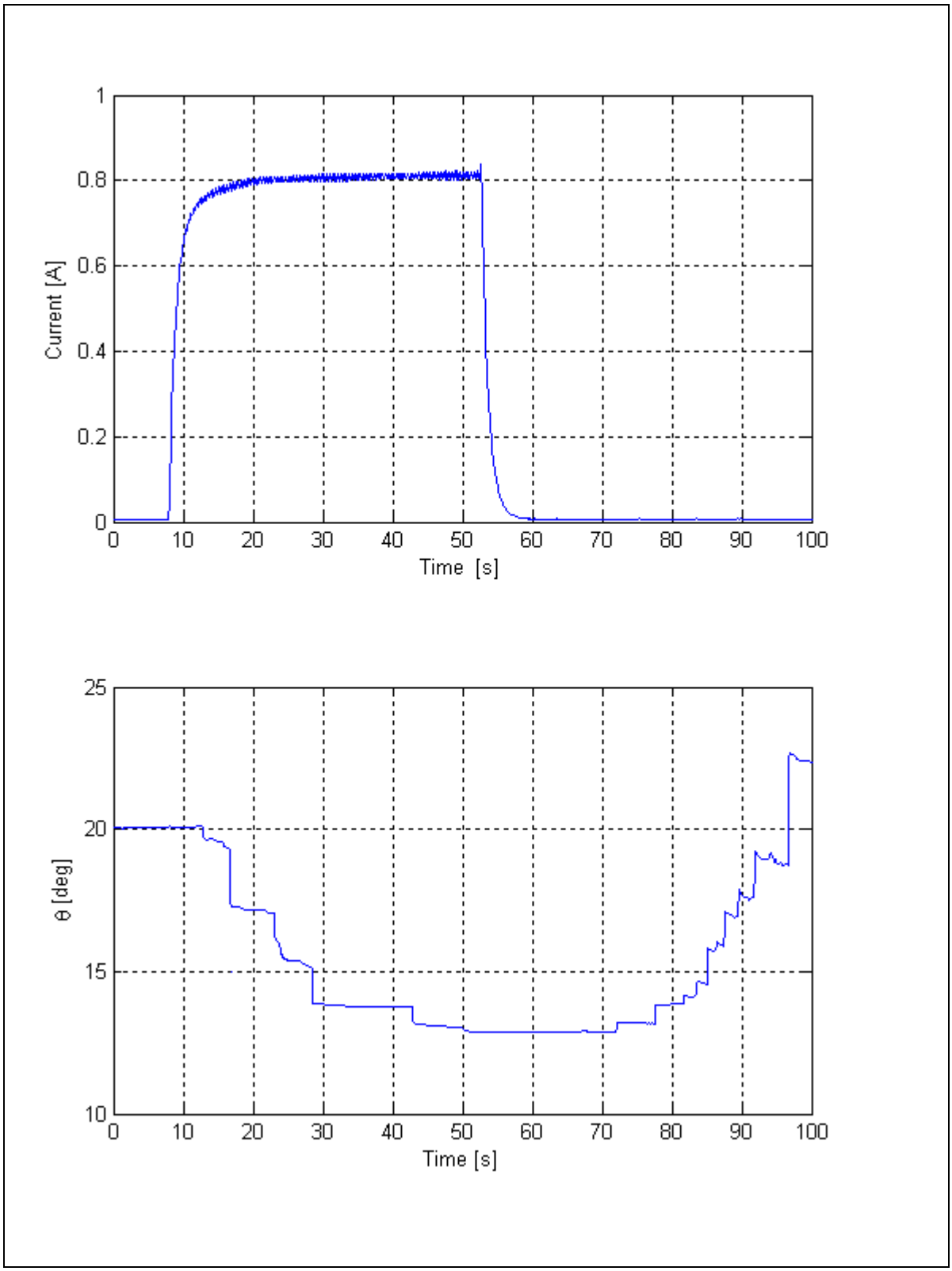

Figure 7.14: PIP Extension open-loop motion profile

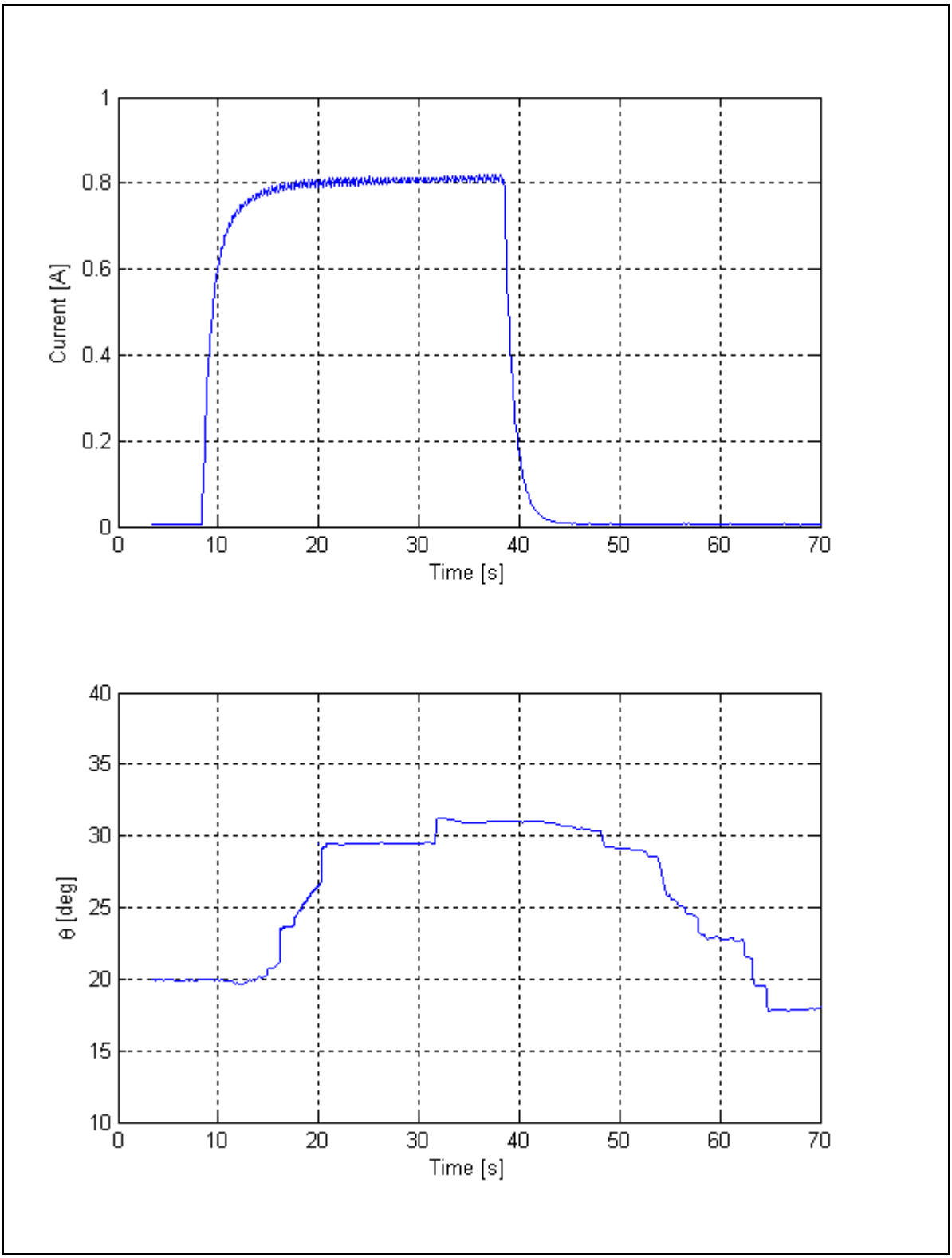

Figure 7.15: PIP Flexion open-loop profile

7.4.1.2 Closed-loop motion

The closed-loop plots (Figure 7.16 to Figure 7.21) showed that the feedback control incorporated into the system significantly improved the performance of the joint motion of the finger. The controller produced signals of variable duty cycle based on the current link's position (as measured by the bend sensors) with respect to the desired position. The current graphs indicate a sharp increase in the current level to a peak value of approximately 1.4 to 1.5 A at the beginning of the joint motion. The current then tapered to a lower level as the desired joint angle was approached. Finally, the current reduced to a still lower value sufficient to hold the finger in position once the desired joint angle was reached. This current profile behaviour suggests that a PWM signal with high duty cycle was initially generated, enabling the SMA wire to heat up rapidly. The PWM duty cycle was then reduced to a value yielding a constant actuator position that corresponds to a desired joint position.

The MCP adduction and abduction closed-loop plots (Figure 7.16 and Figure 7.17) indicate that, with a starting from a nominal position of 0º, the set values of 11º for both adduction and abduction were successfully achieved. The MCP flexion and extension closed loop plots (Figure 7.18 and Figure 7.19) indicate that, from a starting from a nominal position of 40º, the set values of 55º and 25º for flexion and extension, respectively, were successfully achieved. Similarly, closed-loop PIP flexion and extension motion profiles (Figure 7.20 and Figure 7.21) indicate that, from a starting from a nominal position of 20º, the set values of 40º and 10º for flexion and extension, respectively, were successfully achieved.

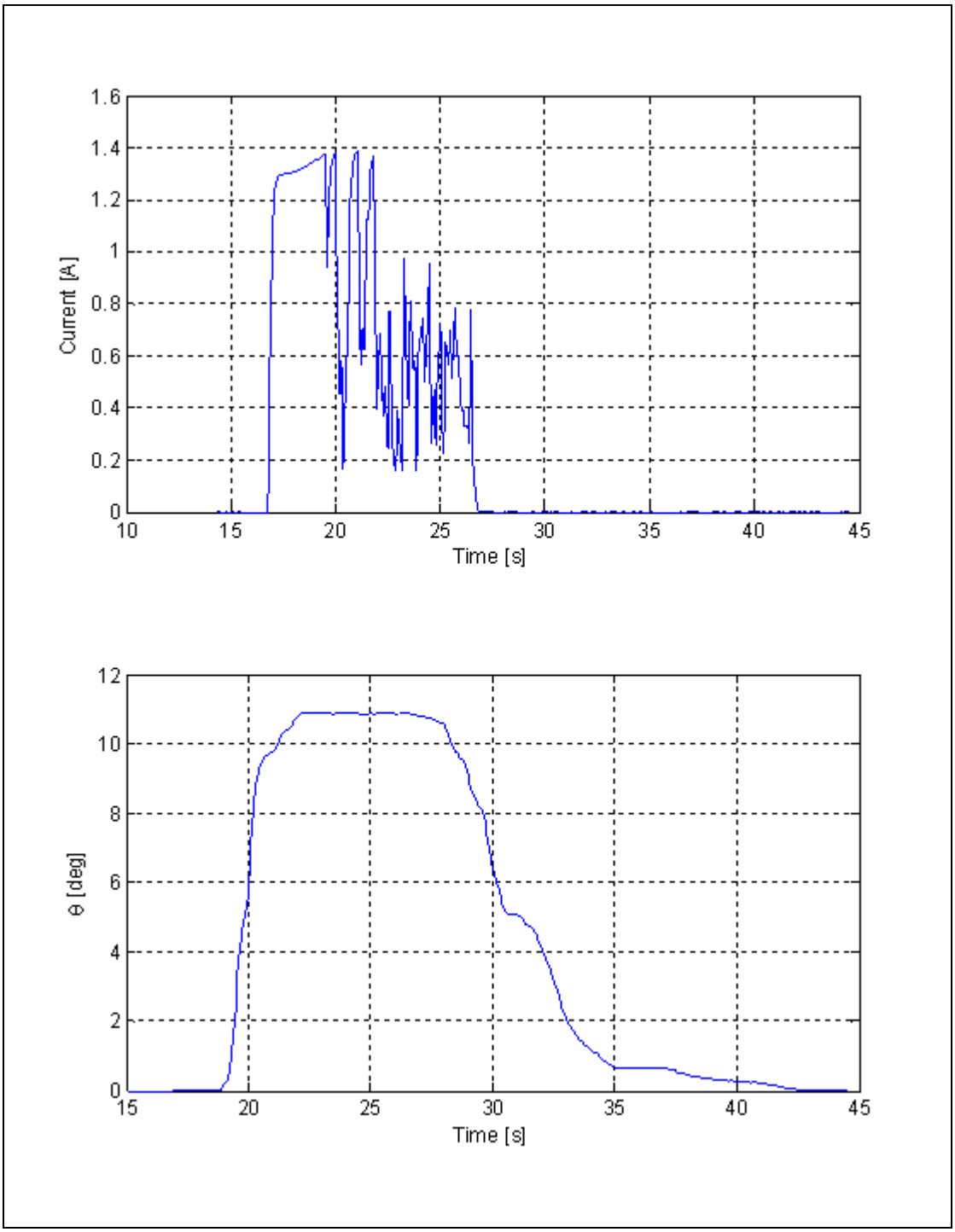

Figure 7.16: Closed-loop MCP abduction motion profile and the current profile of the corresponding SMA actuator.

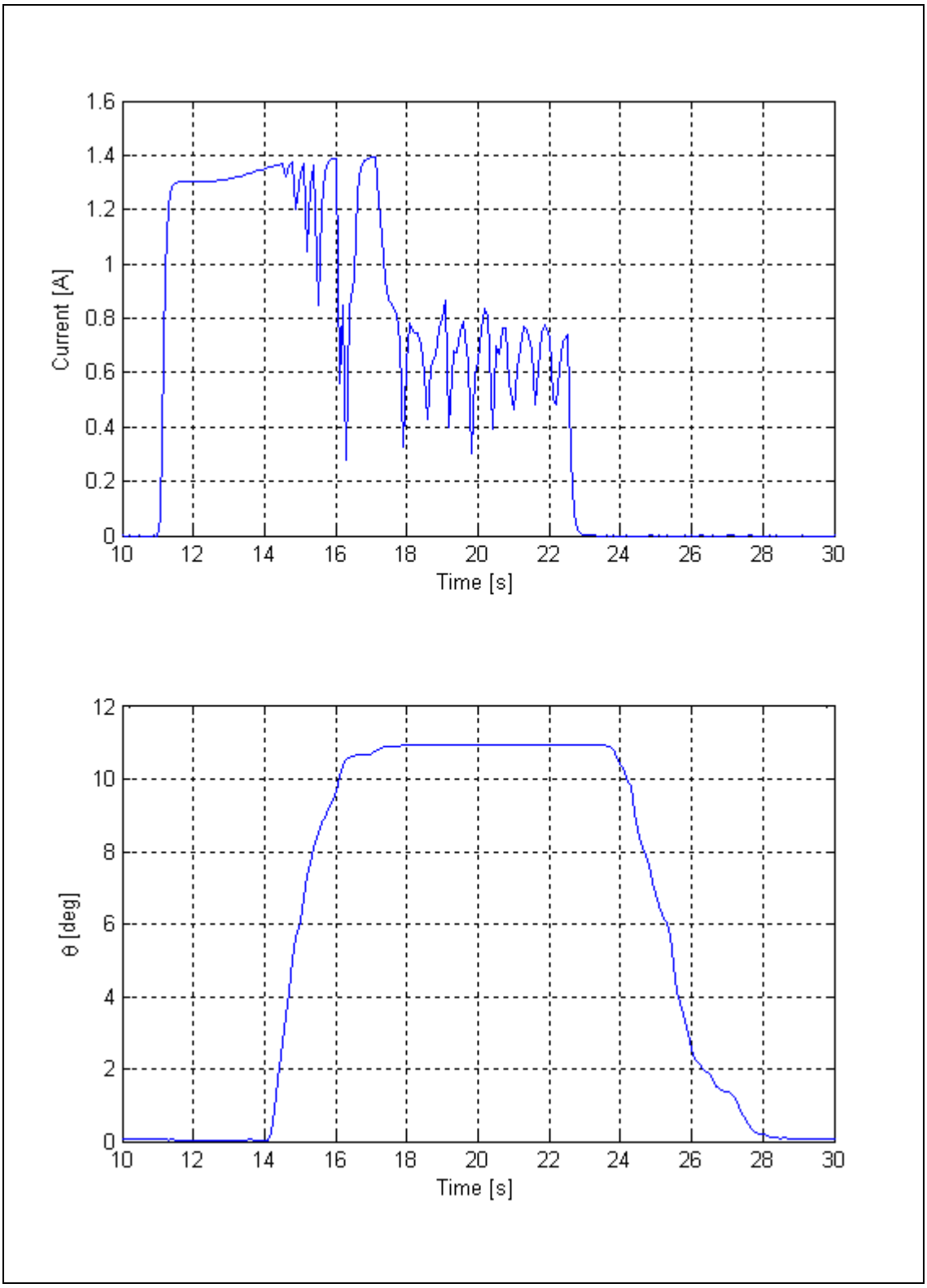

Figure 7.17: Closed-loop MCP adduction motion profile and the current profile of the corresponding SMA actuator

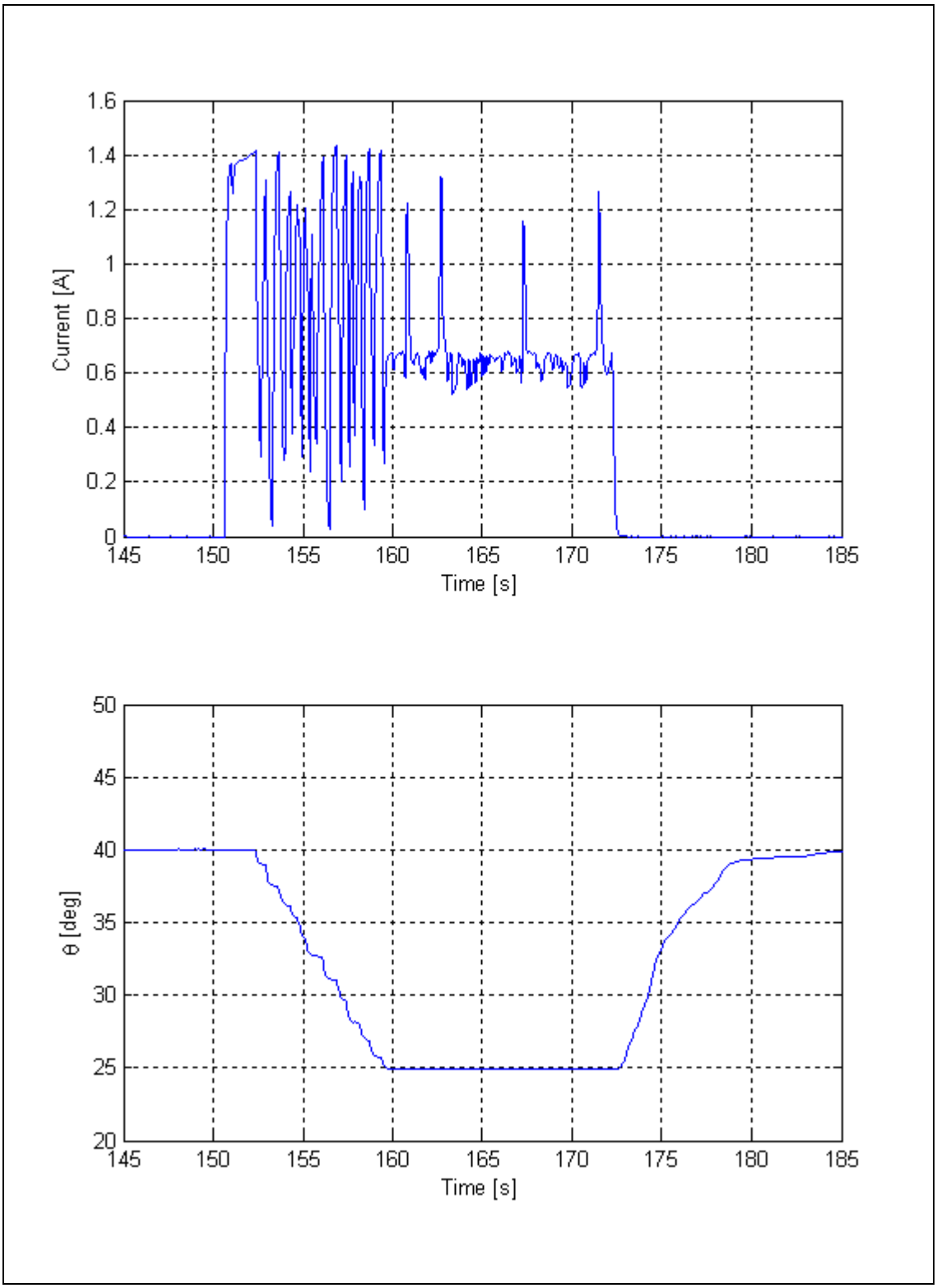

Figure 7.18: Closed-loop MCP extension motion profile and the current profile of the corresponding SMA actuator

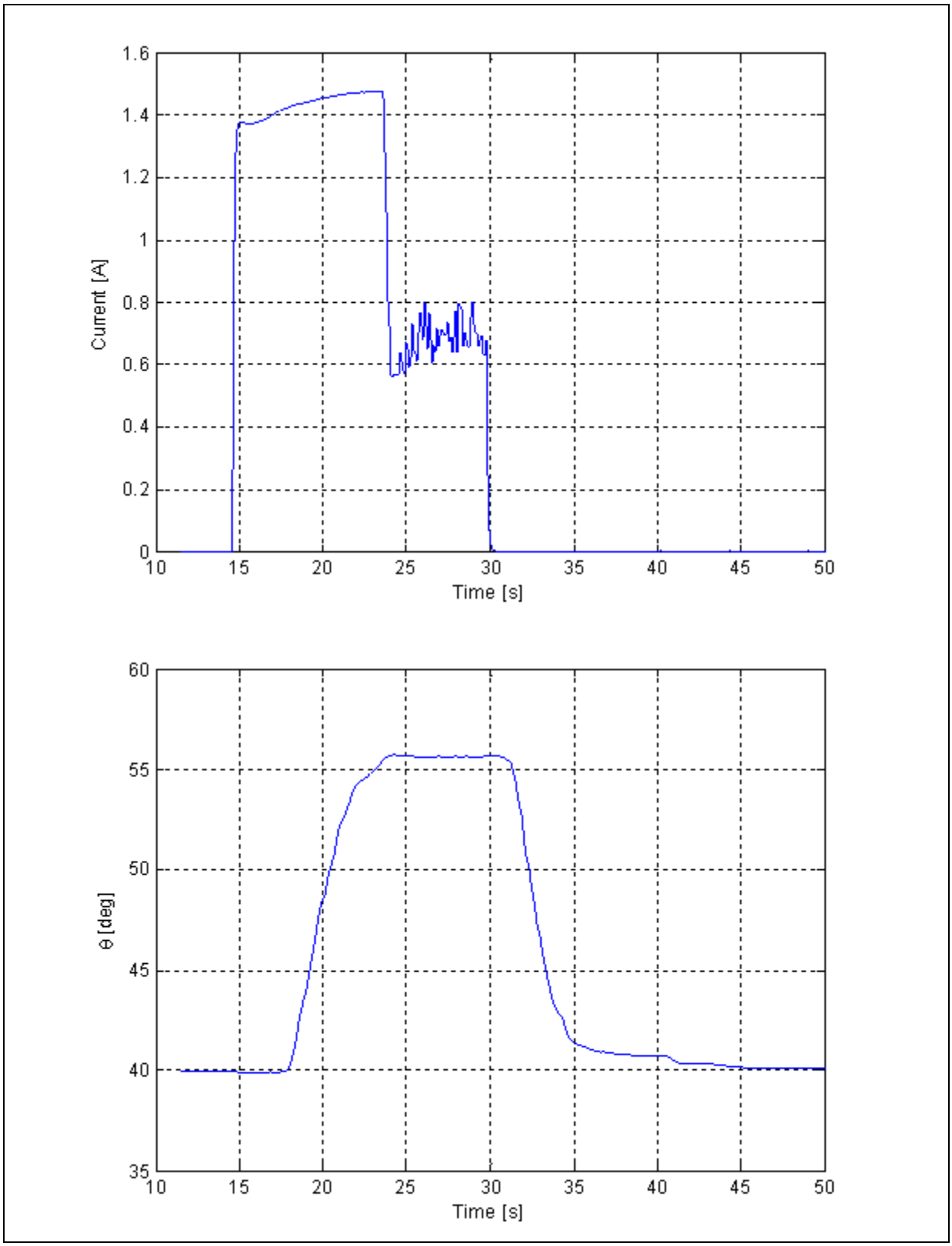

Figure 7.19: Closed-loop MCP flexion motion profile and the current profile of the corresponding SMA actuator

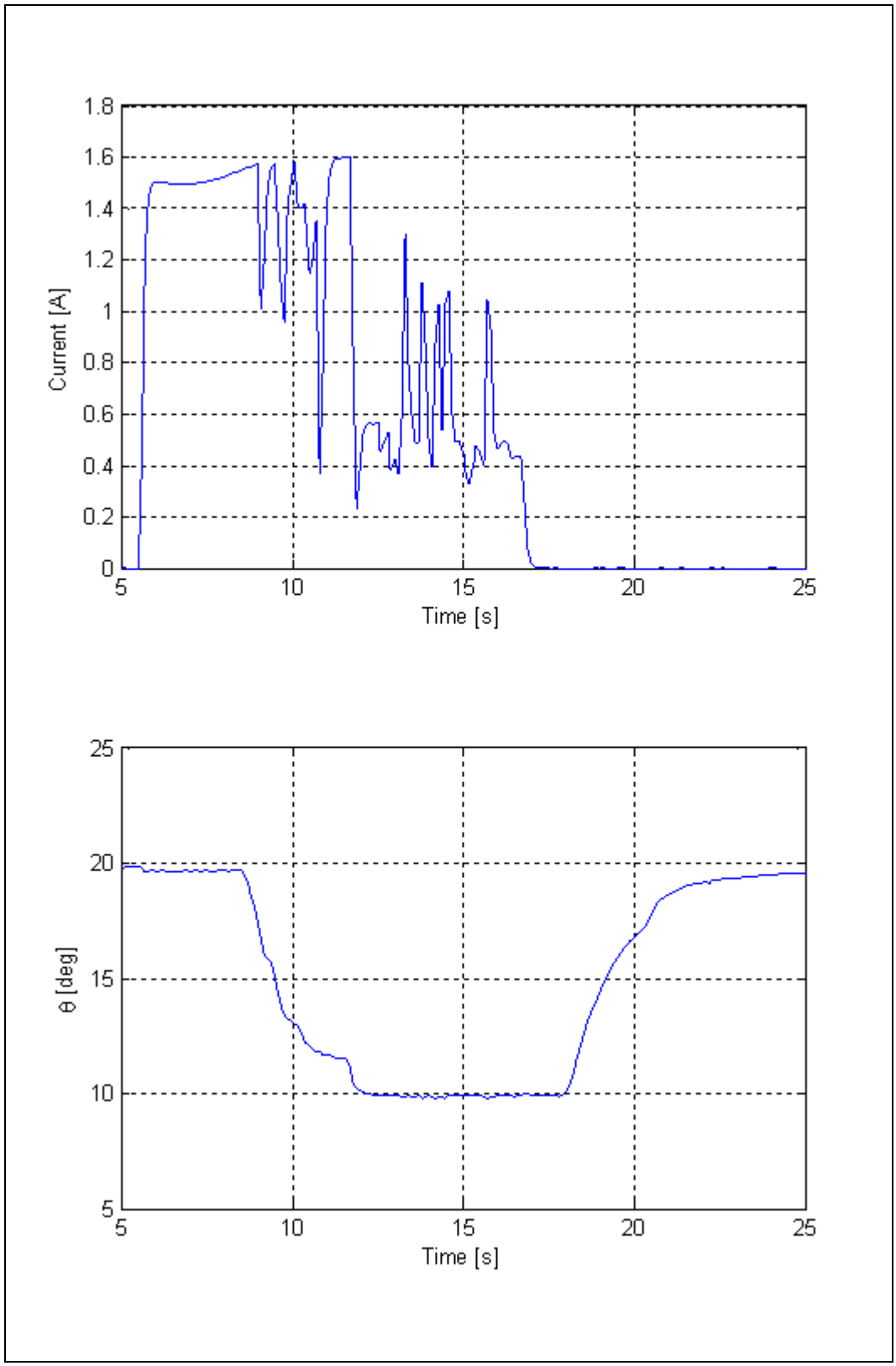

Figure 7.20: Closed-loop PIP extension motion profile and the current profile of the corresponding SMA actuator

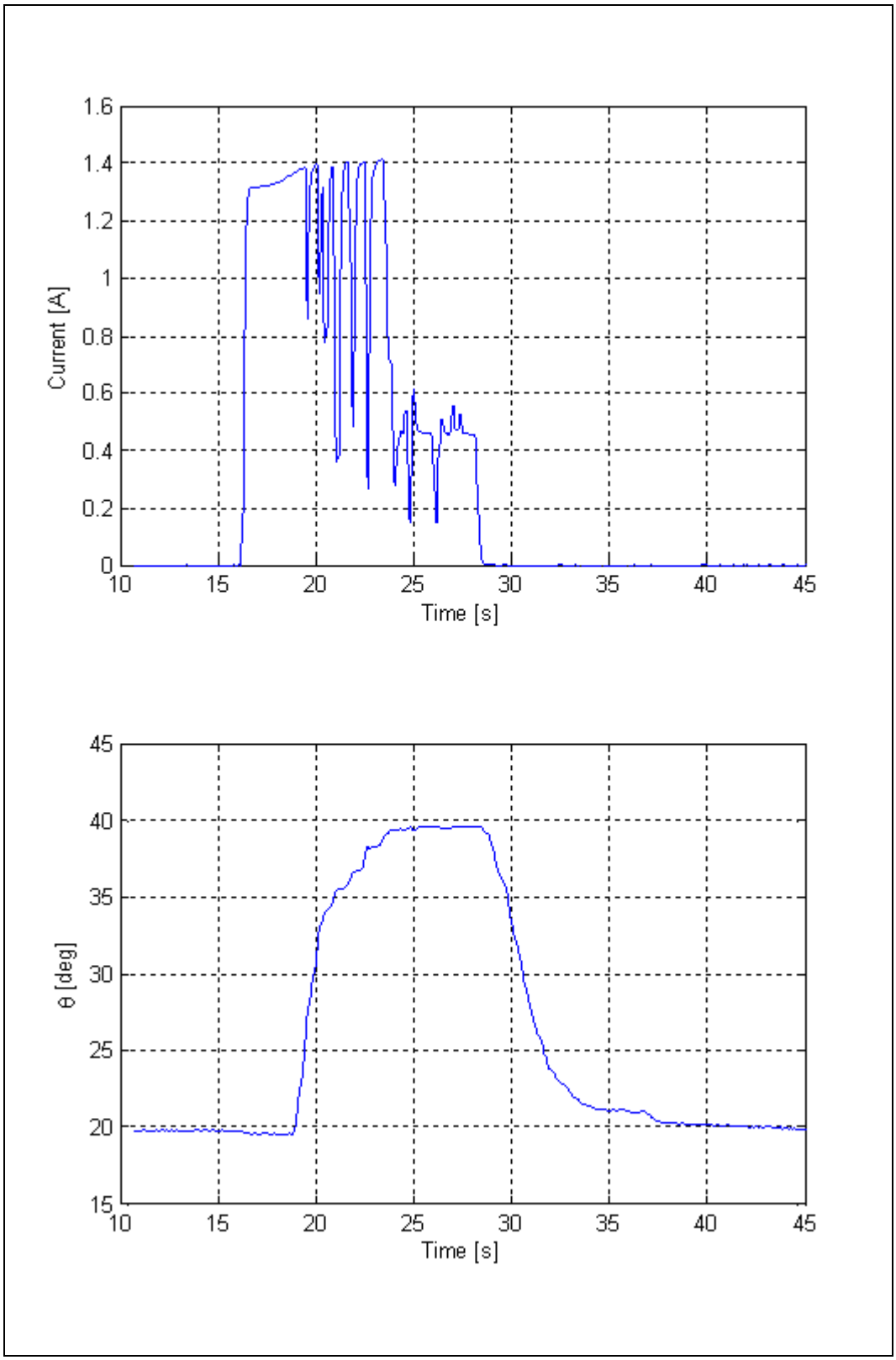

Figure 7.21: Closed-loop PIP flexion motion profile and the current profile of the corresponding SMA actuator

The embedded PWM-PD controller was highly effective in reducing the response time of the system, enabling final positions to be achieved within a matter of seconds. This was mainly due to the fact that closed-loop control enabled variable current levels to be applied whereas open-loop control only permitted fixed current levels for finger motion. As mentioned before, open-loop control required the duty cycle be fixed to 50% to avoid over-heating of the SMA wires and hence permanent damage of the actuator. As such, a steady level of current was used to achieve finger position in open-loop. This was an ineffective control method which resulted in high system response times. Closed-loop control, on the other hand, allowed application of current levels which were high enough when finger motion was initiated (twice the magnitude as that of open-loop currents), resulting in quick finger motions. The controller then reduced the current to a level sufficient to hold the finger in the desired position, without causing overheating of the SMA actuator, that is, actuator damage.

As such, with the embedded PWD-PD controller, joint motion was observed to occur within 3 to 4 seconds. MCP adduction/abduction desired joint position about the resting position was attained within 6 seconds. MCP flexion and extension desired joint positions were achieved within 9 seconds. PIP flexion and extension desired positions was achieved within 7 - 8 seconds. Once the desired angular position was achieved, the current level was maintained such as to keep desired joint angular positions (without actuator over-heating). The finger maintained a steady posture.

The joint response times for open-loop and closed motions of the finger are illustrated in Table 7.1. The finger joint motion was firstly, steady and secondly relatively rapid. The ‘sticky’ effect of the SMA actuator, as described in the previous section, was partly eliminated with the closed-loop control of the finger. The targeted flexion and extension joint angles were successfully achieved. The return to the original/starting position was achievable with no or a minimal margin of error.

Joint Motion	Open-Loop		Closed-Loop	
	Joint response (s)	Desired position (s)	Joint response (s)	Desired position (s)
MCP abduction	5	53	3	6
MCP adduction	9	50	3	6
MCP extension	12	55	2.5	9
MCP flexion	10	47	4	9
PIP extension	5	37	3	6.5
PIP flexion	7	34	3	8

Table 7.1: Joint response times

Although the closed-loop position control produced rapid and steady bi-directional finger motion, spring-biased return to the original resting position was observed to be still slow in the closed-loop configuration as well, which is expected since the return to a neutral position was effected simply by removing actuator power, as in the open-loop case. Powering the opposing actuator during the joint's return phase to its resting position would be a possible solution to this problem, which will be addressed later on in this work. Also, adding some sort of an active heat sink to the SMA actuator should increase the SMA cooling rate and improve the rate at which the finger joints return to their resting position.

7.4.2 Fingertip force

One of the main functional tasks of the human hand is the grasping of objects, and the amount of force applied while holding an object must be precisely controlled. Studies indicate that a maximum force of 5.7 N can occur at the index fingertip, for the average adult, during static grasping [95]. In this work, the fingertip force applicable by the artificial finger was evaluated by measuring the tip force detected by the fingertip sensor as the PIP flexion actuator applies a force to the PIP joint. The PIP joint was chosen as being the most logical approach since the joint is directly linked to the DIP joint.

The fingertip closed-loop force control uses the same control scheme as for finger joint position (see Section 7.3.2). In this case, the set-point for the controller is a desired fingertip force. The controller reads the fingertip force sensor and an error signal is generated

based on the difference between the desired and measured fingertip force. Similar to position control, the error signal is then fed into the controller where a proportional and derivative terms are applied to the actual current PWM signal. The fingertip sensor is read at tha rate of 100hz and the PWM signals are updated every 10ms until the PIP joint flexion sufficient to achieve the desired fingertip force.

7.4.2.1 Open-loop test

The finger was oriented to allow the fingertip pressure sensor, mounted near the end of the underside of the DIP joint, to press against a flat surface parallel to the pressure sensor. Another load cell also measured the flexor tendon force during the simulated static grasp. The plot (Figure 7.22) indicates that the finger tip force generated during open-loop motion of the PIP joint. A maximum fingertip force of 4N is generated with a corresponding PIP flexor force of 10 N. This is consistent with findings of Rempel et al, who investigated the relationship between forces generated by the two flexor tendons of the index finger and the force applied at the fingertip while maintaining a static hand postures [117]. Rempel et al. determined this ratio to be 2.47± 0.7 for the human hand. This ratio is also in close agreement to the model prediction of Chao et al., who defined the flexor tendon tension (FDS and FDP) to be in the range of 9 to 11 N for tip pinch motions of the index finger [70]. This open-loop test validates the biomimetic nature of the tendon mechanism and actuation strategy as the forces generated at the fingertip and in the flexor tendon corresponds to those of the human index finger. Future work will investigate the effects of increasing actuator force on the fingertip force.

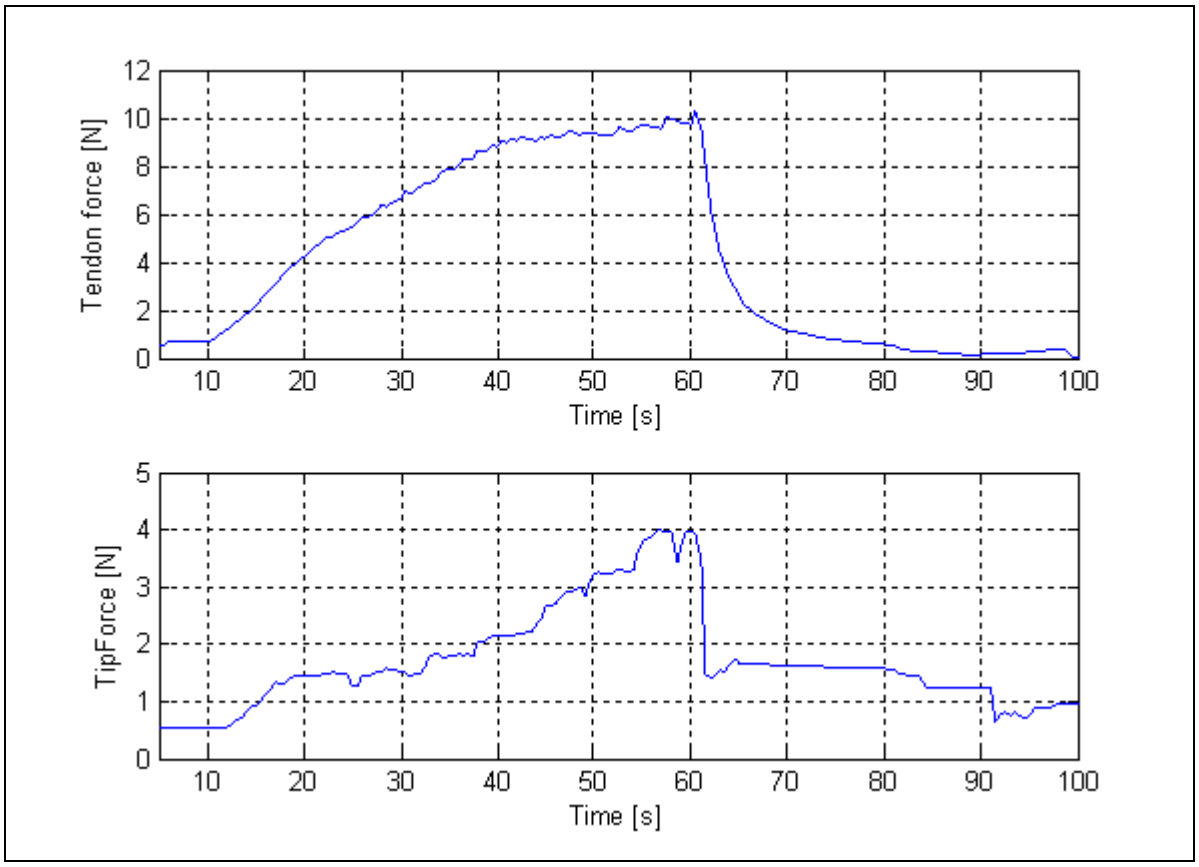

Figure 7.22: Fingertip and tendon force for open-loop motion of PIP joint

7.4.2.2 Closed loop test

Once the ability to move finger joints to set positions under closed-loop control had been evaluated, a subsequent experiment was performed to ascertain how successfully closed-loop force control could be when applied to the fingertip. The finger was oriented similar to the open-loop test (fingertip sensor pressing on a flat surface). The fingertip pressure sensor was allowed to transfer force to a load cell for force measurement. A desired fingertip force, which is an A/D count value corresponding to approximately 2 N force, was input to the controller. The PIP flexion actuator began applying force to the PIP joint, which was transferred to the load cell and the fingertip force sensor. Sensor A to D counts and measured fingertip force while applying a 2 N force using PIP joint force control are shown in Figure 7.23.

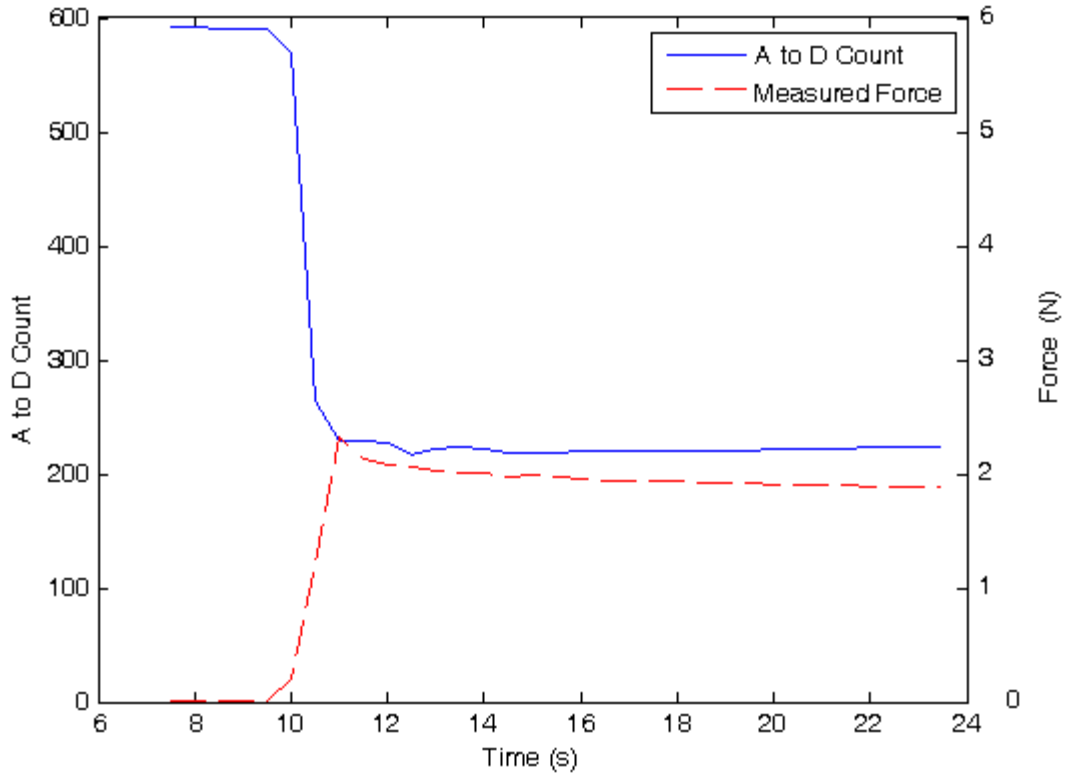

Figure 7.23: Sensor A to D counts and measured fingertip force

It can be seen that the finger reaches a steady-state value where the approximate desired fingertip force of 2 N is applied to the finger tip (due to the particular circuit configuration for this force sensor, decreasing A/D count readings were observed corresponded to increasing force values). However, one potential issue of consequence can be seen in looking at the plot: over time, the actual measured fingertip force decreases while the force reported by the fingertip force sensor stays relatively constant. This is due to the type of sensor (i.e. FSR) chosen to measure the fingertip force. When compressed for long periods of time (more than a few seconds) the resistance of the thick-film sensor slowly changes. All sensors of this type exhibit this shift to a degree, with some manufacturer's sensors being better than others in this regard. However, this effect is reversible once pressure is removed from the sensor. The low cost and lightweight advantages of this type of sensor made its use attractive for the artificial finger and incorporation into rehabilitation robots might still be practical given the relatively small magnitude of the phenomenon, and

the fact that the human hand is not generally required to grasp objects for long periods of time with significant accuracy.

Chapter 8

Conclusion and Future Work

8.1 Conclusion

The aim of this work was to emulate the biological features of the natural muscle–tendon arrangement in the human hand in developing a new actuation scheme for a biomimetic artificial finger. This thesis presents the implementation of the biomimetic tendon-driven actuation mechanism on a four degree-of-freedom anthropomorphic artificial finger (3 active DOFs and 1 passive DOF). The proposed biomimetic tendon-driven actuation mechanism uses spring-biased shape memory alloy (SMA) artificial muscles in a agonist-antagonist configuration with the integration of compliant tendon cables. The underlying mechanical structure of the artificial finger uses the human hand's index finger as basis for emulation, given that this finger has the highest mobility and use of all the hand's digits. The goal of this thesis was not to equal the simplified version of the finger architecture to the biological entities of the natural finger but to define a system with as much anthropomorphic consistency as possible. As such, the joint structure has a 2 DOF head knuckle and a one DOF middle joint coupled to a passive end joint. Tactile feedback was provided by the use of a simple resistive force sensor placed on the fingertip surface, while joint position feedback was obtained by embedding resistive bend sensors and miniature potentiometers into the finger joints. Our approach to anthropomorphic control is limited to a very basic control of finger in flexion and extension. A pulse width modulated proportional derivation (PWM-PD) feedback controller was implemented for each active joint via on-board microcontrollers to enable closed-loop biomimetic control of the artificial finger.

The resulting finger is a biomechanically and anthropomorphically accurate artificial finger. Ranges of motion were measured to be the same as the human hand. Experimental tests carried out indicated that the actuation mechanism successfully permitted bi-directional

motion of the finger joints with respect to the normal resting position. Although the open-loop control was not able to produce repeatable and reliable finger motion, closed-loop control presented very promising results. Desired joint angles were successfully achieved in a reasonable time period.

8.2 Discussion and Future Work

One of the major challenges encountered in the design of the artificial finger was due to its small size. It was difficult to incorporate all the necessary physical features and produce a somewhat equivalent biological shape and size. The implementation of all four DOFs implied limited space within the finger structure for tendon cables and sensors. Much design effort was put in order to ensure that the tendons running in the finger structure did not rub against each other or get entangled. This was especially of consideration since the PIP extensor and flexors and the MCP adduction and abduction tendons all passed through the universal joint at the MCP. Furthermore, we needed to make sure that the tendons running on the outer skull did not interfere with finger joints during flexion movements. This was mostly a concern for the extension cables running over the PIP and DIP joints. Many iterations of the design, including an initial design of the MCP as a ball joint (although this idea was abandoned owing to the difficulty in the keeping that joint stable with motion occurring in only 2 DOFs), were necessary before the final prototype was made. Since the stereolithographed finger parts are too fragile to sustain heavy loads or hard impacts, the next step would be to have the links cast out of a more robust material for durability.

The initial finger design called for the use of bend sensors at all finger joints. The single layer thin film bend sensors were mounted within the upper layer of the finger structure at the MCP and IP and were also embedded on the ulnar and radial sides at the MCP. While the bend sensors proved to be highly sensitive and reliable for monitoring the PIP extension/flexion movements, this sensor was eventually eliminated for the MCP joint. Side to side motions generated sharp bend angles at the MCP level which kinked the sensor and corrupted the resistive substrate. Also, the bend sensor did not have the required stable support surface to maintain the same bent shape for repetitive MCP flexion/extension angles. Since erratic resistive changes were observed with adduction/abduction motions of the finger

and unreliable MCP flexion data was observed, the bend sensors were eventually replaced by miniature, highly accurate linear potentiometers. The latter were embedded in the central axes of the MCP joint for more reliable feedback the MCP's joint motion.

One of the significant issues encountered in the implementation of the actuation mechanism is associated with the poor design of the chosen off-the-shelf SMA actuator. The design of the SMA actuator itself was beyond the scope of this work, which resulted in the use of commercially available SMA actuators (from Miga Motors Company). As mentioned in Chapter 7, the SMA actuator designed consisted layers of SMA wires wound in layers, with the SMA wire layers sandwiched between plastic plates. The plates glided with respect to each other on SMA contraction resulting in the linear motion of the output shaft. Firstly, it was observed that the friction between the plates was substantial. Secondly, as the temperature of the wires increased, they melted into the plates resulting in what we refer to as the 'sticky' effect. This prevented smooth motion of the output shaft, and hence smooth motion of the finger when actuated. Moreover, the SMA wire was soldered in place near the output shaft. This is not recommended given the SMA wire's sensitivity to temperature. In many instances, SMA wire ruptured at the solder joint during actuation of the finger joint. The future step in this project would be to research more reliable actuators or built a custom SMA actuator for our application. This would also enable the production of an actuator with adequate force output and stroke contraction as per the requirements of this work.

Another potential issue in the finger design is the high levels of friction which existed in the system. Friction was introduced by the SMA actuator and by the cables running through the finger structure. Mechanical friction also existed at the finger joints. As discussed above, choosing a more reliable actuator or building a custom-deisgned SMA actuator would help reduce the friction incorporated by the SMA actuator. The finger design can also be revised to reduce friction at the joints. Furthermore, although some work has been done in choosing tendon cables (using Teflon-coated cables) and choosing cable routes (no interference between cables and/or moving finger parts) which provided minimum friction, cable friction still a potential issue which needs to be investigated as the next step of this work.

Chapter 6 looks at the modeling of SMA actuation system. This thesis uses the simulation developed for open-loop control only. Closed-loop simulations of the finger

system are required in the future, which will help fine-tune the actuation scheme for better performance. Parametric analysis and identification also need to be done to identify the effects of changing some of the parameters on the system response. Furthermore, this thesis was looking at a quick testing and evaluation of the actuation mechanism. As such, a simple PD-PWM controller was implemented. An experimental approach for the controller tuning was used, whereby the gains were varied until an optimum actuator response was observed. Future work will require an analytical approach to determine the gains necessary for the optimum performance of the system. Parametric analysis can also be used to identify the gains of the proposed closed-loop control strategy. Furthermore, SMAs are non-linear by nature. The development of a robust non-linear controller is required which will account for all non-linearities and enable a precise control of the actuator.

As it stands the controller input is a desired angular position. The inverse finger kinematics, which defines the joint angular position given a fingertip location in space, can be used to define the desired position in future work. So far, limitations of the microcontroller used prevented the programming of the complex inverse solution in the microcontroller's firmware.

This thesis looks at the actuation scenario where only one actuator is activated at a time. The passive tendon in this case is only used as a bias spring. Future work will investigate the active use of the opposing actuator, when the active actuator is its cooling phase, to return the finger joint to the starting position. This believed to improve response and robustness of the joint motion.

8.3 Future goal

One of the potential applications of this actuation and sensing scheme developed is with rehabilitation robots, with focus on with wearable robotics (e.g. robotic exoskeletons and orthoses) and prosthetics in particular. This is because routine movement therapy typically involves repetitive movements of the injured finger/s in order to improve muscular strength and movement coordination. While proven effective, this process is labor-intensive, lacks repeatability and the measure of the performance and progress of the patient is unreliable [1]. The proposed portable actuation mechanism, when mounted on the human

finger can automate the movement therapy and automatically exercise the human finger during rehabilitative therapies. This methodology provides an effective way to measure the ranges of the motion of the affected joint and accurately evaluate the progress made by the patient with the help of the feedback sensor technology (bend and pressure) used in conjunction with the finger actuating mechanism. Furthermore, the artificial finger was designed to meet the defining criteria of prosthetic devices (anthropomorphic size and weight, shape and noiseless operation) and can be used as a platform for the development of biomimetic prosthetic hands.

References

1. Brown, Alan S., "Why hands matter?", Mechanical Engineering, vol. 130, Issue 7, p24-29, Jul2008.
2. Wybrun, G.M, Pickford, R.W., Hirst, R.J., Human Senses and Perception, London: Oliver and Boyd Ltd., 1969, pp. 15-37
3. Adam P. Cann, Anne Marie Baker, Ally Hansen, Deanna Massie and Anthony A. Vandervoort, "A five year retrospective analysis of occupational injuries and incidence reported at a research intensive Canadian university", Journal of Prevention, Assessment and Rehabilitation, vol. 3, no.2, pp 171-184
4. Sorock, G.S., Lombardi, A., Courtney, T.K., Cotnam, J.P., Mittleman, A., "Epidemiology of occupational acute traumatic hand injuries: a literature review", Safety Science, Vol. 38, Issue 3, August 2001, pp. 241-256
5. World wide Web at http://biomed.brown.edu/Courses/BI108/BI108_2003_Groups/Hand_Prosthetics/stats.html, Marlowe Kulley, April 2003.
6. Chappell, P.H., Light, M., "Development of a lightweight and adaptable multiple-axis hand prosthesis", Medical Engineering & Physics, v 22, n 10, Dec. 2000, 679-84.
7. Paolo Bonato, "Advances in wearable technology and applications in physical medicine and rehabilitation", Journal of Neuroengineering Rehabilitation, vol 2., no 2. pp 1186-96.
8. E. Rocon, A.F Ruiz, J.L. Pons, "Rehabilitation Robotics: a Wearable Exo-Skeleton for Tremor Assessment and Suppression", *Proceedings of the 2005 IEEE International Conference on Robotics and Automation*, Barcelona, Spain, April 2005, pp2271-2276
9. Lisa K. Simonea, Nappinnai Sundarrajanb, Xun Luoc, Yicheng Jiac and Derek G. Kamperc, "A low cost instrumented glove for extended monitoring and functional hand assessment", Journal of Neuroscience Methods, Volume 160, Issue 2, 15 March 2007, Pages 335-348.

10. J-O. Eklundh, Cognitive Robotics, A preparatory workshop for EU Seventh Research Framework Programme, Luxembourg, 20th December 2005., available on the world wide web at: ftp://ftp.cordis.europa.eu/pub/ist/docs/dir_e/cognitive_robotics_workshop20051220.pdf
11. Oudeyer, P.Y,; Kaplan, F., Hafner, V.V., "Intrinsic Motivation Systems for Autonomous Mental Development", IEEE transactions on Evolutionary Computation, vol. 11, Issue 2, Apr 2007, pp 265-286.
12. Dechev, N., Cleghorn, S. and Naumann, S., "Multiple Finger, Passive Adaptive Grasp Prosthetic Hand", *Mechanism and Machine Theory*, vol. 36, no. 10, pp.1157-1173, October 2001.
13. H. Herr, G. Whiteley and D. Childress, "Cyborg Technology – Biomimetic Orthotic and Prosthetic Technology", Biologically Inspired Intelligent Robots, Y. Bar-Cohen and C. Breazeal, Eds. (SPIE Press, Bellingham, WA, 2003).
14. Christine Connolly, "Prosthetic hands from Touch Bionics", *Industrial Robot: An International Journal*, vol. 35, Issue 4, 2008, pp 290-293
15. H.H. Kwee, "Rehabilitation Robotics – Softening the Hardware", IEEE Engineering in Medicine and Biology, 330-335 (1995).
16. G. Bolmsjo, H. Neveryd and H. Eftring, "Robotics in Rehabilitation", IEEE Trans. on Rehabilitation Engineering, 3(1), 77-83 (1995).
17. N. Tejima, "Rehabilitation Robotics: a Review", Advanced Robotics, Vol 14, No. 7, pp. 551-564, 2000.
18. D. Stefanov and Z.Z. Bien, Advances in Human-Friendly Robotic Technologies for Movement Assistance/Movement Restoration for People with Disabilities, Berlin: Springer-Verlag, 2004.
19. H.F.M. Van der Loos, D.S. Reinkensmeyer, Chapter 54. Health Care and Rehabilitation Robotics, *Handbook of Robotics*, Springer-Verlag, 2008.
20. Z. Li and S. Sastry, Dexterous Robot Hands (Springer, New York, 1989).
21. J.L. Pons, R. Ceres and F. Pfeiffer, "Multifingered Dexterous Robotic Hand Design and Control: A Review", *Robotica*, 17, 661-674 (1999).
22. L. Lin and H. Huang, "NTU Hand: A New Design of Dexterous Hands", *ASME Journal of Mechanical Design*, 120, 282-292 (1998).

23. H. Liu, P. Meusel, J. Butterfass and G. Hirzinger, "DLR's Multisensory Articulated Hand, Part II: The Parallel Torque/Position Control System", *Proc. IEEE Int. Conf. on Robotics and Automation*, Leuven, Belgium, 2087-2093 (1998).
24. Lovchik, C.S. and Diftler, M.A., "The Robonaut Hand: A Dexterous Robot Hand For Space", Proc. of the IEEE International Conference on Robotics & Automation, vol. 2, Michigan, USA, May 1999, pp. 907-912
25. D. Popovic and T. Sinkjar, *Control of Movement for the Physically Disabled* (Springer-Verlag, London, 2000).
26. M.C. Carrozza, B. Massa, P. Dario, M. Zecca., S. Micera and P. Pastacalsi, "A Two DOF Finger for a Biomechatronic Artificial Hand", *Technology and Health Care*, 10, 77-89 (2002).
27. C.P. Chou, "Measurement and modeling of McKibben Pneumatic Artificial Muscles", *IEEE Trans. on Robotics and Automation*, 12, 90-103 (1996).
28. Klute, G.K., Czerniecki, J.M., Hannaford, B., "McKibben artificial muscles: pneumatic actuators with biomechanical intelligence", 1999 IEEE/ASME International Conference on Advanced Intelligent Mechatronics, pp.221-6, 1999
29. A.G. Rodriguez, N.E.n Rodriguez, A.G.G Rodriguez, "Design and validation of a novel actuator with adaptable compliance for application in human-like robotics", *Industrial Robot*, Vol. 36, No. 1, pp 84-90, 2009
30. Y. Bar-Cohen, "Biomimetic actuators using electroactive polymers (EAP) as artificial muscles", *Conference Proceedings International SAMPE Symposium and Exhibition (Proceedings)*, Vol. 51, 2006
31. F. El Feninat, G. Laroche, M. Fiset and D. Mantovani, "Shape Memory Materials for Biomedical Applications", *Advanced Engineering Materials*, 4, 91-104 (2002).
32. N. Yoshiyuki, "Hitachi's Robot Hand", *Robotics Age*, 6(7), 18-20 (1984).
33. K.J. De Laurentis and C. Mavroidis, "Mechanical Design of a Shape Memory Alloy Actuated Prosthetic Hand", *Technology and Health Care*, 10, 91-106 (2002).
34. A.D. Price, A. Jnifene and H.E. Naguib, "Design and Control of a Shape Memory Alloy Based Dexterous Robot Hand", Smart Materials and Structures, 16, 1401-1414 (2007).
35. Rohseim, M.E., *Robot Evolution: The Development of Anthrobotics*, New York, NY, USA: John Wiley & Sons, Inc., 1994, pp. 189-225

36. Jacobsen, S.C, Wood, J.E., Knutti, D.F. and Biggers, K.B., "The UTAH/MIT dexterous hand: work in progress", Robotics Research: 1st International Symposium, 1984, pp. 601-653
37. Li-Ren Lin; Han-Pang Huang. **"**Mechanism design of a new multifingered robot hand"**,** *Proc. IEEE Int. Conf. on Robotics and Automation*, Vol 2., Apr 1996, pp. 1471-1476
38. Butterfass, J., Hirzinger, G., Knoch, S. and Liu H., "DLR's Mulitsenosry Articulated Hand Part1: Hard- and Software Architecture", *IEEE Conference of Robotics and Automation*, Belgium, vol.3, Leuven, Belgium, May 1998, pp. 2081-2086
39. Butterfass, J., Grbenstein, M., Liu, H. and Hirzinger G., "DLR-Hand II: Next Generation of a Dexterous Robot Hand", *Proc. of the IEEE International Conference of Robotics & Automation*, vol. 1 , Seoul, Korea, May 2001, pp. 109-114
40. Shadow Robot Company, "Design of a dexterous hand for advanced CLAWAR applications", London, England: Shadow Robot Company, 2003. http: //www.shadow. org.uk/.
41. Kyberd, P.J. and Chappell, P.H., "The Southampton Hand: An intelligent myoelectric prosthesis", *Journal of Rehabilitation Research & Development*, vol. 31, no. 4, pp. 326-335, Nov 94
42. P.J. Kyberd, C. Light, P.H. Chappell, J.M. Nightingale, D. Whatley and M. Evans, "The Design of Anthropomorphic Prosthetic Hands: A Study of the Southampton Hand", *Robotica*, 19, 593-600 (2001).
43. Cotton, D. P. J. C., Cranny, A., Chappell, P. H., White, N. M. and Beeby, S. P. (2006) Control strategies for a multiple degree of freedom prosthetic hand. In: *UKACC Control 2006 Mini Symposia*, Aug 2006, Glasgow, pp. 211-18
44. Connolly, C. , 'Prosthetic hands from Touch Bionics", *Industrial Robot*, v 35, n 4, 2008, p 290-293
45. Garcia-Cordona, F., Lopez-Coronado, J., Guerrero-Gonzalez, A., "Design of an anthropomorphic finger using shape memory alloy springs", Proc. of the IEEE International Conference on Systems, Man and Cybernetics, vol. 2, pp. 794-799, 1999.
46. Terauchi, M., Zenba, K., Shimada, A., Fujita, M., "Controller Design on the Fingerspelling Robot Hand using Shape Memory Alloy", *SICE-ICASE International Joint Conference*, Oct. 2006 , Busan, South Korea

47. Yang, K. and Gu, C.L., "Research on novel shape memory alloy multi-fingered humanoid hand", *Proceedings of the Institution of Mechanical Engineers, Part C: Journal of Mechanical Engineering Science*, v0l. 221, no. 9, Sept 2007, pp.1131-1140
48. Loh, C.S., Yukoi, H., Arai, T., "New shape memory alloy actuator: design and application in the prosthetic hand", *Proceedings of the 2005 27th Annual International Conference of the Engineering in Medicine and Biology Society,* 2005, pp. 6900-6903
49. Cocaud, C., Jnifene, A., "Analysis of a two DOF anthropomorphic arm driven by artificial muscles", Proceedings 2nd IEEE International Workshop on Haptic, Audio and Visual Environments and their Applications, 2003, 37-42
50. Garcia-Cordova, F., Lopez-Coronado, J., Guerrero-Gonzalez, A., "Design of an anthropomorphic finger using shape memory alloy springs", *IEEE SMC'99 Conference Proceedings. 1999 IEEE International Conference on Systems, Man, and Cybernetic)*, vol.2, 1999, pp.794-9
51. Hand Ijnjuries and Disorders, available on the World Wide web at : http://www.nlm.nih.gov/medlineplus/handinjuriesanddisorders.html
52. Tarchanidis, K.N., Lygouras, J.N., **"**Data glove with a force sensor"**,** IEEE Transactions on Instrumentation and Measurement, Vol. 52, Issue 3, June 2003, pp.984 – 989
53. Data gloves [online], available from the World Wide Wen: http://www.vrealities.com/glove.html
54. Bouzit, M., Burdea, G.,Popescu, G., Boian, R., "The Rutgers Master II-new design force-feedback glove", *IEEE/ASME Transactions on Mechatronics*, vol. 7, no. 2, June 2002, pp. 256-63
55. Sarakoglou, I., Kousidou, S., Tsagarakis, N.G., and Darwin G. Caldwell, D. G. , "Exoskeleton-Based Exercisers for the Disabilities of the Upper Arm and Hand", *Rehabilitation Robotics*, Aug 2007, pp. 648
56. Takashi, C.D., Der-Yeghiaian, L., Le, V.H., Cramer, S.C., " A robotic device for hand motor therapy*", Proc. of the IEEE 9th International Conference on Rehabilitation Robotics*, July 2005, pp. 17-20.
57. Worsnopp, T.T., Peshkin, M.A., Colgate, J.E., Kamper, D.G. , "An actuated finger exoskeleton for hand rehabilitation following stroke",, 2007 IEEE 10th International Conference on Rehabilitation Robotics, 2007, pp. 896-901

58. Simone, L.K., Sundarrajan, N., Xun L., Yicheng J., Kamper, D.G., "A low cost instrumented glove for extended monitoring and functional hand assessment", *Journal of Neuroscience Methods*, vol. 160, no. 2, Mar 2007, pp. 335-48
59. Mulas, M., Folgheraiter, M., Gini, G., "An EMG-controlled exoskeleton for hand rehabilitation", *Proceedings of the 2005 IEEE 9th International Conference on Rehabilitation Robotics*, v 2005, 2005, p 371-374
60. Wege, A., Hommel, G., " Development and control of a hand exoskeleton for rehabilitation of hand injuries", *2005 IEEE/RSJ International Conference on Intelligent Robots and Systems*, 2005, pp. 3046-51
61. Simone, L.K., Kamper, D.., "Design considerations for a wearable monitor to measure finger posture, Journal of NeuroEngineering and Rehabilitation, 2005, 2:5
62. I.A. Kapandji. The Physiology of the Joints, volume 1. E&S Livingstone, Edinburgh and London, 2 edition, 1970.
63. Folgheraiter, M. and Gini G., "Blackfingers: an Artificial Hand that Copies Human Hand in Structure, Size and Functions", Proc. of the IEEE Conference on Humanoids 2000, MIT, Cambridge, Ma, Sept 2000
64. White, T.D. and Folkens, P., A., Human Osteology, San Diego, California, USA: Academic Press, Inc., 1991, pp.189-206.
65. Levangie, P.K. and Norkin, C.C., Joint Structure and Function: A comprehensive Analysis, 3rd ed., Philadelphia, PA: F.A Davis Company, 1992, pp. 265-285
66. Palastanga N., Field D. and Soames, R., *Anatomy and Human Movement*, Oxford, UK: Heinemann Professional Publishing Ltd., 1989, pp. 250-275
67. Tyldesley, B. and Grieve, J.I., Muscles, Nerves and Movement: Kinesiology in Daily Living, 1st ed., Oxford, Great Britain: The Alden Press, 1989, pp. 126-153
68. Wilkinson. D.D., Weghe, M., V. and Matsuoka, Y., "An Extensor Mechanism for an Anatomical Robotic Hand", Proc. of the IEEE International Conference on Robotics & Automation, Taipei, Taiwan, Sept 2003, pp. 238-243
69. Barbieri L. and Bergamasco, M., "Net of Tendons and Actuators: an Anthropomorphic Model for the Actuation system of Dexterous Robot Hands", Proc. of the 5th International Conference on Advanced Robotics, Pisa, Italy, June 1991, pp. 357-362

70. Chao, E.Y.S., An, K., Cooney, W.P. and Linscheid, R., Biomechanics of the Hand, Teaneck, NJ. USA: World Scientific Publishing Co. Pte. Ltd., 1989
71. Garrett, J.W., Anthropometry of the Air Force Female Hand. Wright-Patterson Air Force Base, OH: Aerospace Medical Research Laboratory, Aerospace Medical Division, Air Force Systems Command, AMRL-TR-69-26, 1970.
72. Garrett JW (US Air Force). Anthropometry of the Air Force Female Hand. Wright-Patterson Air Force Base, OH: Aerospace Medical Research Laboratory, Aerospace Medical Division, Air Force Systems Command, AMRL-TR-69-26, 1970.
73. Poznanski, A.K., The hand in Radiologic Diagnosis, Philadelphia: W.B Saunders, 1974, pp. 29-49
74. Freivalds, A., Biomechanics of the upper limbs: mechanics, modeling and musculoskeletal injuries, CRC Press LLC, Florida, 2004
75. Buchholz, B., Armstrong, A., and Goldstein, S.A., "Anthropometric data for describing the kinematics of the human hand", Ergonomics, vol. 35, no. 3, March 1992, pp. 261-273.
76. Abada, A., Benson, K., Courtney, A., Minto, J., Davies, B.T., "Comparison of hand anthropometry of females in three ethnic groups", Ergonomics, vol. 23, no. 2, Feb 1980, pp. 179-182
77. Sanchis, L.I. and Ferrando, A.T., "Sensors for application in robotics" Revista Espanola de Electronica, No. 473, Apr 1994, pp. 54-59
78. Roderic A. Grupen, Thomas C. Henderson and Ian D. McCammon, A Survey of General- Purpose Manipulation", *The International Journal of Robotics Research*, Vol. 8, No. 1, pp. 38-62, 1989
79. David J. Hall, Robotic Sensing, The Robotics Institute, Carnegie-Mellon University, Pittsburgh, Pennsylvania, March 1984.
80. Begej, S.**, "**Planar and finger-shaped optical tactile sensors for robotic applications", IEEE Journal of Robotics and Automation, Vol. 4, Issue 5, pp. 472 – 484, Oct 1988
81. Buchholz, B. and Armstrong, T., "Ellipsoidal representation of human hand anthropometry", Human Factors, vol. 33, no. 4, Aug 1991, pp. 429-441.
82. Craig, J.J, Introduction to Robotics, Mechanics and Control, 2nd ed., Don Mills, Ontario: Addison-Wesley Publishing Company Inc., 1989, pp. 69-186.

83. Narasimhan, S., Dexterous Robotic Hands: Kinematics and Control, Technical Report, Artificial Intelligence Laboratory, MIT, 1988, pp. 19-31
84. D. J. Beebe, D. D. Denton, R. G. Radwin and J. G.Webster, "A silicon-based tactile sensor for finger-mounted applications," IEEE Trans. Biomed. Eng. 45(2), 151–159 (1998).
85. J. Engel, J. Chen, Z. Fan and C. Liu, "Polymer micromachined tactile sensors," Sensors Actuators A 117, 50–61(2005).
86. J. Carpaneto, S. Micera, F. Zaccone, F. Vecchi and P. Dario, "A sensorized thumb for force closed-loop control of hand neuroprostheses," *IEEE Trans. Neural Syst. Rehabil. Eng.*11(4), 346–353 (2003).
87. Bar-Cohen, Y., Electroactive Polymer (EAP) Actuators as Artificial Muscles – Reality, Potential and Challenges, Bellingham, WA: SPIE-The International Society for Optical Engineering, 2001, pp. 4-37
88. Bar-Cohen, Y., "Electroactive Polymers as Artificial Muscles – Reality and Challenges", Proc. of the 42nd AIAA Structures, Structural Dynamics and Materials Conference, Paper 2001-1492, Seattle, WA, Apr 2001
89. Bar-Cohen, Y., " Focus issue on Biomimetics Using Electroactive Polymers as Artificial Muscles", BioInspiration & Biomimetics Journal, Vol. 2, No. 2, pp. 1-3, June 2007
90. Gilberston, G., Muscle Wires Project Book, 3rd ed., San Rafael, CA: Mondo-tronics, 1993
91. Mavroidis, C., "Development of Advanced Actuators Using Shape Memory Alloys and Electrorheological Fluids", Research in Nondestructive Evaluation, vol. 14, no. 1, pp. 1-32, March 2002
92. M. Elahania and H. Ashrafoun, "Nonlinear control of a shape memory alloy actuated manipulator," Trans. ASME. J. Vib. Acoust. 124, 566–575 (2002).
93. J. I. Arocena and R.W. Daniel, "Design and control of a novel 3-DOF flexible robot, part 1: Design and evaluation," Int. J. Robot. Res. 17, 1167–1181 (1998).
94. C. Liang and C.A. Rogers, "Design of Shape Memory Alloy Actuator", *ASME Journal of Mechanical Design*, 114, 223-230 (1992).

95. Kargov, A., Pylatiuk, C., Martin, J., Schulz, S. and Doderlein, L. “A comparison of the grip force distribution in the natural hands and in prosthetic hands”, Disability and Rehabilitation, vol. 26, no. 12, 2004 pp. 705-711.
96. Stockel, D., “The Shape Memory Effect – Phenomenon, Alloys, Applications” [online], Fremont, CA: NDC, Nitinol Devices & Components, Inc., available from World Wide Web: http://www.nitinol-europe.com/pdf/l5.pdf
97. Gilardi, G., Haslam, E., Bundhoo, V., and Park, E.J., “Shape memory alloy based tendon-driven actuation system for biomimetic artificial fingers, part II: modeling and control”, Robotica (in press)
98. Lagoudas, D.C., “Detailed Introduction to Shape Memory Alloys” [online], Texas: Department of Aerospace Eng., Texas A & M University, available from World Wide Web http://smart.tamu.edu/overview/overview.html
99. Trochu ,F., Brailovski, V., Meunier, M.A., Terriault, P., Qian, Y.Y, “Design of Shape Memory Devices”, Ecole Polytechnique of Montreal, Mechanical Engineering Department, Canada, pp. 389-403, 1996;6(6):389-403
100. Smith.R.C., Smart Material Systems: Model Development. SIAM Frontiers in Applied Mathematics, 2005.
101. Smith, R., “Model Development for Shape Memory Alloys”, chap. 5 in *Smart Material Systems: Model Development*, to be published by SIAM: January 2005
102. Zak, A.J., Cartmell, MP., Ostachowicz, W.M., and Wiercigroch, M., “One-dimensional shape memory alloy models for use with reinforced composite structures”, Smart Materials and Structures, vol. 12, 2003, pp. 338-346
103. Liang, C. and Rogers, C.A., “Design of Shape Memory Alloy Actuators For Robotics”, *Proc. of the 4th ASME International Symposium on Robotics and Manufacturing*, Santa Fe, New Mexico, vol. 4, pp. 75-80, Nov. 1992.
104. Ghorashi, M. and Inman, D., “Shape Memory Alloy in Tension and Compression and its Application as Clamping Force Actuator in a Bolted Joint: Part 2: Modeling”, Journal of Intelligent Materials Systems and Structures, vol. 15, August 2004, pp. 589 – 600
105. Prahlad, H. and Chopra, I., “Comparative Evaluation of Shape Memory Alloys Constitutive Models with Experimental Data”, *Journal of Intelligent Material Systems and Structures*, vol. 12, June 2001, pp. 383-395

106. Ashrafiuon, H., Mojtaba, M., and Elahinia, M.H., "Position control of a three-link shape memory alloy actuated robot," *Journal of Intelligent Material Systems and Structures*, Vol. 17, pp. 381-392, 2006

107. Paiva, A. and Savi, M. A., "An overview of constitutive models for shape memory alloys," *Mathematical Problems in Engineering.* No. 1-30. 2006

108. De la Flor, S., Urbina. C., and F. Ferrando, "Constitutive model of shape memory alloys: theoretical formulation and experimental validation," *Materials Science and Engineering A,* Vol. 427, No. 1-2, pp.112-122, 2006.

109. Tanaka, K., "A thermomechanical sketch of shape memory effect: one-dimensional tensile behaviour," *Res. Mechanica,* Vol. 18, 251-263, 1986.

110. N. Ma and G. Song, "Control of Shape Memory Actuator Using Pulse Width Modulation", *Smart Materials and Structures*, 12, 712-719 (2003).

111. Song. G. and Ma. N., "Control of Shape Memory Alloy Actuators Using Pulse Width Pulse Frequency (PWPF) modulation", *American Society of Mechanical Engineers, Aerospace Division (Publication) AD*, vol. 64, pp. 351-358. 2001

112. S. Yan, X. Liu, F. Xu, and J. Wang, "A gripper actuated by a pair of differential SMA springs", *Journal of Intelligent Systems and Structures* **,** Vol. 18, pp. 459-466, 2007.

113. K. Singh, J. Sirohi, and I. Chopra, "An improved shape memory alloy actuator for rotor blade tracking," *Journal of Intelligent Material Systems and Structures*, Vol. 14, pp. 767-786 2003.

114. G. Song, "Design and control of a Nitinol wire actuated rotary servo," *Smart Materials and. Structure,* Vol. 16, pp. 1796-1801, 2007.

115. S. Choi, "Position control of a single-link mechanism activated by shape memory alloy springs: experimental results," *Smart Materials and Structure,* Vol. 15, pp.51-58, 2006.

116. Miga Motor Company, Application Notes -DM01 Linear Shape Memory Alloy Actuator, Rev A, 2007

117. Rempel, D. , Kursa, K., Diao, E. and Lattanza, L. "In vivo forces generated by finger flexor muscles do not depend on the rate of fingertip loading during an isometric task." Journal of Biomechanics, Vol. 38, No. 11, pp. 2288-93, Nov. 2005.

118. Riener, R., "Human-Centered Rehabilitation Robotics", Proc. of the IEEE International Conference on Rehabilitation Robotics, Chicago, IL, June 2005.

APPENDIX A

ANTHROPOMETRIC HAND DESCRIPTIONS ADAPTED FROM BUCCHOLZ ET AL.

SUBJECT	*SEX*	*HAND*	*HAND LENGTH (MM)*	*PERCENTILE*	*HAND BREADTH (MM)*	*PERCENTILE*	*WRIST BREADTH (MM)*	*PERCENTILE*
1	M	R	177.90	1	86.60	20	62.99	5
2	M	L	192.50	35	82.21	5	60.71	1
3	F	R	165.58	5	75.96	40	59.13	65
4	M	L	200.20	65	89.92	55	67.49	50
5	M	L	183.36	5	94.88	90	71.76	85
6	F	L	178.09	45	87.59	99	62.87	90

APPENDIX B

FINGER INVERSE KINEMATIC SOLUTION

The first step involves evaluating the elements of the transformation frame that relates the base frame {0} to the fingertip (${}^{0}_{tip}T$). Now, the position and orientation of the finger tip (n, o, a, p) are known. Using Eulerian representation of frames [82], evaluation of fingertip frame with respect to the base frame involves:

i) Rotation of θ_1 about Z_o axis

ii) Rotation of 90^o about the new x-axis

iii) Rotation of - α about the new z-axis

Hence, expressed as a homogeneous transform:

$$ {}^{0}_{tip}T = \begin{bmatrix} n_x & o_x & a_x & p_x \\ n_y & o_y & a_y & p_y \\ n_z & o_z & a_z & p_z \\ 0 & 0 & 0 & 1 \end{bmatrix} = \begin{bmatrix} Rot_z(\theta_1)Rot_x(90^0)Rot_z(-\alpha) & \vec{P} \\ 0 \quad 0 \quad 0 & 1 \end{bmatrix} \ldots\ldots\ldots\ldots \text{(B.1)} $$

where $\vec{P} = (p_x, p_y, p_z)$, that is, the fingertip Cartesian coordinates expressed in terms of the base frame coordinate system. It should be noted that θ_1 is known and is simply given by $a\tan 2(p_y, p_x)$ as will be verified later on.

The ${}^{0}_{tip}T$ matrix of known elements can also be expressed in terms of the joint angles θ_1, θ_2, θ_3 and θ_4 as shown in eq (C.2).

$$ {}^{0}_{tip}T = \begin{bmatrix} n_x & o_x & a_x & p_x \\ n_y & o_y & a_y & p_y \\ n_z & o_z & a_z & p_z \\ 0 & 0 & 0 & 1 \end{bmatrix} = \begin{bmatrix} c_1c_{234} & -s_1 & -c_1s_{234} & -L_3c_1s_{234} + c_1(L_2c_{23} + L_1c_2) \\ s_1c_{234} & c_1 & -s_1s_{234} & -L_3s_1s_{23} + s_1(L_2c_{23} + L_1c_2) \\ s_{234} & 0 & c_{234} & L_3c_{234} + L_3s_{23} + L_1s_2 \\ 0 & 0 & 0 & 1 \end{bmatrix} \qquad \text{(B.2)} $$

Now,

$$\begin{bmatrix} p_x \\ p_y \\ p_z \end{bmatrix} = \begin{bmatrix} -L_3 c_1 c_{234} + c_1(L_2 c_{23} + L_1 c_2) \\ -L_3 s_1 c_{234} + s_1(L_2 c_{23} + L_1 c_2) \\ L_3 s_{234} + L_3 s_{23} + L_1 s_2 \end{bmatrix} \tag{B.3}$$

Pre-multiplying the fingertip position vector by ${}^1_0R$, we obtain:

$$\begin{bmatrix} c_1 & s_1 & 0 \\ -s_1 & c_1 & 0 \\ 0 & 0 & 1 \end{bmatrix} \begin{bmatrix} p_x \\ p_y \\ p_z \end{bmatrix} = \begin{bmatrix} c_1 & s_1 & 0 \\ -s_1 & c_1 & 0 \\ 0 & 0 & 1 \end{bmatrix} \begin{bmatrix} -L_3 c_1 c_{234} + c_1(L_2 c_{23} + L_1 c_2) \\ -L_3 s_1 c_{234} + s_1(L_2 c_{23} + L_1 c_2) \\ L_3 s_{234} + L_3 s_{23} + L_1 s_2 \end{bmatrix} \tag{B.4}$$

$$\begin{bmatrix} c_1 p_x + s_1 p_y \\ -s_1 p_x + c_1 p_y \\ p_z \end{bmatrix} = \begin{bmatrix} L_3 c_{234} + L_2 c_{23} + L_1 c_2 \\ 0 \\ L_3 s_{234} + L_2 s_{23} + L_1 s_2 \end{bmatrix} \tag{B.5}$$

Determining θ_1:

From row #2 of equation (B5):

$$-s_1 p_x + c_1 p_y = 0 \tag{B.6}$$

$$\theta_1 = a\tan 2(p_y, p_x) + n\pi \qquad (\text{n= 0, 1})$$

Determining θ_3:

From equation (B.2):

$$o_x = -c_1 s_{234} \tag{B.7}$$

$$o_y = -s_1 s_{234} \tag{B.8}$$

Multiplying (B.7) by c_1 & (B.8) by s_1:

$$o_x c_1 = -c_1^2 s_{234} \tag{B.9}$$

$$o_y s_1 = -s_1^2 s_{234} \tag{B.10}$$

Adding (B.9) and (B.10)

$$o_x c_1 + o_y s_1 = -(c_1^2 + s_1^2) s_{234} = -s_{234} \tag{B.11}$$

$$s_{234} = -(o_x c_1 + o_y s_1) \tag{B.12}$$

From eq. (B.2):

$$o_z = c_{234} \tag{B.14}$$

From (B.12) and (B.14):

$$\theta_2 + \theta_3 + \theta_4 = a\tan 2(-(o_x c_1 + o_y s_1), o_z) \tag{B.15}$$

Now, row #1 of eq (B.5) gives:

$$c_1 p_x + s_1 p_y = L_3 c_{234} + L_2 c_{23} + L_1 c_2 \tag{B.16}$$

Given that $(\theta_1 + \theta_2 + \theta_3)$ is known,

$$c_1 p_x + s_1 p_y - L_3 c_{234} = L_2 c_{23} + L_1 c_2 \tag{B.17}$$

Let $c_1 p_x + s_1 p_y - L_3 c_{234} = p_x'$

$$p_x' = L_2 c_{23} + L_1 c_2 \tag{B.18}$$

Row #3 of eq. (B.5) gives:

$$p_z = L_3 s_{234} + L_2 s_{23} + L_1 s_2 \tag{B.19}$$

Given that $(\theta_1 + \theta_2 + \theta_3)$ is known,

$$p_z - L_3 s_{234} = L_2 s_{23} + L_1 s_2 \tag{B.20}$$

Let $p_z - L_3 s_{234} = p_z'$

$$p_z' = L_2 s_{23} + L_1 s_2 \tag{B.21}$$

Squaring and adding (B.16) and (B.18):

$$(p_x')^2 + (p_Z')^2 = L_2^2 + L_1^2 + 2L_1 L_2 C_3 \tag{B.22}$$

$$c_3 = \frac{(p_x')^2 + (p_Z')^2 - L_2^2 - L_1^2}{2L_1L_2} \tag{B.23}$$

$$s_3 = \pm\sqrt{(1-c_3^2)} \tag{B.24}$$

Therefore, from (B.23) and (B.24),

$$\theta_3 = a\tan 2(s_3, c_3)$$

where s_3 and c_3 are as given above.

Determining θ_2:

Eq (B.18): $p_x' = L_2c_{23} + L_1c_2$

Eq (B.21): $p_z' = L_2s_{23} + L_1s_2$

From above equations:

$$\begin{bmatrix} p_x' \\ p_z' \end{bmatrix} = \begin{bmatrix} -L_2s_3 & L_2c_3 + L_1 \\ L_2c_3 + L_1 & L_2s_3 \end{bmatrix} \begin{bmatrix} s_2 \\ c_2 \end{bmatrix} \tag{B.25}$$

$$\begin{bmatrix} s_2 \\ c_2 \end{bmatrix} = \begin{bmatrix} -L_2s_3 & L_2c_3 + L_1 \\ L_2c_3 + L_1 & L_2s_3 \end{bmatrix}^{-1} \begin{bmatrix} p_x' \\ p_z' \end{bmatrix} \tag{B.26}$$

$$s_2 = \frac{(L_2L_3p_x') + (L_2c_3 + L_1)p_z'}{L_1^2 + L_2^2 + 2L_1L_2c_3} \tag{B.27}$$

$$c_2 = \frac{(L_2c_3 + L_1)p_x' + L_2s_3(p_z')}{L_1^2 + L_2^2 + 2L_1L_2c_3} \tag{B.28}$$

Therefore,

$$\theta_2 = a\tan 2(s_2, c_2)$$

where s_2 and c_2 are as given above.

Determining θ_4:

From eq. (B.15), the following was previously determined:

$$\theta_2 + \theta_3 + \theta_4 = a\tan 2(-(o_x c_1 + o_y s_1, o_z)$$

Since θ_2 and θ_3 are known:

$$\theta_4 = a\tan 2(-(o_x c_1 + o_y s_1, o_z) - (\theta_2 + \theta_3)$$

APPENDIX C

TENDON ATTACHMENT IN THE NATURAL FINGER

To facilitate the definition of the orientation of the joints, tendon locations and dimensional structure of the bones in 3-D space, Chao et al. defined Cartesian coordinates systems within the finger structure [70]. Chao et al. used primary co-ordinate systems (numbered 2, 4, 6) that are defined at the approximate centre of rotation of the phalanges heads and secondary systems (numbered 3, 5, 6) are located at the approximate centers of the articular concave surfaces of the joints. The x-axis is projected along the phalangeal shafts, through the centre of rotations of the joints. The y-axis is projected dorsally and the z-axis radially (for the right hand). The tendons are further assumed to be straight lines from one point to the other. The linkage structure of the bony segments with respect to the above defined co-ordinate systems is shown in Figure C.1.

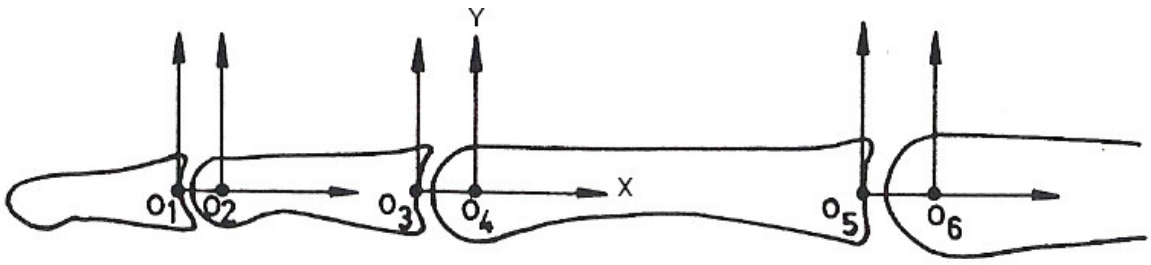

Figure C.1: Bone segments with respect to assigned co-ordinate systems

The tendon locations of the index finger on the bone segments, given in Table D.1, are presented with respect to the above-defined coordinates system. The values are expressed in dimensionless terms by normalizing the tendon location coordinates according to the length of the middle phalange of the finger in order to minimize anthropomorphic variations.

		Distal Point			Proximal Point		
Joint	Tendon	X	Y	Z	X	Y	Z
IP	TE	0.004	0.199	-0.101	0.000	0.196	-0.009
	FDP	0.004	-0.184	0.026	0.300	-0.245	0.054
PIP	FDP	-0.212	-0.308	0.009	0.400	-0.409	0.027
	RB	-0.112	-0.186	0.223	0.100	0.181	0.268
	UB	-0.112	0.151	-0.290	0.100	0.131	-0.312
	FDS	-0.212	-0.249	0.015	0.400	-0.311	0.028
	ES	-0.038	0.278	-0.027	0.000	0.266	-0.026
MP	FDP	-0.118	-0.386	0.031	0.300	-0.619	0.004
	FDS	-0.118	-0.477	-0.074	0.300	-0.689	-0.114
	RI	-0.318	-0.033	0.443	0.400	-0.362	0.629
	LU	-0.318	-0.148	0.370	0.400	-0.704	0.541
	UI	-0.318	-0.039	-0461	0.400	-0.379	-0.442
	LE	-0.018	0.421	-0.033	0.000	0.483	-0.026

Table C.1: Normalized tendon locations of the index finger with respect to the middle phalange length

APPENDIX D

STATIC TORQUE ANALYSIS

Jacobian Derivation

The Jacobian for the robotic finger is given by:

$$ {}^{0}_{=n}J = \begin{bmatrix} \dfrac{\partial {}^{0}P_{0\to n}}{\partial \theta_i} & \dfrac{\partial {}^{0}P_{0\to n}}{\partial \theta_{i+1}} & \cdots & \dfrac{\partial {}^{0}P_{0\to n}}{\partial \theta_n} \\ {}^{0}\hat{Z}_i & {}^{0}\hat{Z}_{i+2} & \cdots & {}^{0}\hat{Z}_4 \end{bmatrix} \text{ for } i = 1 \cdots n $$

where $P_{0\to n}$ is the vector position of a point on the finger expressed in terms of the joint angles and vector (${}^{0}\hat{Z}_i$) are the vectors of the transformation matrices (**n**, **o**, **a**, **p**) defined for a given joint *i* with the respect to the base frame.

I. Forces Acting On The Proximal Phalange

Let the force acting on the proximal joint be F_A and the point of application of the force be (x_A, y_A, z_A). A frame {A} is assigned at the point of application of the force F_A.

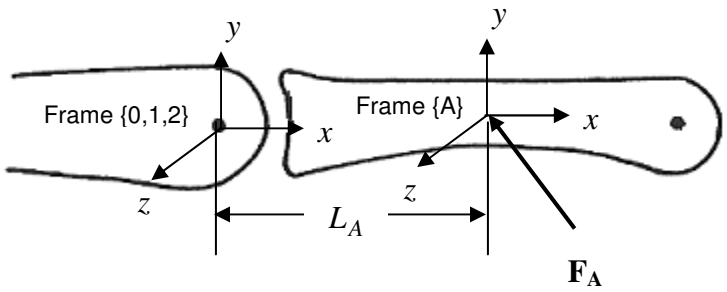

The D-H parameters for a one-link manipulator is:

i	α_{i-1}	a_{i-1}	d_i	θ_i	**i+1**
0	0	0	0	θ_1	1
1	90^o	0	0	θ_2	2
2	0	L_A	0	0	3

The link transforms (**n**, **o**, **a**, **p**) are evaluated as

$${}^0_1T = \begin{bmatrix} c_1 & -s_1 & 0 & 0 \\ s_1 & c_1 & 0 & 0 \\ 0 & 0 & 1 & 0 \\ 0 & 0 & 0 & \end{bmatrix} \qquad {}^1_2T = \begin{bmatrix} c_2 & -s_2 & 0 & 0 \\ 0 & 0 & 0 & 0 \\ s_2 & c_2 & 1 & 0 \\ 0 & 0 & 0 & 1 \end{bmatrix} \qquad {}^2_AT = \begin{bmatrix} 1 & 0 & 0 & L_A \\ 0 & 1 & 0 & 0 \\ 0 & 0 & 1 & 0 \\ 0 & 0 & 0 & 1 \end{bmatrix}$$

This force will only induce joint moments at the MCP joint, that is, joint at frame {2}. Hence, the torque induced at the MCP joint by F_A is given by

$$\tau_A = {}^0J_2{}^T\,{}^0_2F$$

Evaluating the Jacoabian, ${}^oJ_2$:

$${}^0\underline{\underline{J}}_2 = \begin{bmatrix} \dfrac{\partial {}^0P_{0\to 2}}{\partial \theta_1} & \dfrac{\partial {}^0P_{0\to 2}}{\partial \theta_2} \\ {}^0\hat{Z}_1 & {}^0\hat{Z}_2 \end{bmatrix}$$

The position vector is the **p** vector of the transformation matrix ${}^0_2T$ and given by:

$${}^0P_{0\to 2} = \begin{pmatrix} 0 \\ 0 \\ 0 \end{pmatrix}$$

$$\frac{\partial {}^0P_{0\to 2}}{\partial \theta_1} = \begin{pmatrix} 0 \\ 0 \\ 0 \end{pmatrix} \qquad \frac{\partial {}^0P_{0\to 2}}{\partial \theta_2} = \begin{pmatrix} 0 \\ 0 \\ 0 \end{pmatrix}$$

$$ {}^{0}\hat{Z}_1 = \underline{a}\left({}^{o}_{1}R\right) = \begin{bmatrix} 0 \\ 0 \\ 1 \end{bmatrix} \qquad {}^{0}\hat{Z}_2 = \underline{a}\left({}^{0}_{2}R\right) = \begin{bmatrix} s_1 \\ -c_1 \\ 0 \end{bmatrix} $$

As such,

$$ {}^{0}\underline{\underline{J}}_2 = \begin{bmatrix} 0 & 0 \\ 0 & 0 \\ 0 & 0 \\ 0 & s_1 \\ 0 & -c_1 \\ 1 & 0 \end{bmatrix} $$

Evaluating the force ${}^{0}_{2}F$:

The known force acting at the middle of the proximal link is ${}^{2}F_A$. This force needs to be expressed as ${}^{0}_{2}F$, that is, transformed to the MCP joint and written with respect to the base reference frame {0}. This force transformation is given as:

$$ {}^{0}F_2 = {}^{0}_{2}TF_{A\to 2}\,{}^{2}F_A $$

The force-moment transform is given by:

$$ {}^{0}_{2}TF_{2\to A} = \begin{bmatrix} {}^{0}_{2}R & 0_{3x3} \\ ({}^{0}\tilde{P}_{2\to A}\,{}^{0}_{2}R) & {}_{2}R \end{bmatrix} $$

where: ${}^{0}\tilde{P}_{2\to A}$ is a skew-symmetric matrix of the position vector defining MCP frame with respect to the point of application of the force at frame {A}and expressed in terms of the base frame {0} and ${}^{0}_{2}R$ is rotation matrix representing the orientation of frame {2} with respect to the base frame {0}.

$$ {}^{0}P_{2\to A} = {}^{0}_{2}R\,{}^{2}P_{2\to A} = {}^{0}_{2}R\begin{pmatrix} L_A \\ 0 \\ 0 \end{pmatrix} $$

$$ {}^{0}_{2}R = (n,o,a)^{0}_{2}T = \begin{pmatrix} c_1c_2 & -c_1s_2 & s_1 \\ s_1c_2 & -s_1s_2 & -c_1 \\ s_2 & c_2 & 0 \end{pmatrix} $$

$$ {}^{0}_{2}TF_{2\to A} = \begin{pmatrix} c_1c_2 & -c_1s_2 & s_1 & 0 & 0 & 0 \\ s_1c_2 & -s_1s_2 & c_1 & 0 & 0 & 0 \\ s_2 & c_2 & 0 & 0 & 0 & 0 \\ 0 & L_As_1 & L_As_2c_1 & c_1c_2 & -c_1s_2 & s_1 \\ 0 & -L_Ac_1 & L_As_2s_1 & s_1c_2 & -s_1s_2 & -c_1 \\ 0 & 0 & -L_Ac_2 & s_2 & c_2 & 0 \end{pmatrix} $$

Let $ {}^{2}F_A = \left(f_{x_A}, f_{y_A}, f_{z_A}, m_{x_A}, m_{y_A}, m_{z_A}\right) $

Then, $ {}^{0}F_2 = {}^{0}_{2}TF_{A\to 2}\,{}^{2}F_A $

$$ {}^{o}_{2}F = \begin{pmatrix} f_{x_A}c_1c_2 - f_{y_A}c_1s_2 + f_{z_A}s_1 \\ f_{x_A}s_1c_2 - f_{y_A}s_1s_2 - f_{z_A}c_1 \\ f_{x_A}s_2 + f_{y_A}c_2 \\ f_{y_A}L_As_1 + f_{z_A}L_Ac_1s_2 + m_{x_A}c_1c_2 - m_{y_A}c_1s_2 + m_{z_A}s_1 \\ -f_{y_A}L_Ac_1 + f_{z_A}L_As_1s_2 + m_{x_A}s_1c_2 - m_{y_A}s_1s_2 - m_{z_A}c_1 \\ -f_{z_A}L_Ac_2 + m_{x_A}s_2 + m_{y_A}c_2 \end{pmatrix} $$

Evaluation torque at MCP induced by $ F_A $

$$ \tau_A = {}^{o}J_2{}^{T}\,{}^{0}_{2}F $$

$$ \tau_A = \begin{pmatrix} -f_{Z_A}L_Ac_2 + m_{x_A}s_2 + m_{x_A}s_2 + m_{y_A}c_2 \\ f_{y_A}L_A + m_{z_A} \end{pmatrix} $$

Since the forces on the proximal link does not produce any torque on the PIP and DIP joints, then τ_A can be rewritten as:

$$\tau_A = \begin{pmatrix} -f_{Z_A} L_A c_2 + m_{x_A} s_2 + m_{x_A} s_2 + m_{y_A} c_2 \\ f_{y_A} L_A + m_{z_A} \\ 0 \\ 0 \end{pmatrix}$$

II. Forces Acting On The Middle Phalange

Let the force acting on the proximal joint be F_B and the point of application of the force be (x_B, y_B, z_B). A frame {B} is assigned at the point of application of the force F_B.

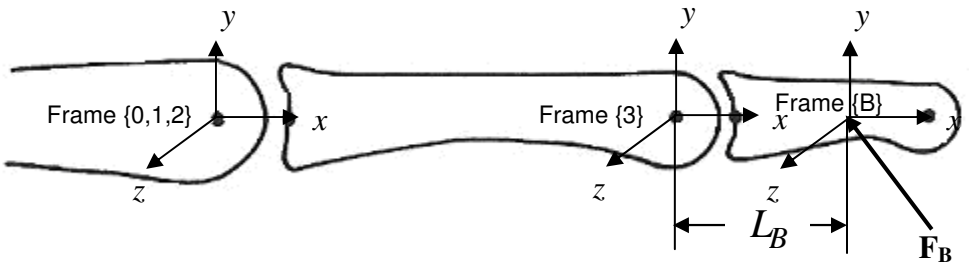

The D-H parameters for a two-link manipulator are:

i	α_{i-1}	a_{i-1}	d_i	θ_i	i+1
0	0	0	0	θ_1	1
1	90^o	0	0	θ_2	2
2	0	L_1	0	θ_3	3
3	0	L_B	0	0	4

The link transforms (**n**, **o**, **a**, **p**) are evaluated as

${}^0_1T$ and ${}^1_2T$ are the same as described in Section I.

$$ {}^{2}_{3}T = \begin{bmatrix} c_3 & -s_3 & 0 & L_1 \\ s_3 & c_3 & 0 & 0 \\ 0 & 0 & 1 & 0 \\ 0 & 0 & 0 & 1 \end{bmatrix} \qquad {}^{3}_{B}T = \begin{bmatrix} 1 & 0 & 0 & L_B \\ 0 & 1 & 0 & 0 \\ 0 & 0 & 1 & 0 \\ 0 & 0 & 0 & 1 \end{bmatrix} $$

This force will induce joint moments at the MCP and PIP joints, that is, joint at frames{2} and {3}. Hence, the torque induced at the MCP and PIP joints by F_B is given by

$$ \tau_B = {}^{0}J_3{}^{T}\,{}^{0}_{3}F $$

Evaluating the Jacoabian, ${}^{o}J_3$:

$$ {}^{0}\underline{\underline{J}}_3 = \begin{pmatrix} \frac{\partial {}^{0}P_{0\to 3}}{\partial \theta_1} & \frac{\partial {}^{0}P_{0\to 3}}{\partial \theta_2} & \frac{\partial {}^{0}P_{0\to 3}}{\partial \theta 3} \\ {}^{0}\hat{Z}_1 & {}^{0}\hat{Z}_2 & {}^{0}\hat{Z}_3 \end{pmatrix} $$

The position vector is the **p** vector of the transformation matrix ${}^{0}_{3}T$ and given by:

$$ {}^{0}P_{0\to 3} = \begin{pmatrix} L_1 c_1 c_2 \\ L_1 s_1 c_2 \\ L_1 s_2 \end{pmatrix} $$

$$ \frac{\partial {}^{0}P_{0\to 3}}{\partial \theta_1} = \begin{pmatrix} -L_1 s_1 c_2 \\ L_1 c_1 c_2 \\ 0 \end{pmatrix} \qquad \frac{\partial {}^{0}P_{0\to 3}}{\partial \theta_2} = \begin{pmatrix} -L_1 c_1 s c_2 \\ -L_1 s_1 s_2 \\ L_1 c_2 \end{pmatrix} \qquad \frac{\partial {}^{0}P_{0\to 3}}{\partial \theta_3} = \begin{pmatrix} 0 \\ 0 \\ 0 \end{pmatrix} $$

$$ {}^{0}\hat{Z}_1 = \underline{a}\left({}^{o}_{1}R\right) = \begin{bmatrix} 0 \\ 0 \\ 1 \end{bmatrix} \qquad {}^{0}\hat{Z}_2 = \underline{a}\left({}^{0}_{2}R\right) = \begin{bmatrix} s_1 \\ -c_1 \\ 0 \end{bmatrix} \qquad {}^{0}\hat{Z}_3 = \underline{a}\left({}^{0}_{3}R\right) = \begin{bmatrix} s_1 \\ -c_1 \\ 0 \end{bmatrix} $$

As such,

$$ {}^{0}\underline{\underline{J}}_{3} = \begin{bmatrix} -L_1 s_1 c_2 & -L_1 c_1 c_2 & 0 \\ L_1 c_1 c_2 & -L_1 s_1 s_2 & 0 \\ 0 & L_1 c_2 & 0 \\ 0 & s_1 & s_1 \\ 0 & -c_1 & -c_1 \\ 0 & 0 & 0 \end{bmatrix} $$

Evaluating the force ${}^{0}_{3}F$:

The known force acting at the middle of the proximal link is ${}^{3}F_{B}$. This force needs to be expressed as ${}^{0}_{3}F$, that is, transformed to the PIP joint and written with respect to the base reference frame {0}. This force transformation is given as:

$$ {}^{0}F_{3} = {}^{0}_{3}TF_{B\to 3}\,{}^{3}F_{B} $$

The force-moment transform is given by:

$$ {}^{0}_{3}TF_{3\to B} = \begin{bmatrix} {}^{0}_{3}R & 0_{3x3} \\ ({}^{0}\tilde{P}_{3\to B}\,{}^{0}_{3}R) & {}_{3}R \end{bmatrix} $$

where: ${}^{0}\tilde{P}_{3\to B}$ is a skew-symmetric matrix of the position vector defining PIP frame with respect to the point of application of the force at frame {B}and expressed in terms of the base frame {0} and ${}^{0}_{3}R$ is rotation matrix representing the orientation of frame {3} with respect to the base frame {0}.

$$ {}^{0}P_{3\to B} = {}^{0}_{3}R\,{}^{3}P_{3\to B} = {}^{0}_{3}R \begin{pmatrix} L_B \\ 0 \\ 0 \end{pmatrix} $$

$$ {}^{0}_{3}R = (n,o,a)^{0}_{3}T = \begin{pmatrix} c_1 c_{23} & -c_1 s_{23} & s_1 \\ s_1 c_{23} & -s_1 s_{23} & -c_1 \\ s_{23} & c_{23} & 0 \end{pmatrix} $$

$$ {}^{0}_{3}TF_{3\to B} = \begin{pmatrix} c_1c_{23} & -c_1s_{23} & s_1 & 0 & 0 & 0 \\ s_1c_{23} & -s_1c_{23} & c_1 & 0 & 0 & 0 \\ s_{23} & c_{23} & 0 & 0 & 0 & 0 \\ 0 & L_Bs_1 & L_Bc_1s_{23} & c_1c_{23} & c_1c_{23} & s_1 \\ 0 & -L_Bc_1 & L_Bs_1s_{23} & c_1c_{23} & s_1c_{23} & -c_1 \\ 0 & 0 & -L_Bc_{23} & s_{23} & c_{23} & 0 \end{pmatrix} $$

Let $ {}^{3}F_B = \left(f_{x_B}, f_{y_B}, f_{z_B}, m_{x_B}, m_{y_B}, m_{z_B}\right) $

Then, $ {}^{0}F_3 = {}^{0}_{3}TF_{B\to 3}\,{}^{3}F_B $

$$ {}^{0}_{3}F = \begin{pmatrix} f_{x_B}c_1c_{23} - f_{y_B}c_1s_{23} + f_{z_B}s_1 \\ f_{x_B}s_1c_{23} - f_{y_B}s_1s_{23} - f_{z_B}c_1 \\ f_{x_B}s_{23} + f_{y_B}c_{23} \\ f_{y_B}L_Bs_1 + f_{z_B}L_Bc_1s_{23} + m_{x_B}c_1c_{23} - m_{y_B}c_1s_{23} + m_{z_B}s_1 \\ -f_{y_B}L_Bc_1 + f_{z_B}L_Bs_1s_{23} + m_{x_B}s_1c_{23} - m_{y_B}s_1s_{23} - m_{z_B}c_1 \\ -f_{z_B}L_Bc_{23} + m_{x_B}s_{23} + m_{y_B}c_{23} \end{pmatrix} $$

Evaluation torque at MCP and PIP induced by $ F_B $

$$ \tau_B = {}^{0}J_3{}^{T}\,{}^{0}_{3}F $$

$$ \tau_B = \begin{pmatrix} -f_{z_B}L_1c_2 - f_{Z_B}L_Bc_{23} + m_{x_B}s_{23} + m_{x_B}s_{23} + m_{y_B}c_{23} \\ f_{x_B}L_1s_3 - f_{y_B}L_1c_3 + f_{y_B}L_Bm_{z_B} \\ f_{y_B}L_B + m_{z_B} \end{pmatrix} $$

Since the forces on the middle does not produce any torque on the DIP joints, then τ_B can be rewritten as:

$$ \tau_B = \begin{pmatrix} -f_{z_B}L_1c_2 - f_{Z_B}L_Bc_{23} + m_{x_B}s_{23} + m_{x_B}s_{23} + m_{y_B}c_{23} \\ f_{x_B}L_1s_3 - f_{y_B}L_1c_3 + f_{y_B}L_Bm_{z_B} \\ f_{y_B}L_B + m_{z_B} \\ 0 \end{pmatrix} $$

III. Forces Acting On The Distal Phalange

Let the force acting on the proximal joint be F_C and the point of application of the force be (x_C, y_C, z_B). A frame {C} is assigned at the point of application of the force F_B.

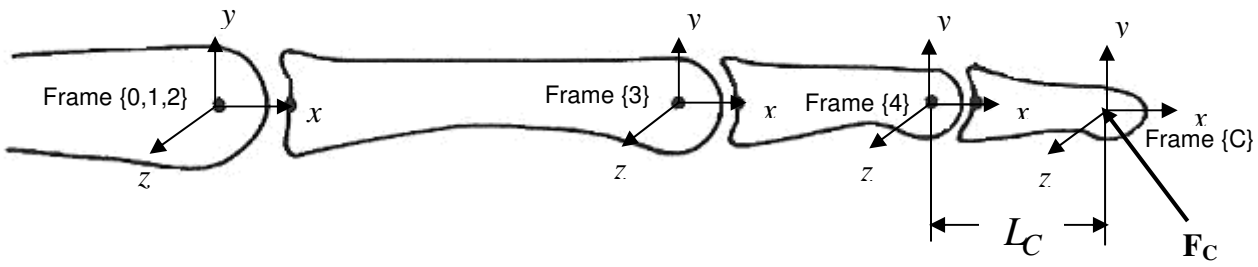

The D-H parameters for a two-link manipulator are:

i	α_{i-1}	a_{i-1}	d_i	θ_i	i+1
0	0	0	0	θ_1	1
1	90^o	0	0	θ_2	2
2	0	L_1	0	θ_3	3
3	0	L_2	0	θ_4	4
4	0	L_C	0	0	5

The link transforms (**n**, **o**, **a**, **p**) are evaluated as

${}^0_1T$, ${}^1_2T$ and ${}^2_3T$ are the same as described in Section I and Section II.

$$ {}^3_4T = \begin{bmatrix} c_4 & -s_4 & 0 & L_2 \\ s_4 & c_4 & 0 & 0 \\ 0 & 0 & 1 & 0 \\ 0 & 0 & 0 & 1 \end{bmatrix} \qquad {}^4_CT = \begin{bmatrix} 1 & 0 & 0 & L_C \\ 0 & 1 & 0 & 0 \\ 0 & 0 & 1 & 0 \\ 0 & 0 & 0 & 1 \end{bmatrix} $$

This force will induce joint moments at the MCP, PIP and DIP joints, that is, joint at frame{2}, {3}, {4}. Hence, the torque induced by F_C is given by

$$\tau_C = {}^0J_4{}^T\,{}^0_4F$$

Evaluating the Jacoabian, ${}^0J_4$:

$${}^0\underline{J}_4 = \begin{pmatrix} \dfrac{\partial {}^0P_{0\to4}}{\partial\theta_1} & \dfrac{\partial {}^0P_{0\to4}}{\partial\theta_2} & \dfrac{\partial {}^0P_{0\to4}}{\partial\theta_3} & \dfrac{\partial {}^0P_{0\to4}}{\partial\theta_4} \\ {}^0\hat{Z}_1 & {}^0\hat{Z}_2 & {}^0\hat{Z}_3 & {}^0\hat{Z}_4 \end{pmatrix}$$

The position vector is the **p** vector of the transformation matrix ${}^0_4T$ and given by:

$${}^0P_{0\to4} = \begin{pmatrix} c_1(L_1c_{23} + L_1c_2 \\ s_1(L_2c_{23} + L_1c_2 \\ (L_2s_{23} + L_1s_2 \end{pmatrix}$$

$$\frac{\partial {}^0P_{0\to4}}{\partial\theta_1} = \begin{pmatrix} -s_1(L_2c_{23} + L_1c_2) \\ -c_1(L_2c_{23} + L_1c_2) \\ 0 \end{pmatrix} \qquad \frac{\partial {}^0P_{0\to4}}{\partial\theta_2} = \begin{pmatrix} -c_1(L_2s_{23} + L_1s_2) \\ s_1(L_2s_{23} + L_1s_2) \\ L_2c_{23} + L_1c_2 \end{pmatrix}$$

$$\frac{\partial {}^0P_{0\to4}}{\partial\theta_3} = \begin{pmatrix} -L_2c_1s_{23} \\ -L_2s_1s_{23}) \\ L_2c_{23} \end{pmatrix} \qquad \frac{\partial {}^0P_{0\to4}}{\partial\theta_4} = \begin{pmatrix} 0 \\ 0 \\ 0 \end{pmatrix}$$

$${}^0\hat{Z}_1 = \underline{a}\left({}^o_1R\right) = \begin{bmatrix} 0 \\ 0 \\ 1 \end{bmatrix} \qquad {}^0\hat{Z}_2 = \underline{a}\left({}^0_2R\right) = \begin{bmatrix} s_1 \\ -c_1 \\ 0 \end{bmatrix}$$

$${}^0\hat{Z}_3 = \underline{a}\left({}^0_3R\right) = \begin{bmatrix} s_1 \\ -c_1 \\ 0 \end{bmatrix} \qquad {}^0\hat{Z}_4 = \underline{a}\left({}^0_4R\right) = \begin{bmatrix} s_1 \\ -c_1 \\ 0 \end{bmatrix}$$

As such,

$$ {}^{0}\underline{\underline{J}}_{4} = \begin{bmatrix} -s_1(L_1c_{23}+L_1c_2) & -c_1(L_1s_{23}+L_1s_2) & -L_2c_1s_{23} & 0 \\ c_1(L_1c_{23}+L_1c_2) & s_1(L_1s_{23}+L_1s_2) & -L_2s_1s_{23} & 0 \\ 0 & L_1c_{23}+L_1c_2 & L_2c_1s_{23} & 0 \\ 0 & s_1 & s_1 & s_1 \\ 0 & -c_1 & -c_1 & -c_1 \\ 1 & 0 & 0 & 0 \end{bmatrix} $$

Evaluating the force ${}^{0}_{4}F$:

The known force acting at the middle of the proximal link is $4F_C$. This force needs to be expressed as ${}^{0}_{4}F$, that is, transformed to the DIP joint and written with respect to the base reference frame {0}. This force transformation is given as:

$$ {}^{0}F_4 = {}^{0}_{4}TF_{C\to 4}\,{}^{4}F_C $$

The force-moment transform is given by:

$$ {}^{0}_{4}TF_{4\to C} = \begin{bmatrix} {}^{0}_{4}R & 0_{3x3} \\ ({}^{0}\tilde{P}_{4\to C}\,{}^{0}_{4}R) & {}^{0}_{4}R \end{bmatrix} $$

where: ${}^{0}\tilde{P}_{4\to C}$ is a skew-symmetric matrix of the position vector defining DIP frame with respect to the point of application of the force at frame {C}and expressed in terms of the base frame {0}) and ${}^{0}_{4}R$ is rotation matrix representing the orientation of frame {4} with respect to the base frame {0}.

$$ {}^{0}P_{4\to C} = {}^{0}_{4}R\,{}^{4}P_{4\to C} = {}^{0}_{4}R\begin{pmatrix} L_C \\ 0 \\ 0 \end{pmatrix} = \begin{pmatrix} L_Cc_1c_{234} \\ L_Cs_1c_{234} \\ L_Cs_{234} \end{pmatrix} $$

$$ {}^{0}_{4}R = (n,o,a)^{0}_{4}T = \begin{pmatrix} c_1c_{234} & -c_1s_{234} & s_1 \\ s_1c_{234} & -s_1s_{234} & -c_1 \\ s_{234} & c_{234} & 0 \end{pmatrix} $$

$$ {}^{0}_{4}TF_{4\to C} = \begin{pmatrix} c_1c_{234} & -c_1s_{234} & s_1 & 0 & 0 & 0 \\ s_1c_{234} & -s_1c_{234} & c_1 & 0 & 0 & 0 \\ s_{234} & c_{234} & 0 & 0 & 0 & 0 \\ 0 & L_Cs_1 & L_Bc_1s_{23} & c_1c_{234} & c_1c_{234} & s_1 \\ 0 & -L_Cc_1 & L_Bs_1s_{23} & c_1c_{234} & s_1c_{234} & -c_1 \\ 0 & 0 & -L_Bc_{23} & s_{234} & c_{234} & 0 \end{pmatrix} $$

Let $ {}^{4}F_C = \left(f_{x_C}, f_{y_C}, f_{z_C}, m_{x_C}, m_{y_C}, m_{z_C}\right) $

Then, $ {}^{0}F_4 = {}^{0}_{4}TF_{C\to 4}\,{}^{4}F_C $

$$ {}^{0}_{4}F = \begin{pmatrix} f_{x_B}c_1c_{234} - f_{y_c}c_1s_{234} + f_{z_C}s_1 \\ f_{x_c}s_1c_{234} - f_{y_C}s_1s_{234} - f_{z_C}c_1 \\ f_{x_C}s_{234} + f_{y_C}c_{234} \\ f_{y_c}L_Cs_1 + f_{z_C}L_Cc_1s_{234} + m_{x_C}c_1c_{234} - m_{y_c}c_1s_{234} + m_{z_C}s_1 \\ -f_{y_C}L_Bc_1 + f_{z_C}L_1s_1s_{234} + m_{x_C}s_1c_{234} - m_{y_C}s_1s_{234} - m_{z_C}c_1 \\ -f_{z_C}L_Cc_{234} + m_{x_C}s_{234} + m_{y_C}c_{234} \end{pmatrix} $$

Evaluation torque at MCP, PIP and DIP joints, induced by $ F_C $:

$$ \tau_C = {}^{0}J_4{}^{T}\,{}^{0}_{4}F $$

$$ \tau_C = \begin{pmatrix} -f_{Z_C}L_2c_{23} - f_{Z_C}L_1c_2 - f_{Z_C}L_Cc_{234} + m_{x_C}s_{234} + m_{y_C}c_{234} \\ f_{x_C}L_2s_4 - f_{y_C}L_2c_4 + f_{x_C}L_1s_{34} + f_{y_C}L_1c_{34} + f_{y_C}L_C + m_{z_C} \\ f_{x_C}L_2s_4 + f_{y_C}L_2c_4 + f_{y_C}L_C + m_{z_C} \\ f_{y_C}L_C + m_{zC} \end{pmatrix} $$